Analysis of Spacecraft Data for the Study of Diverse Lunar Volcanism and Regolith Maturation Rates

by

Sarah E. Braden

A Dissertation Presented in Partial Fulfillment
of the Requirement for the Degree
Doctor of Philosophy

Approved November 2013 by the
Graduate Supervisory Committee:

Mark S. Robinson, Chair
James F. Bell III
Philip R. Christensen
Amanda B. Clarke
Samuel J. Lawrence

ARIZONA STATE UNIVERSITY

December 2013

ABSTRACT

Lunar Reconnaissance Orbiter (LRO) and MErcury Surface, Space ENvironment, GEochemistry, and Ranging (MESSENGER) spacecraft missions provide new data for investigating the youngest impact craters on Mercury and the Moon, along with lunar volcanic end-members: ancient silicic and young basaltic volcanism.

The LRO Wide Angle Camera (WAC) and Narrow Angle Camera (NAC) in-flight absolute radiometric calibration used ground-based Robotic Lunar Observatory and Hubble Space Telescope data as standards. In-flight radiometric calibration is a small aspect of the entire calibration process but an important improvement upon the pre-flight measurements. Calibrated reflectance data are essential for comparing images from LRO to missions like MESSENGER, thus enabling science through engineering.

Relative regolith optical maturation rates on Mercury and the Moon are estimated by comparing young impact crater densities and impact ejecta reflectance, thus empirically testing previous models of faster rates for Mercury relative to the Moon. Regolith maturation due to micrometeorite impacts and solar wind sputtering modifies UV-VIS-NIR surface spectra, therefore understanding maturation rates is critical for interpreting remote sensing data from airless bodies. Results determined the regolith optical maturation rate on Mercury is 2 to 4 times faster than on the Moon.

The Gruithuisen Domes, three lunar silicic volcanoes, represent relatively rare lunar lithologies possibly similar to rock fragments found in the Apollo sample collection. Lunar nonmare silicic volcanism has implications for lunar magmatic evolution. I estimated a rhyolitic composition using morphologic comparisons of the Gruithuisen Domes, measured from NAC 2-meter-per-pixel digital topographic models (DTMs), with terrestrial silicic dome morphologies and laboratory models of viscoplastic dome growth.

Small, morphologically sharp irregular mare patches (IMPs) provide evidence for recent lunar volcanism widely distributed across the nearside lunar maria, which has implications for long-lived nearside magmatism. I identified 75 IMPs (100-5000 meters in dimension) in NAC images and DTMs, and determined stratigraphic relationships between units common to all IMPs. Crater counts give model ages from 18-58 Ma, and morphologic comparisons with young lunar features provided an additional age constraint of <100 Ma. The IMPs formed as low-volume basaltic eruptions significantly later than previous evidence of lunar mare basalt volcanism's end (∼1-1.2 Ga).

I dedicate this thesis to my parents, Margaret and Robert Braden, who encouraged me to study science and gave me everything I needed to grow.

To Trevor Olson: Thank you for sharing this entire journey with me. I am so grateful I found you along the way!

To Sarah Brewer and Jenica Watts: You are always there for me. Your constant encouragement and confidence means everything.

To Polly and Bill Olson: Thank you for all the support and warm meals.

ACKNOWLEDGEMENTS

This thesis would not have been possible without the guidance of my advisor, Professor Mark Robinson. I also acknowledge my other committee members, Professors Amanda Clark, James Bell, and Phil Christensen, and Dr. Samuel Lawrence for useful and insightful conversations. Special thanks goes to Dr. Samuel Lawrence for hours of discussion, professional advice, and support from the beginning of my time at Arizona State University. I appreciate the consistent hard work and camaraderie of the entire Lunar Reconnaissance Orbiter Camera Science Operation Center Team and the SOCET SET DTM production team. I would also like to thank Professor John Shumway for maintaining the github repository with the LaTeX dissertation template.

I gratefully acknowledge support for this research by NASA through Lunar Reconnaissance Orbiter Project and the MErcury Surface, Space ENvironment, GEochemistry, and Ranging mission.

TABLE OF CONTENTS

CHAPTER Page

CHAPTER Page

CHAPTER Page

LIST OF TABLES

LIST OF FIGURES

Figure Page

Figure Page

Chapter 1

INTRODUCTION

This dissertation uses a multiple-path approach to planetary science including in-flight instrument calibration and data analysis. Three scientific studies are presented here, focused on geologically young terrains and two distinct varieties of lunar volcanism. Two recent spacecraft missions to the Moon and Mercury, the Lunar Reconnaissance Orbiter (LRO) and MESSENGER (MErcury Surface, Space ENvironment, GEochemistry, and Ranging), provided new data for interpreting surface geology, ages, and composition. The LRO spacecraft launched on June 18, 2009 and achieved lunar orbital insertion on June 23, 2009. The MESSENGER spacecraft, launched in August 2004, had a series of three flybys in January 2008, October 2008, and September 2009 before it successfully entered Mercurys orbit on March 18, 2011 and became the first spacecraft to orbit the planet Mercury. Since the Mariner 10 flybys of Mercury in 1974 and 1975, many scientists thought that Mercury was essentially a larger version of the Moon because both are rocky, airless bodies in the inner solar system. The MESSENGER mission has uncovered much more evidence describing how Mercury and the Moon are fundamentally different in composition, magnetism, and thermal environment. The influx of petabytes of new remote sensing data from LRO and MESSENGER provided a veritable goldmine of new information to explore.

Chapter 2, Engineering in Support of Science: Preliminary LROC In-Flight Radiometric Calibration, describes the LROC in-flight absolute radiometric calibration, which enables science through engineering. Understanding the camera mechanics and image calibration processes is key to using images and creating mosaics for research.

The in-flight radiometric calibration of the Lunar Reconnaissance Orbiter Cameras (LROC) Narrow Angle and Wide Angle cameras uses planetary and ground-based datasets (the Hubble Space Telescope and Robotic Lunar Observatory, respectively), and significantly improves upon the pre-flight laboratory values. The process of calculating the radiometric calibration factors is discussed further in Chapter 2.

Chapter 3 uses a study of young impact crater density on Mercury and the Moon to quantitatively estimate the relative optical regolith maturation rates. Previous studies (Hapke, 1977; Cintala, 1992; Hapke, 2001; Noble and Pieters, 2003) modeled that the rate of optical maturation must be greater on Mercury than on the Moon, and this is the first study where observational evidence supports those models. Optical maturity of regolith due to space weathering effects modifies the UV-VIS-NIR spectra of the surface, and therefore understanding processes and rates is critical for the interpretation of remote sensing data on airless bodies. Analysis of Copernican and Kuiperian craters (youngest time-stratigraphic units on the Moon and Mercury, respectively) determines that the optical maturation rate of regolith on Mercury is up to 4 times faster than on the Moon, leading to the conclusion that the Kuiperian crater population is overall younger than the Copernican crater population. Chapter 3 also examines the range of maturity and reflectance within the population of immature materials. The state of regolith maturity indicates the relative ages of geologically young materials on the Moon and Mercury. This study finds that the range of states of maturity is smaller on Mercury compared to the Moon, which may be due to the faster rate of maturation on Mercury. The average reflectance of immature lunar material is a factor of 1.9 ± 0.4 higher than the reflectance of immature materials on Mercury, which is attributable to differences in surface composition. An analysis of ray length to diameter ratios is consistent with similar relative ages for a subset of immature craters on Mercury and the Moon.

Chapter 4, The Gruithuisen Domes: Age and Morphology of Silicic Nonmare Volcanism, examines the Gruithuisen Domes, using LROC mosaics and stereo NAC derived digital topographic models to further constrain the ages, explain the observed morphology, and determine the mode of emplacement for the three domes. The Gruithuisen Domes are a set of three ancient (∼3.6 Ga old) silicic domes located at (36.6°N, 319.9°E), which belong to a group of lunar features called red-spots (Whitaker, 1972; Malin, 1974) for their spectral characteristics: strong absorption in the ultraviolet and high reflectance in longer (red) wavelengths. The Gruithuisen Domes may be the source region for fragments of granitic or felsite material found in lunar breccias within the Apollo sample inventory (Jolliff et al., 1991, 1998; Korotev, 1998; Papike et al., 1998). Silicic volcanism might have been more widespread during the Moon's early history, however even small volumes of silicic, non-mare volcanic material challenge current models of lunar magmatic evolution. Recently, new data from the Diviner instrument on the LRO spacecraft confirmed that the Gruithuisen Domes are silicic (Glotch et al., 2010; Greenhagen et al., 2010). No other study has used high-resolution LROC images (50 cm scale) or DTMs (2 meter horizontal scale) to determine the processes through which the domes formed, or explain the observed morphology. Datasets used in this chapter include LROC NAC topography, LROC WAC topography, NAC images at 50 cm per pixel, LROC WAC multispectral observations, Clementine TiO_2, FeO, and OMAT maps, and Diviner maps of relative silica content (at 256 m/px scale). NAC topography provides detailed information on the ridges found on the slopes of the domes, which are remnants of the original volcanic flows. DTMs also provide volume estimates and elevation profiles use to compare the morphology of the Gruithuisen Domes to terrestrial examples of silicic volcanism. A previous study of the Gruithuisen Domes using Diviner and images from the Moon Mineralogy Mapper (Kusuma et al., 2012) called for new NAC-based crater counts to

determine if the domes erupted contemporaneously or if there was a significant pause between eruptions. Crater size frequency distributions from the summit plateau regions of the Delta and Gamma domes, which reveal a resurfacing event due to crater impact, and confirm that the Delta and Gamma domes erupted at about the same time.

Chapter 5 is a study of small, morphologically sharp Irregular Mare Patches, or IMPs, for the larger purpose of investigating the temporal extent of mare basalt volcanism. IMPs are possibly the most recent volcanic activity on the lunar surface based on the low density of impact craters and the sharp morphology within the geologic units of the IMPs, which are further discussed in Chapter 5. The IMPs are hypothesized here to be remnants of late-stage mare basalt vents and the youngest examples of volcanism on the lunar surface (largest IMP is 5 km in the longest dimension). Recent crater number density data from the textbook example IMP Ina are consistent with a contemporary or younger age compared to the surrounding mare (Robinson et al., 2010). Previous studies have suggested that the units within Ina formed relatively recently as a caldera (Whitaker, 1972; El-Baz and Worden, 1972; El Baz, 1973), through explosive volcanism (Schultz et al., 2006), or through lava flow inflation processes (Garry et al., 2012). At this time, studies have been limited to the Ina and Hyginus calderas, and the Cauchy-5 dome (Carter et al., 2013). I documented 75 IMPs (largest dimension >100 m), which are distributed widely across the nearside lunar maria, with occurrences in Mare Tranquillitatis over to Aristarchus crater and up to the Gruithuisen region. I used Lunar Reconnaissance Orbiter Narrow Angle Camera (NAC) images to identify IMPs and further study a subset of the IMPs with the multispectral Wide Angle Camera and Digital Topographic Models (DTM) derived from NAC stereo pairs. I examined the relationship between the IMPs and multiple variables to determine their origin. Methods used include crater

size-frequency distributions and morphological analysis to further constrain the ages of the IMPs based on comparisons of other young Copernican lunar features. Studying the whole population of IMPs determined the stratigraphic relationships of the two units common to all IMPs: smooth and uneven. The smooth units within the IMPs are proposed to be volcanic in origin based on their occurrence in mare basalt, spectral signature, and association with volcanic structures and effusive deposits. I demonstrate that the topography of the smooth units is consistent with single layer mare flows. The stratigraphically older uneven units are interpreted here to be fractured mare basalt, which is consistent with the spectral signatures and appearance at different lighting conditions. I conclude that the IMPs studied here were formed as small basaltic eruptions and are <100 Ma in age, which is significantly younger than all previous estimates for the end of lunar mare basalt volcanism at ∼1-1.2 Ga (e.g. Schultz and Spudis, 1983; Hiesinger et al., 2003, 2011). Lunar volcanism <100 Ma old is a paradigm shift in our understanding of the current lunar thermal regime, as well as the current ideas on thermal evolution of the lunar interior. No samples of lunar material as young as ∼100 Ma have been found, with the youngest lunar sample in the literature being the lunar meteorite NWA 773, which is ∼2.8 Ma old (Borg et al., 2004). Sample return from Ina or one of the other major IMPs should be added to the list of critical materials to be returned from the Moon for radiometric age dating. The science based on new data challenges old hypotheses developed during the era of lunar exploration after Apollo, and the models of the lunar interior will require an update.

Through the study of a diverse group of spacecraft datasets, this dissertation describes the calibration methods that tie new remote sensing image data to scientific units, examines the lifetimes of fresh, young craters on the airless surfaces of Mercury and the Moon, and explores extremes of lunar volcanism. In Chapter 3, the basic

concepts of comparative planetology are leveraged to use our knowledge of the Moon to learn more about rates of optical regolith maturation on Mercury. Chapter 4 uses new data from LRO to revisit the geology of the ancient Gruithuisen Domes and add to the story of these rare, yet significant silicic, nonmare volcanoes. Finally, the curious Ina caldera, studied from the time of the Apollo missions (Whitaker, 1972; El-Baz and Worden, 1972), is joined by a series of similar features discovered through the high-resolution LROC NAC to make a compelling story of the IMPs as evidence for long-lived nearside magmatism.

Chapter 2

ENGINEERING IN SUPPORT OF SCIENCE: PRELIMINARY LUNAR RECONNAISSANCE ORBITER CAMERA IN-FLIGHT RADIOMETRIC CALIBRATION

2.1 Introduction

Here ultraviolet and visible (UV-VIS) spectral reflectance data from the US Geological Survey (USGS) RObotic Lunar Observatory (ROLO) (e.g. Kieffer and Stone, 2005) and the Hubble Space Telescope (HST) are analyzed to provide in-flight radiometric calibration coefficients for the Lunar Reconnaissance Orbiter Cameras (LROC) (Robinson et al., 2010). This chapter documents the methods used to derive the preliminary radiometric calibration coefficients (work from 2010-2011) for the lronaccal and lrowaccal programs within the ISIS3 software package (Anderson et al., 2004). After an introduction to the motivation for in-flight radiometric calibration and the ROLO images, two sections will address the calibration process for both LROC cameras.

Radiometric calibration relates pixel digital number (DN) values to physical parameters. Radiance is a physical parameter defining the power received by the optical system and characterizes the total reflection from the surface which is tied to material properties. While the laboratory calibration includes derivation of calibration coefficients (multiplicative factors) for each band which translate DNs to radiance, an in-flight calibration is also required. The need for in-flight calibration is based on the realities of spaceflight. Instruments in-flight commonly experience changes from their pre-launch calibrations and some in-flight calibration system, such as solar diffusers,

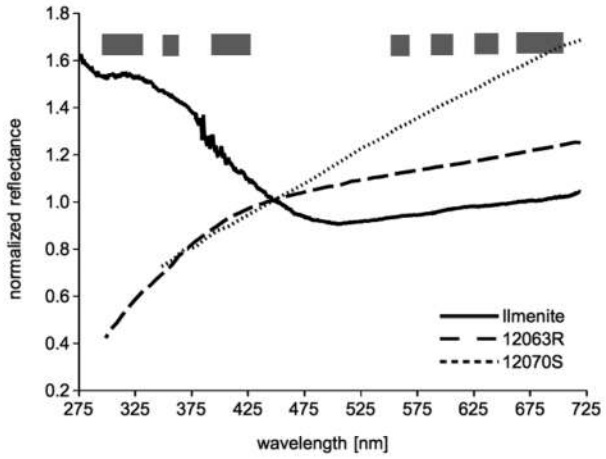

Figure 2.1: Spectra of ilmenite (solid line) shows a distinctive downturn in reflectance near 500 nm. The LRO Wide Angle Camera (WAC) has the unique ability to acquire measurements in the UV (321, 360 nm) that are well suited to separate ilmenite from basalt. Low titanium rock (dashed line 12063R) and soil samples (dotted line 12070S) are plotted for reference (normalized at 450 nm). Figure after (Robinson et al., 2010).

can be affected by exposure to the space radiation environment or contamination (e.g. Gellman et al., 1993; Thome et al., 1993; Slater et al., 1995; Guenther et al., 1996; Alhajjah et al., 2004). In-flight calibration is critical for the long-term stability of data collection and calibration traceability. Calibration traceability and stability over time for climate records is a notable terrestrial example of in-flight calibration's importance (Mekhontsev and Hanssen, 2007). In the lunar case, traceable absolute radiometric calibration allows for comparisons between images collected with different spacecraft cameras. In order to perform an in-flight radiometric calibration a reference is required. The ground-based ROLO data provides a multispectral standard for both Earth-observing and Moon-observing spacecraft cameras alike (Kieffer and Stone, 2005; Sun et al., 2006). ROLO began operations in 1996 as a NASA-sponsored project to accurately determine the irradiance and radiance of the Moon (Kieffer and Anderson, 1998; Stone and Kieffer, 2002; Kieffer and Stone, 2005).

Radiometric calibration provides scientifically useful units that can be used to quantify the UV-VIS spectra of various lunar geologic terrains. Surface spectra are used to determine mineralogy and maturity of the lunar regolith. The LROC WAC was specifically built to improve estimates the amount of titanium in the lunar regolith (Robinson et al., 2010). Previous studies (Lucey et al., 2000a, 2000b) tested the relationship between the Clementine color bands and TiO_2 content of the mare. The spectra of ilmenite compared to basalts (Figure 2.1) illustrates the importance of UV bands in separating the spectral signature of ilmenite from basalt. In the Clementine dataset the 415/750 nm ratio indicates relative titanium content (Lucey et al., 2000b). The LROC WAC UV bands at 320 and 360 nm should be able to better constrain the relative titanium content, based on the spectra of ilmenite (Figure 2.1).

Early lunar remote sensing with ground-based (UV-VIS) spectral reflectance data first revealed the presence of large-scale ($>$ 10 km) color units within the nearside mare (Pieters, 1978). Using the Apollo samples as ground truth, subsequent studies (Charette et al., 1974, Whitaker, 1972) found correlations between the color units and compositional variations, especially for iron and titanium in the mare. Later, observations with the Clementine UV-VIS camera determined color units (lava flow units) globally and led to an effective method for deriving iron abundance from the multispectral data (Lucey et al., 1998, 2000b). Similar analysis determined titanium abundance (Lucey et al., 1998, 2000b), however a comparison with TiO_2 maps derived from the Lunar Prospector Neutron Spectrometer (Elphic et al., 1998, Elphic et al., 2002) shows a difference in absolute abundance of up to 50% in some mare areas. Recently, Hubble Space Telescope results showed that UV observations can be used to map TiO_2 variations within the mare at the Taurus-Littrow Valley (Robinson et al., 2007). Accurately characterizing TiO_2 variations in the mare is not only important for mapping lava flows, studying the heterogeneity of mantle sources, and understanding

differentiation early in the history of the Moon, but also for identifying areas suitable for in situ resource utilization.

2.2 Robotic Lunar Observatory (ROLO)

The ROLO dataset consists of over six years of regular ground-based telescopic multispectral measurements of the Moon spanning phase angles from -90° to +90° and wavelengths from 350 nm to 2450 nm in 32 spectral filters with a resolution of approximately 7 kilometers/pixel (Anderson, 1999a). The primary goal of the ROLO project is to develop a multispectral, spatially resolved photometric model of the Moon for the calibration of Earth-orbiting spacecraft (Kieffer and Stone, 2005). Consequently, the ROLO data are the most accurate measurements and radiometric calibration of spectral reflectance of the Moon. An empirical model fit to the disk-integrated phase curve in each filter provides a relative accuracy of $\sim 1\%$, although the absolute accuracy in any filter is on the order of 5-10% (Kieffer and Stone, 2005). From this model a discrete spectrum of the lunar nearside can be produced at an arbitrary phase angle. Absolute calibration (and atmospheric correction) of the ROLO data is derived from nightly stellar extinction measurements of the star Vega, (Kieffer and Stone, 2005).

Calibration, map projection, and data collection for the ROLO full-disk observations data used ISIS3[1] and IDL. Using an ISIS3 program (rolo2isis) written by Kris Becker of the USGS, the ROLO data files were calibrated and reprojected from the original azimuthal lambertian equal-area to orthographic projection (Kieffer and Stone, 2005). An additional step is required to convert the ROLO data from radiance in units of $W/m^2/sr/nm$ to I/F reflectance or reflectivity (considered unitless). Radiance is converted to I/F by taking into account the observation geometry and the

[1] http://isis.astrogeology.usgs.gov/

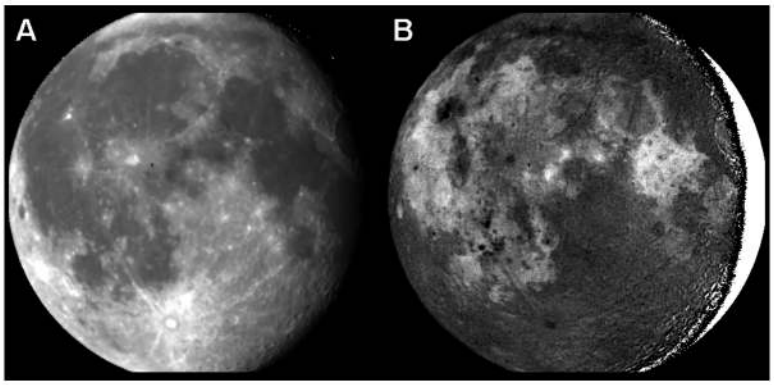

Figure 2.2: A) 415 nm ROLO image of the nearside of the Moon. Incidence angle is $\sim 30°$. B) ROLO ratio image of 350/415 nm (similar to the 360/415 nm WAC ratio, but lower resolution).

solar radiance coming from a normally illuminated Lambertian surface (Minnaert, 1961). The term I/F is also called radiance factor by Hapke (1993). The solar spectrum in units of irradiance (Cox, 2000) is interpolated to the ROLO bands, and then the ROLO data are converted from spectral radiance to I/F reflectance (a unitless ratio of reflected light over the incident solar radiation). The equation for converting radiance into I/F reflectance is:

$$I/F = \frac{\pi \cdot L_\lambda \cdot d^2}{I_{Sun,\lambda}}$$

where: I/F is unitless reflectance, L_λ is spectral radiance in units of W/m^2/sr/nm, $I_{Sun,\lambda}$ is the spectral solar irradiance in units of W/m^2/nm, and d is the Sun-Moon distance in astronomical units.

Absolute radiometric calibration of the LROC Narrow Angle Camera (NAC) and Wide Angle Camera (WAC) used ROLO data with specific photometric geometries (incidence, emission, and phase angles) in the same location with uniform terrain on the lunar surface. Since the ROLO data is of much lower resolution (7 km/px) than the LROC NAC (0.5-1.5 m/px) and WAC ($\sim$ 200 m/px), the values of all pixels in the NAC, WAC, and ROLO images for the same location were averaged to give one value

for the entire scene. No region of interest in the LROC data should be significantly smaller than the size of a ROLO pixel or else the surface reflectance which contributed to the single ROLO pixel will not coincide to the surface reflectance accounted for in the LROC scene.

2.3 Narrow Angle Camera In-Flight Radiometric Calibration

LROC and ROLO data were selected for a phase angle $\sim 30°$, emission angle $\sim 1°$, and incidence angle $\sim 30°$. Due to the large difference in pixel scale between the NACs and ROLO images, there is uncertainty in the match of sample areas. However, uniform terrains (mare basalt) on the lunar surface were chosen to minimize the percentage difference due to a mismatch. The ROLO pixels for comparison to the LROC NAC images came from a single ROLO image, mm185801 (Figure 2.2). The NAC pairs used in the comparison (Table 2.1) are all from LROCs commissioning phase (June 2009 to 15 September 2010). The commissioning phase NAC frames were chosen because they are lower resolution due to a higher orbit and therefore a better spatial match to the ROLO images. The NAC frames were reprojected to the resolution of the ROLO pixels to provide a better match. To minimize the error due to differences in emission angle between the ROLO and LROC datasets, the calibration process was restricted to NACs from within a sample area of $\pm 10°$ lat/lon from the sub-Earth point of the ROLO observation ($-1.65°$N, $1.01°$E).

After the selection of the NACs, the calibrated DN pixel values were averaged for each NAC. Calibrated DN values have ha the dark correction, flat-field, special pixel mask, and temperature correction applied to the image pixels (as opposed to raw DN, which do not have these corrections applied) (see Robinson et al., 2010 for more information). For an accurate comparison between the ROLO data and the NAC cameras, the ROLO I/F reflectance must be weighted by the responsivity function

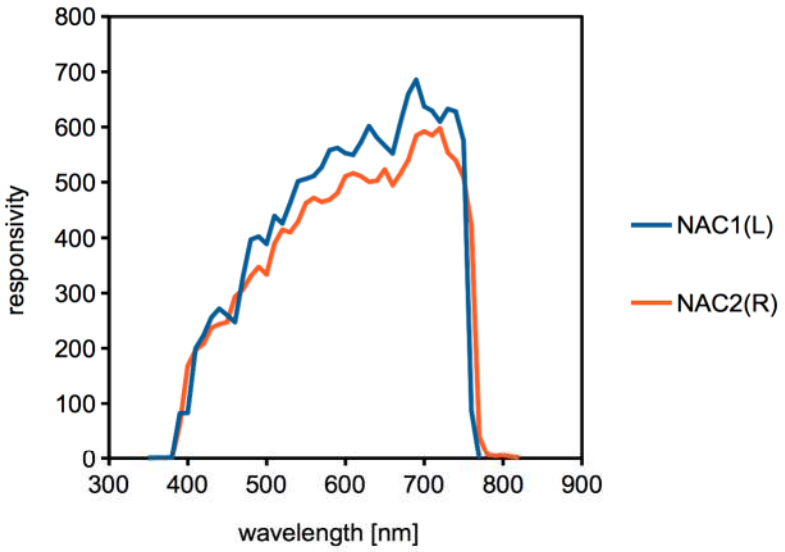

Figure 2.3: Spectral responsivity of NAC-L and NAC-R in units of (DN/s)/(μW/cm^2/steradian) from the pre-flight laboratory calibration (Robinson et al., 2010).

of the NAC cameras (Figure 2.3) and integrated across the range of NAC optical sensitivity. The ROLO bandpasses are narrower (see Kieffer and Stone, 2005) than the single, wide bandpass of the LROC NAC cameras, and thus require a normalization. The ROLO I/F values are weighted by the NAC responsivity and then the area under the curve is calculated. The equation used for ROLO weighted I/F is:

$$I/F_{weightedROLO} = \frac{\int I/F_{ROLO}(\lambda) \cdot I_{Sun}(\lambda) \cdot r(\lambda)}{\int I_{Sun}(\lambda) \cdot r(\lambda)}$$

where: $I_{Sun}(\lambda)$ is solar irradiance at a distance of 1 AU in units of W·m^2, $r(\lambda)$ is spectral responsivity with units of (DN/s)/(W/(m^2·sr·nm), and I/F$_{ROLO}(\lambda)$ is the ROLO reflectance. With the weighted ROLO I/F values the I/F calibration factor (or coefficient) can be calculated using the average NAC calibrated DN and the image exposure time:

$$IFCF = \frac{(\mathrm{DN}/\tau)}{I/F_{weightedROLO}}$$

where: IFCF is the I/F calibration factor, τ is the exposure time in units of ms, and

DN is the average calibrated DN of the NAC image.

This IFCF converts calibrated NAC DNs to I/F (reflectance). The resulting absolute calibration coefficients are preliminary (Table 2.1). A wider range of photometric geometries need to be tested on images from throughout the LROC commissioning and primary mission in order to constrain the error and limitation of the absolute calibration coefficients across many viewing geometries and examine any time dependent changes in the LROC data.

NAC Name	**I/F CF NAC L**	**I/F CF NAC R**
M106834367	15957	15659
M106849054	15854	15495
M106856083	15535	15193
M106863144	16023	15978
M106870401	16039	15733
M106884630	16043	15505
M106884914	15663	14968
M106913277	14921	15041
M106913598	15238	15665
M106920449	15196	14731
Average	15647	15397
Standard Deviation	409	396
Laboratory	6890	6890

Table 2.1: Radiometric conversion factors derived from ROLO data and 10 LROC NAC L and R pairs from lunar orbit. The pre-launch laboratory calibrated radiometric conversion factors are listed at the bottom for comparison (CF=Conversion Factor). Laboratory calibration of the two cameras is documented in (Robinson et al., 2010).

2.4 Wide Angle Camera (WAC) In-Flight Radiometric Calibration

The WAC has two ultraviolet filters (320 and 360 nm) and five visible filters (415, 565, 605, 645, and 690 nm) (Table 2.2). These bandpasses were selected to characterize spectral features for some common minerals found on the lunar surface, and to compliment Clementine UV-VIS and NIR datasets (Nozette et al., 1994), as well as VIS-NIR image data collected by Chandrayaan-1 and the SELenological and ENgineering Explorer (SELENE) (Green et al. 2007; Haruyama et al., 2008). A summary of the complete laboratory calibration process for the WAC images is found in Robinson et al., 2010.

ROLO was used to provide absolute radiometric coefficients to convert calibrated LROC WAC DN into units of radiance and I/F for the 360, 415, 566, 604, 643, and 689 nm bands. The two shortest wavelength bands of ROLO are 347 nm and 353 nm, so the absolute radiometric coefficient for the LROC WAC 320 nm was preliminarily based on the ratio of the 321/360 nm band laboratory calibration.

band [nm]	λ_{eff} **[nm]**	**FWHM [nm])**	**RC** $([W/m^3/sr)/(DN/s)]$
320	321	32	865
360	360	15	918
415	415	36	3727
565	566	20	3310
605	604	20	3377
645	643	23	3273
690	689	39	2612

Table 2.2: Table 4 from Robinson et al. (2010). WAC filter bandpasses and laboratory derived responsivity coefficient (RC).

At wavelengths shorter than $\sim$ 300 nm scattering and continuum absorption by

gases and airborne particles (aerosols) the Earth's atmosphere is nearly opaque (Crisp, 2000). For cloud-free conditions, Rayleigh scattering by the N_2 and O_2 molecules in the atmosphere accounts for most of the scattering (Crisp, 2000). Rayleigh scattering in the Earth's atmosphere is wavelength dependent, causing increased scattering at shorter (bluer) wavelengths, and only accounts for scattering from particles up to one tenth of the wavelength of the incident light. The amount of Rayleigh scattering that occurs for light depends upon the size of the particles and the wavelength of the light. Strong dependence on wavelength (λ^{-4}) causes shorter wavelengths to be scattered more strongly than longer wavelengths. In this case, the intensity of Rayleigh scattering for a single particle is given by:

$$I = I_0 \frac{8\pi^4 \alpha^2}{\lambda^4 R^2}(1 + cos^2\theta)$$

where I_0 is the intensity of unpolarized light, α, is molecular polarizability, which describes how much the electrical charges on the molecule will move in an electric field, R is the distance to the particle, and θ is the scattering angle. If the secondary variables of α, R, and θ are ignored, the intensity of scattering is a function of $8\pi^4/\lambda^4$ (Figure 2.4). Even at the ROLO band wavelengths of 347 and 353 nm Earth's atmosphere is significantly opaque, so ground-based telescopic observations of the UV reflectance of the Moon are problematic.

Hubble Space Telescope data from the Apollo 17 landing site included I/F values for the 250, 344, 502, and 658 nm bands. A second set of calibration coefficients were derived using the HST I/F values and WAC data. Robinson et al., 2007 used the Hubble Space Telescope (HST) Advanced Camera for Surveys High Resolution Camera (ACS/HRC (Pavlovsky et al., 2002)) to acquire UV-VIS images of three lunar targets. The HST lunar observations had two primary objectives: 1) assess the magnitude and spatial relations of contrast variations in the UV, and 2) assess

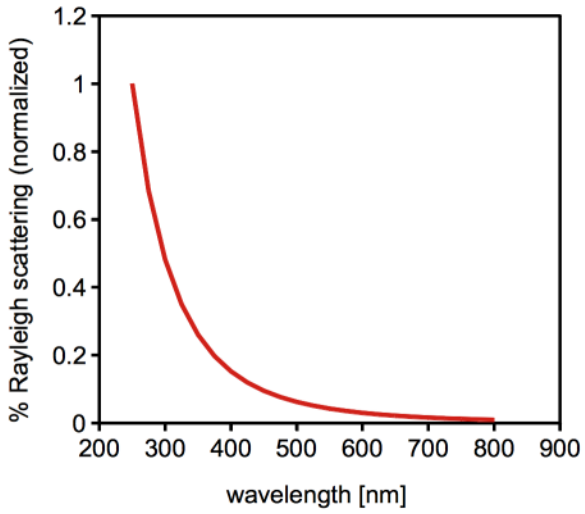

Figure 2.4: Plotting the wavelength dependence of Rayleigh scattering to demonstrate the difficulty of ground-based measurements of lunar reflectance from 320-360 nm compared to longer wavelengths. Normalized to 1 at 250 nm.

the ability of UV reflectance to measure TiO_2 content within mare soils (Robinson et al., 2007). The multi-spectral data consist of ACS/HRC four-filter observations (F250W, F344N, F502N, F658N) with an angular resolution of 60 m/pixel of three targets: the Apollo 17 landing site, the Apollo 15 landing site, and the Aristarchus crater and plateau (Robinson et al., 2007). The Apollo sites allow calibration of the HST measurements in association with known compositions of lunar soil samples. The Apollo 17 landing site at Taurus-Littrow provided a topographically smooth, geologically uniform mare surface to use as a calibration reference (Figure 2.5). The phase angle of the Apollo 17 observation is 39°, which is comparable to the ROLO images and the estimated incidence angle is 19°. The Apollo 17 image was taken on 2005-08-17, solar latitude was 1.2°, solar longitude was 34.8°, and the integration time was 4, 4, 1.5, 0.7 seconds for the F250W, F344N, F502N, F658N filters, respectively (Robinson et al., 2007). The estimated emission angle for the HST observations was cited as 20° (Robinson et al., 2007), however this estimate was refined to 36° based

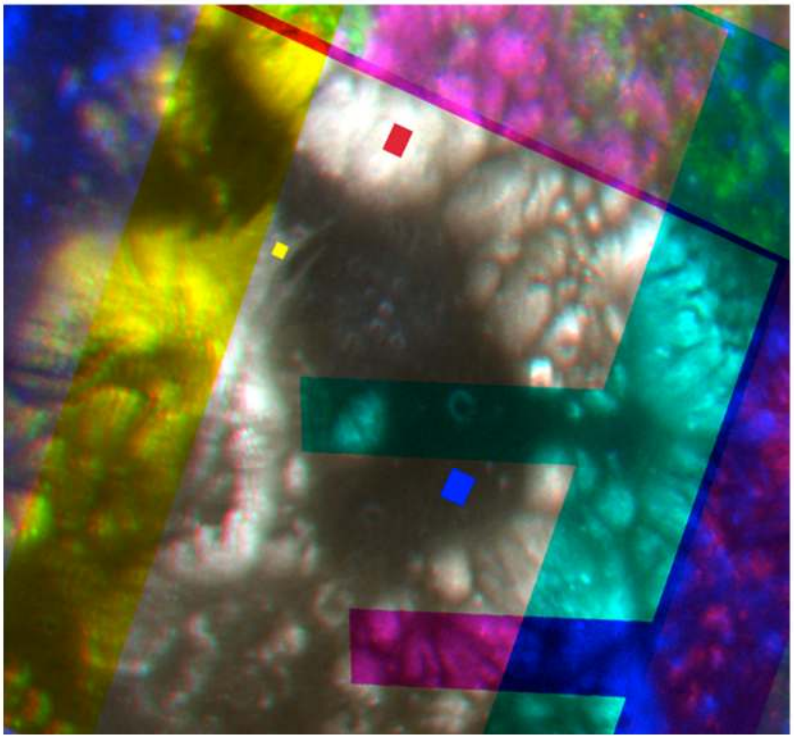

Figure 2.5: Subsection of Hubble Space Telescope multi-spectral images of the Apollo 17 landing site at Taurus-Littrow Valley. The blue box is a sample of mare basalt the area used in calibration. The red box on a mound of highland material (on a slope) and the yellow box is a topographically flat region on part of a landslide deposit (not used in calibration). Colors on the edge of the image are from misregistered portions of bands.

on the sub-Earth latitude and longitude at the time of the Apollo 17 observation acquisition. Radiometrically calibrated and spatially coregistered multi-spectral data were provided by Professors Robinson and Bell for the purposes of this work. The calibration process for the HST data is described in Robinson et al., 2007 as follows:

> Standard HST radiometric processing (Pavlovsky et al., 2002) was used to calibrate the lunar observations into units of radiance and radiance factor (I/F) (Bell et al., 1997). After the removal of instrumental geometric distortions the filter sets were coregistered using an automated subpixel scheme that employs a weighted least squares fit to account for local dis-

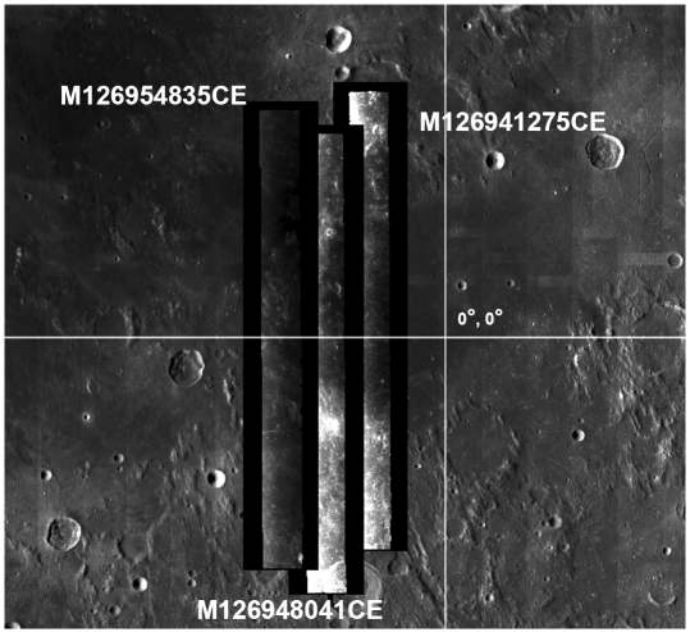

Figure 2.6: The location of the three WACs near the sub-Earth point for comparison to the ROLO data. A large region is required for a comparison to the $\sim$ 7 km/px ROLO scale. The black margins around each WAC represent the area masked out by restricting the emission angle to $< 20°$.

tortions, which was required due to parallax-induced distortions between each filter set.

Image Name	Center Lat	Center Lon	Incidence
M126954835C	0.097°	356.28°	28°
M126948041C	−0.44°	357.28°	28°
M126941275C	0.52°	358.27°	28°

Table 2.3: Properties of the 3 WAC images chose for proximity to the sub-Earth point of the ROLO observations to provide a match of photometric angles.

First WAC and ROLO observations similar in location and illumination geometry were selected. Backplanes were created from the ROLO and LROC image metadata (Figures 2.7 and 2.8). WACs were selected based on geographic location from images

acquired during the commissioning phase (June 2009 to 15 September 2010). As close a match of illumination geometry as possible was the primary constraint on image selection, with a secondary constraint on lunar terrain type (maria or highlands). In the ROLO images, the only location with low emission angles was a 5° longitude by 5° latitude box around the sub-Earth point (−1.65°N, 1.01°E). WACs in the latitude and longitude box with incidence angles of $30 \pm 2°$ (at the center of the WAC) were queried from the image database and 33 WAC images fit those criteria. Of those 33 image, only 3 (Table 2.3) had a majority of the frame within a mare basalt terrain (Figure 2.6). A mare basalt terrain is preferable for calibration since it is relatively topographically flat compared to the highlands terrain. Topography changes the local incidence angles of sunlight and adds uncertainty to the correction if not accounted for. At the time of the preliminary correction no global topography product was available for the calculation of local incidence angle. Selected WACs were cropped to a limited range of emission angles (within 20°). The ROLO images are at a scale of 7000 meters/pixel, while the WAC data is on average (UV and VIS) 200 meters/pixel. Due to the large difference in scale, the pixel values within the matching region of interest were averaged. While the difference in illumination conditions was minimized, small changes may add to the uncertainty (Figure 2.9). After the ROLO data were projected to match the spatial coverage of the WAC region of interest, the average pixel values per wavelength were collected. In the ROLO data this was wavelengths between 347 and 766 nm. The ROLO values were then interpolated to match the WAC bandpasses. The ROLO values (originally in units of radiance) were converted to I/F (Figure 2.10) and then compared to each band of the LROC WAC calibrated DN.

With the WAC data in calibrated DN and the ROLO data in I/F for each WAC band, the I/F conversion factor is simply calculated by:

$$IFCF = \frac{\mathrm{DN} \cdot \tau}{\mathrm{I/F}}$$

where IFCF is the I/F calibration factor, τ is the exposure time in ms, DN is the WAC calibrated DN value, I/F is the normalized reflectance, in this case from the ROLO data. The resulting calibration coefficients, or IFCFs, are the values used in the ISIS3 program lrowaccal, and are stored in a file called WAC_RadiometricResponsivity.pvl (Figure 2.11). When the calibration coefficients are applied to WAC images by the program lrowaccal, the coefficients are applied to the calibrated DN in the following manner, producing I/F values for each pixel and band: 1) divide the DN values by the WAC exposure duration (in units of ms), 2) multiply by the solar distance (from the Moon to the Sun), 3) divide by the IFCF for that band.

As previously discussed, the ROLO images of the Moon do not provide a IFCF value for the 320 and 360 nm UV bands. A second set of calibration coefficients were derived using the HST I/F values from the Taurus-Littrow mare and WAC data. One WAC image was chosen as the closest match of photometric angles to the HST image, M137346144CE. A region of interest in the mare was chosen with the range of 19.9234-19.9652°N latitude and 30.9447-30.9921°E longitude. Within the region of interest the average incidence angle is 41°, emission is 3°, and phase is 41°. This WAC image was chosen because it provided the best match of phase angle to the HST data, which has an estimated phase angle of 39°. Using the ratio of WAC DN/τ to HST I/F values interpolated to the WAC bands yielded another set of calibration coefficients (Figure 2.11).

At this point in the effort to calculate in-flight radiometric calibration coefficients, there was an important conflict between the HST-derived and the ROLO-derived coefficients. The HST coefficients from the Taurus-Littrow Apollo 17 landings gave higher I/F values (lower IFCF) compared to the ROLO sub-Earth point derived

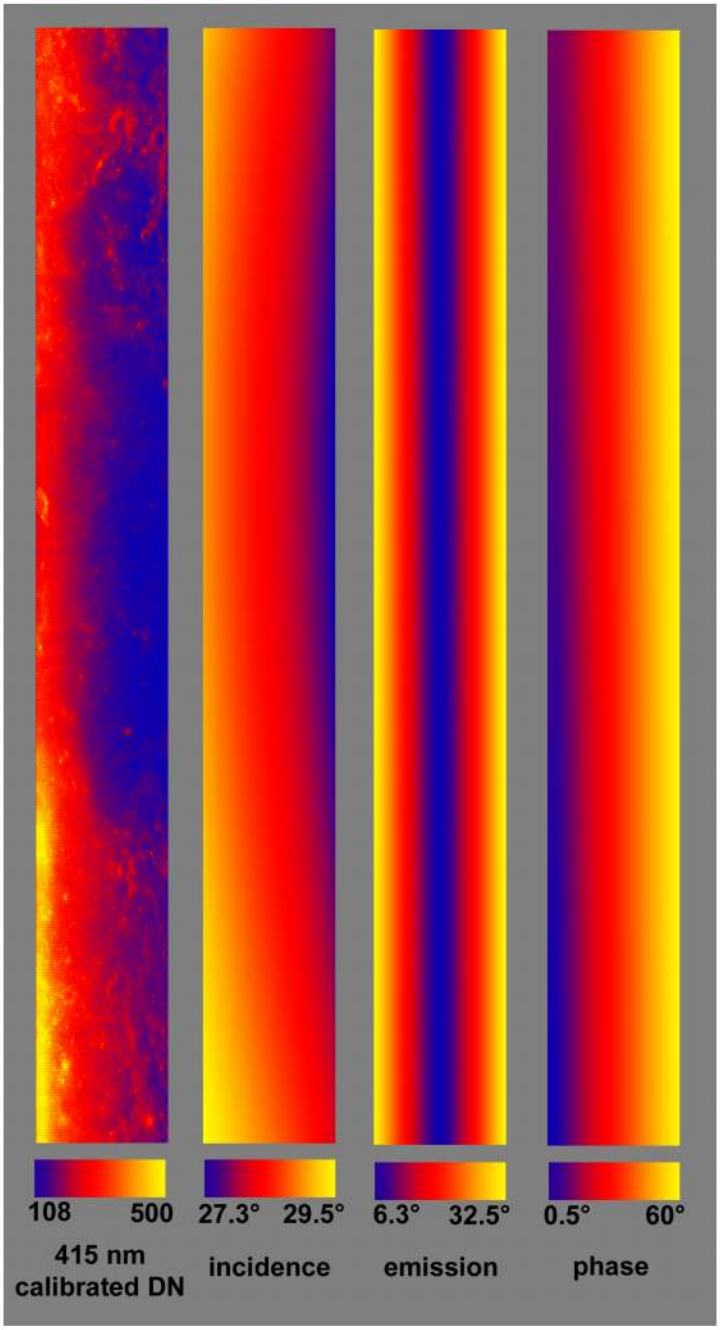

Figure 2.7: Calibrated DN and photometric backplanes for a typical WAC observation, M126941275C. The image is not map projected. Figure after Mahanti et al. (2012).

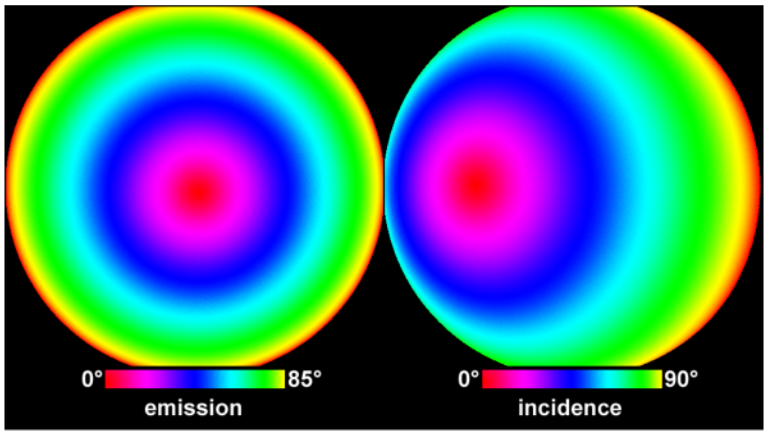

Figure 2.8: Photometric backplanes for a typical full-disk ROLO observation of the nearside of the Moon. The emission angle is 0° at the sub-Earth point near 0°N, 0°E. The incidence angles are 0° at the subsolar point.

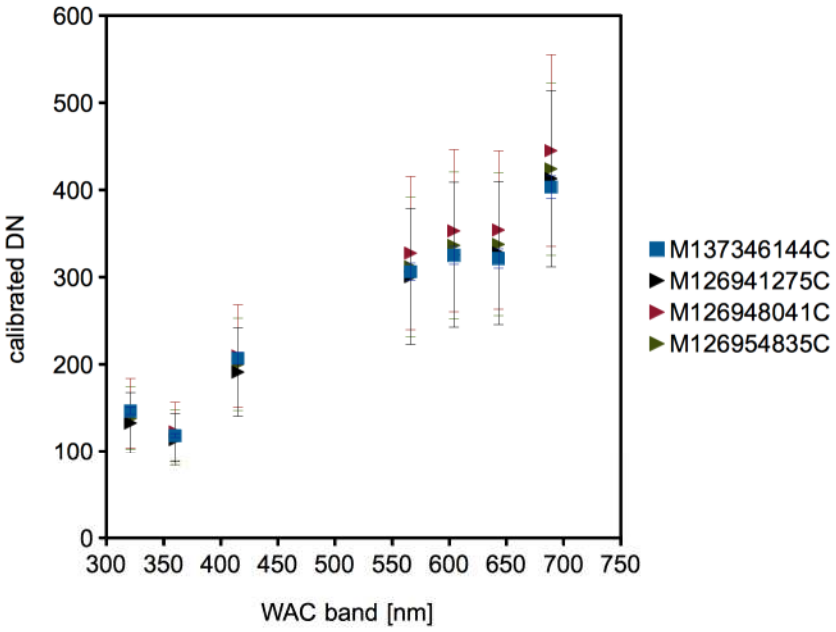

Figure 2.9: Plot of WAC calibrated DN values from regions of interest (mare) used for the absolute radiometric calibration. All WACs plotted here are near the sub-Earth point except for M137346144C, which was used for the comparison to the HST data from the Apollo 17 Taurus-Littrow site. The standard deviation of the average pixel values is smaller for M137346144C since the region of interest is significantly smaller in area compared to the larger regions used to compare to the ROLO data ($\sim$ 7 km/px scale). It is important to note that the standard deviation gets larger as wavelength increases.

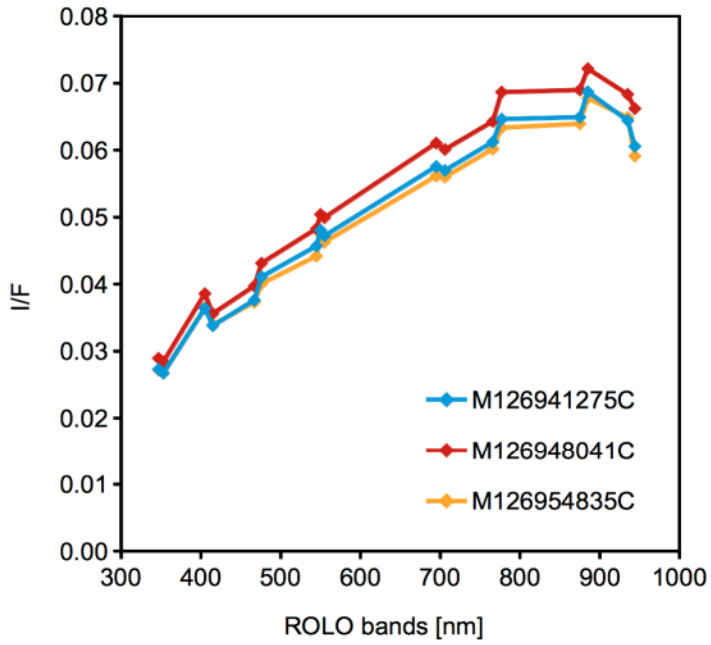

Figure 2.10: ROLO I/F data for the regions defined by the three WACs near the sub-Earth point. Before interpolation to the WAC bands.

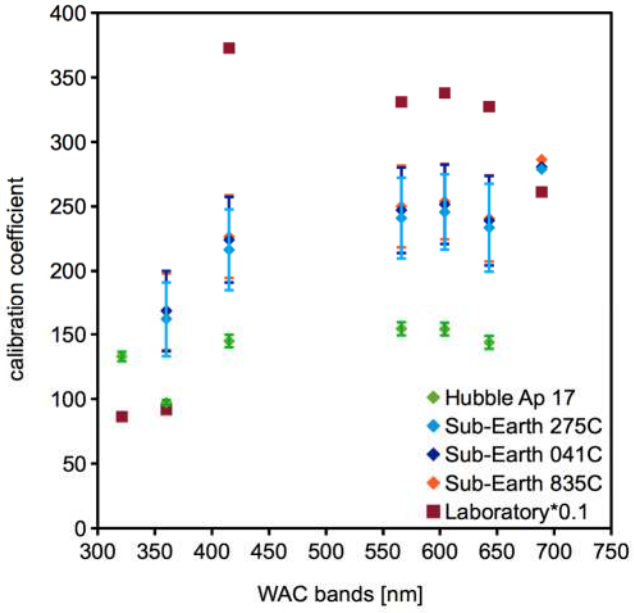

Figure 2.11: Calibration coefficients derived from ROLO data, three WACs near the sub-Earth point, and one WAC near the Apollo 17 site. Note that the actual values from the laboratory calibration are divided by ten to fit on the plot relative to the in-flight derived coefficients. The standard deviation bars show the variation due to the range of DN values with the WAC regions of interest.

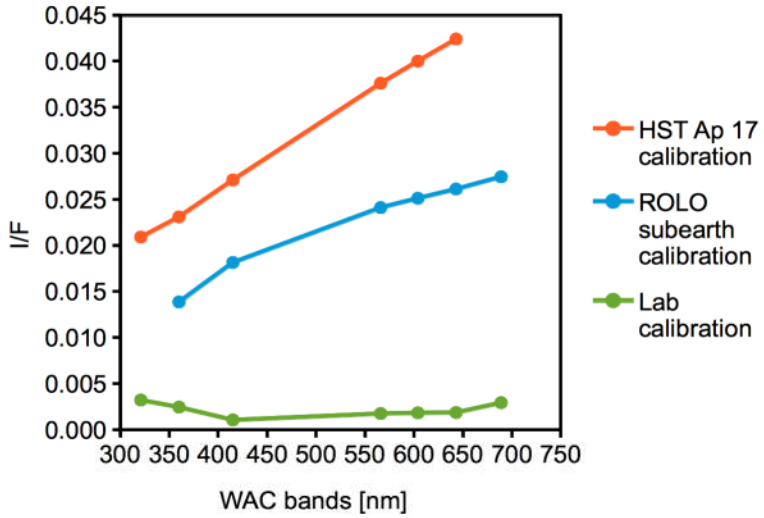

Figure 2.12: Comparison of I/F values for Apollo 17 mare with different calibration coefficients based on pre-flight calibration, ROLO images at the sub-Earth point, and HST data of Taurus-Littrow Valley. The laboratory coefficients yield I/F that are unreasonably low, as well as spectrally flat compared to the ROLO and HST derived coefficients.

calibration coefficients (Figures 2.11 and 2.12). The overall accuracy of the HST observations of the Moon is unknown, in part due to the fact that the Moon is a much higher reflectance target than the HST was designed to observe. Unfortunately, the low spatial resolution of the ROLO data makes a one-to-one match to the relatively small area of the Taurus-Littrow mare region of interest impossible, since a single ROLO pixel (7 km/pixel) contains light from a much larger region of the Moon.

The current solution used the ROLO data from the sub-Earth point to calibrate the VIS bands, but preserves the relative shape of the two UV bands from the Hubble data. The rationale for using the ROLO data values based on the level of calibration and characterization of ROLO (known) compared to the HST observations (unknown). ROLO has better coverage in the visible wavelengths compared to the HST observations. The absolute accuracy of spatially resolved (versus disk-integrated spectra) ROLO spectra in any filter is estimated to be about 5-10% (Keiffer and Stone,

2005). Hubble may have scattered light (causing an increase in brightness) since it was not designed to look at a large, bright target like the Moon (Robinson et al., 2007). The HST image illumination angles are also estimates. However, the WAC UV bands radiometry should be tied to the relative HST IFCF values since ROLO data is influenced by the atmosphere and Rayleigh scattering as previously discussed. The in-flight coefficient values (Table 2.4) used both the ROLO and the HST data.

WAC band [nm]	**Laboratory**	**In-flight**
320	865	150
360	918	166
415	3727	222
566	3310	246
605	3377	250
645	3273	238
690	2612	282

Table 2.4: Laboratory and Preliminary in-flight absolute calibration coefficients calculated from WAC and ROLO image. The values in this table convert WAC calibrated DN to I/F.

2.5 Conclusions and Future Work

While the radiometric calibration coefficients provided here are an improvement over the laboratory coefficients, further work is required to more robustly determine variations in the IFCF values over a larger range of WAC images and illumination geometries. The goal for the absolute radiometric calibration is a total uncertainty between 5-10%, almost entirely contributed by the uncertainty in the ROLO dataset. Note that the relative accuracy of the ROLO disk-integrated lunar model is 1%, but here the spatially resolved data is required, which has a higher uncertainty (5-10%).

Additional ROLO images, as well as more WAC images, would be used to better constrain the uncertainty of the calibration coefficients. A method, partially implemented by Mahanti et al. (2012), is an approach were individual pixels are selected within many WAC images to match the photometric angles in a wider range of pixels within the ROLO images. For example, the emission angle in a small part of a WAC may match the emission angle of a pixel in the ROLO images (not necessarily near the sub-Earth point). This method would provide a larger sample size and a better understanding of how the IFCF values may be influenced by changes in illumination angle (incidence) or terrain type (mare versus highlands). An independent derivation of WAC calibration coefficients by Mahanti et al. (2012) were between 2-10% lower than results presented here, with increased percent difference for the longer wavelengths (an expected difference based on the increased standard deviation of WAC DN values in the longer wavelength bands (643 and 689 nm) over the same lunar terrain).

A wider range of photometric geometries need to be tested on images from throughout the LROC commissioning and primary mission phases in order to constrain the uncertainty of the absolute calibration coefficients across many viewing geometries and examine any time-dependent changes in the LROC data over the duration of the mission. Efforts continue to use the much larger set of WAC observations and the now available global topographic mosaic to correct illumination geometry for topography. Finally, initial work to compare WAC observations to another lunar spacecraft dataset from the SELENE (Kaguya) Multi band Imager (Haruyama et al., 2008). A comparison of the I/F reflectance across additional lunar datasets would be of value to the planetary community.

Chapter 3

RELATIVE OPTICAL MATURATION RATES OF REGOLITH ON MERCURY AND THE MOON

3.1 Introduction

Global image sets at high resolution and high signal-to-noise ratio obtained by the Mercury Dual Imaging System (MDIS) (Hawkins et al., 2007) and the Lunar Reconnaissance Orbiter Camera (LROC) (Robinson et al., 2010) provide the means to investigate differences in optical maturation rates on Mercury and the Moon (Hapke, 1977; Cintala, 1992; Hapke, 2001, Noble and Pieters, 2003; Denevi and Robinson, 2008), and in a first-order sense, differences in composition. Quantifying relative and absolute differences in optical maturation rates of the regolith is critical to interplanetary comparisons of crustal composition using multispectral reflectance observations. Previous lunar studies focused on decoupling the spectral effects of regolith maturity from compositional signatures (Fischer and Pieters, 1994, 1996; Lucey et al., 2000a). Studies using Mariner 10 images in the 355 and 575 nm wavelength bands demonstrated that impact crater rays have high contrast with the hemispheric average and a relatively blue color (high 355/575 nm ratio), characteristics considered to be consistent with exposure of fresh, immature material (Hapke et al., 1975b; Rava and Hapke, 1987; Robinson and Lucey, 1997; Denevi and Robinson, 2008). Further analysis of image data from the MErcury Surface, Space ENvironment, GEochemistry, and Ranging (MESSENGER) spacecraft demonstrated that surface materials undergo optical maturation consistent with the accumulation of nanophase metallic iron ($npFe^0$) (Blewett et al., 2009). Analysis of VIS-NIR color trends successfully separated re-

gional and global color units from surface maturity. In derived maturity images, regional color differences were mostly suppressed, but variations in the brightness of high-reflectance crater materials remained apparent (Blewett et al., 2009). While the lunar OMAT parameter is calibrated to returned samples (Lucey et al., 1995; Blewett et al., 1997a; Lucey et al., 2000a, 2000b), no mercurian returned samples exist to link the maturity images to ground truth (Blewett et al., 2009).

Immature materials, such as the continuous ejecta blankets and rays of Copernican (lunar) and Kuiperian (mercurian) craters, are exposed to space weathering for less time than other time stratigraphic units (Shoemaker and Hackman, 1962; Spudis and Guest, 1988). This study uses relative abundances and reflectances of these craters and surrounding material as indicators of the relative rate of regolith maturation for both bodies. Additionally, determining the relative reflectance of immature material provides a first-order comparison of crustal composition. Previous work with Mariner 10 data indicated that immature lunar highlands materials were ∼1.5 times higher in reflectance than analogous immature mercurian materials (Denevi and Robinson, 2008). This result was interpreted as indicating a compositional difference between mercurian crust and lunar highlands crust (Denevi and Robinson, 2008; Robinson et al., 2008). This result from the Mariner 10 data can be improved by the higher resolution and radiometric accuracy of MDIS and LROC Wide Angle Camera (WAC) data,which allows for the study of a larger set of craters over a greater area of the planetary surfaces. MDIS and LROC WAC images have comparable wavelengths and bandwidths (see Methods) as well as higher resolution, better signal-to-noise ratio, and more spatial coverage (subhemispheric Mariner 10 to near-global MESSENGER) at a wider range of viewing and lighting geometries than Mariner 10.

3.2 Background: Regolith Maturation on Airless Bodies

3.2.1 Regolith Maturation and Rayed Craters

The term space weathering encompasses multiple processes that affect the surface of an airless body. These processes are primarily driven by exposure to the solar wind and bombardment by meteoroids and micrometeoroids. The solar wind sputters, irradiates, and implants solar wind particles, resulting in a reducing environment. Meteoroid and micrometeoroid impacts melt, vaporize, and comminute surface material. Regolith maturity is a measure of exposure time to the physical and chemical changes caused by these processes. Changes in maturity affect the optical properties of the regolith on airless silicate bodies such as asteroids, the Moon, and Mercury (Gold, 1955; Hapke et al., 1970, 1975a; Morris, 1976; Hapke, 2001). On the Moon, mature material exhibits lower reflectance, a steeper (redder) spectral slope from visible to near-infrared wavelengths, and shallower absorption features relative to fresh, immature material of the same composition (Adams and Jones, 1970; Hapke et al., 1970, 1975a; Adams and McCord, 1971; Pieters et al., 1993; Fischer and Pieters, 1994). These optical effects are primarily the result of reduced (metallic) iron grains (tens of nanometers in size) found in amorphous silicate coatings on lunar regolith grains (Hapke et al., 1975a; Keller and McKay, 1993; Morris, 1980, Noble et al., 2001, 2007). Small ($npFe^0$) (<10 nm) particles increase the spectral slope over visible to near-infrared wavelengths, and large particles (>40 nm) lower the albedo across the same range (Noble et al., 2007). The iron grains, called nanophase iron or npFe0, or submicroscopic metallic iron (SMFe), are produced through impact vapor deposition (Hapke et al., 1975a; Hapke, 2001).

The physical mechanisms thought to be responsible for vapor deposition of SMFe are micrometeoroid impacts and sputtering by both high-energy particles (protons)

from the solar wind and galactic cosmic rays (Hapke et al., 1975a; Hapke, 2001). Energy released through micrometeoroid impacts and solar wind sputtering melts and vaporizes portions of regolith grains, which produces impact glass and condensation products from the impact vapor. SMFe is created during vaporization when the reduction of ferrous iron to metallic iron occurs through the selective loss of oxygen (and a gain of two electrons) (Hapke et al., 1975a; Hapke, 2001). The metallic iron then condenses into grains on the rim of a mineral grain. Previous workers proposed that the production of metallic iron required the implantation of solar wind protons (H ions) as a reducing agent (Housley et al., 1973; Allen et al., 1993). Hapke (2001) demonstrated that a synthetic lunar sample, irradiated with H ions and then rapidly melted to simulate heating from an impact event, did not show either significant changes in spectral transmission or production of metal. Thus, hydrogen implantation due to the solar wind may not be necessary to create SMFe.

Lunar rayed craters were the first indicators of the optical effects of regolith maturation. If only the youngest craters(based on stratigraphic relationships) have rays, then the optical properties of rays must gradually change over some finite period of time, until the rays appear similar to the surrounding terrain (Gold, 1955; Shoemaker and Hackman, 1962). During the impact cratering process, excavation from depth and subsequent deposition of relatively immature material results in high-reflectance crater rays (Oberbeck, 1975; Schultz and Gault, 1985; Hawke et al., 2004). Crater rays of this type are known as maturity rays, in contrast to rays that persist because of compositional differences (Hawke et al., 2004). Lunar and mercurian craters with maturity rays (Figure 3.1) define the most recent lunar and mercurian time periods: the Copernican and Kuiperian, respectively (Shoemaker and Hackman, 1962; Spudis and Guest, 1988). Since the rays of young craters are still visible, they have been exposed to maturation processes for less time than most other surface units.

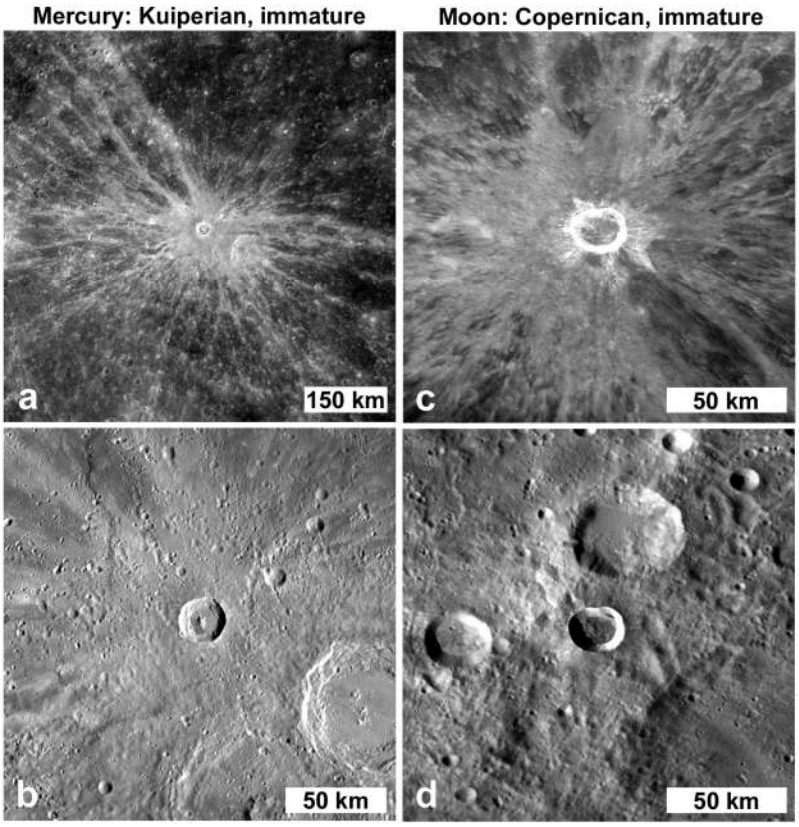

Figure 3.1: Examples from the mercurian Kuiperian and the lunar Copernican crater populations. The top two images show reflectance (low incidence angle), and the bottom two images show morphology (high incidence angle) for the same craters. (a, b) Xiao Zhao, a Kuiperian crater, located at 10.57°N, 123.91°E, with a diameter of 24.0 km. Image a: MDIS image number EW0218585120D, incidence=25° , emission=3° . Image b: mosaic of EW0216025147G and EW0216025060G, incidence=57, emission=0. (c, d) Giordano Bruno, a Copernican crater, located at 35.92°N, 102.74°E, with a diameter of 22.1 km. Compare to the relatively mature craters in Figure 2. Image c: image from 565 nm LROC WAC mosaic normalized to incidence=30° . Image d: image from LROC WAC 100 m/pixel morphologic map (incidence angles in the mosaic range from 55°-75°) (Speyerer et al., 2011). Images are in a sinusoidal projection.

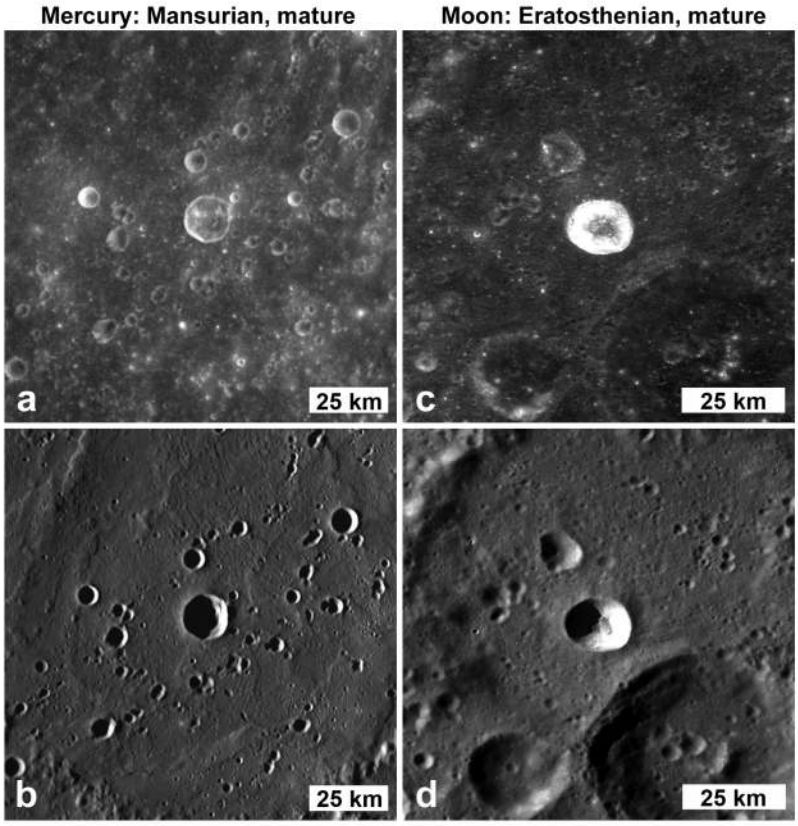

Figure 3.2: Examples from the mercurian Mansurian and the lunar Eratosthenian crater populations. The top two images show reflectance (low incidence angle), and the bottom two images show morphology (high incidence angle) for the same craters. (a, b) An unnamed Mansurian crater, located at 2.5°S, 156.7°E, with a diameter of 15.0 km. Image a: mosaic of EW0215590743G and EW0215590880G, incidence=24°, emission=4°. Image b: EW0235727312G, incidence=80°, emission=27°. (c, d) Pizzetti W, a Eratosthenian crater, located at −34.05°N, 118.26°E, with a diameter of 13.8 km. Image c: image from 565 nm LROC WAC mosaic normalized to incidence=30°. Image d: image from LROC WAC 100 m/pixel morphologic map (incidence angles in the mosaic range from 55°-75°) (Speyerer et al., 2011). Images are in a sinusoidal projection.

Morphologically fresh (sharp rim, few subsequent impacts) craters whose rays now display no reflectance contrast with the local substrate (Figure 3.2) formed during the Eratosthenian (lunar) and Mansurian (mercurian) time periods (Wilhelms, 1987; Shoemaker and Hackman, 1962; Spudis and Guest, 1988; Grier et al., 2001).

3.2.2 Differences in the Mercurian and Lunar Maturation Environments

Differences between the environments on Mercury and the Moon led to the hypothesis that regolith maturation on Mercury occurs faster than on the Moon (Hapke, 1977; Cintala, 1992; Hapke, 2001; Noble and Pieters, 2003). The environmental differences include micrometeoroid impact flux, higher temperatures on Mercury, and Mercury's magnetic field.

From extrapolations of the terrestrial micrometeoroid flux, the flux of micrometeoroids at Mercury is expected to be 5.5 times that of the Moon, and the average velocity of micrometeoroids is 60% greater (Cintala, 1992). As a result, a given impactor encountering Mercury should produce 14 times more melt and 20 times more vapor than on the Moon (Cintala, 1992). Increased melt and vapor production on Mercury imply faster production of vapor-deposited SMFe in glassy coatings on regolith grains, and therefore a faster regolith maturation rate compared with the lunar surface. Results of a comparative analysis of surface reflectance between immature and mature material (using Mariner 10 images and Clementine images of the Moon) were consistent with the hypothesis of more intense maturation of regolith on Mercury (Denevi and Robinson, 2008).

The surface temperature conditions on Mercury may cause SMFe to form larger grains over time compared with those formed on the Moon, which could cause relatively faster (and/or more extensive) optical maturation at Mercury (Noble and Pieters, 2003). Experiments have shown that the grain size of SMFe affects the optical properties of material in the laboratory. Smaller grains (<10 nm) contribute to darkening and spectral slope effects, whereas larger grains (> 40 nm) primarily lower reflectance without producing large changes in spectral slope (Noble et al., 2007). Repeated exposure to high temperatures during Mercury's day may cause SMFe par-

ticles to coalesce to larger grain sizes through a process known as Ostwald ripening (Noble and Pieters, 2003). Mercury has a higher surface temperature than the Moon due to its proximity to the Sun. Equatorial regions of Mercury reach temperatures >700 K (Morrison, 1970; Davies et al., 1978), on the Moon the maximum temperature is ∼390K (Lucas et al., 1967; Lucas et al.,1968; Vasavada et al., 1999). Experimental annealing of adjacent SMFe particles has shown that the mean grain diameter is stable to ∼473 K, but at higher temperatures the grain diameter increases (Gleiter, 1989). The lunar surface maintains temperatures well below 473 K, so Ostwald ripening should not occur on the Moon (Noble and Pieters, 2003). If Ostwald ripening does produce larger SMFe grains (>40 nm) within Mercurian vapor deposits, then the optical effect would produce a surface with a normalized reflectance lower than that of the Moon (given the same composition) (Noble and Pieters, 2003).

Mercury, unlike the Moon, has a magnetic field that partially protects its regolith from solar wind proton sputtering. However, Mercury's magnetosphere behaves differently during normal, moderate, and extreme solar wind conditions (Slavin et al., 2010). The short-term variability of the solar wind flux at Mercury's surface makes it difficult to estimate the comparative effects of solar wind sputtering on the regolith maturation rate on Mercury and the Moon. Under normal conditions, the solar wind is deflected by the magnetic field, except at the north and south magnetospheric cusps, where solar wind protons have regular access to the surface (Slavin et al., 2010). A model derived from measurements during the first MESSENGER flyby of the magnetic field and ambient solar wind conditions gave a proton flux of 1×10^8 to 8×10^9 $cm^{-2}s^{-1}$ at the north and south cusps (Sarantos et al., 2009). For comparison, the solar wind proton flux at the Moon is estimated to range from 1×10^8 to 8×10^8 $cm^{-2}s^{-1}$ (Vaniman et al., 1991b). Under moderate solar wind conditions, the north and south cusp regions move equatorward (Slavin et al., 2010). Under extreme

solar wind conditions, the north and south cusp regions merge at the equator and the dayside surface near the equator is broadly exposed to the solar wind (Slavin et al., 2010). The long-term rate of regolith maturation may be faster in the cusp regions than the global mercurian average, but this effect has not been quantified.

3.2.3 Differences in Lunar and Mercurian Composition and Reflectance

Previous studies and measurements indicate that surface materials on Mercury are lower in FeO than the lunar maria. Images from the Mariner 10 spacecraft suggested that the mercurian surface was low in iron and titanium (Hapke et al., 1975b). Earth-based telescopic measurements were unable to detect a ferrous iron band (near 1 μm), suggesting an average surface abundance of FeO less than 6 wt% (Vilas and McCord, 1976; Adams and McCord, 1977; Vilas et al., 1984; Vilas, 1985, 1988). From laboratory measurements of spectral reflectance, the average FeO content on the surface of Mercury has been estimated to be between 3 and 6 wt% (Hapke, 1977). A reassessment of Earth-based telescopic data and laboratory spectra with models for the reflectance of iron-bearing silicate regolith on an airless body suggested a composition of FeO + TiO_2 of 4 wt% for Mercury's smooth plains (Blewett et al., 1997b). In early orbital observations during solar flares, MESSENGER's X-ray Spectrometer (XRS) detected low abundances of Fe and Ti from scattered areas, most located in the southern hemisphere between longitudes of -180°E and -60°E, with upper limits of ~4 wt% Fe and ~0.8 wt% Ti (Nittler et al., 2011). The surface of Mercury is richer in Mg and S and poorer in Al, Ca, and Fe than the lunar surface (Nittler et al., 2011). Later, spatially resolved XRS measurements demonstrated that the major element composition of Mercury's northern smooth plains differs from that of the older surrounding terrain (intercrater plains and heavily cratered terrain) (Weider et al., 2012). The older terrain generally has higher Mg/Si, S/Si, and Ca/Si ratios, and

a lower Al/Si ratio than the northern plains (Weider et al., 2012). High-degree partial melts of enstatite chondrite material provide a compositional and mineralogical match for much of the surface of Mercury, with the exception of Fe, for which the low surface abundance on Mercury is still higher than that of melts from enstatite chondrites and may indicate an exogenous contribution from meteoroid impacts (Weider et al., 2012). Gamma-ray emission measurements from orbital data show an average northern hemisphere Fe abundance of 1.9 wt% $\pm$ 0.3 wt% standard deviation (Evans et al., 2012).

Mercury's disk-integrated reflectance is lower than that of the lunar nearside, (Harris, 1961; Veverka et al., 1988; Mallama, 2002; Warell, 2004; Holsclaw et al., 2010). Both compositional differences and an increased state of regolith maturation on Mercury may contribute to the lower reflectance on Mercury compared to the Moon. If the mercurian regolith reaches a more advanced state of maturity due to an increased space weathering environment compared with that on the Moon, then the expected spectral result is an average lower reflectance and steeper spectral slope for mature mercurian surfaces compared with mature lunar surfaces (Cintala, 1992; Denevi and Robinson, 2008; Holsclaw et al., 2010). Radiative transfer analysis demonstrated that mercurian spectra are consistent with more space weathering product than on the Moon (Lucey and Riner, 2011). However, from Mariner 10 data, the reflectance of immature mercurian materials ($\sim$0.13-0.18 at 490 nm and 30° phase angle) was shown to be lower than that of immature lunar highland materials ($\sim$0.20-0.26), which suggests the presence of a low-reflectance component in Mercury's surface material (Denevi and Robinson, 2008).

3.2.4 *Asteroid Regolith Maturation*

Regolith material returned from the asteroid Itokawa exhibits physical products of regolith maturation due to solar wind bombardment occurring in asteroidal regolith as young as 8 Ma (Noguchi et al., 2011; Nagao et al., 2011). Asteroidal surfaces do not necessarily experience lunar-style space weathering (Strazzulla et al., 2005; Vernazza et al., 2009), so it is unclear how the results from the asteroid Itokawa relate to the maturation environment on Mercury. Out of 10 Itokawa particles (average diameter of 52 mm) studied, five were found to have glassy rims. Two distinct layers within the rims were found. The surface layer, 5-15 nm thick, contains FeS nanoparticles, and the underlying layer, 20 to 50 nm thick, contains metallic iron (Fe^0) nanoparticles (Noguchi et al., 2011). FeS nanoparticles may also be present in the rims of Mercurian regolith grains, since Mercury has a sulfur abundance at least 10 times higher than that of the silicate portion of Earth or the Moon, with a S abundance of up to $\sim$4 wt% in surface materials (Nittler et al., 2011). The rims of lunar regolith grains from Apollo samples do not contain FeS nanoparticles. In the Itokawa study, the average grain size of iron nanoparticles was $\sim$2 nm (Noguchi et al., 2011).

3.2.5 *Crater Chronostratigraphic Ages and Impact Flux*

The chronostratigraphic sequence for the Moon has been divided, from youngest to oldest, into the Copernican, Eratosthenian, Imbrian (subdivided into upper and lower epochs), Nectarian, and pre-Nectarian periods (Shoemaker and Hackman, 1962; Stuart-Alexander and Wilhelms, 1975). A similar time-stratigraphic classification scheme was developed for Mercury by Spudis and Guest (1988) with the Kuiperian, Mansurian, Calorian, Tolstojan, and pre-Tolstojan periods generally corresponding to the respective periods for the Moon. An important note is that while the stratigraphic

classification schemes on Mercury and the Moon are assumed to be similar, the time intervals of corresponding periods are not necessarily equivalent (Spudis and Guest, 1988). Radiometric age dating of returned lunar samples from the Apollo and Luna missions, as well as extensive stratigraphic and crater counting analyses, allowed the assignment of absolute time constraints for lunar time units (Vaniman et al., 1991a). In the case of Mercury, no samples exist to allow radiometric age determinations. The best age estimates of mercurian surfaces rely on the cratering records of the Moon and Mercury.

Strom et al. (2005) divided lunar and martian craters into Populations 1 and 2, distinguished on the basis of crater size-frequency distributions, whether most craters were produced during the Late Heavy Bombardment (LHB) (Population 1) or afterward (Population 2). Strom et al. (2005) went on to propose that the source of Population 1 craters was the main asteroid belt whereas the source of Population 2 craters was near-Earth asteroids on the basis of comparisons to the size-frequency distributions of populations of asteroids. In the analysis of Strom and colleagues, craters within the Copernican and Eratosthenian systems are considered part of Population 2 (Strom et al., 2005). Population 1 craters were identified on Mercury using Mariner 10 images (Strom and Neukum, 1988), but Population 2 craters were not identified until images from the MESSENGER mission covered a sufficiently large area of the smooth plains units interior and exterior to the Caloris basin to complete the crater size-frequency analysis (Strom et al., 2008). This general age assignment of Population 2 craters is relevant because models of the current flux of near-Earth objects at the Moon and Mercury can then provide estimates of impact rates for Population 2 craters. Observations of near-Earth objects used to create models of flux include asteroids, active comets, and extinct comets (Bottke et al., 2002). Models of impact flux indicate that Mercury has a near-Earth object impact rate 1.8-1.9 times

higher than that of the Moon (Le Feuvre and Wieczorek, 2008, 2011; Greenstreet et al., 2012). The link between young craters (Kuiperian and Mansurian) on Mercury, Copernican and Eratosthenian craters on the Moon, and near-Earth asteroids provides a compelling and useful narrative of inner solar system impact history. However, it should be re-emphasized that these relationships are relative age estimates and no absolute age estimates for Mercury's surface exist.

3.3 Methods

In this paper, craters on Mercury and the Moon were identified and characterized based on their physical properties (Figure 3.3). For fresh craters, these properties include the reflectance of ejecta, crater diameter, a description of the high-reflectance ejecta, ray length, and in lunar cases the Clementine optical maturity parameter (OMAT) and FeO wt% values for the high-reflectance ejecta (Blewett et al., 1997a; Grier et al., 2001). The number of craters with high-reflectance ejecta per unit area quantifies the relative difference in optical maturation rates of regolith on Mercury and the Moon. If the rate of regolith maturation is faster on Mercury, then the expected result is that fewer craters with high-reflectance ejecta (per unit area) should exist on Mercury than on the Moon. While reflectance measurements were made for craters $\geq$ 3 km in diameter, only craters $\geq$ 10 km diameter are considered in the craters per unit area results to minimize the influence of secondary craters. The need for a 10 km diameter cutoff is due to two factors. First, on Mercury a crater at a given size has larger secondaries than the same size crater on the Moon (Gault et al., 1975). Second, the crater size-frequency distribution for the mercurian surface has been affected by secondary impact craters at diameters less than about 10-15 km (Strom et al., 2008). In addition to the number of craters with high-reflectance ejecta per unit area (Copernican and Kuiperian craters), Eratosthenian and Mansurian craters were

also identified and counted. The number of Eratosthenian and Mansurian craters per unit area provides a way to relate the number of Copernican and Kuiperian craters per unit area to the rest of the young crater population (Population 2, as in Strom et al. (2005, 2008)). Finally, the uncertainty (high or low) of identification was recorded for each crater. The uncertainty refers to the confidence of the crater classification. For example, Eratosthenian and Mansurian craters with high uncertainty (see Table 3.1) may be sufficiently degraded to be Imbrian or Calorian (respectively) in relative age. Craters with high uncertainty are not included in the total count for each type of crater, but the number of craters with high uncertainty is used to estimate the error in classification.

	Copernican	Kuiperian	Eratosthenian	Mansurian
# Craters $\geq$ 10 km	131	132	577	1533
Uncertain craters	4	8	78	40
Total area [km^2]	21.8×10^6	41.3×10^6	22.2×10^6	51.1×10^6
Craters/10^{-6}km^2	6.0	3.2	26.0	30.0
$\pm$ Craters/10^{-6}km^2	0.2	0.2	3.5	0.7

Table 3.1: Results of crater counting and identification for craters with diameters larger than 10 km. The supporting information for this paper contains the crater locations and diameters for each crater in the table.

The craters were further classified based on the characteristics of their high-reflectance ejecta. Copernican and Kuiperian craters have high-reflectance continuous ejecta blankets formed by fresh material excavated by impacts. Some of these fresh craters also have rays, which are albedo features extending radially from the impact crater (Shoemaker and Hackman, 1962). For each of the craters in this study, it was noted if the crater had rays, or just a high-reflectance continuous ejecta blanket, here

referred to as a "halo" of high-reflectance material, consistent with the terminology of Grier et al. (2001). Craters with both rays and halos are referred to as rayed craters, and craters with only halos of high-reflectance material are referred to as haloed craters. The two groups of craters together are high-reflectance ejecta (HRE) craters. Ray length measurements were taken for a set of rayed craters $\geq$ 15 km in diameter to examine the relationship between ray length, crater diameter, and ejecta reflectance on the Moon and Mercury. When multiple rays were visible for a crater, the longest 5 to 10 rays were measured.

For the Kuiperian and Copernican craters $\geq$ 3 km in diameter, photometrically normalized reflectance measurements of high-reflectance ejecta were obtained by averaging a group of pixels (at least 5 by 5) over a uniform area within the continuous ejecta. Two 1 km scale mosaics with comparable wavelengths were used: the LROC Wide Angle Camera (WAC) 566 nm filter (full width at half maximum, or FWHM, of 20 nm) and the MDIS WAC 560 nm filter (FWHM = 5 nm). The two mosaics were made from images corrected to 30° phase angle (incidence angle, the angle between the incident solar radiation and the normal to the surface, given by i = 30°, and emission angle, the angle between the view direction and the normal to the surface, given by e = 0°) (Sato et al., 2011; Domingue et al., 2011, 2013). Only areas imaged with incidence angles less than 45 degree were included in the mosaic. The sample area was restricted to between 40°S and 40°N latitude. Steep, Sun-facing slopes were avoided while collecting the reflectance values. Both the LROC WAC and MDIS WAC mosaics have estimated absolute reflectance uncertainties of about 10% of the signal (Hawkins et al., 2007; Robinson et al., 2010). Additional morphology mosaics (high incidence angle) from LROC and MDIS images (200 m/pixel) were used to identify the Eratosthenian and Mansurian craters $\geq$ 10 km. Again, the count area included images only from 40°S to 40°N latitude.

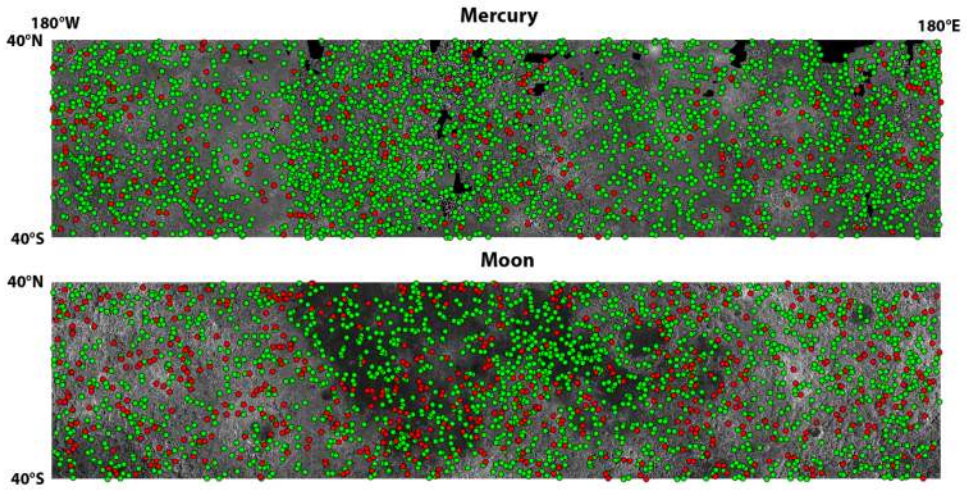

Figure 3.3: Red dots mark the locations of craters with high reflectance ejecta and rays (Copernican and Kuiperian craters). Green dots mark the locations of craters with sharp rims, but not maturity rays (Eratosthenian and Mansurian craters). Data are potted on morphology mosaics from LROC and MDIS.

To minimize the inclusion of compositional rays and ejecta in the lunar case, only high-reflectance ejecta craters located in the highlands were included. To further verify that the measurement areas on high-reflectance ejecta were from immature and compositionally similar material, measurements from the Clementine OMAT and FeO wt% maps were collected (Blewett et al., 1997a; Lucey et al., 2000a, 2000b). Differences in Fe content distinguish the lunar highlands (average Fe content 3 wt% (Lucey et al., 1995)) from the maria (mostly >10 wt% Fe), and from the South Pole-Aitken basin (∼7-8 wt% Fe). Not all of the measurement areas from the LROC data set were included since the Clementine maps have gores where no data are available. For Mercury, while optical maturity was shown to be separable from major color units, no ground truth exists to distinguish immature crater rays and ejecta from composition (Blewett et al., 2009). Mercury is more spectrally homogenous than the Moon due to Mercury's low Fe and Ti abundances (Nittler et al., 2011), and as a result, methods that determine lunar surface maturity are not applicable to Mercury. There are no

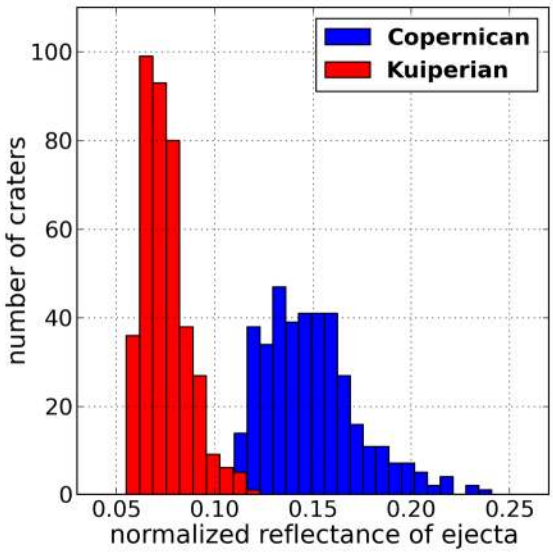

Figure 3.4: Distribution of photometrically normalized reflectance from immature crater ejecta blankets on Mercury and the Moon. Very immature craters plot toward the right. At the lower end of each distribution is the transition point where maturity rays have blended into the background. The mode of the Copernican population is 0.14 with n = 388, mean = 0.15, standard deviation = 0.02. The mode of the Kuiperian population is 0.07 with n = 394, mean = 0.08, standard deviation = 0.01.

rays on Mercury large enough to be compositionally characterized with XRS data and also no XRS observations of high-reflectance continuous ejecta of sufficient resolution to determine composition within the group of craters studied.

3.4 Observations

3.4.1 Immature Craters per Unit Area

There are ∼2 times fewer Kuiperian craters per unit area on Mercury than Copernican craters per unit area on the Moon, and only ∼1.2 times more Mansurian craters per area than Eratosthenian craters (Table 3.1). The numbers of craters per unit area measured here are not consistent with the models for the flux of near-Earth objects (Le Feuvre and Wieczorek, 2008, 2011; Greenstreet et al., 2012). Those models predict 1.8-1.9 times more impacts at Mercury than at the Moon, so the observed counts

of Kuiperian and Copernican impact craters disagree with the models by a factor of ~4.

3.4.2 Comparison of Reflectance of Immature Material on Mercury and the Moon

The distribution of the photometrically normalized reflectance of immature material is non-Gaussian with positive skew for both bodies (Figure 3.4). High-reflectance ejecta from immature lunar highland craters have reflectances ranging from 0.11 to 0.24 (average = 0.15, standard deviation = 0.02, n = 388). For comparison, mature lunar highlands have an average reflectance of 0.09 (standard deviation = 0.01). The photometrically normalized reflectance of mercurian high-reflectance crater ejecta ranges from 0.06 to 0.12 (average = 0.08, standard deviation = 0.01, n = 394). Average mature mercurian material has a reflectance of 0.06 (standard deviation = 0.01). There may be some compositional dependence in the mercurian high-reflectance crater ejecta data set on the basis of the overlap of the average mature mercurian material (0.06) with the lower end of the high-reflectance crater ejecta (also 0.06).

The reflectance of lunar highland ejecta has a positive correlation with the Clementine OMAT parameter (Figure 3.5). This correlation indicates that for lunar highland craters, it is valid to use reflectance as a proxy for state of maturity. Scatter is likely due to variation in distance from the crater rim (local mixing) and variations in FeO abundance (1-8 wt%) in the highlands. All craters in the data set have OMAT values > 0.14, which is considered the boundary value between mature and immature material (Grier et al., 2001). FeO wt% values from the same areas of fresh lunar ejecta (Figure 3.6) range from 1 to 8 wt%, and when plotted against the LROC reflectance values show no correlation. For comparison, orbital data from MESSENGER's XRS detected abundances of Fe with upper limits of ~4 wt% (Nittler et al., 2011).

The MDIS reflectance images from after 24 May 2011 are thought to be affected by

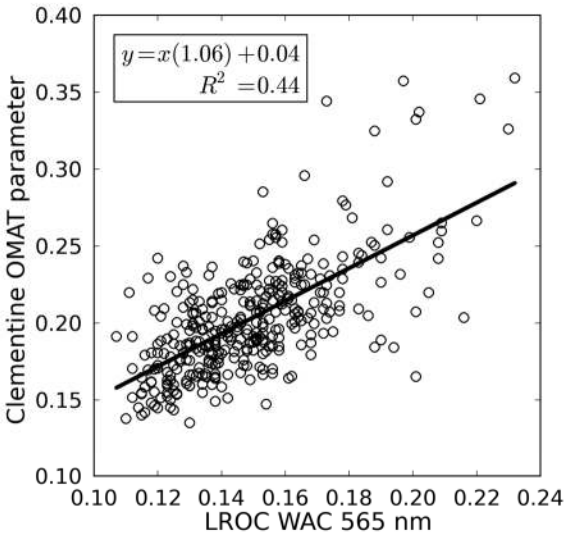

Figure 3.5: Correlation between the LROC 565 nm reflectance of ejecta from lunar highland craters $\geq$ 3 km in diameter (n = 365) and the Clementine optical maturity parameter or OMAT (Blewett et al., 1997a; Grier et al., 2001). The general trend (best fit line, with y = OMAT parameter and x = LROC 565 nm reflectance) is consistent with the assumption that reflectance is a proxy for maturity. The quantity R^2 is the coefficient of determination.

a lens contamination event due to spacecraft outgassing from elevated temperatures as the spacecraft passed through the mercurian subsolar point (Keller et al., 2013). This event caused time and filter-dependent changes in the apparent MDIS sensitivity (Keller et al., 2013). A comparison of mosaics made with images acquired before and after the contamination event shows a change in apparent surface reflectance and allows a quantification of errors introduced to the 560 nm data used in this study. On average, the residual between the two reflectance mosaics was ~0.005, which is 0.0005% of the reflectance from a typical rayed crater. This amount is not enough of a difference in reflectance to change the results from our reflectance values.

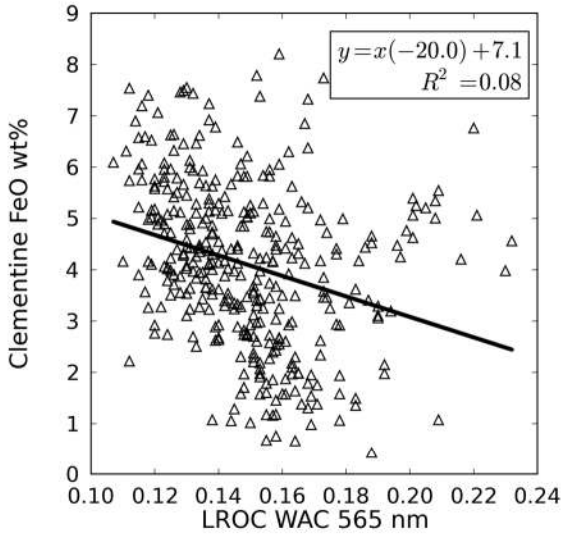

Figure 3.6: Distribution of LROC 565 nm reflectance of ejecta from lunar highland craters $\geq$ 3 km in diameter (n = 365) versus FeO wt% derived from Clementine UV-VIS data (Lucey et al., 2000b). The low R^2 value indicates no relationship between the reflectance of ejecta and FeO wt%.

3.4.3 Rays, Halos, and Reflectance

On average, lunar rayed craters have higher OMAT values (∼0.23) than craters with only halos (∼0.19), indicating a relationship between optical maturity (a proxy for age) and the characteristics of the high-reflectance ejecta. Ray length was measured and compared with the parent crater diameter, as well as the reflectance of the proximal ejecta to test the hypothesis that rayed craters transition into haloed craters. For this study, the data set included 18 lunar craters and 81 rays, and 30 mercurian craters and 145 rays (Figure 3.7). The comparison of the ratio of ray length to crater diameter plotted as a function of crater diameter for Mercury and the Moon showed that a majority of craters have ratios of ray length to crater diameter between 2 and 13; however, there were five outliers with high ratios: two lunar craters, Giordano Bruno, Byrgius A, and three mercurian craters, Debussy, Xiao Zhao, and Qi Baishi. The average ratio of ray length to crater diameter is 8 ± 4 on the Moon and Mercury.

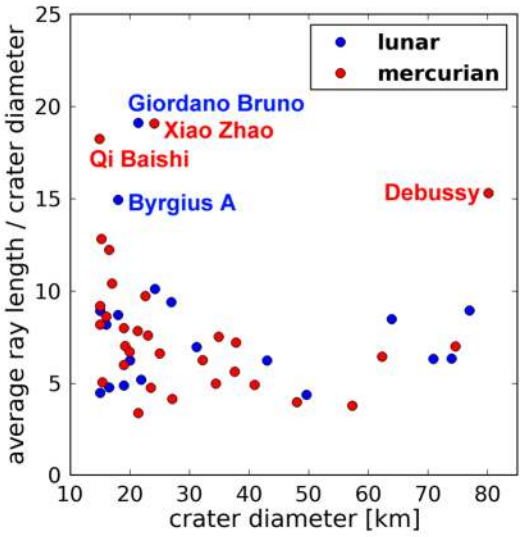

Figure 3.7: The ratio of average ray length to crater diameter versus crater diameter for a set of distinct-rayed craters $\geq$ 15 km in diameter. The data set includes 18 lunar craters with 81 rays, and 30 mercurian craters with 145 rays. A majority of craters have ratios of ray length to crater diameter in the range 2 to 15; however, there are five outliers with high ratios: Giordano Bruno, Byrgius A (lunar), and Debussy, Xiao Zhao, and Qi Baishi (mercurian).

3.5 Results and Discussion

3.5.1 Craters per Unit Area

A mechanism is required to account for the observed deficit of immature craters on Mercury relative to the Moon. The theorized faster regolith maturation environment on Mercury (Hapke, 1977; Cintala, 1992; Hapke, 2001; Noble and Pieters, 2003) is most likely responsible for post-impact changes, resulting in the optical darkening of the diagnostic high-reflectance ejecta. Given a faster maturation rate at Mercury, lunar ejecta will remain immature, and thus visible, over longer timescales than mercurian examples. Faster regolith maturation on Mercury can explain the difference between the modeled impact flux ratios (Le Feuvre and Wieczorek, 2008, 2011; Greenstreet et al., 2012) and our observations of the ratio of Kuiperian to Copernican craters

per unit area. The optical effects of maturation are modifying the Kuiperian-aged craters so that they no longer have rays or halos and are therefore not classified within the Kuiperian period. In the literature, the approximate base of the Kuiperian system is 1.0 Ga, assuming a lunar-type impact flux history on Mercury (roughly equivalent to the Copernican period) (Spudis and Guest, 1988). If the time intervals of the two periods were similar, then considering the observed value of 6.0 Copernican craters per 10^6 km^2 and the modeled impact rate ratio of Mercury to the Moon of ~ 2, the expected number of Kuiperian craters per 10^6 km^2 would be 12. The actual observed value is 3.2 craters per 10^6 km^2, so there is a (model) deficit of ~ 8.8 craters/10^6 km^2. This deficit is caused by either a greater regolith maturation rate at Mercury compared to the Moon, or the impact flux models overestimate the impact rates on Mercury by a factor of four.

If a greater regolith maturation rate at Mercury is solely responsible for the discrepancy between the near-Earth object impact flux models and the observed counts of Kuiperian and Copernican craters, then the rate of optical regolith maturation on Mercury is as much as a factor of ~ 4 times higher than that for the lunar surface. If the impact flux models are incorrect by a factor of 2 and overestimate the impact rates on Mercury, then the rate of optical regolith maturation on Mercury would be closer to a factor of ~ 2 times higher. In either case, the consequence is that Kuiperian craters are on average younger than Copernican craters (Figure 3.8). The assertion that the HRE crater population on Mercury is on average younger than the HRE crater population on the Moon was previously suggested in Denevi and Robinson (2008) and confirmed here.

Observations show ~ 1.2 times more Mansurian craters per area on Mercury than Eratosthenian craters per area on the Moon (initially assuming the durations of the Mansurian and the Eratosthenian are equivalent), whereas the models for impact flux

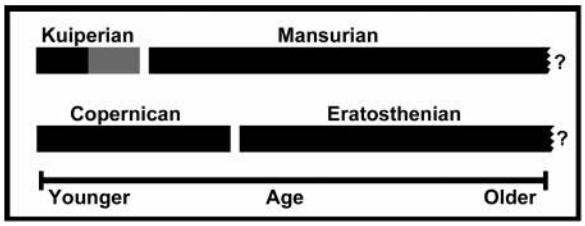

Figure 3.8: Relative ages of time-stratigraphic units on Mercury and the Moon. The Kuiperian period may be from 2 to 4 times shorter than the Copernican depending on the accuracy of the relative modeled impact flux at Mercury and the Moon, and assuming the impact rates remained constant during the past 1 Ga. The half black, half gray bar representing the Kuiperian period demonstrates this uncertainty. Kuiperian craters with high-reflectance rays and halos are younger on average than Copernican craters because of the faster reduction of reflectance for immature craters on Mercury.

suggest that there should be ~ 2 times more Mansurian craters than Eratosthenian craters per area (Le Feuvre and Wieczorek, 2008, 2011; Greenstreet et al., 2012), assuming constant impact flux on both bodies for the past ~ 3 Ga (e.g., Grieve and Shoemaker, 1994). Furthermore, the increased rate of space weathering on Mercury should result in Kuiperian craters transitioning into Mansurian-aged craters at a faster rate than their lunar counterparts (thus adding craters to the Mansurian population). This difference between observations and theory may be explained by an increased rate of near-Earth object-sized impacts at Mercury. The increased impact flux at Mercury relative to the Moon should not only result in more Mansurian craters but also erode the morphology of the Mansurian craters faster than their Eratosthenian counterparts. This increased impact erosion more rapidly transitions Mansurian craters into the Calorian-aged crater population. The comparison of the Kuiperian and Copernican craters is consistent with the Mansurian period ending later than the Eratosthenian. It follows that increased impact erosion results should cause the Mansurian period to be relatively shorter than the Eratosthenian, although how much shorter is unknown. Observations of Calorian- and Imbrian-aged craters are required to define the rate of Mansurian craters eroding and transitioning into Calorian-aged

craters, relative to Eratosthenian craters transitioning to Imbrian craters (based on crater morphologic degradation states).

The ratios of Kuiperian to Mansurian and Copernican to Eratosthenian craters per unit area provide a comparison of crater rim erosion rates and space weathering on Mercury and the Moon, assuming the rate of cratering on each body is constant over time up to 3-3.2 billion years ago. If the Copernican period is $\sim$ 800 Ma long and the Erastosthenian period is $\sim$ 2400 Ma long, then the ratio of Copernican-aged to Eratosthenian-aged craters should be $\sim$ 0.33 based on time (and degradation state) alone. The measured ratio of Copernican to Eratosthenian craters in this work was slightly less: 0.23 ± 0.03. The discrepancy may be due to changes in the cratering rate over time, or dependencies on our criteria for Eratosthenian crater classification. The ratio of Kuiperian to Mansurian craters per unit area is 0.11 ± 0.01, which is half the ratio of Copernican to Eratosthenian craters, implying that the Kuiperian is shorter in duration relative to the Mansurian than the Copernican is to the Eratosthenian. It follows that the Kuiperian is $\sim$ 10 times shorter than the Mansurian, but only if the cratering rate has remained constant over time. That the Kuiperian to Mansurian ratio is approximately half the lunar Copernican to Eratosthenian ratio provides another indicator of increased (large-scale) impact erosion and space weathering on Mercury than on the Moon.

Secondary craters and compositional ejecta may have a small influence on the final observations of craters per unit area. If secondary craters are mistakenly included (see Methods) in the count, then the number of primary Kuiperian craters is lower than the reported count, resulting in a greater difference between our observations and the modeled impact flux ratios. Since lunar secondaries are on average smaller than Mercurian secondaries (Gault et al., 1975), the likelihood of a bias in the lunar crater numbers is even less. Although the lunar OMAT data show that

high-reflectance ejecta from young craters is the result of the immaturity of the regolith, no proven method for verification of maturity differences exists forMercury (see section 2). Considering this point, the final number of Kuiperian craters per unit area may include some number of craters with compositional ejecta. Removing the compositional craters from the count would decrease the number and result in a greater difference between the observations and the modeled impact flux ratios.

3.5.2 Comparison of Reflectance of Immature Material on Mercury and the Moon

The distribution of reflectance values of high-reflectance ejecta on the Moon and Mercury, as described in section 3.2, is shown in Figure 3.4. The range of reflectance values is interpreted as a continuum of maturity states within the immature crater populations. Both distributions show positive skew, where positive deviations from the mean are much larger than the negative deviations. A comparison of LROC WAC reflectance values and the Clementine FeO wt% map (see Figure 3.6) indicates that reflectance values from the LROC WAC are not correlated with FeO wt%, demonstrating that variations in FeO wt% are not responsible for the positive skew of the lunar distribution. The positive tails of the distributions contain the youngest ejecta material, which is not yet optically darkened by regolith maturation to the same extent as the average of all immature craters measured. The positive tails of the distributions are defined as the observations more than one standard deviation from the mean of the distribution (see Figure 3.9). In the lunar case, the positive tail contains all immature craters with reflectance values >0.17, and in the mercurian case, the tail includes all immature craters with reflectance values >0.085. A comparison with lunar OMAT values shows that the average OMAT value of crater ejecta within the positive tail is 0.25, with a standard deviation of 0.05, whereas the average OMAT value of the rest of the craters in the lunar distribution is 0.19, with a standard de-

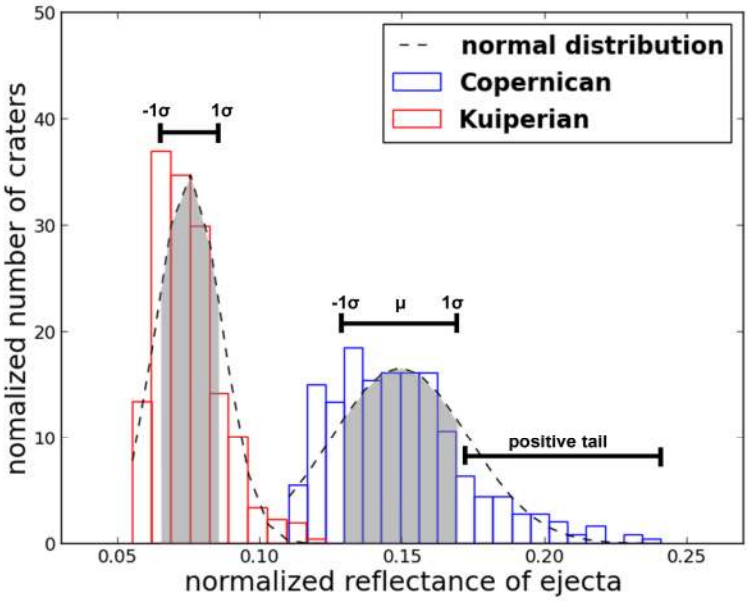

Figure 3.9: Same data as in Figure 3.4 except that the number of craters is normalized to 100, and the plot includes the normal probability distribution functions for Copernican and Kuiperian immature crater ejecta reflectance. The shaded area under each curve shows the part of the distribution within one standard deviation of the mean (μ). The positive tails are defined by observations with reflectance values more than one standard deviation above the mean.

viation of 0.03. Grier et al. (2001) assigned relative ages to fresh craters based on their OMAT value at 2 crater diameters from the crater center. Craters with OMAT values 0.22 are considered the youngest, and craters with OMAT values between 0.15 and 0.22 are considered intermediate in age (surfaces with OMAT values <0.14 are considered mature) (Grier et al., 2001). From this comparison with the work of Grier et al. (2001), the craters within the positive tails in this study are on average younger than the rest of the fresh crater population.

Average immature lunar highland material has a reflectance ∼1.9 higher than average immature material on Mercury. The uncertainty in the calibration of photometrically normalized reflectance for both cameras is 10%, so the propagation of uncertainty shows the ratio to be 1.9±0.4 (Hawkins et al., 2007; Robinson et al.,

2010). While immature material has some finite amount of darkening due to space weathering, the ratio of the average reflectance of immature materials on Mercury and the Moon is not completely dominated by differences in regolith maturity, but is likely also a measure of compositional differences. Within the population of rayed crater ejecta measured, we assume that at least a few craters have minimal (∼1%) spectral changes due to space weathering. A comparison of the highest reflectance values (assumed to be least mature; 0.12 on Mercury and 0.24 on the Moon) shows two times higher reflectance for immature lunar material than for immature mercurian material.

There are two possibilities for the difference between the average reflectance of immature crater ejecta on Mercury and the Moon. Either there is a compositional difference between the lunar highlands and Mercurys surface (between -40 to 40 latitude) or the lower reflectance of Mercurys immature material is caused by the faster space weathering environment on Mercury compared to the Moon. Based on what is known about Mercurys composition and space weathering, it is plausible that both compositional differences and space weathering are affecting the reflectance of immature materials on Mercury causing the lower reflectance.

Initially Mercurys crustal composition was thought to be analogous to anorthosites (>90% plagioclase feldspar) in the lunar highlands based on similar low ferrous iron wt% (Blewett et al., 2002). However, data from the MESSENGER X-Ray Spectrometer (XRS) has established that Mercurys surface is compositionally different from the lunar highlands. XRS spectra indicate that the surface, normalized to the Si abundance, has relatively high abundances of Mg and S, but is low in Al and Ca and very low in Fe, Ti, Cl, Cr, and Mn (Nittler et al., 2011, Weider et al., 2012) compared with typical terrestrial and lunar crustal materials.

Mercurys average mature reflectance is comparable to the average reflectance of

the lunar maria (Figure 3.10), however, spectral observations of Mercurys surface do not have a ∼1-micron absorption feature (e.g., Vilas, 1988; Robinson and Taylor, 2001; Blewett et al., 2002; Denevi and Robinson, 2008; McClintock et al., 2008; Blewett et al., 2009; Riner et al., 2010). This means that Mercurys surface does not have sufficient FeO (2-5 wt% FeO limit from Sprague et al., 2009; Nittler et al., 2011) to produce a ∼1-micron absorption feature in reflectance spectra. Therefore lunar mare basalts (∼15-25 wt% FeO) are not appropriate analogs for the average surface of Mercury.

A significant opaque component in Mercurys crust has been suggested to account for the low reflectance of Mercury and satisfy the 2-5 wt% FeO limit (e.g. Denevi and Robinson, 2008; Sprague et al., 2009; Riner et al., 2010). Many opaque minerals, rich in Fe and Ti, do not have diagnostic absorptions at 1 μm (Wagner et al., 1987, Riner et al., 2009; Cloutis et al., 2008) and may increase the amount of iron permitted on the surface by near-infrared (NIR) spectral observations. The opaque mineral geikielite, part of the ilmenite-geikielite ($FeTiO_3 - MgTiO_3$) solution series could provide a darkening component for the mercurian crust (Riner et al., 2010). The solution series of chromite-ulvöspinel ($(Mg, Fe)Cr_2O_4 - (Mg, Fe)_2TiO_4$) was another possibility, since spinels are the dominant opaque mineral in the lunar highlands and make up as much as 10 vol.% of the basalts from Apollo 12 to 15 (Papike et al., 1998; Lucey, 2006). Chromites have a steep spectral slope and while they have similar reflectances to the Fe-Ti oxides in the UV, they are 2-7 times brighter in the NIR (Cloutis et al., 2004) and thus are not candidates for the primary opaque component on Mercury.

Recent models of space weathering on Mercury combined with models of opaque minerals as a component of the crustal composition suggest that the total albedo variations on Mercurys surface (Figure 3.10) cannot be explained by the addition of an

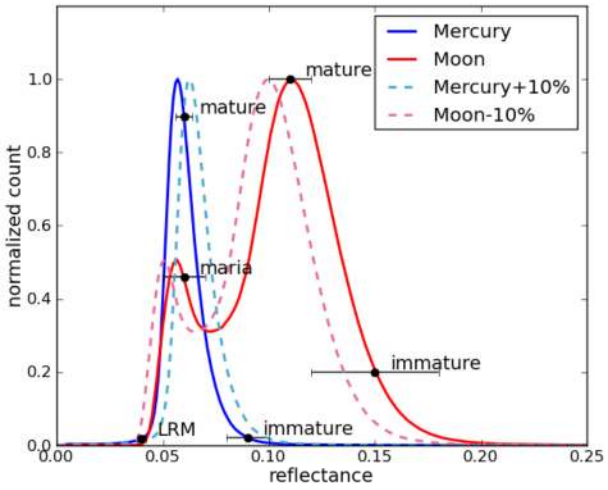

Figure 3.10: Values are from photometrically corrected monochrome mosaics of Mercury and the Moon at comparable wavelengths (566 and 560 nm) between -40 and 40° latitude. LRM stands for Low Reflectance Material, which is the lowest reflectance material on Mercury. Average mature and immature mercurian and lunar material are included as black dots, as well as the average reflectance of the lunar maria. Counts are normalized to 1.0 at the mode, and errors shown are ±1 standard deviation. Dashed lines show the worst case uncertainty (±10%) for reflectance on the basis of absolute calibration requirements, indicating that differences in the distribution of reflectance between the Moon and Mercury are robust.

opaque mineral alone (Lucey and Riner, 2011; Riner and Lucey, 2012). These models hypothesize that abundant space weathering derived iron (submicroscopic metallic iron, SMFe) is required to darken the surface, in addition to compositional variations across the crust (Riner and Lucey, 2012). Estimates indicate average mature mercurian surface material has at least 2.5 wt% SMFe, more than five times the average of returned lunar soils but within the XRS limit (Fe ≥4 wt%) (Riner and Lucey, 2012).

Petrologic modeling of mercurian analogs based on MESSENGER-derived compositions for a range of Mg-rich terrestrial rocks including magnesian basalt, basaltic komatiite, and peridotitic komatiite as defined by the Basaltic Volcanism Study Project (1981) (Stockstill-Cahill et al., 2012). Magnesian basalts contain 8.5-12 wt% MgO (11.6 wt% FeO), basaltic komatiites contain 12-20 wt% MgO (9.9 wt% FeO), and peridotitic komatiites contain >20 wt% MgO (11.5 wt% FeO) (Basaltic Volcanism

Study Project, 1981). Modifications to the terrestrial compositions were made prior to crystallization modeling to account for differences in FeO contents between terrestrial analog and Mercury compositions (Stockstill-Cahill et al., 2012). The FeO contents of the terrestrial Mg-rich rocks are higher than the limit of 2-5 wt% FeO for the surface of Mercury (Sprague et al., 2009; Nittler et al., 2011). Therefore, the FeO contents of these rocks were decreased to 3 wt% by replacing molar FeO with MgO to mimic expected Mercury magmas (Stockstill-Cahill et al., 2012). Results showed that the surface composition of Mercury is most similar to that of a terrestrial magnesian basaslt (with lowered FeO), composed predominantly of Mg-rich orthopyroxene and plagioclase (Stockstill-Cahill et al., 2012). The modeled Mercury compositions are dominated by orthopyroxene (enstatite) and plagioclase, and as such are classified as norites, while the Mg-adjusted terrestrial magnesian basalts are classified as gabbronorites (Stockstill-Cahill et al., 2012).

3.5.3 Ray Length Comparison

Observations of the ratios of ray length to crater diameter produced similar ratios for Mercury and the Moon, which is consistent with models of gravity-dominated crater excavation and ballistic ejecta range given by Melosh (1989). These models show that the calculated ejecta range is the same for Mercury and the Moon since the effects of higher gravity and higher average impactor velocity on Mercury than on the Moon counteract each other, and as a result the ejecta range is dependent only on the crater diameter. The model is restricted to cases in which the ballistic range of the ejecta is much smaller than the radius of the planet. Differences in the ratio of ray length to crater diameter between Mercury and the Moon might be expected as a result of faster optical maturation on Mercury, but no systematic differences were detected in this study.

Although the ratio of ray length to crater diameter is shown to be similar on Mercury and the Moon, there were outliers. A majority of craters have ratios of ray length to crater diameter between 2 and 13, but five outliers have ratios between 15 and 19 (see Figure 6). The average ratio of ray length to crater diameter is 8±4 on the Moon and Mercury. The five craters have ray length to crater diameter ratios approximately two standard deviations higher than the average. The lunar outliers are Giordano Bruno and Byrgius A, and the Mercurian outliers are Debussy, Xiao Zhao, and Qi Baishi. The OMAT values for the lunar craters show that Giordano Bruno and Byrgius A have higher OMAT values (0.33 and 0.30, respectively) than the other craters in the data set (average OMAT value of 0.22, standard deviation is 0.02), indicating a relatively younger age. Additionally, previous work indicates that the ratio of ray length to diameter should decrease with time due to a decrease in the thickness of the ejecta material with distance from the crater rim, the optical maturation of the regolith, and impact gardening (Melosh, 1989; Hörz et al., 1991; Grier et al., 2001). The ejecta at the crater rim is thicker and less mixed with local material than within the rays, which are thinner and more mixed with local mature soils (Hörz et al., 1991). Grier et al. (2001) showed that the ejecta material closest to the crater rim is the most immature of all ejecta and appears to be so for longer timescales than rays and distal ejecta. Other factors in the maturation rate of ejecta include the excavation of large blocks, which provide a continuous source of immature material as they are broken down over time, and steep slopes (such as those found at central peaks), which continually refresh the regolith as immature material is exposed by downslope movement (McKay et al., 1974). As a consequence, one should expect that the youngest craters would have the highest ratios of ray length to diameter. By this argument, Qi Baishi, Xiao Zhao, and Debussy are among the youngest rayed craters on Mercury.

3.6 Conclusions

1. Our measurements show there are ∼2 times fewer Kuiperian craters per unit area on Mercury than Copernican craters per unit area on the Moon. Initially equating the duration of the Copernican and Kuiperian periods, models for the impact flux of near-Earth objects (Le Feuvre and Wieczorek, 2008, 2011; Greenstreet et al., 2012) and the observed counts of Kuiperian and Copernican impact craters disagree by a factor of ∼4.

2. A faster rate of optical maturation on Mercury than on the Moon can account for the deficit of Kuiperian craters on Mercury. Faster regolith maturation on Mercury causes maturity rays to fade faster than on the Moon. A consequence of this explanation is that optical maturation on Mercury is up to 4 times faster than on the Moon. This faster rate of optical maturation shortens the Kuiperian period relative to the Copernican. On average, rayed Kuiperian craters are then younger than rayed Copernican craters, consistent with previous suggestions (Denevi and Robinson, 2008).

3. Our observations show ∼1.2 times more Mansurian craters per area on Mercury than Eratosthenian craters per area on the Moon. Impact flux models, in contrast, indicate that the ratio should be closer to 2. This difference between observations and theory can be explained by an increased rate of near-Earth object-sized impacts at Mercury. The same increased rate of impacts at Mercury than at the Moon, which produces more Mansurian craters than Eratosthenian craters per time, should also degrade the morphology of the Mansurian craters faster than their Eratosthenian counterparts. The increased rate of morphologic degradation would result in the observed deficit of Mansurian craters, but also causes the Mansurian period to be relatively shorter than the Eratosthenian, although how much shorter is unknown.

4. The average photometrically normalized reflectance of immature lunar highland material is a factor of 1.9±0.4 higher than the reflectance of immature material on Mercury. Assuming that the immature materials have a minimal amount of exposure space weathering, the difference in reflectance of immature materials is likely caused by differences in composition between the lunar highlands and average Mercury surface material, a finding consistent with those of previous work (Denevi and Robinson, 2008).

5. Differences in the ratio of ray length to crater diameter between Mercury and the Moon might be expected due to faster optical maturation on Mercury, but no differences were detected in this study. Our observations showed five craters with higher ratios of ray length to crater diameter than the rest of the rayed crater population: Giordano Bruno and Byrgius A on the Moon, and Debussy, Xiao Zhao, and Qi Baishi on Mercury. Previous work on the properties of crater rays and ejecta suggests that the youngest craters should have higher ratios of ray length to diameter. Thus, Qi Baishi, Xiao Zhao, and Debussy are among the youngest rayed craters on Mercury.

Chapter 4

THE GRUITHUISEN DOMES: AGE AND MORPHOLOGY OF SILICIC NONMARE VOLCANISM

4.1 Introduction

The Gruithuisen Domes are three silicic volcanic domes (Gamma, Delta, and Northwest) located at 36.43°N, −40.19°E, with distinct morphology and spectral signatures compared to the lunar maria and highlands (Whitaker, 1972; Scott and Eggleton, 1973; Smith, 1973; Malin, 1974; Head and McCord, 1978; Wagner et al., 2002; Glotch, 2010) (Figure 4.1). The presence of silicic volcanism such as the Gruithuisen Domes represents a compositional end-member of planetary differentiation. The lunar magma ocean (LMO) model for early lunar differentiation was a concept arising from the Apollo missions (Wood et al., 1970; Warren, 1985). In the LMO model, an anorthositic lunar crust floated as it crystallized out of a denser basaltic magma, forming the highlands regions of the Moon (Warren, 1985). At the time the LMO model was developed other lunar rock types, such as the high-magnesian and high-alkali suites, were not yet identified. The presence of highly evolved magma and the processes that must take place to produce such magma may be used to place constraints on mantle sources, early mantle processes, and lunar crustal evolution.

While the Gruithuisen Domes are small in volume compared to the basaltic maria and the anorthositic highlands, the domes and other similar structures are an important part of lunar geologic history. Examples of extrusive silicic materials are rare in the Apollo sample collection (Robinson and Taylor, 2011). However, recent results from the Lunar Reconnaissance Orbiter (LRO) mission have shown that highly silicic

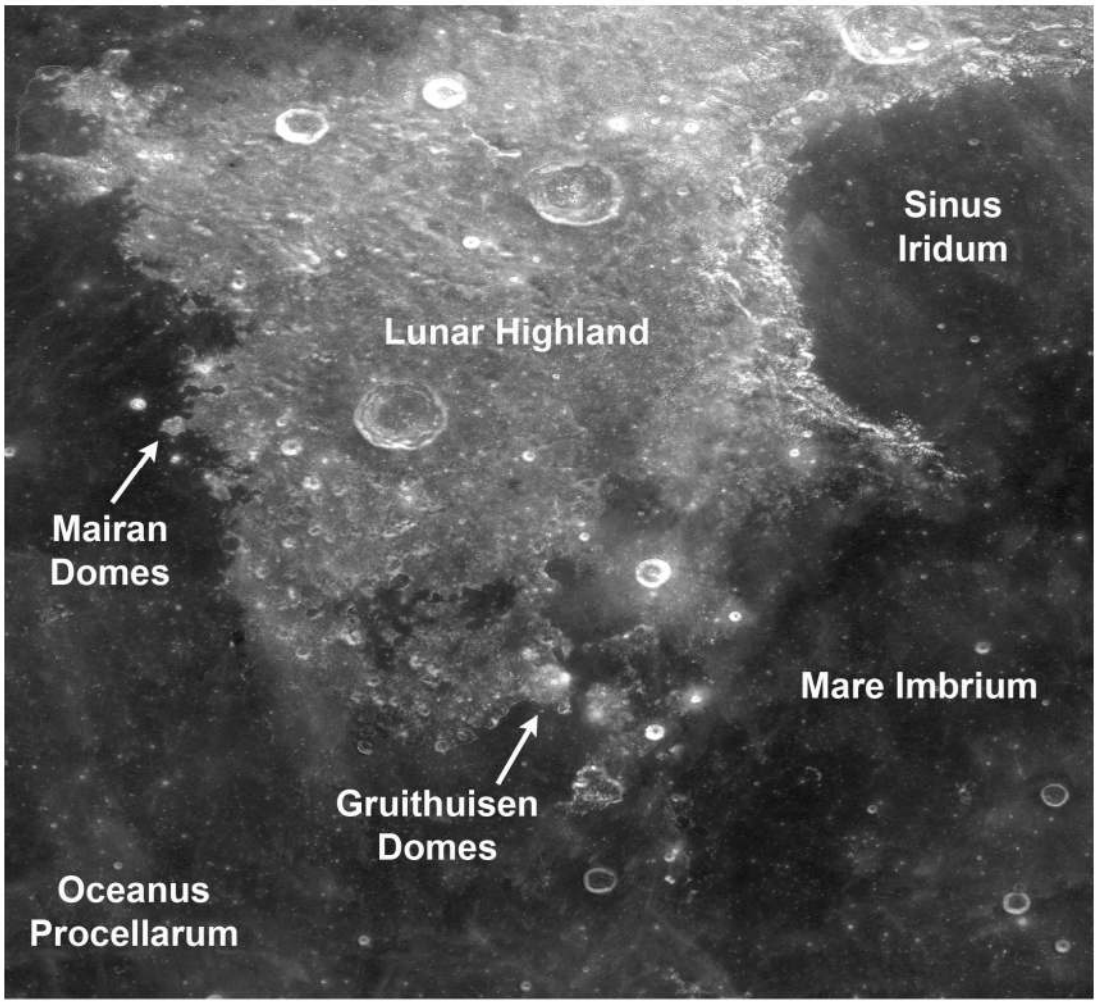

Figure 4.1: Lunar Reconnaissance Orbiter Wide Angle Camera 643 nm mosaic showing the region surrounding the Gruithuisen Domes, with other key lunar features noted. The region shown here extends from 30.7° to 49.2°N and -50.9°to -30.6°E.

lunar rocks are more volumetrically important in the lunar crust than is evident from the Apollo sample suite (Glotch et al., 2010; Jolliff et al., 2011). The material from the Gruithuisen Domes is an under-represented lunar rock type, a sample of which would lead to a more complete picture of lunar magmatic evolution.

In this work data from Diviner, Lunar Prospector (LP) Gamma Ray Spectrometer (GRS), Clementine, Lunar Reconnaissance Orbiter Camera (LROC) Wide Angle Camera (WAC), and high resolution LROC Narrow Angle Camera (NAC) images

are used to investigate the composition, age, and morphology of the Gruithuisen Domes. One focus of this study is to compare the dome morphologies to terrestrial silicic domes and other lunar silicic domes. Details of the emplacement history of the domes may be discovered through a comparative study of the morphology. LROC NAC images (50 cm/px to 2 m/px) and Digital Topographic Models (DTMs) at a scale of 2 meters/pixel provide the ability for unprecedented topographic analysis. These observations aid in the determination of emplacement mode. New crater size-frequency distributions from the summit plateaus of the Gamma and Delta domes determine if the two main domes formed contemporaneously, or if a geologically significant period of time separated the two events. Finally, the distribution of high silica signals in the Diviner Christiansen Feature maps at the Gruithuisen Domes are compared to other compositional maps, spectra, and topography to determine the reasons for high silica signals in certain locations on the domes.

4.2 Background

The Gruithuisen Domes are nonmare extrusive volcanic features most likely of Imbrian age (Whitaker, 1972; Scott and Eggleton, 1973; Smith, 1973; Malin, 1974; Head and McCord, 1978; Wagner et al., 2002). The domes occur at the western edge of Mare Imbrium, south of Sinus Iridum. Studies of stratigraphy in this region show that the domes are superposed on the edge of a plateau of highland material (Whitaker, 1972; Wagner et al., 2002). After the formation of the domes, mare flood basalts embayed the area, likely concealing the original extent of the domes. According to Chevrel et al. (1999), viscous flows of silica-rich, nonmare material may have occurred locally as well as regionally prior to 3.8 Ga, and nonmare, silicic material may have been more common in the early part of lunar history than the current extent of slicic volcanism suggests.

The domes are located within the Procellarum KREEP terrane (PKT), a region on the nearside of the Moon, defined as a continuous area where the Lunar Prospector GRS detected thorium $>$ 3.5 ppm (Jolliff et al., 2000). KREEP is an acronym used to describe lunar materials containing anomalous amounts of potassium (K), rare earth elements (REE), and phosphorus (P) compared to chrondrites. These incompatible elements preferentially concentrate in the melt phase of magma. The PKT is notable for the abundance of thorium and other heat-producing elements that are concentrated in late-stage melts (e.g. Jolliff et al., 2000). Models based on the Lunar Prospector GRS thorium maps show that Gruithuisen Gamma and Delta have calculated thorium values of 43 ± 3 and 17 ± 6 ppm, respectively (Hagerty et al., 2006). The presence of domes and shield volcanoes in the PKT hints at a possible petrologic connection between these morphologic features and KREEP-rich rock chemistries or thorium (Hagerty et al., 2006). While most areas high in thorium are within the PKT, the Compton-Bel'kovich thorium anomaly is located on the lunar farside. Recent LROC images show that the thorium anomaly is a low dome with unusual morphologies at the 10-m scale (Greenhagen et al., 2010; Jolliff et al., 2011). Greenhagen et al. (2010) noted that the presence of the Compton-Bel'kovich silica-rich dome implies that the process through which high-silica features form did not require the thermal conditions of the PKT, or alternatively that volcanism driven by radiogenic heating is more extensive than the spatial boundaries of the PKT suggest. Other features on the farside also have enhanced thorium values, such as the Dewar cryptomare (Lawrence, et al., 2008), but are not lunar red spots or silicic domes.

Early morphologic studies comparing the Gruithuisen Domes to terrestrial features (using height-width relationships) found that the lunar nonmare domes resemble terrestrial volcanic domes of silicic composition characterized by viscous lava and low extrusion rates (Head and McCord, 1978). Wilson and Head (2003) modeled the

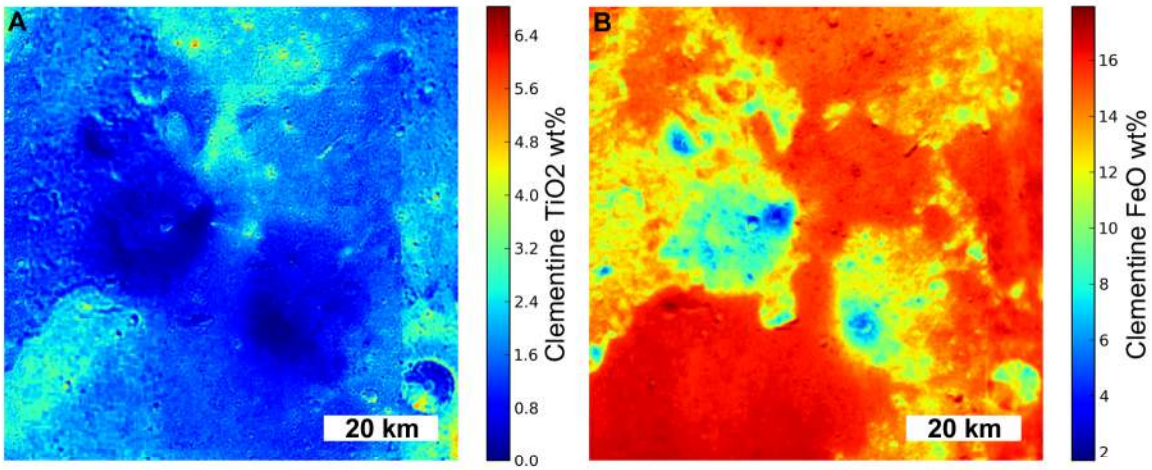

Figure 4.2: Clementine TiO2 and FeO wt% data sampled at 200 m/px (Lucey et al., 1995, 1998, 2000a).

yield strength, plastic viscosity, and effusion rates for the material that formed the Gruithuisen Domes and concluded values were consistent with terrestrial formations characterized by viscous, silicic magmas of rhyolite, dacite, or basaltic andesite composition. In terms of dome formation, feldspathic magmas could produce lavas of the proper viscosity, but it is possible that the domes could be highly differentiated products related in composition to plutons of granitic material, which may occur below the lunar crust (Head and McCord, 1978). It is important to note that the Gruithuisen Domes differ both spectrally and morphologically from flatter and generally smaller shield volcanoes seen in many areas within lunar maria (Chevrel et al., 1999; Wagner et al., 2002; Lawrence et al., 2013). Spectra indicate more silicic compositions compared to mare domes due to lower iron and titanium values in the Clementine TiO_2 and FeO wt% maps (Figure 4.2) (Lucey et al., 1995, 1998, 2000a).

The Gruithuisen Domes are members of a group of spectral features known as "red spots" (Whitaker, 1972; Malin, 1974; Head and McCord, 1978; Bruno et al., 1991). Red spots are spectral anomalies characterized by high albedo and strong ultraviolet absorption that do not match spectral characteristics of common lunar

samples (Malin, 1974; Head and McCord, 1978). Red spot features on the nearside of the Moon include, but are not limited to, Mons LaHire, Hansteen Alpha, Lassell Massif, and Montes Ripaeus, all of which are found within the PKT (Hagerty et al., 2006). Red spots are thought to be products of volcanism and suggest a connection with KREEP-rich basalts (surface manifestations of KREEP-rich basalts) or even more evolved highland compositions such as dacite or rhyolite (Malin, 1974; Wood and Head, 1975; Head and McCord, 1978; Raitala et al., 1999; Hagerty et al., 2006).

Recent results from the Diviner Lunar Radiometer Experiment (Paige et al., 2010) on board the Lunar Reconnaissance Orbiter have shown that some red spot domes on the Moon exhibit thermal infrared spectra consistent with highly silicic compositions (Glotch et al., 2010; Greenhagen et al., 2010; Glotch et al., 2011; Jolliff et al., 2011). These features, which include the Gruithuisen Domes, Hansteen Alpha, Lassell Massif, and the Compton-Bel'kovich anomaly, also exhibit strong thorium anomalies in Lunar Prospector (LP) Gamma Ray Spectrometer (GRS) data, suggesting that they formed from highly evolved magmas (Lawrence et al., 2003, 2005; Hagerty et al., 2006).

While the Apollo missions sampled a range of materials, including volcanic glasses from fire fountains, mare basalts, and crustal rocks, these samples come from a small portion of the lunar crust. Results from past remote-sensing missions (Lunar Prospector and Clementine) show that lunar samples returned during the Apollo and Luna missions are not representative of the entire lunar surface and that other rock chemistries exist (e.g. Jolliff, 1999; Giguere et al., 2000). The present view of lunar magmatic evolution is limited because the sampling of the Moon is limited. Within the lunar sample inventory there are silicic volcanic intrusive materials that may be similar to the Gruithuisen Domes, but they are rare and only occur within breccias or the regolith as small fragments of felsic rocks variably referred to as granite, felsite, or rhyolite (Jolliff et al., 1991, 1998; Korotev, 1998; Papike et al., 1998). The

largest granitic sample, 12013, is actually a granitic breccia containing two lithologies, granitic material and a mafic, KREEP-rich phase (Seddio et al., 2011). The origin of these rocks is unknown, however high thorium red spots like the Gruithuisen Domes are candidate source regions (Hagerty et al., 2006). Some of these samples have thorium concentrations as high as 50-60 ppm. Spatial deconvolution of Lunar Prospector GRS thorium data from the Gruithuisen Domes permit thorium values that match the high measured sample concentrations (Hagerty et al., 2006). Knowledge of the petrogenesis of these rare fragments will be incomplete until the geologic setting of their origins is known.

Many workers have considered lunar magmatic evolution, including Warren (1985), Shearer and Papike (1999), and Shearer et al. (2006). A generalized framework of lunar magmatic evolution includes the formation of (1) an anorthositic crust, (2) high-magnesian suite lithology, (3) high-alkali suite lithology, (4) KREEP-rich rocks, and (5) mare basalts. However, petrogenetic relationships between major lunar igneous rock suites are not well understood. The chemistry of primary highlands rocks (e.g., ferroan anorthosites) indicates that extensive melting occurred in the outermost part of the Moon, forming a silicate magma ocean (LMO) (Warren, 1985). If such an ocean cooled and crystallized, the physical separation of crystals (the floating of lower-density plagioclase feldspar, following extensive crystallization of olivine and pyroxene at depth) produced the original lunar crust between 4.6 and 4.3 Ga ago (Warren, 1985). Eventually late-stage cumulates, rich in higher density, Fe-bearing minerals including ferropyroxene and ilmenite ($FeTiO_3$) sank to form the source areas for high-Ti mare basalts (Warren, 1985). Negative Europium (Eu) anomalies (deficiencies) in mare basalts indicate that they formed by partial melting of these cumulates, which developed from the magma ocean after plagioclase crystallized and incorporated the Eu (Warren, 1985).

Between the formation of the anorthositic crust (> 4.3 Ga) and the mare basalts (mostly < 3.8 Ga), another group of igneous rocks formed, including the Magnesian-suite (Mg-suite), and related, more chemically evolved rocks with KREEP-rich or alkali-rich compositions. Both Mg-suite magmas and some mare basalt magmas seem to have been affected by KREEP-rich material, either as a component in their source area or as an assimilated component (Wood, 1975; Papike and Vaniman, 1978). Whereas the ferroan anorthosites appear to be flotation cumulates from solidification of the magma ocean, the Mg-suite rocks have the characteristics of layered mafic intrusive rock bodies, and their relationship to the ferroan anorthosites, geologic and petrologic, remains poorly understood (Wood, 1975; Papike and Vaniman, 1978; Vaniman and Papike, 1978). The Mg-suite rocks most likely formed by partial melting of magma-ocean-derived mantle cumulates that intruded and variably reacted with early crustal rocks (Wood, 1975; Papike and Vaniman, 1978; Vaniman and Papike, 1978). These ages are mostly ancient (> 4.0 Ga), but some samples have been dated that have considerably younger ages, extending their parent magmatic activity in some parts of the Moon to perhaps as young as 3.0 Ga (Head, 1976). A volumetrically minor group of rock types known as the alkali suite (granite, alkali anorthosite, alkali norite, and monzogabbro) may be related to the Mg-suite by extreme fractionation of residual melts, but the sample set is too sparse to prove geologic relationships (Lindstrom, 1984; Jolliff et al., 1991, 1998; Korotev, 1998; Papike et al., 1998). KREEP-rich basalts may also be related to the Mg-suite rocks by similar parent magmas and lines of descent. What is not known is if the chemically and petrologically evolved KREEP-rich basalts and alkali-suite rocks exist only as small, insignificant late stage separations of residual melt, or if they actually form large intrusive or extrusive bodies in some parts of the Moon (e.g., Hagerty et al., 2006). These rock types, rich in silica and feldspar, including K-feldspar, may actually be concentrated in some locations,

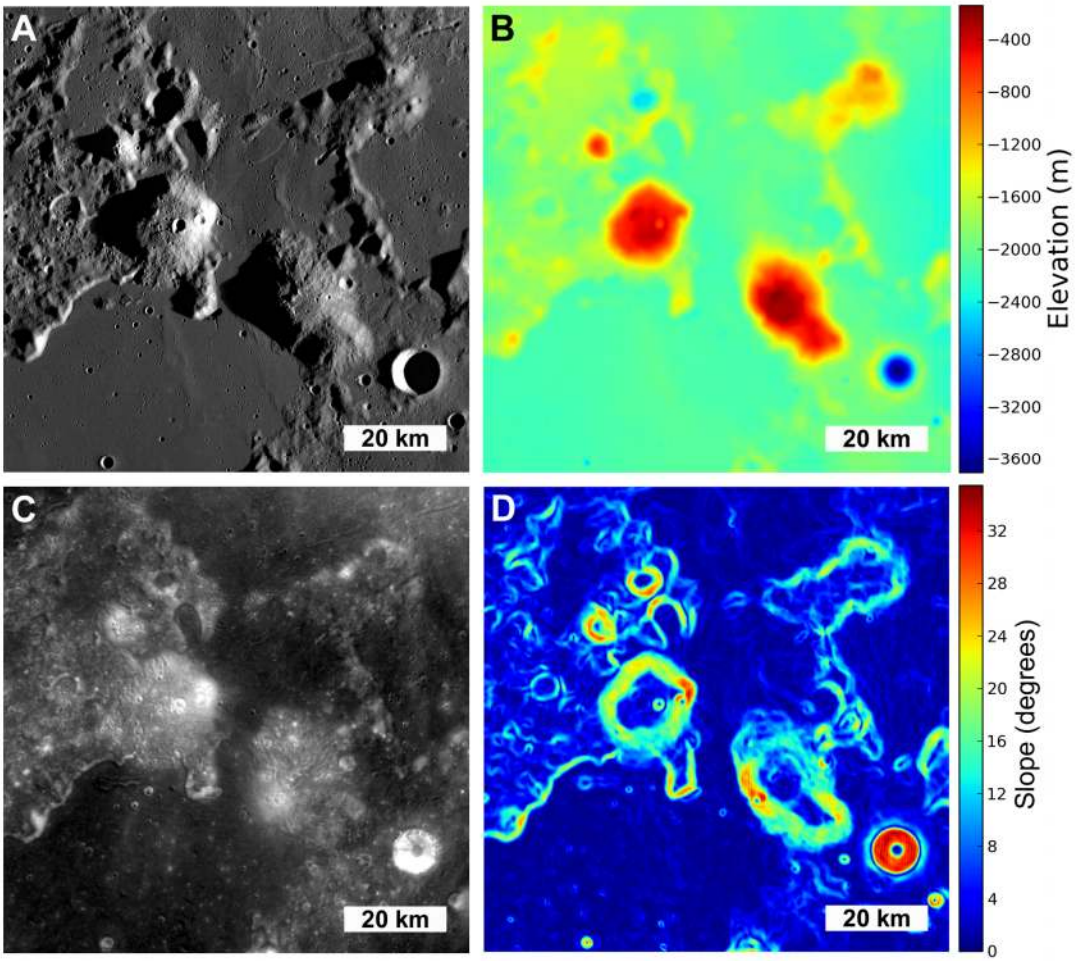

Figure 4.3: Four WAC views of the Gruithuisen Domes region at 100 meters per pixel resolution. A) High beta angle (the angle between the solar vector and the orbital plane of the spacecraft) mosaic emphasizing morphology. B) WAC GLD 100 colorized topography. C) 643 nm normalized reflectance. D) Colorized slope map derived from the WAC GLD 100 DTM.

including the nonmare domes (Hagerty et al., 2006).

There are two primary mechanisms proposed as the origin of the magma that formed the Gruithuisen Domes: silicate liquid immiscibility and basaltic underplating (Jolliff et al., 1999; Hagerty et al., 2006). In both mechanisms, the radiogenic heating of a KREEP-rich source material provides the heat for differentiation that caused the formation of the silicic anomalies. This is not difficult to imagine in the central

to northern Procellarum region of the Moon where volcanism was extensive (e.g. Jolliff et al., 2000). KREEP-rich basalt itself does not have especially high SiO_2 (< 50 wt%) (Meyer, 1977), so fractionation is needed to yield the distinctive silica enrichment found at the Gruithuisen Domes and other high thorium red spots.

Silicate liquid immiscibility is exhibited by certain silicate melts at high temperatures, where a melt of a given bulk composition cannot exist as a single homogeneous liquid, but splits into two liquids that will not mix (Roedder, 1951, 1953; Roedder and Weiblen, 1970). The compositions and properties such as viscosity and density of the two liquids are different (Roedder, 1951, 1953; Roedder and Weiblen, 1970). Silicate liquid immiscibility is caused by difference in the bonding between atoms in the two liquids, and thus each element in the bulk composition distributes itself between the two liquids in a way to achieve a minimum energy state (Greig, 1927). The process is used to explain cases where pairs of igneous rock types, one silicic and the other mafic, occur with no intermediate types but seem to intrude or extrude simultaneously (Roedder and Weiblen, 1970). Roedder and Weiblen (1970) found evidence for immiscibility in lunar magmas, however it occurred in only a very small amount of material in the late stages of crystallization. Silicic magma may originate through silicate-liquid immiscibility during fractionation of KREEP-rich parent magmas, but it is unclear that this process could occur on a large enough scale to source volcanic constructs such as the Gruithuisen domes (Jolliff et al., 2012). Alternatively, thorium-rich high-silica features may represent direct extrusive examples of the incompatible element-rich residual liquids from the LMO (Greenhagen et al., 2010).

Another proposed mechanism is heating of an already KREEP-rich source by basaltic underplating which could produce felsic partial melts directly through fractionation or could generate KREEP-rich melts that intrude to shallow levels where they further differentiate to produce evolved lavas (Hagerty et al., 2006). Underplat-

ing occurs when basaltic magmas are trapped during their rise to the surface due to "stalling out" within in the crust because of the difference in relative densities between the rising magma and the surrounding rock. In a lunar context, this could happen to any magma with a density higher than the anorthositic crust. Through this process basaltic intrusive magmatism may have remelted and subsequently differentiated a more silica-rich precursor like the anorthositic lunar crust (Hagerty et al., 2006). For example, the Compton-Bel'kovich occurrence may have involved the heating of deeper KREEP-rich sources, generating KREEP-rich melts that intruded to the near the surface before stalling and differentiating (Jolliff et al., 2012). The isolation of Compton-Bel'kovich from the PKT favors this interpretation (Jolliff et al., 2012).

4.3 Methods

The methods used in this paper to investigate the Gruithuisen Domes primarily use LROC data. LROC consists of three separate instruments: a Wide Angle Camera (WAC) and two Narrow Angle Cameras (NAC) (Robinson et al., 2010). The LROC NAC provides up to 50 cm/px scale images of the Gruithuisen Domes at a range of incidence angles. In addition, LRO can be rolled off-nadir to acquire a limited number of stereo observations (Burns et al., 2011). 24 NAC pairs with offset viewing geometries (parallax angles of $> 20°$) were used to create a 2 m/px LOLA-controlled digital topographic model (DTM) mosaic of sections of the Gruithuisen Domes region with the SOCET SET toolkit. The DTM mosaic was used for morphometric measurements of specific features on the domes, including heights, profiles, and slopes. LROC DTMs were also used to measure the morphology of three of the nearby Marian Domes (Glotch et al., 2011) for comparision. This includes the Mairan T (41.79°N, -48.39°E), Mairan South (40.75°N, -47.73°E), and Mairan Central

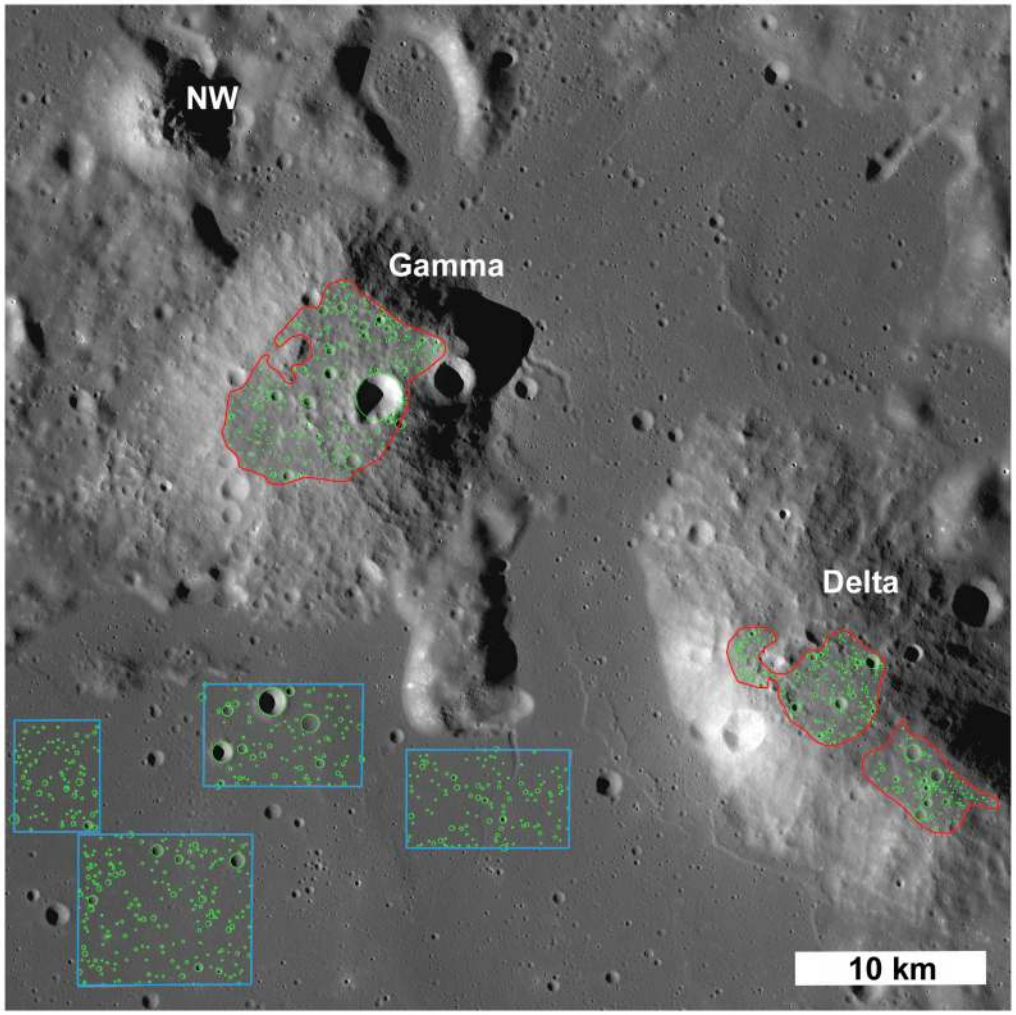

Figure 4.4: Areas on the summit plateaus of Gruithuisen Gamma and Delta are outlined in red. Areas for the mare CSFD are outlined in blue. Craters counted are outlined in green.

(or Middle) (41.36°N, -47.75°E) domes.

4.3.1 Crater size-frequency distributions

The purpose of measuring the crater size-frequency distributions (CSFDs) was to confirm the model ages from previous work, which used $\sim$ 60 m/px Lunar Orbiter images (Wagner et al., 2002), and determine if there are any significant age differences between the domes. CSFDs were measured using NAC data at 1.55 meters per

pixel, with an incidence angle of 71°. LROC NAC images M196764863, M196750574, M196743429, and M196757719 were processed using Integrated Software for Imagers and Spectrometers (ISIS) (Anderson et al., 2004) and imported into ArcGIS. The summit plateau areas were mapped (Figure 4.4). Crater counts were only performed on the summit plateaus since any sloped areas would have biased the statistics, as craters do not maintain their shapes and do not accumulate at the same rate when on steep slopes (Basilevsky, 1976). There was not a sufficiently flat area on the NW dome (summit areas were constrained to slopes of <2° for crater counting), so craters were only counted on the Gamma and Delta domes. The smallest crater size counted on the summit plateau regions is 30 m in diameter. There were no areas on the summit plateaus with identifiable secondary cratering. However in the surrounding mare there were areas with secondary craters and these areas were excluded from the count area. Craters on each plateau and a series of mare basalt terrains were digitized using ArcGIS CraterTools (Kneissl et al., 2011). The measured CSFDs were plotted with CraterStats2 (Michael and Neukum, 2010). Model ages are based on the chronology function and production function of (Neukum et al., 2001) for lunar craters 0.01 <D< 100 km. Results are shown in Figure 4.5. Sources of error in crater density analysis include human bias (counts change from individual to individual), individual bias (counts change from day-to-day for one person), and the inclusion of secondary craters in the count area.

4.3.2 Morphologic Measurements and Comparisons to Terrestrial Domes

Using 0.5-1.5 m/px NAC images and 2 m/px NAC DTMs, the units in the Gruithuisen Domes region were investigated. Characterization of unit contacts, dome ridges, and flank slopes provided further insight into the domes. Elevation profiles and contour maps derived from the DTMs allowed for a better estimation of height

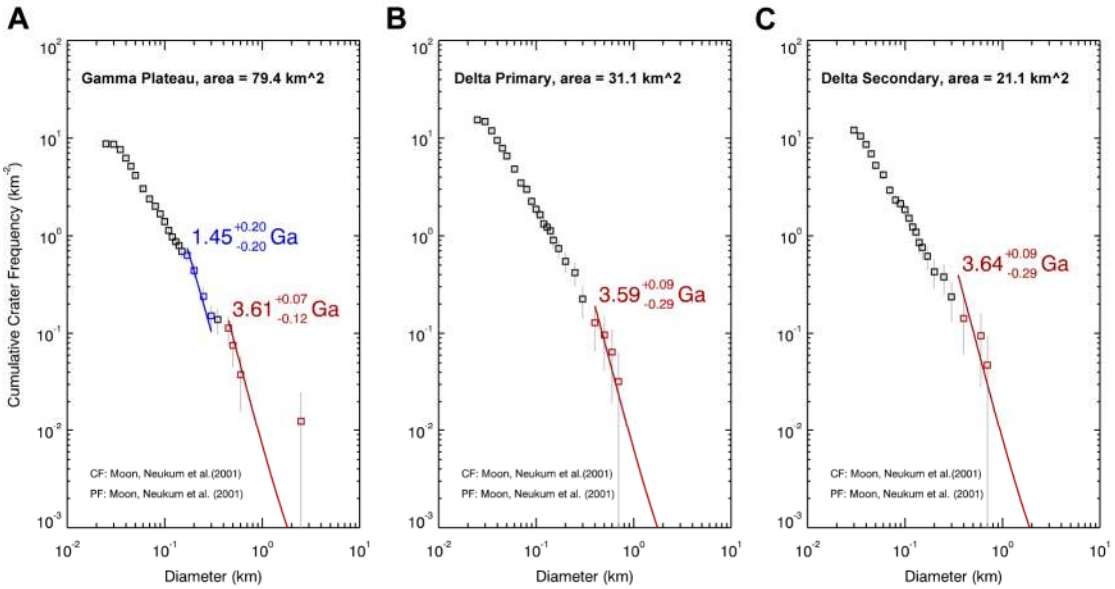

Figure 4.5: Crater size-frequency distributions for the three summit plateau areas on Gruithuisen Gamma and Delta domes. A) The Gruithuisen Gamma dome shows a resurfacing event at a model age of $\sim$ 1.45 Ga. B) The Delta dome's primary summit plateau with model age and C) The Delta dome's secondary summit plateau with model age.

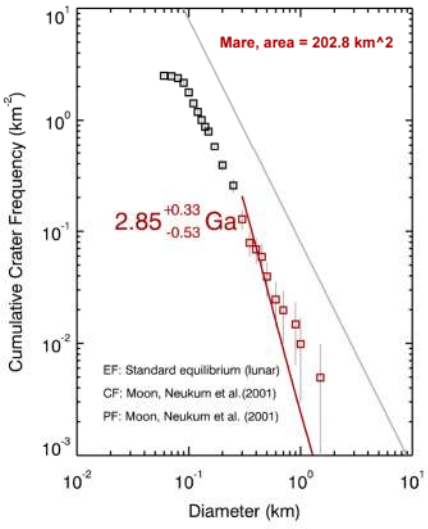

Figure 4.6: Crater size-frequency distributions from the mare south of Gruithuisen Gamma for comparison to the CSFD from the summit plateau areas.

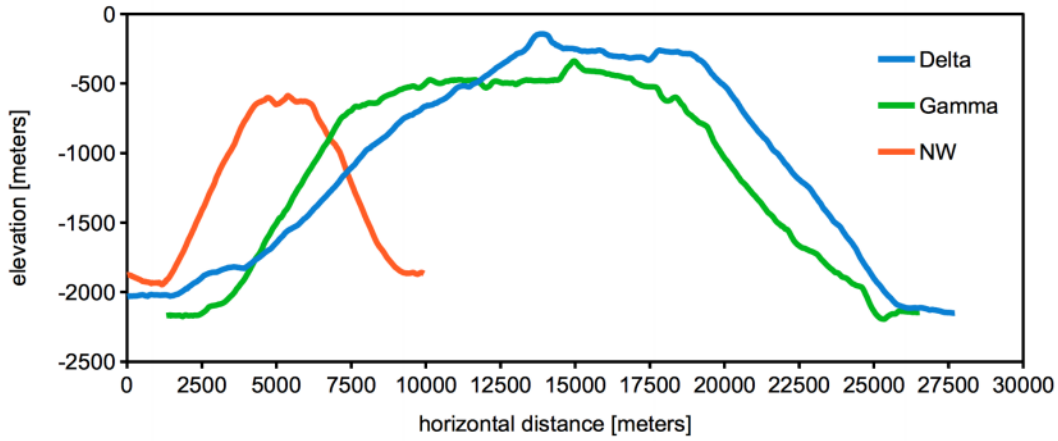

Figure 4.7: NAC DTM 2 meter/px (horizontal scale) elevation profiles across each of the three Gruithuisen Domes. Vertical exaggeration is 5×. Note the smaller radius of the NW dome. Locations for each profile are shown in Figure 4.8.

and the detailed morphology of the summit plateau regions (Figure 4.7). The height of the dome ridges relative to the average slope height was measured and the elevation was plotted.

Comparing the Gruithuisen Dome morphologies to terrestrial silicic domes could indicate the details of the emplacement history of the domes, such as eruption rate. Dome aspect ratio is the height of the dome divided by the diameter. Aspect ratios can be very useful for identifying the emplacement and general composition of a volcanic formation (Pike, 1978; Whitford-Stark, 1982). Height and diameter for the Gruithuisen Domes were measured using LROC 100 m/px WAC DTM data and LROC NAC DTMs. Terrestrial height and radius came from measurements in the literature (Tables 4.2 and B.1).

4.3.3 Multispectral Analysis

Diviner Lunar Radiometer (DLRE) on board LRO is a multispectral push broom sensor collecting information in 9 spectral channels (Paige et al., 2010). Diviner iden-

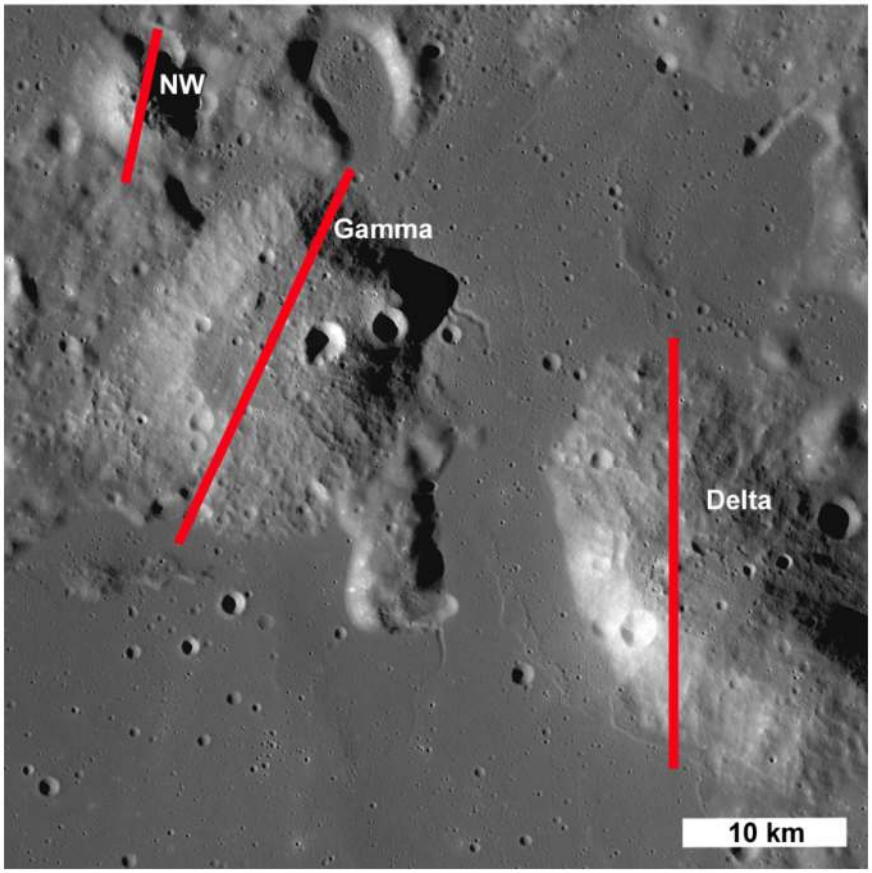

Figure 4.8: LROC WAC basemap with lines indicating the locations of the profiles shown in Figure 4.7. The name of each dome indicates the start of the profile line.

tifies lunar silicate minerals using three wavelengths in the thermal infrared channels near 8 μm: 7.55 to 8.05 μm, 8.10 to 8.40 μm, and 8.38 to 8.68 μm (Paige et al., 2010; Greenhagen et al., 2010). The three channels characterize the Christiansen feature (CF), a compositional indicator of silicate mineralogy (Conel, 1969; Logan et al., 1973). CF is the mid-infrared maxima that coincide with the strongest absorption due to fundamental vibration of crystal lattice, whose position shifts to a shorter wavelength with increased silica polymerisation (Glotch et al., 2010). Silicate polymerisation is the process of chemically reacting monomer molecules together to form polymer chains or three-dimensional networks (Conel, 1969; Logan et al., 1973). The Diviner concavity index map used here has data binned at 256 pixels per degree

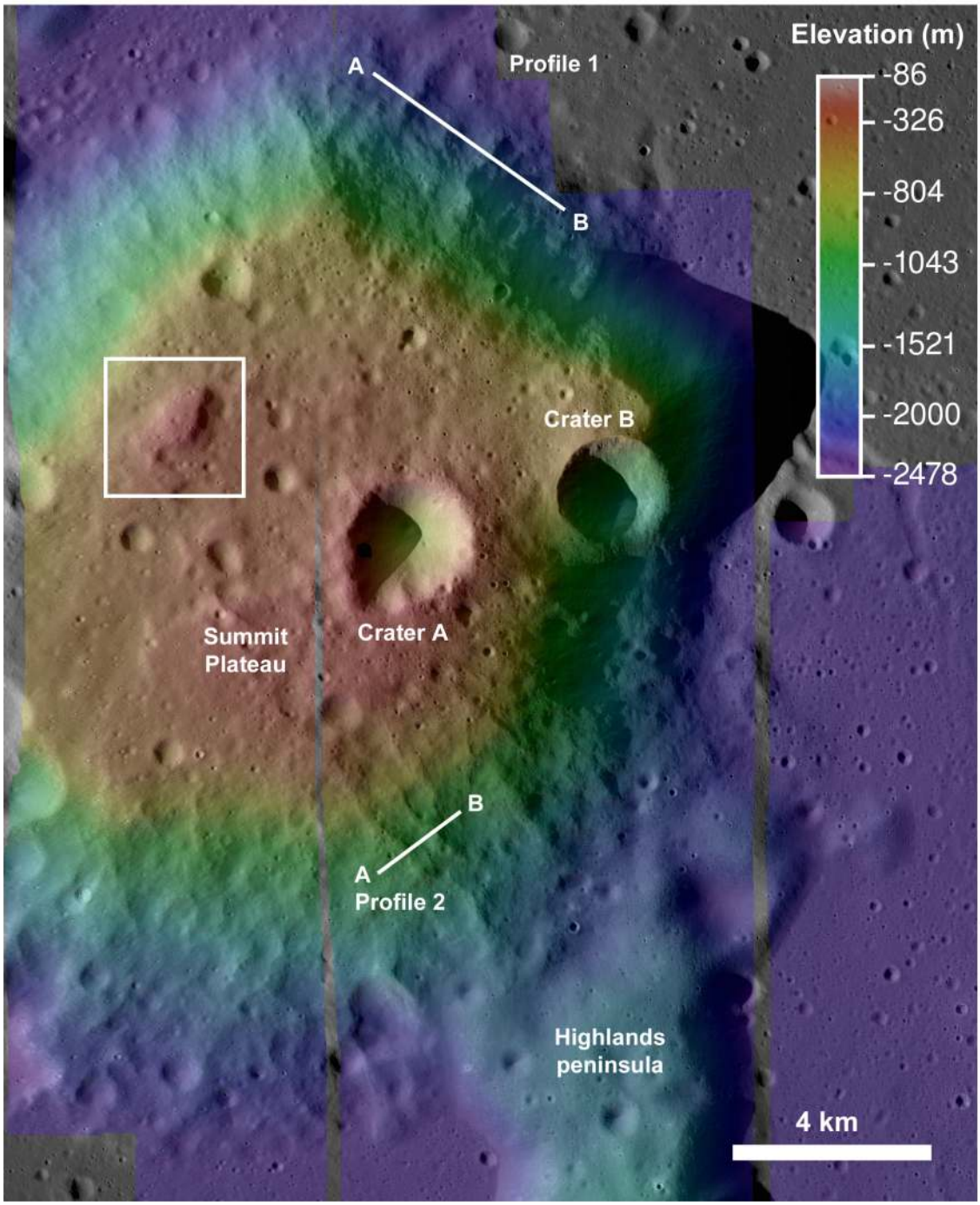

Figure 4.9: Overview of Gruithuisen Gamma for areas with NAC DTM coverage. Profiles are perpendicular to topographic ridges along the slopes of the dome. The summit plateau area is at approximately the same elevation, with a topographic high in the white box.

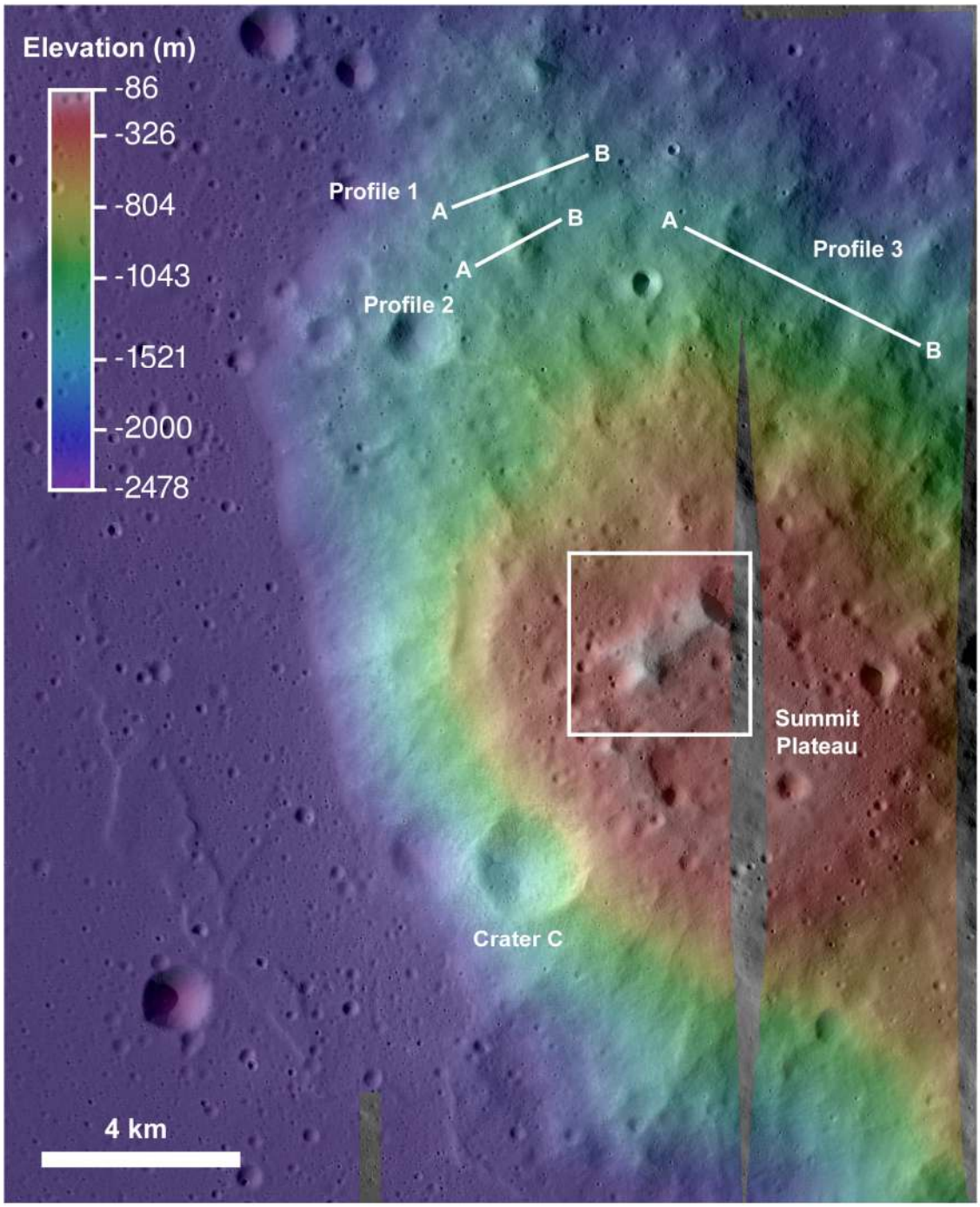

Figure 4.10: Overview of Gruithuisen Delta for areas with NAC DTM coverage. Profiles are perpendicular to topographic ridges along the slopes of the dome. The primary summit plateau area is at approximately the same elevation, with a topographic high in the white box.

and was produced through the same algorithm as in Glotch et al. (2010) (provided by the Diviner science team). Here we compare the Diviner map to LROC WAC color data, Clementine FeO and TiO_2 wt% maps, and topography.

Optical maturity (OMAT) derived from multispectral Clementine data is used to determine relative ages for lunar surfaces, especially fresh craters (Lucey et al., 2000b; Grier et al., 2001). Here the OMAT data was compared to the Diviner and Clementine FeO and TiO_2 wt% maps to determine if regolith maturity might influence the distribution of Diviner CF signal.

For the study of compositional differences across the surface of the Gruithuisen Domes, data from the Moon Mineralogy Mapper (M3) on board India's Chandrayaan-1 spacecraft were included to see if there was a detectable 2 micron band at the Gruithuisen Domes. M3 is a hyperspectral sensor operating in the range of 0.46-3.0 μm (Pieters et al., 2009). A single M3 image (Level 1B, acquired during the OP1A period of the mission) of Gruithuisen Gamma was radiometrically calibrated (Boardman et al., 2011). The image had a 20-40 nm spectral resolution (85 bands) and a spatial resolution of 140 m/pixel.

4.4 Observations

4.4.1 Crater size-frequency distributions

Analysis of the CSFDs gave model ages for each of the summit plateau regions on the Gamma and Delta domes, as well as an area of mare basalt to the south of Gruithuisen Gamma (Figures 4.4, 4.5). The resulting model ages and statistical errors are listed in Table 4.1. There is no statistically significant difference in model age for the three summit plateau regions. A combined CSFD of the three summit plateau regions gives a model age of $\sim 3.60^{+0.06}_{-0.09}$ Ga (Figure 4.12B). The CSFD for

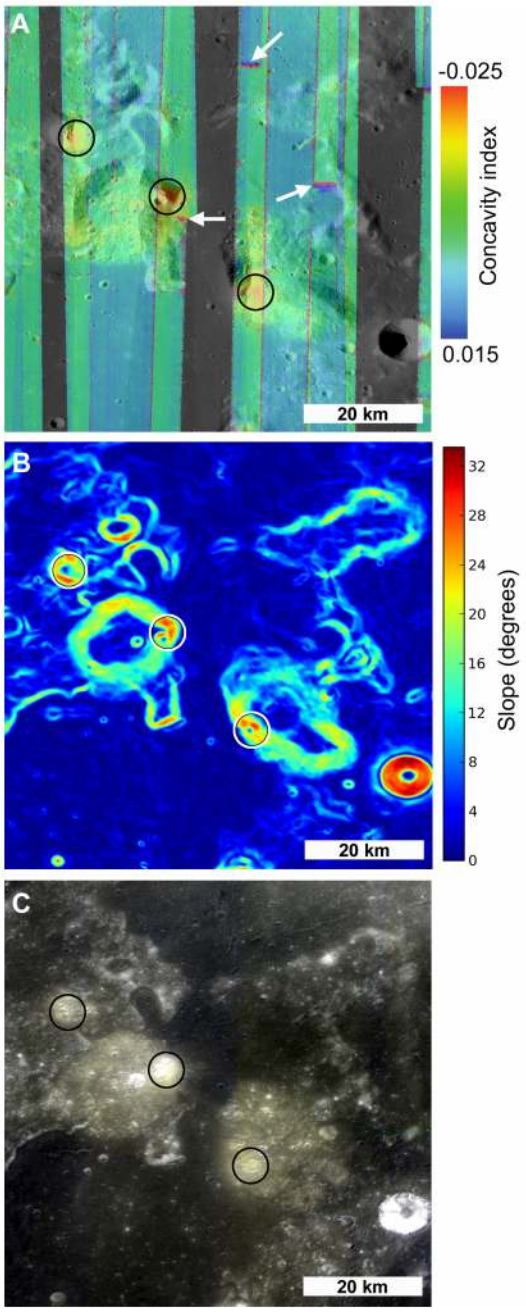

Figure 4.11: A comparison of the A) Diviner concavity index map to the B) LROC WAC slope map and the C) WAC 100 m/px color. In the Diviner data red colors indicate higher silica content. The white arrows point to seams between observations on the map, where the colors do not represent data.

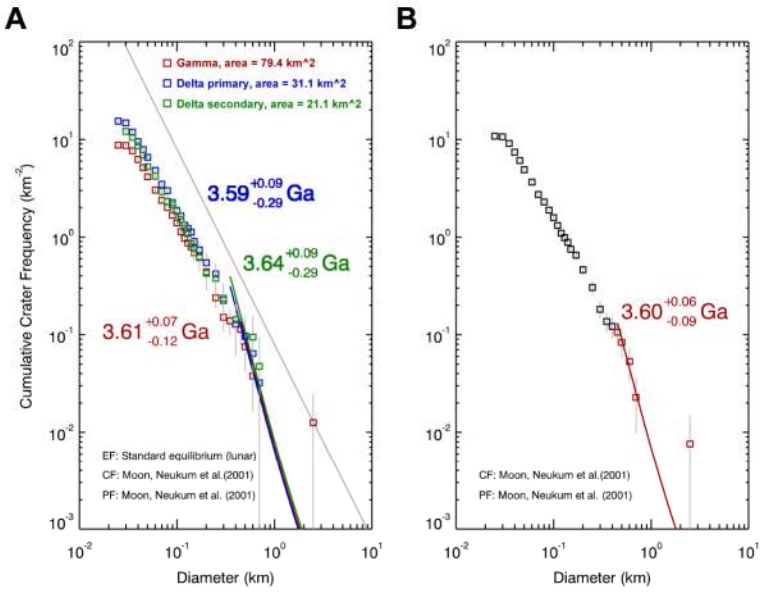

Figure 4.12: A) Overlay of the crater size-frequency distributions for the three summit plateau regions. All model ages are within the statistical errors. The gray line represents the standard lunar equilibrium population. B) CSFD of three summit plateau regions combined with a model age of $\sim$ 3.60 Ga.

the Gamma dome summit plateau shows a resurfacing event at a model age of $\sim$ 1.45 Ga (Figure 4.5A). Combined CSFDs from the four mare basalt count areas give a model age of $2.85^{+0.33}_{-0.53}$ Ga.

4.4.2 Units and Morphology

The geologic sketch map shows the location of contacts between the various units for the domes and the immediate area (Figure 4.13). The dome materials can be split into two main units (as in Head et al. (1978)), the summit plateau unit and the dome slope unit (Figure 4.13). Gruithuisen Gamma, Delta, and NW have contacts with both highland and mare materials. The contacts with the highland material provide stratigraphic evidence that the domes are younger than the highlands, as noted first by Scott and Eggleton (1973) and then later in Wilhelms (1987). Another example is to the west of the main Gamma dome, where there is terrain previously identified

Name	Area [km^2]	Model Age [Ga]	Equilibrium D. [m]
Gamma	79.4	$3.61^{+0.07}_{-0.12}$	N/A
Gamma resurfacing	79.4	$1.45^{+0.20}_{-0.20}$	165
Delta primary	31.1	$3.59^{+0.09}_{-0.29}$	300
Delta secondary	21.1	$3.64^{+0.09}_{-0.29}$	300
All Mare	202.8	$2.85^{+0.33}_{-0.53}$	250

Table 4.1: Results of crater counting and details on model age fits.

as a flow lobe (Head et al., 1978). In the WAC GLD 100, this area is topographically above the highlands and forms a relatively shallow flow superposing the highlands material. The overall ridged morphology and spectral signal of this area is consistent with the units of Gamma, Delta, and NW domes. Gruithuisen Gamma is superposed on the highlands material between a continuous section of highlands to the west, and a smaller elongate section of highlands directly southeast of the dome. At the contacts between the Gamma dome and the highlands material, the dome flank slope is reduced to 0° and then the highland topography rises above the elevation of the edge of the dome. The topographic depression immediately south of the elongate section of highlands material is likely a volcanic feature formed as part of the mare basalt extrusion. Mare materials embay the domes along the contacts, although in some places down slope movement of material from the domes has covered the mare unit. An area of mare adjacent to the Gamma dome contains a small rille which has been partially filled in with material from the dome, in part due to downslope movement and excavation initiated by the formation of impact crater B (Figure 4.14). The impact crater C on the Delta dome also caused ejecta material from the domes to be superposed on the mare basalt (Figure 4.20).

The summit plateau areas of Gamma and Delta are relatively flat in terms of

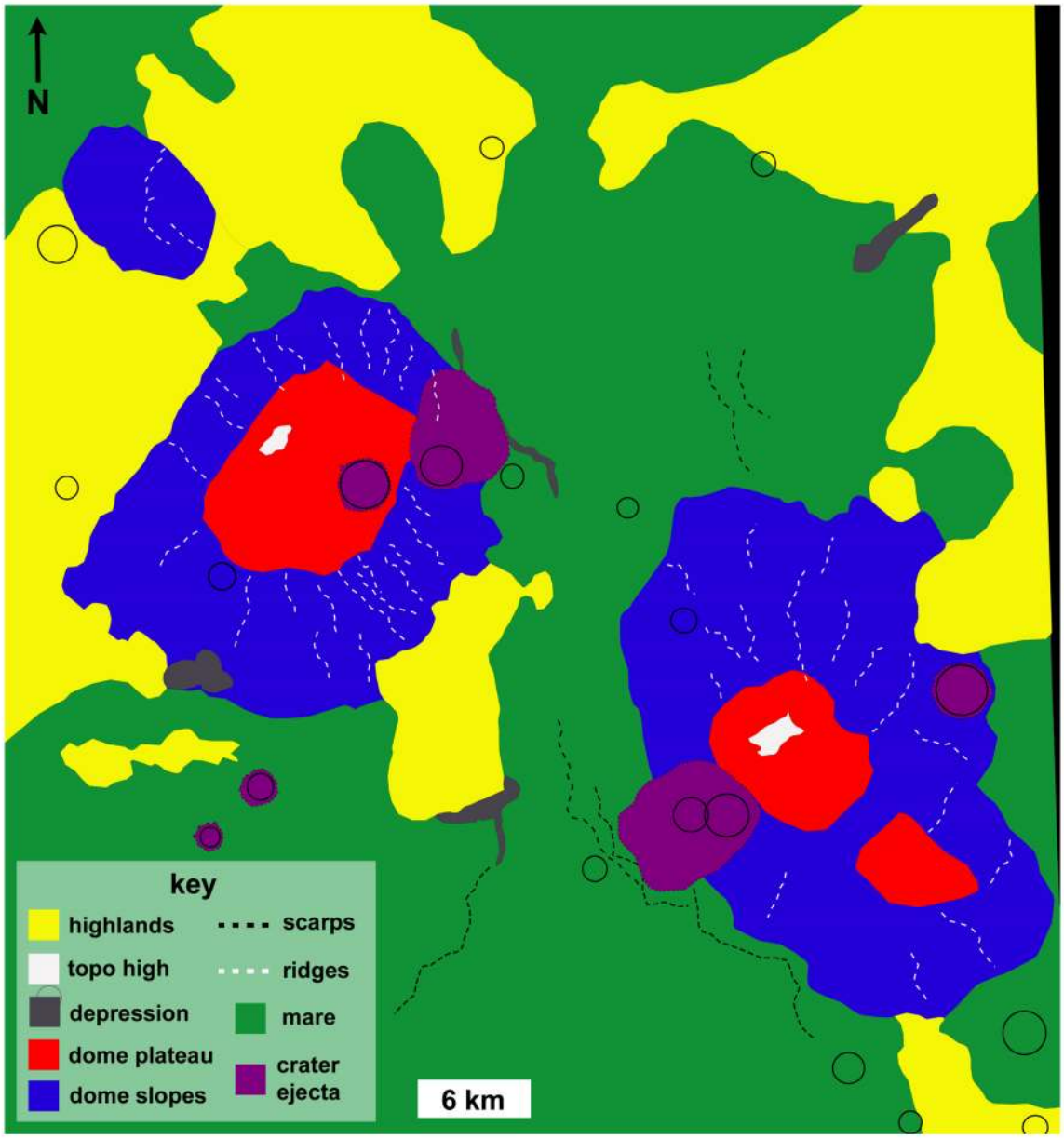

Figure 4.13: A sketch map of the Gruithuisen Domes and the surrounding terrain marks the location of the major units. Only impact craters > 1 km in diameter are noted here.

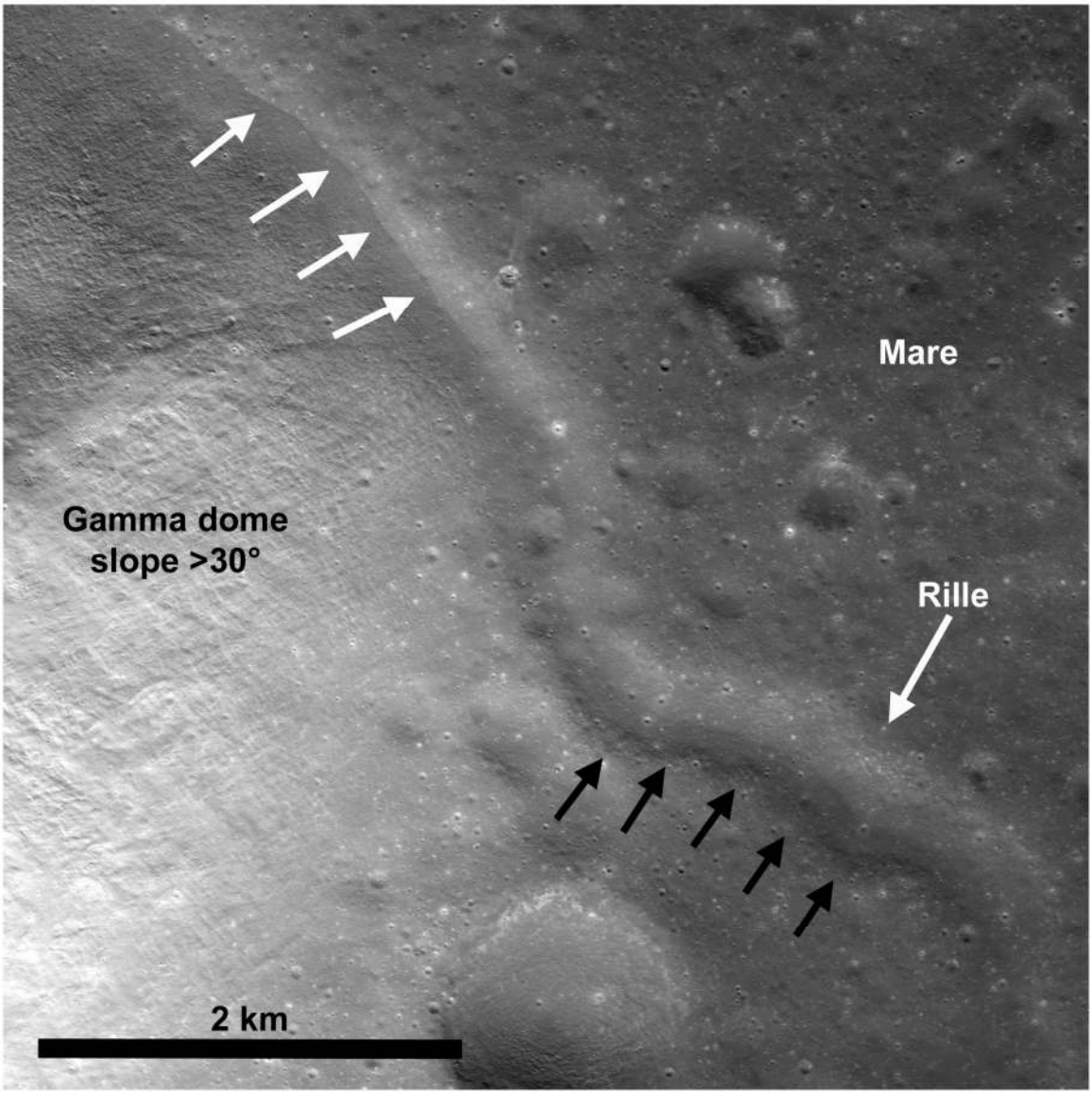

Figure 4.14: Material from a steep slope of $> 30°$ partially covers a rille at the northeastern edge of the contact between Gruithuisen Gamma and the mare. The landslide was likely initiated by the formation of impact crater B (Figure 4.20). The black arrows show the edge of the rille and the white arrows show the edge of the dome slope covering the rille. LROC NAC M1101473365 (1.6 m/px, i=40)

slope and relief (change in elevation) compared to the rest of the domes, although the summit areas are not completely devoid of topography. The Delta dome has two summit areas. The larger, higher elevation summit area will be referred to as the primary summit plateau and the smaller, lower elevation summit area will be referred to as the secondary summit plateau. The summit areas have morphologic variations that may represent flow margins, although due to the age of the domes and cratering, interpretation is difficult. The Gamma dome's summit plateau and the Delta dome's primary summit plateau both have small, positive topographic features (inside white boxes in Figures 4.9 and 4.10). On the Delta dome the topographic high reaches an elevation of -86 m, which is $\sim$ 190 m above the average elevation of the primary summit plateau (-270 m). The secondary summit plateau of the Delta dome does not have a similar topographic high. On the Gamma dome the topographic high reaches an elevation of -326 m, which is $\sim$ 218 m above the average elevation of the summit plateau (-544 m). The NW dome does not have a broad summit plateau area like the Gamma or Delta domes, but it does have a smaller summit $\sim$ 2.5 km in diameter (Tran et al., 2011). The NW dome also has a topographic high (maximum elevation of -589 m) that rises above the rest of the dome summit (average elevation of -650 m) (Figure 4.15). The summit plateau on Gruithuisen Gamma has an elevation range of approximately -640 m to a height of -370 m, excluding crater rims (Craters A and B) and the topographic high feature. The primary summit plateau on Gruithuisen Delta has an elevation range of approximately -395 m to -240 m, again excluding the topographic high at the summit plateau. The average slopes within the summit areas (excluding $>$ 2 km craters A, B, and the topographic highs) are $7 \pm 5°$. For reference, the average slopes in the surrounding mare are $4 \pm 4°$.

The flank slopes of the Gamma and Delta domes are asymmetric (Figure 4.3), while the NW dome has more symmetric slopes, ranging from 22 to 28°, with an

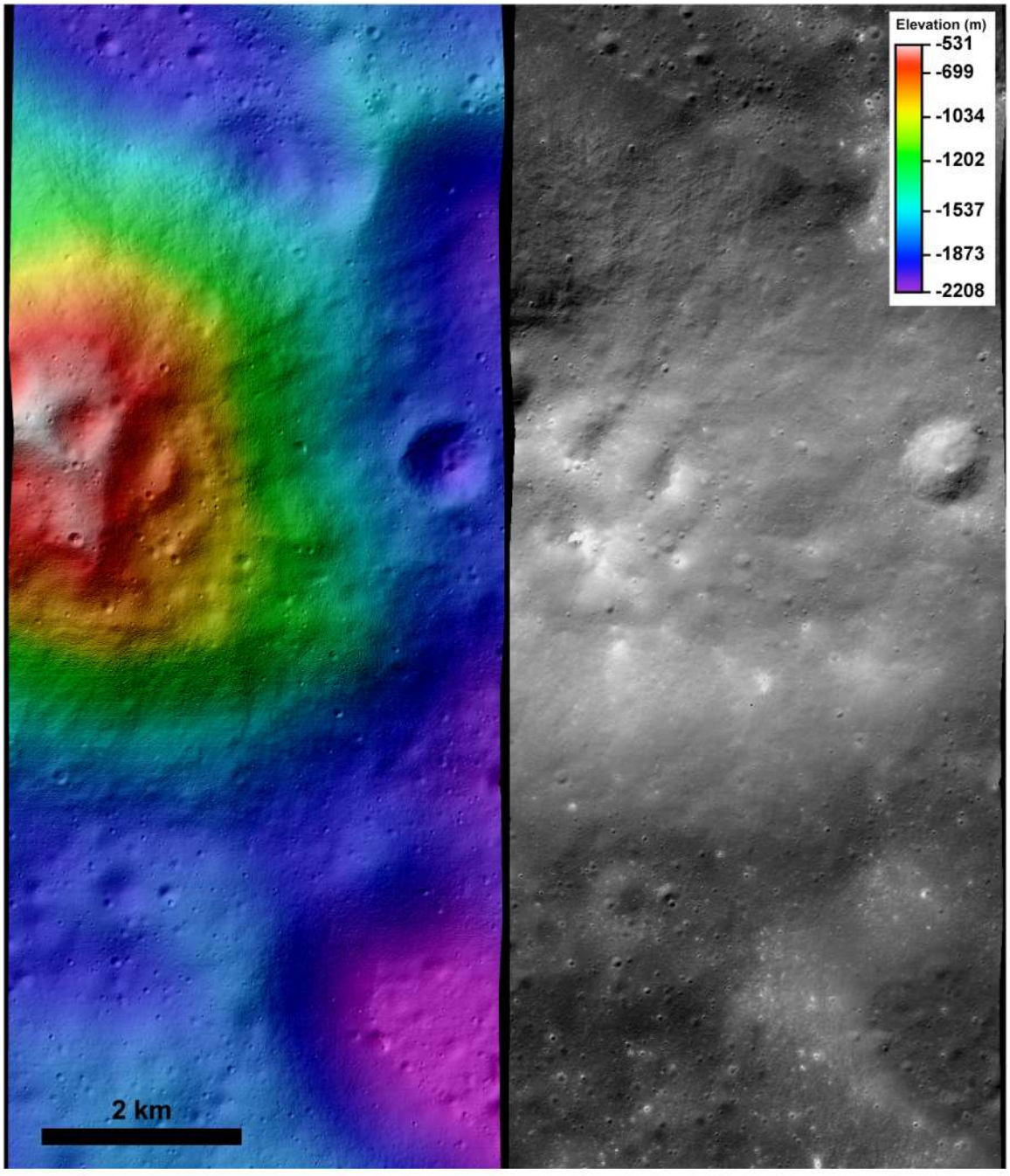

Figure 4.15: The eastern portion of the northwest Gruithuisen Dome (NW). LROC NAC M142529593.

average of 24°. The Gamma dome has slopes $\sim 20°$ except for two notable locations. The flank which extends to the south is embayed by mare basalt and does not share a contact with the highlands has shallower slopes. The southern flank slope is split into an upper and lower portion, where the upper portion has slopes $\sim 15°$ and the lower portion has slopes $\sim 8°$. While the slope measurements reported here come from the NAC DTM, the subtle change in slope along the southern flank is also visible in the WAC topography (Figure 4.3). Directly northeast of crater B steep flank slopes occur $\sim 28 - 30°$. The flank slopes around the southern half of the Delta dome, around the secondary summit plateau, have slopes $\sim 20 - 22°$. The western flank slope has higher slopes $\sim 25 - 28°$, while the northern flanks slopes around the edge of the primary summit plateau have shallower slopes, $\sim 8 - 13°$.

The flanks of the domes have a texture previously noted in the literature as hummocky, but rougher than the highlands (Head et al., 1978; Head and McCord, 1978; Wagner et al., 2002). With the NAC DTM the topography which causes the distinct texture of the domes can be measured and described quantitatively. Figures 4.9 and 4.10 show the locations of elevation profiles (A to B) approximately perpendicular to the radial direction across the flanks of the Gamma and Delta domes. The texture mentioned by previous authors is due to topographic highs and lows roughly linear in the radial direction. We refer to them here as ridges (Figure 4.13). Elevation profiles show the relief of the ridges, which ranges from 20 to 155 m for these examples (Figure 4.16 and 4.17). The section of Gruithuisen Gamma to the west of the main dome structure has topographic highs, but they are not linearly aligned as ridges along a radial direction. This section of the dome is topographically higher than the highlands terrain it superposes, but does not have steep slopes along its margins. The ridges occur on the flank slopes only and not the summit plateaus.

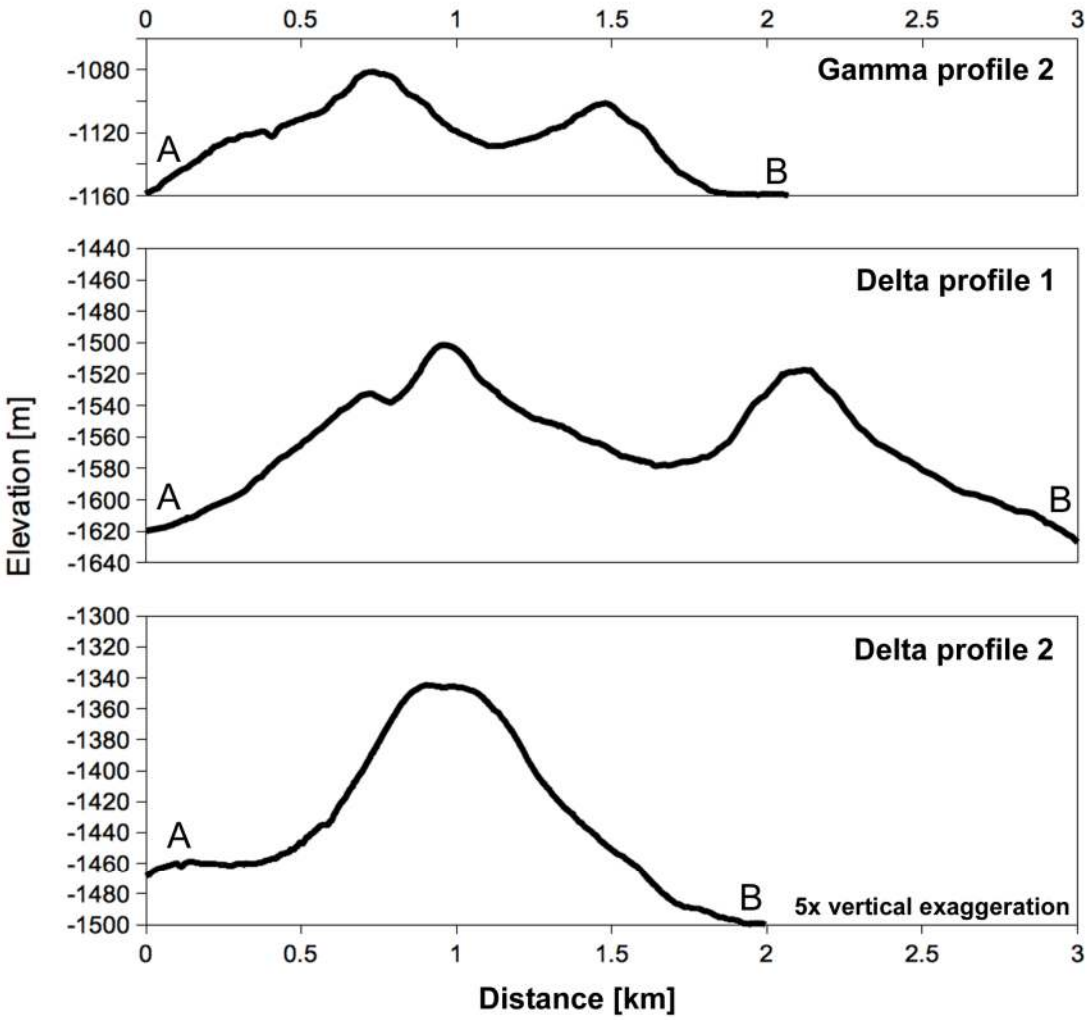

Figure 4.16: Elevation profiles of ridges on the flank slopes of Gruithuisen Gamma and Delta. Location of profiles specified in Figures 4.9 and 4.10. All plots have a vertical exaggeration of 5×.

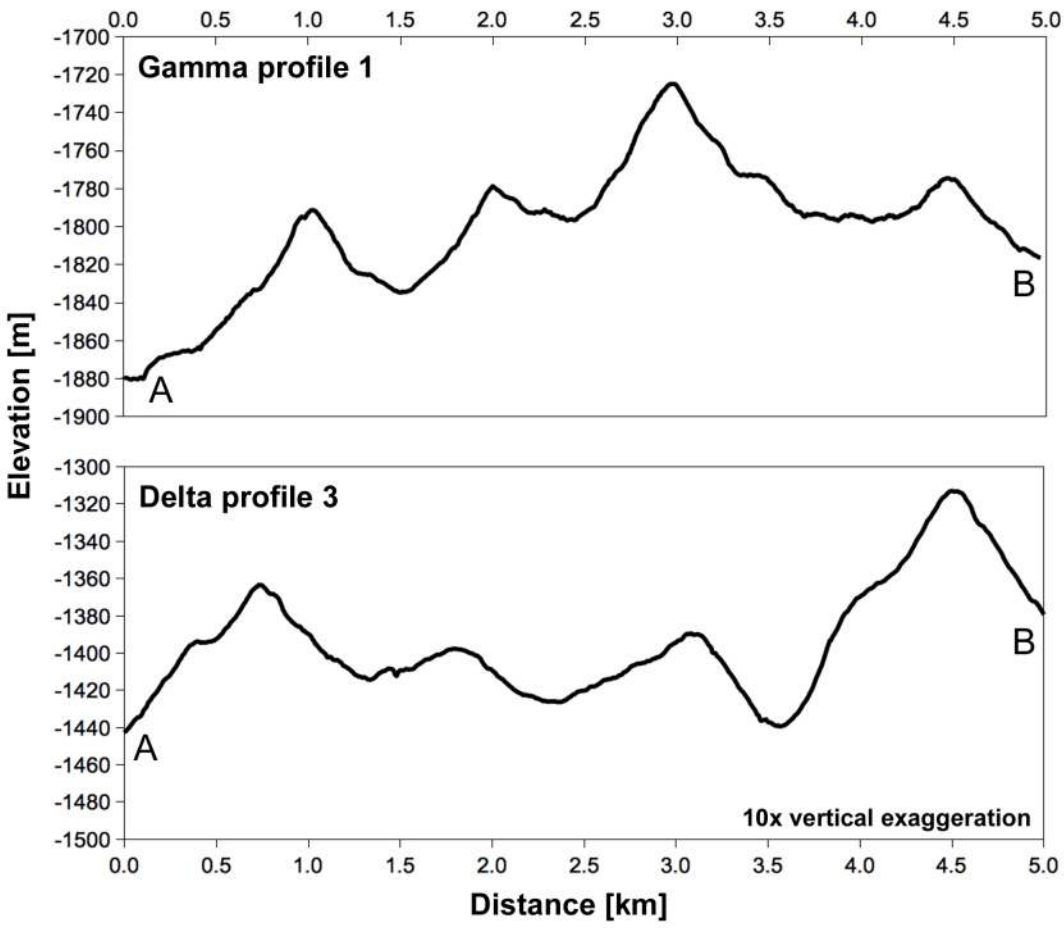

Figure 4.17: Elevation profiles of ridges on the flank slopes of Gruithuisen Gamma and Delta. Location of profiles specified in Figures 4.9 and 4.10. All plots have a vertical exaggeration of 10×.

4.4.3 Comparison to Aspect Ratio of Terrestrial Silicic Domes

Measurements of the Gruithuisen Domes' relative height and basal diameter were compared to different types of silicic terrestrial domes as well as lunar mare shields and the Mairan Domes (41.79°N, 311.61°E), another example of silicic nonmare volcanism on the lunar surface (Figure 4.18). The plot of aspect ratio (height/diameter) as a function of height shows a range of aspect ratios with low-shield volcanoes at the low-aspect ratio end of the spectrum and terrestrial silicic domes like Mt. St. Helens

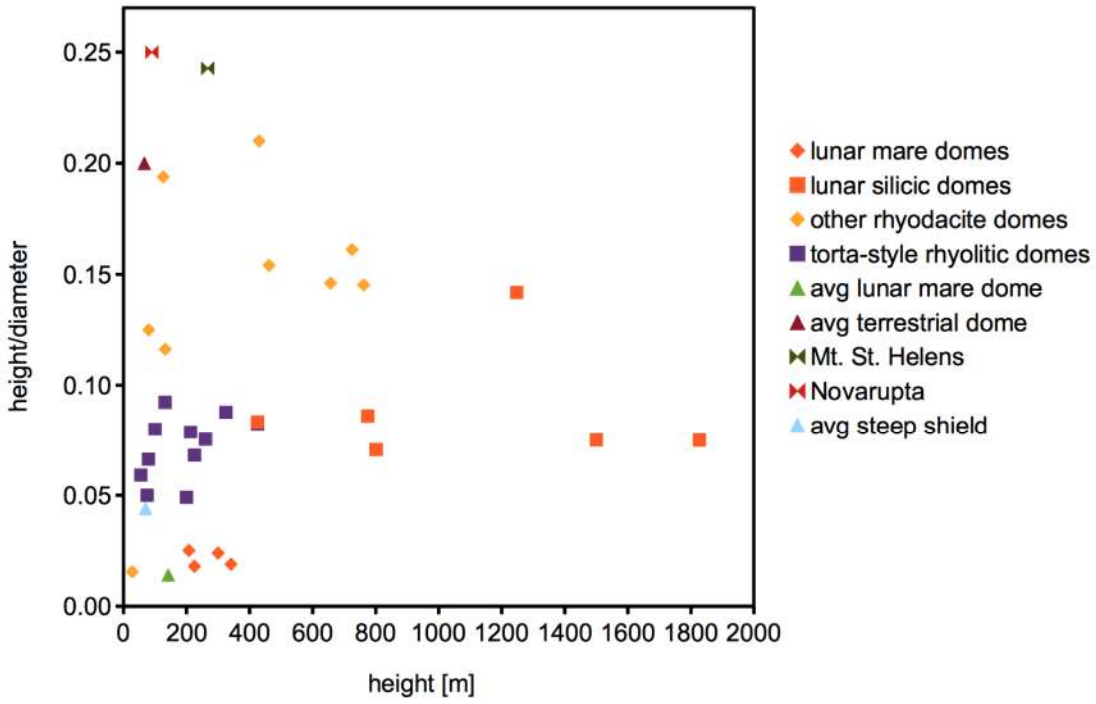

Figure 4.18: Aspect ratio as a function of height for lunar and terrestrial effusive volcanism. Data listed in Tables B.1 and 4.2.

and Novarupta at the high-aspect ratio end. Average height and diameter values for common domes and shield volcanoes were taken from Pike (1978) and plotted here for comparison. While the Gruithuisen domes are much taller than any of the terrestrial domes, their aspect ratios are most similar to the population of torta-style rhyolitic domes. The heights and diameters for the terrestrial domes were taken from the literature (appendix table B.1). The NW dome has a higher aspect ratio (~ 0.15) than the Gamma and Delta domes.

4.4.4 Diviner image comparison

NAC images, WAC topography, WAC spectral ratios, Clementine FeO wt%, and Clementine OMAT parameter maps provided context for the Diviner CF data. The Diviner concavity index map shows that the three domes have areas where the concav-

Volcano	Description	D [m]	H [m]	Source
Hortensius 1	mare shield	16000-20000	307-375	Tran et al., 2011
Hortensius 2	mare shield	7500-9000	200-215	Tran et al., 2011
Hortensius 3	mare shield	12000-13000	250-350	Tran et al., 2011
Hortensius 4	mare shield	12000-13000	200-250	Tran et al., 2011
G. Northwest	silicic dome	8800	1248	This paper
G. Gamma	silicic dome	20000	1500	This paper
G. Delta	silicic dome	24400	1828	This paper
Mairan T.	silicic dome	6600-7100	765-785	Tran et al., 2011
Mairan central	silicic dome	11350	800	This paper
Mairan southern	silicic dome	5100	425	This paper

Table 4.2: Dimensions of Lunar Volcanoes. Height (H) is relief with respect to the surrounding terrain. D is average basal diameter.

ity index values are higher than the surrounding mare and highlands terrain (Figure 4.11). High concavity index values are marked by red and yellow colors on the map (circled in the figure). Few minerals have a spectral shape in the three 8 μm bands required to produce the signal seen in the map. Minerals which are consistent with the spectral shape include quartz and other SiO_2 polymorphs, K-feldspars, and plagioclase feldspars more sodic than labradorite (Glotch et al., 2010). The detailed mineralogy cannot be determined from only the Diviner spectra. The areas in Figure 4.11 with a high concavity index do not cover the whole surface of the Gamma or Delta domes, but are rather localized to specific areas. The high concavity index areas correspond to areas of particularly low FeO wt% and TiO_2 wt% values (Figure 4.2). Craters are visible in the NAC images at each of the high concavity index areas on Gruithuisen Gamma and Delta contain impact craters as well as higher than average

slopes, $> 30°$ (Figure 4.11). LROC WAC 321/415 nm spectral ratios show that the areas with Diviner high-silica are also relatively more absorbing in the 321 nm band (Figure 4.19).

Values from the Clementine OMAT map were collected for comparison to the Diviner data. OMAT values do not vary much between the various units corresponding to the areas in the WAC spectral ratio measurements (Figure 4.19). The average OMAT values for dome material is 0.15. The ejecta around the B and C craters have OMAT values ~ 0.16. The surrounding mare has two distinct values, with the younger mare to the south at an average OMAT value of 0.18 and the older mare to the north with an OMAT value of 0.15. These values are consistent with the mare age relationship described in Wagner et al., 2002. The highlands terrain is 0.14 on average. For reference, any OMAT value from 0.09-0.12 is considered very mature, while very immature ejecta near the rim of a fresh crater may have OMAT values of 0.29-0.42 (Grier et al., 2001).

4.5 Discussion

4.5.1 Crater size-frequency distributions

CSFDs of the Gamma and Delta domes give model ages slightly younger, but still statistically consistent with the previous work of Wagner et al. (2002) (Figure 4.12, Table 4.1). Wagner et al., (2002) used lower resolution ($\sim$60 m/px) Lunar Orbiter images (LO-IV frame 151-H2) for their crater counts, and part of their count area (from what they considered to be the summit area) is on a $\sim 10°$ slope, which may have biased their counts. Wagner et al., (2002) found that the model age of material on the Gruithuisen domes ranged from 3.85 to 3.72 Ga and thus formed in the early part of the Late Imbrian. This age is consistent with the local stratigraphy, which

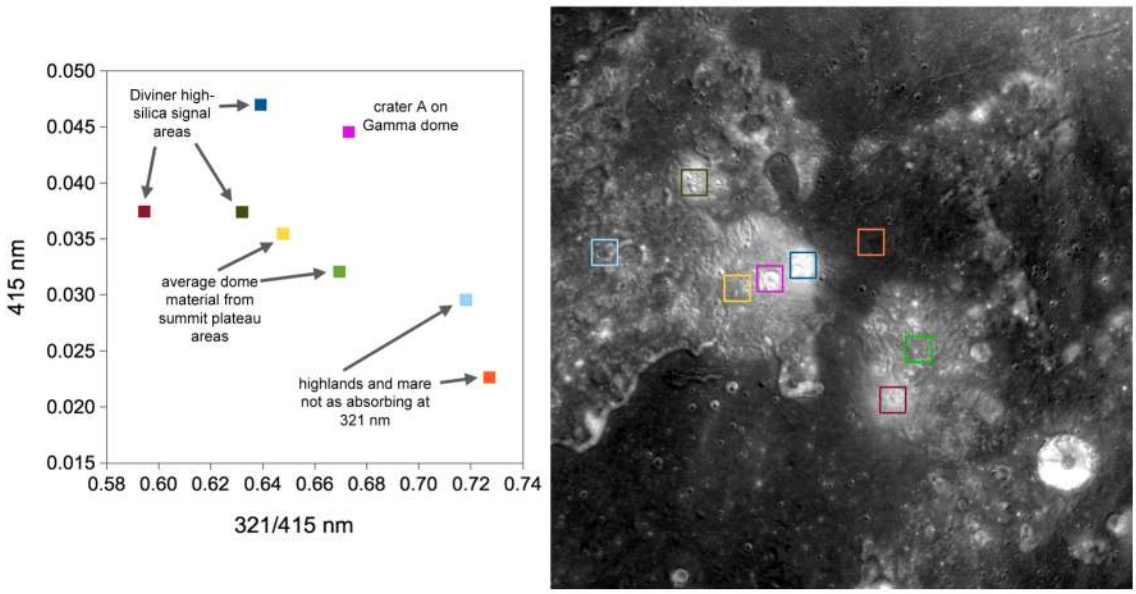

Figure 4.19: The plot on the left shows the 321/415 nm ratio values for various units in the Gruithuisen Domes region. The Diviner high-silica areas have relatively lower 321/415 nm ratios, which may indicate fresher material at the surface. The figure on the right shows the location of each sample area. The highlands and mare areas are not as absorbing at 321 nm compared to the dome materials.

places the Gruithuisen domes as relatively younger than the surrounding ejecta from the impact event that formed Sinus Iridum (3.7-3.8 Ga), but older than the mare basalt emplaced around the domes (Wagner et al., 2002) (Figure 4.1). Model ages from LROC NAC data reported here are 3.60 +0.06 -0.09 Ga for all summit plateau areas on the Gamma and Delta domes. This places the model ages from the LROC NAC images on the younger end (3.7 Ga) of the age range from Wagner et al. (2002). We attribute this difference to the availability of higher resolution images and better identification of appropriate ($< 2^\circ$ slope) count areas. The mare area counted here corresponds to the terrain mapped as "EIm" in Wagner et al. (2002), meaning a mare basalt flow of Eratosthenian and/or upper Imbrian age. The age estimate calculated here is 2.85 +0.33 -0.53 Ga, which is consistent with the Wagner et al. (2002) estimate of 3.5-3.55 Ga for the same unit (Wagner et al. (2002) did not give statistical error

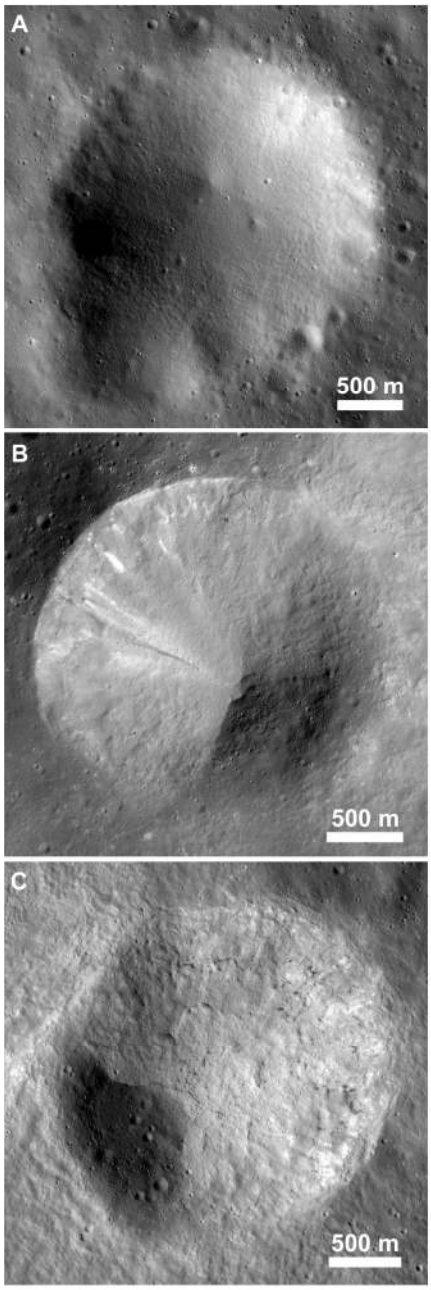

Figure 4.20: Three largest impact craters on the Gamma and Delta domes, as labeled in Figures 4.9 and 4.10. A) 2.5 km diameter crater on the summit plateau of Gamma. Located at 36.594°N, −40.623°E. B) 2.3 km diameter crater on the steep slopes of the Gamma dome. Located at 36.630°N, −40.458°E. C) 2.4 km diameter crater on the steep western slope of the Delta dome. Located at 35.995°N, −39.817°E.

bars for their model ages). The change in the CSFD which indicated a resurfacing event observed for the Gruithuisen Gamma dome (Figure 4.5, A) was likely caused by the impact of the $\sim$ 2 km crater on the summit plateau (no resurfacing population was reported in Wagner et al. (2002)). The CSFDs from the summit plateau regions of the Gamma and Delta domes are not statistically different enough to determine if one dome formed before the other. The NW dome may be younger than the other two domes, based on its comparatively small size, however, there is not a large enough flat area on the summit of the NW dome to perform CSFD analysis. In conclusion, CSFDs from NAC data are consistent with the local stratigraphy compared to previous crater counts using Lunar Orbiter images and still suggest that the Gruithuisen Gamma and Delta domes both formed relatively shortly (in terms of the lunar geologic timescale) after the Iridum impact.

4.5.2 Diviner Data and the Source of the High-Silica Signal

While almost the entire surface of the Gruithuisen Domes is low in FeO and TiO_2 wt% relative to the surrounding highlands and mare basalt (Figure 4.2), only specific areas have a high-silica signal in the Diviner concavity index maps (Figure 4.11). Observations collected from NAC images, WAC topography, WAC spectral ratios, and Clementine OMAT values are consistent with the interpretation that a combination of steep slopes ($> 30°$) and material excavated by impact craters (Figure 4.20) may continually provide fresh dome material at the surface as debris move downslope. This effect is responsible for the high-silica signal in the Diviner data, while the rest of the domes appear less silica-rich. The lack of OMAT contrast around the impact crater ejecta may suggest that the primary cause of the low FeO and high concavity index signals is not directly regolith maturity, but is primarily the composition of the excavated dome material itself. The areas of the dome which have shallower

slopes would not have as much downslope movement, which would cause an overall older surface layer to accumulate. This layer of regolith would have incorporated more material from the highlands and mare basalt regions due to the domes' close proximity to both terrains. The deposition rate for material originating more than 1 m away is $\sim$ 8 mm/10^6 years (Arvidson et al., 1975). Over the estimated age of the domes, $\sim$ 3.60 Ga, the estimated amount of deposition of ejecta material sourced from $>$ 1 m away would be $>$ 24 mm. Both the ultraviolet and thermal infrared wavelengths would be looking at the same layer of mixed ejecta material, based on the penetration depth of the electromagnetic waves. Penetration depth is a measure of how deep electromagnetic radiation can penetrate into a material, defined as the depth where the intensity of the radiation falls to 1/e ($\sim$37%) of the original intensity at the material surface. For a given material, penetration depth is generally a function of wavelength, and for the UV-infrared is $\sim$ 10 times the wavelength. For a wavelength of 320 nm, the penetration depth is 3.2 microns (or 4.2 microns for 420 nm). For 7000 - 9000 nm (7-9 microns) the penetration depth is 70 to 90 microns (0.07 mm). Alternatively, it is possible that the domes have compositional heterogeneity from one flow to another, or between the flow crust and the flow interior. The range in composition could account for the variation in the remote sensing data, with the impact craters excavating material of a different composition.

For the study of compositional differences across the surface of the Gruithuisen Domes that might explain the distribution of the high-silica signal in the Diviner data, we examined the M3 data. However, the level of noise was too high for the data to be useful in determining compositional variations. No information at 2 microns was discernible to investigate the presence of high silica glasses. Kusuma et al. (2012) also examined the M3 data in detail. Integrated band depth analysis was used to study spectral absorption features at 1000 and 2000 nm (which are indicators for the study

of mafic minerals such as olivine and pyroxenes). Kusuma et al. (2012) used two radiometrically calibrated (Boardman et al., 2011) M3 images acquired during the OP1A period of the mission. The data had high levels of noise and no photometric or thermal corrections were applied to the images, however the 1000 nm band was not affected by thermal effects (Kusuma et al., 2012). The integrated band depth analysis was only able to discriminate the mare basalt units from the non-mare (domes and highlands) units (Kusuma et al., 2012). The Gruithuisen domes and surrounding highland terrain had relatively high reflectance at 1548 nm, and low reflectance at 1000 and 2000 nm, which indicates a lack of mafic absorption (Kusuma et al., 2012).

4.5.3 Magma Properties and Morphology

We begin the discussion of relationships between the morphology and the eruption properties of the Gruithuisen Domes with verification that the observed topography of the dome is original and related to the emplacement of the domes and not to erosion over time. The estimated erosion rate for lunar material due to meteorite bombardment $\sim$ 1 mm/10^6 years (Arvidson et al., 1975). The Gruithuisen Domes have a model age of 3.60 +0.06, -0.09 Ga for all summit plateau areas on Gamma and Delta, giving a conservative estimate of 4 meters of erosion since dome formation. The measured relief of the ridges ranges from 20 to 155 m, which indicates that erosional processes did not significantly degrade the current morphology of the ridges.

The documentation of the Gruithuisen Domes' detailed surface morphology may help determine the properties of the magma or eruption conditions based on comparisons with studies of terrestrial silicic dome formation. Fink and Griffiths (1998) proposed that the behavior of lava dome growth depends on eruption rate, magma rheology, and thickness of the cooling surface. Through laboratory experiments using kaolin wax slurries (a Bingham plastic) erupting into water Griffiths and Fink (1997)

and Fink and Griffiths (1998) related the dome morphology and texture to the thickness of its cooled carapace, and thus to eruption conditions. A Bingham plastic is a viscoplastic material that flows as a viscous fluid at high stress but behaves as a rigid body at low stresses (Bingham, 1916). As the fluid cools it spreads radially under gravity, forming a dome with a surface crust stronger than the extruded fluid (Griffiths and Fink, 1997). The flow regime changes depending on the rate of solidification relative to the rate of lateral flow (Griffiths and Fink, 1997). The experiments had variable extrusion rates, eruption temperatures, and water temperatures. From these experiments four main dome types were identified as spiny, lobate, platy, and axisymmetric, with progressively higher effusion rates, lower cooling rates, and lower yield strengths (Fink and Griffiths, 1998). The four main dome types from the experiments were compared to the morphology of natural lava domes, which then yielded a model where eruption rate could be estimated based on the dome morphology and composition (Fink and Griffiths, 1998). A detailed description of the morphological properties and growth of each dome type is found in Fink and Griffiths (1998).

Before further discussion of the Gruithuisen domes in the context of experimental lava dome types, some caveats should be observed. Fink and Griffiths (1998) warns, "Classification of volcanic structures is subjective." Furthermore, "Assigning any given magmatic dome to one of the four laboratory-based types may be problematic, especially because natural domes rarely have effusion rates or rheologic properties that remain constant throughout extrusion" (Fink and Griffiths, 1998). Finally, although lavas with a given silica content typically have a range of eruption viscosities (2 to 3 orders of magnitude (Murase and McBirney, 1973; Williams and McBirney, 1979)), each lava type also has a range (several orders of magnitude) of viscosities as it crystallizes and cools, so that composition and lava viscosity are not uniquely related (Gregg and Fink, 1996).

The morphology of the Gruithuisen Domes can be compared to the descriptions of the four main silicic dome types (Griffiths and Fink, 1997; Fink and Griffiths, 1998). The platy dome type is an overall match to the Gruithuisen Domes. While the platy domes have lobes, they are less defined than for a lobate type dome and the individual lobes may merge with a circular central region rather than extend all the way back to the vent (Fink and Griffiths, 1998). This behavior describes the relatively flat, circular summit plateaus found on the Gruithuisen Domes, which may have formed through a similar merging of multiple flow lobes. The outlines of platy domes are more circular than lobate domes, which tend to be stellate in outline (Fink and Griffiths, 1998). During the emplacement of platy domes flow-parallel ridges form as they erupt through subradial fractures as the dome margin undergoes circumferential stretching (Fink and Griffiths, 1998). The behavior may describe the ridges along the flank slopes of the Gruithuisen Domes. However, platy domes can also develop straight transverse ridges as folds at sites of compression. No transverse ridges or folds are seen on the Gruithuisen Domes. If the domes did form in a similar manner as a platy-type terrestrial dome, perhaps the amount of compression during the eruption was relatively low. The Soufriére of St. Vincent dome, 1979 (Shepherd et al., 1979; Huppert, 1982; Huppert et al., 1982) is an example of a dome extruded with the yield stress and eruption rate of a platy dome type (Fink and Griffiths, 1998). If the Gruithuisen Domes are in the platy type regime, then based on the model of Fink and Griffiths (1998) for an andesitic composition, the eruption rate would be between $\sim 1-2$ m^3/s, for a dacitic composition between $\sim 4-60$ m^3/s, and for a rhyolitic composition between $\sim 10-200$ m^3/s.

The characteristics of the Gruithuisen Domes compared to terrestrial silicic dome types are further discussed here. The spiny domes are tall and steep sided, conical in profile (aspect ratios higher than that of the Gamma and Delta domes), with tops

punctured by one or more subvertical spines with curving sides (Fink and Griffiths, 1998). The spines may be covered with striations scraped into their sides by the cracks through which they emerged from the flow interior and the structures collapse into piles of rubble (Fink and Griffiths, 1998). The topographic highs on the summit plateaus of Gamma and Delta are broad, with shallow slopes and no evidence of rubble or boulders. The Gamma and Delta domes are not conical, although the NW dome is approximately conical. The other end-member dome type, the axisymmetric domes, are uniform in overall morphology which suggests deformation that is between Bingham plastics and viscous fluids (Fink and Griffiths, 1998). The axisymmetric domes are formed primarily through endogenous inflation (Griffiths and Fink, 1997). Laterally extensive, transverse folds (1-5 m wide) may parallel the entire margin of an axisymmetric dome, and radial fractures are limited to the area of flow directly over the vent, or near the flow front (Fink and Griffiths, 1998). The Gruithuisen Domes all exhibit radial ridges over the flank slopes and have no transverse folds at the scale of 50 cm/px. The Gruithuisen Domes are each split into two sections: the summit plateau and the flank slopes, with indications of separate flows, so they are not uniform like an axisymmetric dome morphology. The lobate domes are made up of distinct flow lobes that erupt sequentially from a central vent in a single direction, forming a stellate outline (Fink and Griffiths, 1998). Near the beginning of its growth a dome may inflate endogenously before individual lobes being to emerge (Fink and Griffiths, 1998).

The comparison between aspect ratios (Figure 4.18) of the Gruithuisen Domes and different types of terrestrial silicic domes showed that the Gamma and Delta domes were most similiar in aspect ratio to a population of low rhyolitic "torta" domes. However, the Gruithuisen Domes are generally an order of magnitude taller than the terrestrial domes. The NW dome has a higher aspect ratio, matching a set

of rhyodacite domes. Terrestrial domes such as Mt. St. Helens and Novarupta had much higher aspect ratios than the other terrestrial silicic dome or the lunar silicic domes. We find that the aspect ratios of the Gruithuisen Domes are consistent with a rhyolitic or rhyodacite composition.

Critical height was used as a diagnostic tool for comparing dome aspect ratio with respect to different gravitational accelerations. Eruptions are driven by overpressure, which is opposed by the pressure of the lava mass above the vent. Assuming a large enough amount of magma is available, the volume of the lava erupted onto a flat surface will be limited by atmospheric pressure and the mass of the lava above the vent (de Silva et al., 1994):

$$P_e > \rho g h + P_a$$

where ρ is the density of the lava in kg/m^3, g is the gravitational acceleration in m/s^2, h is the height of the dome in m, P_a is the atmospheric pressure in Pa, P_e is the overpressure in the magma chamber in Pa. Once the critical height is reached, the overpressure is exceeded and no further lava can erupt (de Silva et al., 1994). The vent may migrate horizontally in order to continue the eruption. An exception is when magma is erupted onto a slope sufficiently steep to allow lava to flow away from the vent, which prevents the critical height from being reached, producing an eruption only limited by the volume of magma available (de Silva et al., 1994). If silicic domes adhere to the behavior described in the critical height relationship, then most observed domes emplaced on relatively flat surfaces should be near the critical height limit. In some cases terrestrial domes can exceed the critical height. Cerro Chascon in Bolivia is highly crystalline (45-48%) with 68-76% SiO_2, which may cause increased yield strength (de Silva et al., 1994). Based on the increased yield strength, the critical height for the dome would exceed the average value for rhyolitic magma. Surface cooling causing a crust to form can also dominate over yield strength (Griffiths

and Fink, 1993).

The Gruithuisen Domes have similar heights and relatively circular flat summit plateaus. The similar heights may be due to the simple principle of critical height. If the eruption halted once the critical height was reached, then the vent may have migrated slightly in order to continue erupting. This may explain the roughly circular, flat summit plateaus of each dome. The Delta dome has two summit plateaus which may indicate two main vents. The NW dome is the smallest in radius and volume. NW may have formed last in the sequence of the domes as the magma source volume was depleted.

Another major relationship of morphology to magma properties is the viscoplastic model of lava dome growth based on magma yield strength and density (Blake, 1990):

$$\tau = 0.323(H^2 \rho g / R)$$

where H is the dome vertical thickness in m, g is gravitational acceleration m/s^2, R is basal radius in m, τ is yield strength in Pa, ρ is dome density in kg/m^3, and 0.323 is a constant derived from laboratory measurements of viscoplastic domes (Blake, 1990). This equation can be plotted with height as a function of basal radius. Here the height curves on Earth and the Moon are calculated for a rhyolitic, dacitic, and andesitic magmas (Figure 4.21). The lunar and terrestrial gravitational accelerations used were 1.6 and 9.8 m/s^2, respectively. The Gruithuisen Domes morphology is most consistent with the curve for lunar rhyolitic domes, compared to the curves for dacitic or andesitic domes (Figure 4.21). This indicates that the domes are rhyolitic in composition.

Composition	η [Pa s]	ρ [kg/m^3]	τ [10^5 Pa]	SiO_2 wt%
Basalt	10^2	2700	N/A	45-55
Andesite	10^5	2600	1.0	57-63
Dacite	10^7	2500	2.0	63-69
Rhyolite	10^9	2400	3.0	> 69

Table 4.3: Magma Properties in Table 4.3 are from Gregg and Fink (1996) and Fink and Griffiths (1998). η is viscosity, ρ is density, and τ is yield strength.

4.5.4 Future Sample Return

While the analysis of critical dome height in this paper suggests a rhyolitic composition, a sample collected from one or more of the domes would test hypotheses of their lithology, and origin, including their relationships to other major lunar rock types. Example science objectives for a mission to the Gruithuisen Domes (as discussed in Braden and Robinson (2011)) include: a) unambiguous determination of the composition of the domes, b) identifying and measuring the distribution of any KREEP- and thorium-rich materials, c) placing materials in context with genetically related lithologies, and d) collecting samples for age dating of key units to investigate the geologic evolution of the region in which they are located. A sample return mission to the Gruithuisen Domes would fulfill a number of high priority objectives for lunar science as outlined by the National Research Councils 2007 Report on the Scientific Context for Exploration of the Moon. High priority science objectives listed in the report include determining the extent and composition of the primary feldspathic crust, KREEP layer, and other products of planetary differentiation (National Research Council, 2007). A diversity of lunar samples is required for major advances and a landing site should be selected that can fill in the gaps in the diversity of lunar samples (National Research Council, 2007). As discussed in the introduction,

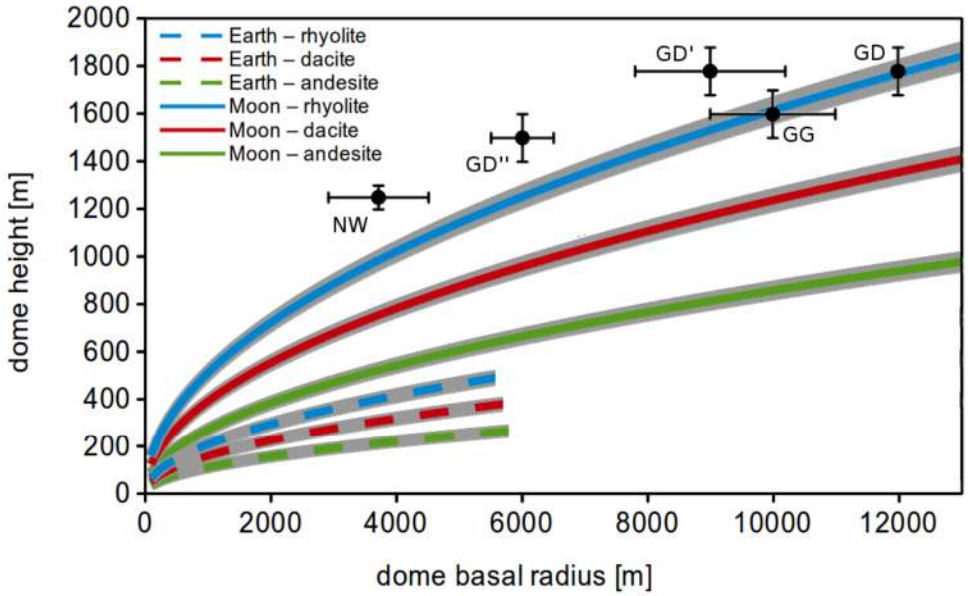

Figure 4.21: Lunar and terrestrial height curves for three different silicic compositions as a function of dome basal radius. The curves take into account gravitational differences between the Earth and Moon. The Gruithuisen domes are plotted as black dots. Error bars on the height and radius of the Gruithuisen Domes are due to changes in the relative elevation of the surrounding mare basalt and highlands material. Gruithuisen Delta (GD) is separated into two domes, a primary (GD') and secondary dome (GD") based on the two summit plateaus. Gruithuisen Delta as a whole has an oblong shape with highly variable radius. The gray bars on the curves show the uncertainty in Blake's (1990) model of dome morphology.

the Gruithuisen Domes present an entirely new facet of slicic lunar volcanism, which remains only weakly hinted at in the current sample inventory. The rocks present in the silicic domes may lead to new conclusions about the lower crust of the Moon, and returned samples would help constrain our current estimates on the complexity of the lunar crust. Our understanding of the lunar crust will contain a deficit of knowledge until questions about the variety, age, distribution, and origin of rock types in the domes are answered.

4.6 Conclusions

Data from Diviner, Lunar Prospector Gamma Ray Spectrometer, Clementine VIS spectra, LROC WAC, and NAC images were used to investigate the composition, age, and morphology of the Gruithuisen Domes. Crater size-frequency distributions measured from the summit plateaus of the Gamma and Delta domes were used to model the ages of the domes. LROC DTMs at 2 m/px scale were used to measure the relief and morphology of the Gruithuisen Domes, which was then compared to terrestrial silicic domes in the literature. The comparisons with terrestrial silicic domes were used to help determine what composition of magma formed the domes, and what processes were involved in the formation of the domes. Evidence supports the following conclusions:

1. Crater size-frequency distributions give a model age of 3.60 +0.06 -0.09 Ga for all summit plateau areas on the Gamma and Delta domes, which is at the younger end (3.7 Ga) of the age estimates from Wagner et al. (2002) using 60 m/px Lunar Orbiter data. The model age reported here is consistent with the local stratigraphy, which places the Gruithuisen domes as relatively younger than the surrounding ejecta from the Iridum impact (3.7-3.8 Ga), but older than the mare basalt emplaced around the domes. The CSFD for Gruithuisen Gamma was consistent with a resurfacing event due to a ~ 2 km impact crater at 1.45 ± 0.20 Ga.

2. Areas indicating high silica in the Diviner data are associated with relatively fresh craters and steep slopes, which is consistent with immature dome material being uncovered or excavated in those areas.

3. The Gamma and Delta domes are at the critical height expected for domes with a rhyolitic composition (versus an andesitic or dacitic composition).

4. The domes formed through effusive volcanic processes as indicated by the

original volcanic topography of ridges parallel to the flow direction (radial from the center of the domes, not compressional).

5. The concept of critical height may explain the relatively flat summit plateau areas and the similar height of each dome.

6. Sample return is required to determine the lithology of the Gruithuisen Domes and understand the composition of the domes in relation to the magmatic evolution on the Moon and implication for the LMO model. Obtaining samples of the Gruithuisen Domes is key to understanding the full suite of lunar volcanic material.

Chapter 5

IRREGULAR MARE PATCHES (IMPS), COPERNICAN VOLCANISM, AND IMPLICATIONS FOR LONG-LIVED NEARSIDE MAGMATISM

5.1 Introduction

Previous studies concluded that Ina (or Ina-D; 18.65°N, 5.30°E) represents relatively young mare volcanism, though estimates of its age of formation vary (Whitaker, 1972; El-Baz, 1972, 1973; Strain and El-Baz, 1980, Schultz, 1976; Schultz et al., 2006; Garry et al., 2012). Here in a new study 75 (from 100 to 5000 meters in the largest dimension, L) other lunar features with morphologies similar to Ina are investigated including 27 discussed by previous authors (Whitaker, 1972; Schultz, 1976, 2006; Stooke, 2012, pers.comm) (Figure 5.1). Ina and the Ina-like features are characterized by the presence of an uneven unit, which is sometimes accompanied by distinct smooth units (Figure 5.2). Flow lobes of mare basalt, which are connected to the surrounding larger maria, always embay the uneven unit (Figure 5.2). These Ina-like occurrences are named irregular mare patches (IMPs) since they are irregular in morphology and texture compared to most of the maria, they are found within the lunar maria, and they are small in spatial extent, thus "patches." The term "irregular mare patches" also avoids confusion with the mercurian hollows, which are similar (both are topographic depressions), but fundamentally different in key aspects and likely formed in a different manner (Blewett et al., 2011; Blewett et al., 2013). Each IMP exhibits sharp, meter-scale morphology and relatively few superposed impact craters with diameters (D) >10 m, suggesting a relatively young age. Constraints on the ages of these units are important for developing improved lunar thermal models

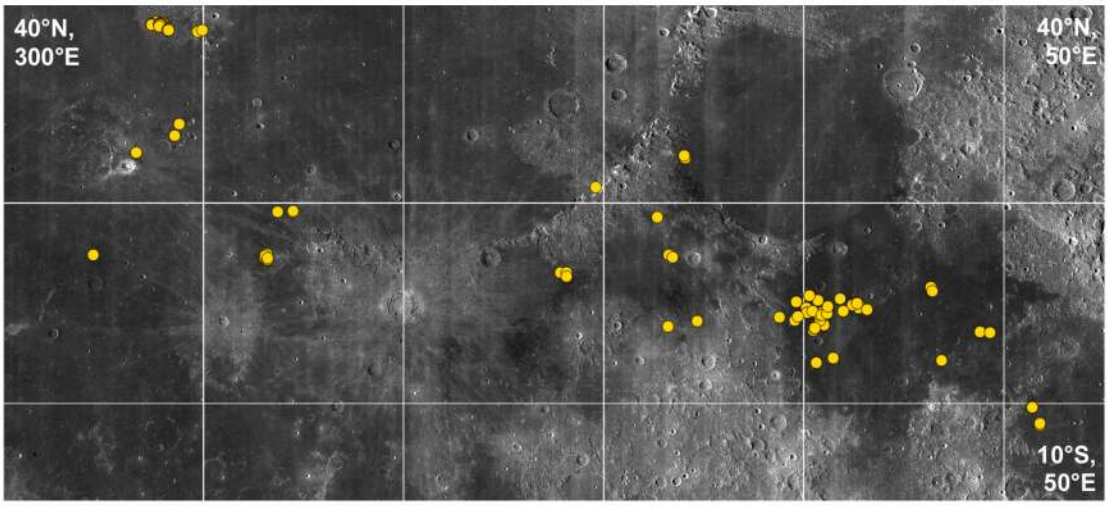

Figure 5.1: Locations of more than 70 young, small Ina-style volcanic features here called IMPs. Each yellow dot represents either a single feature, or a cluster of small features. Basemap is the LROC WAC 100 m/pixel mosaic.

and understanding the lunar heat inventory over time. Most IMPs are at least 100 m but typically less than 500 m in their longest dimension, which means they are well resolved in Lunar Reconnaissance Orbiter Camera Narrow Angle Camera (LROC NAC) images (pixel scales from 25 to 150 cm) as well as the Kaguya Terrain Camera (∼10 m/pixel) (Haruyama et al., 2009).

Extending the work of Robinson et al. (2010), small area crater counts on a subset of IMPs gave constraints on their ages relative to the lunar maria. Local stratigraphic relationships for some IMPs provided geologic context for interpretation of the crater counts. LROC NAC Digital Terrain Models (DTMs) (Burns et al., 2011) enabled quantitative assessment of the morphological differences between the smooth and uneven units, as well as determined their stratigraphic relationships. The identification of a larger population of IMPs (n=75, L>100 m) also allowed for an examination of a wider range of geologic associations between the IMPs and volcanic features, which provided new insights into the formation and context of these small, young features. In this paper the morphology, size, spatial distribution, and crater

densities of the IMPs were examined. The overarching goal was to understand origin of the IMPs and their ages relative to other young lunar features, such as impact melt from craters Tycho (∼100 Ma) (Drozd et al., 1977) and Giordano Bruno (∼1-10 Ma) (Morota, et al., 2009; Williams et al., 2013).

5.2 Background

Ina (18.65°N, 5.30°E) is a topographic depression at the summit of a shallowly sloped positive relief feature first described by Whitaker (1972) using orbital images from the Apollo 15 mission. The shallowly sloped positive relief feature was interpreted as an extrusive low-shield volcano (El-Baz, 1973; Strain and El-Baz, 1980). Crater densities around the base of the shield volcano were greater than near the rim of the depression, which indicated a relatively younger age for material in and immediately around Ina compared with the mare basalt unit, Lacus Felicitatis, that surrounds Ina (El-Baz, 1973; Strain and El-Baz, 1980). Robinson et al. (2010) demonstrated the utility of the high resolution LROC NAC data for quantifying the overall crater densities in and around Ina using small area crater counts, as well as close examination of the surface morphology and reflectance properties. Previous age estimates for Ina determined it is relatively young in terms of mare volcanism as a whole (Strain and El-Baz, 1980; Schultz et al., 2006; Robinson et al., 2010).

The literature regarding Ina had differing interpretations in terms of its origin. Early hypotheses included the deposition of sublimates to account for the high reflectance of the uneven unit (Whitaker, 1972) and the more widely accepted origin as a collapse caldera created through episodic volcanic activity (El-Baz, 1972; 1973), where each mound in the interior (smooth unit) was formed by discrete effusion events (El-Baz, 1973; Strain and El-Baz, 1980). Schultz et al. (2006) suggested that geologically recent (∼10 Ma ago) explosive volcanism exhumed patches of high-titanium,

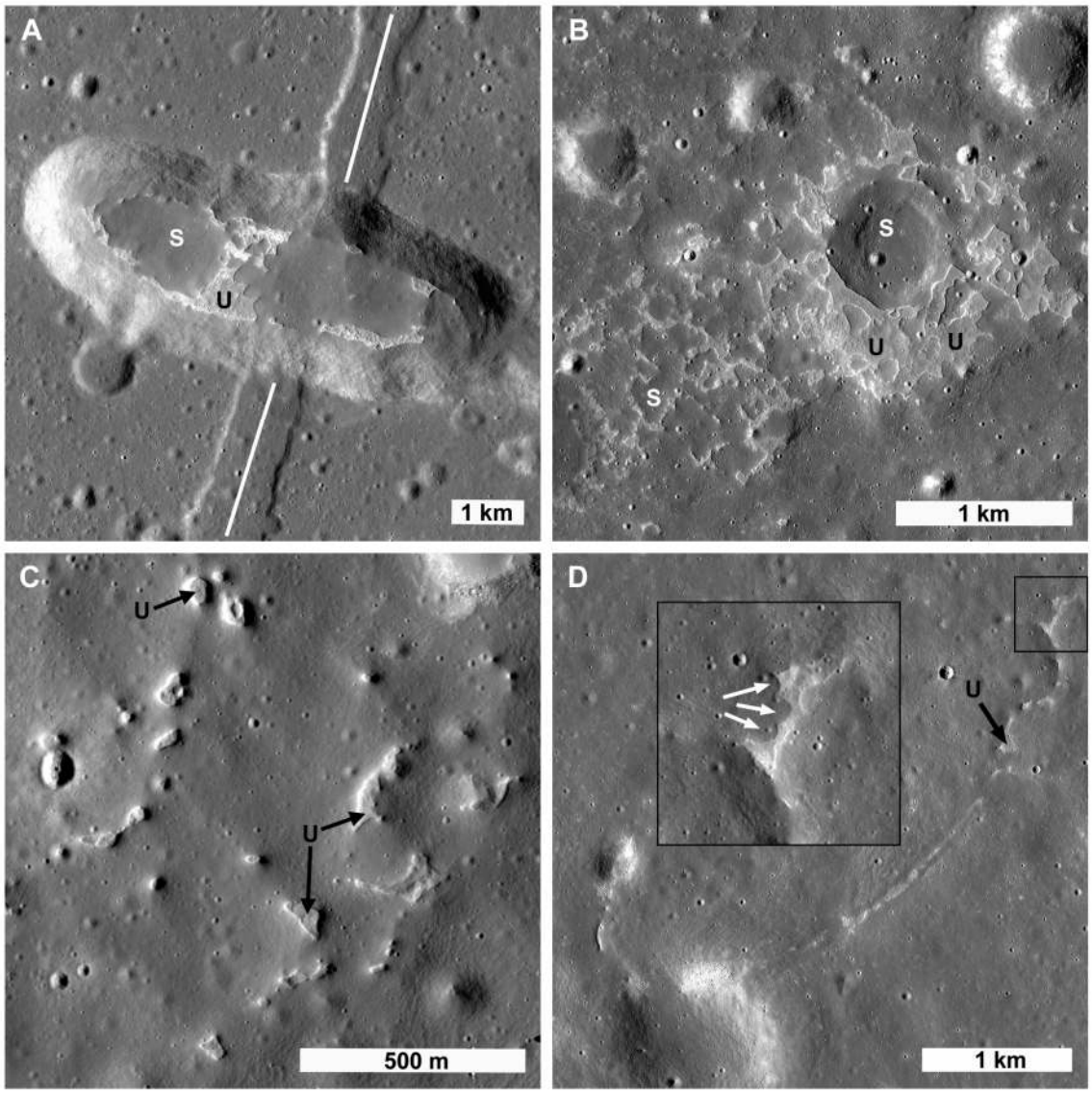

Figure 5.2: "S" and "U" mark examples of the smooth and uneven units. All images are ∼70° incidence angle, which is the angle between the incident solar radiation and the normal to the surface. A) The topographic depression containing the Sosigenes IMP (8.335°N, 19.071°E) crosscuts a smaller northeast-trending graben (white line). LROC NACs M192832116 and M192824968. B) The IMP Maskelyne (#8, Table C.1) (4.330°N, 33.750°E). The circular topographic high may mark the location of the largest vent. NAC M1123370138R. C) The IMP in the floor of Hyginus crater (7.726°N, 6.350°E) represents a group of IMPs formed of clusters of small uneven units. NAC M1108239463. D) IMP Carrel-1 (#10, Table C.1) (9.817°N, 25.519°E), represents a distinct morphology of IMPs where narrow, discontinuous sections of uneven units follow a curved path. The inset highlights a section of uneven unit superposed by three lobate contacts (white arrows). NAC M1096329585.

high-reflectance, blocky material on the floor of Ina. In this scenario, the original basaltic surface (including the smooth mounds in Inas interior) was assumed to be at least 3.5 Ga, and more recent episodic outgassing of subsurface volatiles (juvenile CO_2 and possibly H_2O) removed a thick (>12 m) layer of regolith or pyroclastic material (Schultz et al., 2006). Schultz et al. (2006) further proposed that Ina may still be active based on the topographic relief, the spectral maturity of the regolith, and the superposition of only two ∼30 m diameter craters within Ina. Most recently, Garry et al. (2012) used LROC images and topography to demonstrate similarities between the morphology of Ina and terrestrial lava flows that formed through a series of inflation events. This inflation model suggested that as the mounds (smooth unit) inflated, breakout flows along their margins created the stratigraphically lower unit (uneven unit) and subsequent mass wasting created the fresh, blocky surfaces in the uneven unit (Garry et al., 2012). Unresolved differences between Ina and terrestrial inflated lava flows remained: no vent source is observed at Ina and no cracks are found on the smooth unit mounds which are found in terrestrial inflated lava flows (Garry et al., 2012).

The general consensus was that Ina is young relative to major mare basalt forming eruptions (Strain and El-Baz, 1980; Schultz et al., 2006; Robinson et al., 2010). Current understanding of the duration of mare volcanism placed it between 4.2 and 1 Ga. A majority of mare basalts sampled by the Apollo and Lunar missions provided geochemical ages from 4.2-3.1 Ga (e.g., Ryder and Taylor, 1976; Ryder and Spudis, 1980; BVSP, 1981). However, a clast within the lunar meteorite NWA 773 had a geochemical age of ∼2.87 Ma (Borg et al., 2004) and remote sensing data (crater size-frequency distributions) supported mare basalt ages as young as ∼1.0 Ga (Schultz and Spudis, 1983; Hiesinger et al., 2003; Hiesinger et al., 2011). These younger ages indicated that mare volcanism persisted over a longer period of time

than suggested by the Apollo and Luna samples. The IMPs discussed in this paper are significantly smaller in volume than the lunar maria. However, the IMPs are more widespread on the lunar surface than previously thought, which warrants further examination to understand how the IMPs fit into the sequence of mare volcanism. The topographic analysis of IMPs and crater size-frequency distributions presented in this paper provide evidence for IMPs <100 Ma in age. Younger, small volume extrusions of mare basalt are consistent with a thermal history where mare volcanism did not end abruptly but rather decreased gradually over time (Schultz and Spudis, 1983; Head and Wilson, 1992).

IMPs are fundamentally different from the mercurian hollows. At lower image scales (>50 m/px) both IMPs and hollows appear as topographic depressions with areas of relatively high reflectance, however, new data from the MESSENGER and LROC missions have increased the understanding of differences between mercurian hollows and lunar IMPs. Mercurian hollows are shallow, flat-floored irregular depressions with relatively high reflectance (Blewett et al., 2013) and spectrally bluer than even fresh craters on Mercury (Robinson et al., 2008; Blewett et al., 2009, 2011). Most hollows are associated with impact structures and many occur preferentially on topographic slopes of maximum potential for solar heating (Blewett et al., 2013). IMPs are not associated with impact craters, but rather volcanic collapse craters, mare basalt deposits, and volcanic domes. Hollows can be much larger in areal coverage than the largest IMPs (3-5 km in largest dimension); hollows in Tyagaraja and Sander craters are several tens of kilometers across (Blewett et al., 2011).

5.3 Methods

LROC NAC image data were calibrated and projected using the Integrated Software for Imagers and Spectrometers (ISIS) (Anderson et al., 2004) and imported into

ArcGIS. For a subset of IMPs (Sosigenes, Ina, Manilus-1, Cauchy-5, Tranquillitatis Whale, and Hyginus), the smooth (usually topographically higher) and uneven (usually topographically lower) units within each IMP were mapped. Then craters on each unit and the surrounding mare were digitized (diameter and center location) using ArcGIS CraterTools (Kneissl et al., 2011). The measured crater size frequency distributions (CSFDs) were plotted with CraterStats2 (Michael and Neukum, 2010). Model ages were based on the chronology function and production function of (Neukum et al., 2001) for lunar craters 0.01<D<100 km. Model ages were derived only for craters with D $\geq$0.01 km, although the NAC pixel scale (50 to 150 cm) allows the measurement of smaller craters (e.g., Hiesinger et al., 2012). Results presented here are from NAC images of the following IMPs: Sosigenes Depression (M192824968, incidence angle = 70°, scale = 1.2 m/px), Ina (M113921307, incidence angle = 58°, scale = 0.5 m/px), and Cauchy-5 (M1108039362, incidence angle = 63°, scale = 1.2 m/px).

Feature	Average Slope [°]	Std. Dev. Slope [°]	Average H* [m]	Std. Dev. H* [m]	# of profiles
Sosigenes	16	6	8	3	41
Ina	26	6	8	2	28
Cauchy-5	8	2	7	3	26
Hyginus	22	5	14	4	22
Manilus-1	14	6	6	2	9
Tranq. Whale	16	9	7	3	17
Imbrium Flow	7	3	24	8	37

Table 5.1: Slope and Height Measurements from Elevation Profiles. *H is the thickness of the flow.

LROC NAC stereo pairs (Burns et al., 2011) from adjacent orbits (parallax angle

>20°; incidence angle 40°<i<65°) were acquired and reduced to DTMs at six IMPs (Ina, Hyginus, Sosigenes Depression, Tranquillitatis Whale, the Cauchy-5 dome, and Manilus-1; Table C.1). The DTMs were used to examine stratigraphic relationships between the uneven and smooth units as well as the surrounding mare basalt and to provide quantitative measures of slope. Elevation profiles across the contacts between the uneven and smooth units at each site provided measurements (n=143) of the thickness of the smooth units, and the slopes along the edges of the smooth units (Figure 5.3). Elevation profiles across the smooth/uneven unit contacts were compared to profiles across young impact melt flow fronts in the crater Tycho (109±4 Ma (Drozd et al., 1977)) and the Eratosthenian-aged Imbrium lava flows (Schaber, 1973). Further comparisons using DTMs involved examining slopes within Tycho, Larmor Q, Moore F, and Giordano Bruno craters, all Copernican in age. Relief and slope were used as indicators of age assuming steady erosion through micrometeorite and small (relative to the size of a feature under study) bolide bombardment (e.g. Arvidson et al., 1975). All slope measurements were taken using elevation profiles and a fit to the steepest part of the slope (Table 5.1), a line which always included at least 3 pixels. Each DTM was sampled at either 2 or 5 meters per pixel scale (Table 5.2), depending on the original pixel scale of the NAC images. Since not all the DTMs were at the same scale, smoothing may be in effect at IMPs were the scale is 5 m/px (Cauchy-5, Hyginus, Manilus-1). For these IMPs, the slopes measured are a lower bound and steeper local slopes may be present.

Each IMP occurrence was plotted on a WAC 100 m/px basemap (Figure 1). The context of the area surrounding each IMP was investigated using LROC NAC, LROC WAC, Clementine OMAT, Clementine TiO_2 and FeO wt% maps (Lucey et al., 1995; 1998; 2000a; 2000b; Blewett et al., 1997) to document any color or stratigraphic relationships that might constrain the age of each IMP, as well as search for clues as to

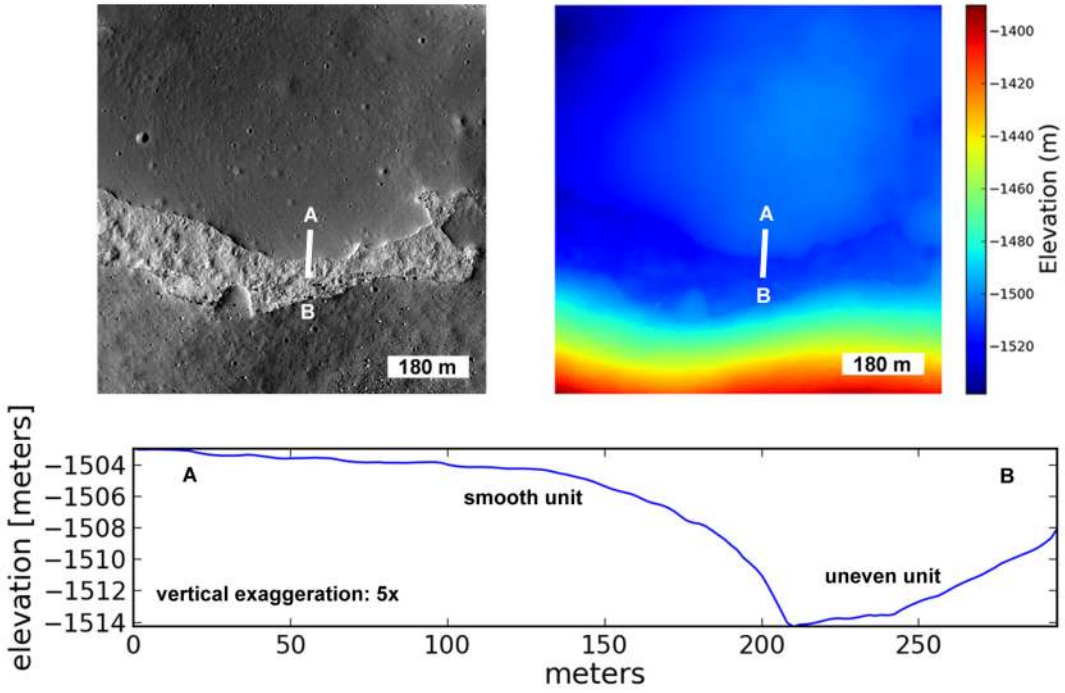

Figure 5.3: An example profile across the boundary of the smooth and uneven units. The thickness of the smooth unit is measured as the difference in elevation between the average flat surface of the smooth unit (here -1504 meters elevation) and the base of the uneven unit, (here -1514 meters elevation). For this particular profile the smooth unit thickness recorded is 10 meters.

their origin. Due to the small size of a majority of IMPs (average size for IMPs >100 m in longest dimension is ∼450 m, n=75), the Clementine datasets only provided information for the larger features (>800 m diameter, n=7), but the characteristics of the mare basalt in which the units occur were readily resolved. The locations of the IMPs were also compared to cataloged locations of known mare domes (e.g. Head and Gifford, 1980), pyroclastic deposits (e.g. Gaddis et al., 1998), and large mare shield volcanoes (Spudis et al., 2013).

A subset of seven IMPs were large enough to be resolved in the Clementine UVVIS global mosaic (here sampled at 200 meter/pixel; Eliason et al., 1999). Low altitude WAC observations (∼35-45 km orbital altitude) were used to provide the highest resolution possible for each IMP (∼180-350 m/px in the UV and ∼55-70 m/px in the

Feature	Lat [°]	Lon [°]	NACs	DTM scale[m/px]
Sosigenes	8.335	19.071	M177508146, M177514916	2
Ina	18.650	5.300	M119808916, M119815703	2
Cauchy-5	7.169	37.592	M1108039362, M1108025067	5
Hyginus	7.730	6.350	M1114121068, M1114135273	5
Manilus-1	14.889	6.467	M1121188383, M1121202582	5
Tranq. Whale	8.891	21.487	M144483945, M144490730	2
Imbrium	28.940	-26.100	M183697099, M183711393, M1106080949, M1106095239	5

Table 5.2: Parameters of LROC NAC DTMs used for elevation profile measurements.

VIS bands). The WAC images were calibrated and projected using ISIS (Anderson et al., 2004) and photometrically corrected with an empirical algorithm (Boyd et al., 2012).

5.4 Observations

5.4.1 Spatial Distribution and Associations

The current spatial distribution of IMPs, based on investigations of LROC NAC images (Figure 5.1), narrows the possibilities in terms of their origin. First, IMPs are only found in the nearside maria (to-date). About half of the IMPs are located within the currently defined boundaries of the Procellarum KREEP Terrain (PKT) (Wieczorek and Phillips, 2000; Jolliff et al., 2000), with the exception of thirty-five IMPs found in Mare Tranquillitiatis and four (small) examples in Mare Fecunditatis (Table C.1). The PKT is defined as the region where thorium concentrations generally exceed 3.5 ppm (Lawrence et al., 1998); Mare Tranquillitatis is not considered

part of the PKT, but it embays the PKT. However, there is a small-area thorium high (>3 μg/g) in southwestern Mare Tranquillitatis centered on the crater Arago (5.9°N, 20.1°E), near the boundary of the PKT (Lawrence et al., 2003). The concentration of IMPs (n=31) in the western half of Mare Tranquillitatis is just north of the crater Arago. The western and eastern halves of Mare Tranquillitatis have thorium concentrations of 2.5-3.0 and 1.5-2.5, respectively (Lawrence et al., 1998, 2003). This east-west dichotomy correlates to a large shield volcano dominating the eastern half of Mare Tranquillitatis (Spudis et al., 2013). Thirty IMPs occur in the western half of Mare Tranquillitatis and five formed on the flanks of the large shield volcano. Another notable concentration of small, clustered IMPs (n=23) occurs in a mare deposit between the craters Gruithuisen E and Gruithuisen M. The role of radiogenic heating from materials like thorium in the emplacement of IMPs will be further addressed in the discussion section.

IMPs are found in association with a variety of mare basalt compositions (high to low titanium, average FeO content), as well as known mare domes, large shield volcanoes, and pyroclastic deposits. Of the large mare shield volcanoes identified in Spudis et al. (2013), Cauchy, Marius Hills, Aristarchus, Rimae Prinz, T. Mayer-Hortensius all exhibit IMPs within the extent of the slopes of the shield volcanoes. Examples of IMPs associated with pyroclastic deposits include four in the Rima Bode region and two in Mare Vaporum. Clementine TiO_2 and FeO wt% maps show that IMPs occur in a range of mare basalt compositions from ~3-13 wt% TiO_2 and ~15-20 wt% FeO. Some IMPs are found on the flanks of small shield volcanoes, (examples: Cauchy-5 and Arago 5 domes), while other IMPs are found in simple mare basalt with no remarkable surroundings. Figure 5.2 shows examples of IMPs in diverse contexts. The IMP east of the crater Sosigenes (#1 from Table C.1) is located within a topographic depression (8.335°N, 19.071°E, Figure 5.2a). Another IMP (4.330°N,

33.75°E), west of the crater Maskelyne F (#8 from Table C.1) (Figure 5.2b), occurs at elevations similar to the surrounding mare basalt, but formed a topographic high in its center. Some IMPs form regional or local clusters of smaller uneven units such as the examples inside Hyginus crater (#4 from Table C.1) (Figure 5.2c). Finally, some IMPs occur as narrow, discontinuous sections of uneven units following a curved path (e.g., #10, Carrel-1) (Figure 5.2d).

5.4.2 Description of Units

We divided the terrain within the IMPs into two main units: the smooth unit and the uneven unit (Figure 5.2, 5.4). Previous authors (Garry et al., 2012) split the uneven unit into subunits within Ina, but for the purposes of examining the known global population of IMPs, two units are sufficient. The smooth unit has a smooth, uniform appearance, with sharp boundaries at the uneven unit contact, and few superposed impact craters. No fractures or ridges are visible on the smooth units, and relatively few boulders are present compared to the uneven unit. In some instances smooth unit lobes transition to the surrounding mare with no discernible contact, although in other cases there is a slight (∼2 m) decrease in elevation down to the smooth unit. The reflectance of the uneven unit is generally uniform with the exception of boulder clusters. Sections of the uneven unit with high block density exhibit ∼30% higher reflectance (measured from 15° to 20° incidence angle images) compared to the smooth unit (Figure 5.4), likely due to the many reflective surfaces (facets) provided by the blocks and related breakdown of material exposing fresh surfaces (relative maturity). Portions of the uneven unit exhibiting few meter-scale or larger block had reflectance values comparable to that of the smooth unit. While these areas of the uneven unit have similar reflectance as the smooth unit, the uneven unit is still distinctly different in visible texture and the smooth unit is topographically

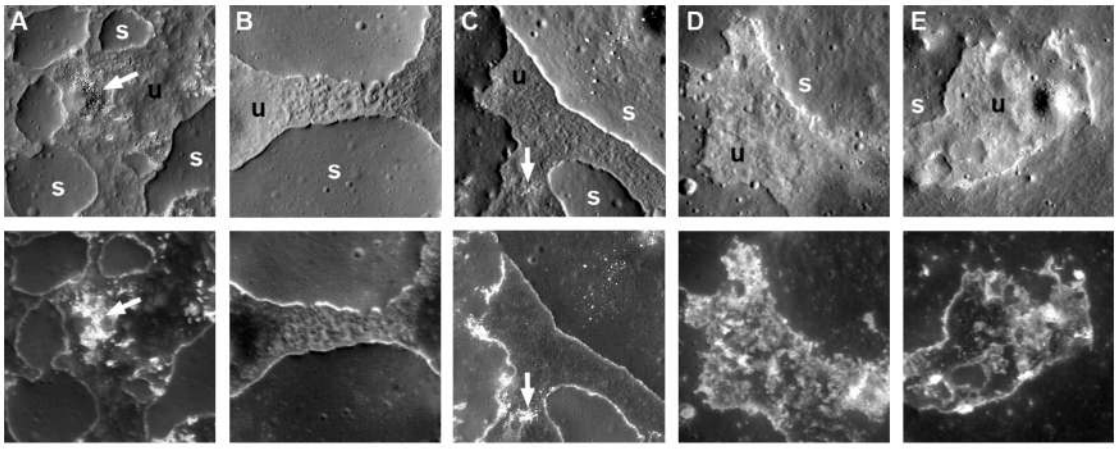

Figure 5.4: Large incidence angle images (58°-74°) emphasize topography (top row) while small incidence angle (14°-20°) images emphasize reflectance differences of the surface (bottom row). The "S" and "U" mark examples of the smooth and uneven units respectively. A and B) Ina, C) Maskelyne, D) Jansen-2, E) Tranq. Whale. The white arrows highlight areas where boulders are clearly visible in large incidence angle images and correspond to high reflectance material in the small incidence angle images. Each frame is 360 m across (NAC images sampled at 1.2 m/pixel).

higher than the uneven unit. Meter-scale fractures similar to those seen in impact melt deposits (Bray et al., 2010; Ashley et al., 2012; Denevi et al., 2012) were not found within the uneven unit.

5.4.3 Crater Density

CSFDs yielded model ages for the smooth and uneven units within the IMPs. The model ages of the smooth units for Ina (area=1.7 km^2), the Sosigenes feature (area=4.5 km^2), and the Cauchy feature (area= 1.3 km^2) were ~33, ~18, and ~58 Ma, respectively (Figure 5.5). These model ages indicated that the smooth units are younger than the surrounding maria, but not as young as 10 Ma, the previously suggested maximum age for Ina (Schultz et al., 2006). There were no detected dependencies on incidence angle, which can affect the number of craters identified in an image (Soderblom, 1972; Young, 1975; Wilcox et al., 2005). Two Ina-style formations in Mare Tranquillitatis covered $\leq$0.2 km^2 and did not contain enough craters to create

meaningful CSFDs. On each of the three smooth units the number of craters with D $\geq$0.01 km was small, $\sim$230-290 craters. The model ages from the uneven units of Ina (total area 2.2 km^2), the Sosigenes feature (total area 1.1 km^2) and the Cauchy feature (total area 0.9 km^2) were $\sim$4, $\sim$3.5, and $\sim$28 Ma, respectively. The number of total craters on each unit was small, from $\sim$15-60 craters. The uneven units had fewer craters per unit area compared to the smooth units, however for craters with D $>$20-25 m the uneven and smooth unit CSFDs overlapped (Figure 5.5). The smooth and uneven units had different crater densities for craters D $\geq$10 m, but not for D $\geq$50 m.

5.4.4 Stratigraphy

The stratigraphic relationship between the smooth and the uneven units was consistent across all IMPs found to-date; the smooth unit always superposed the uneven unit. Depending on the general topography within an IMP the uneven unit was sometimes topographically higher than portions of the smooth unit. In the case of Ina, the detailed DTM shows where the preexisting topography of the uneven unit determined the flow direction of the smooth unit (Figure 5.6).

The young model ages from CSFDs were consistent with stratigraphic relations at the Sosigenes IMP and the IMP north of Aristarchus crater (25.044°N, 313.233°E). The east-west oriented Sosigenes Depression cross-cut a stratigraphically older graben in the mare (Figure 5.2a). The smooth, lobate unit within the Sosigenes feature showed no signs of tectonic activity and must be younger than both the surrounding mare and the north-south trending graben (Figure 5.2a). Clementine OMAT parameter values showed that the IMP north of Aristarchus (#11, Table C.1) crater was immature relative to Aristarchus impact ejecta, which combined with the small scale morphology of the feature, indicated that the feature was younger than the

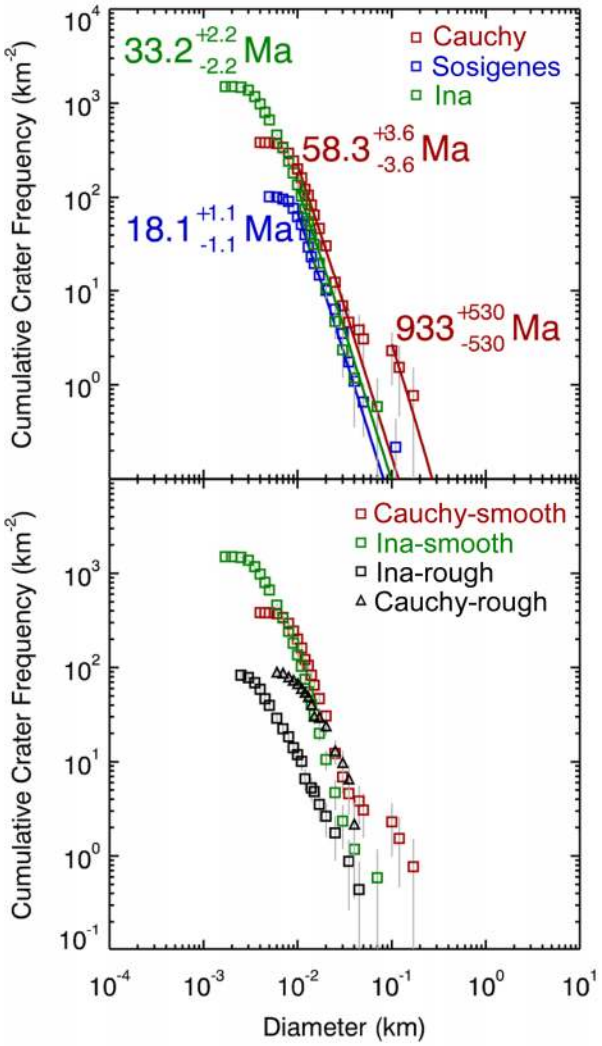

Figure 5.5: (top) CSFDs from crater counts on the smooth units within the Cauchy-5, Sosigenes, and Ina formations give a range of model ages from 18-58 Ma. Three D>100 m craters give an older model age, however these craters are highly degraded and may have formed before the formation of the Cauchy-5 IMP. Statistical error bars shown in gray. (bottom) CSFDs from the uneven units compared to the smooth units.

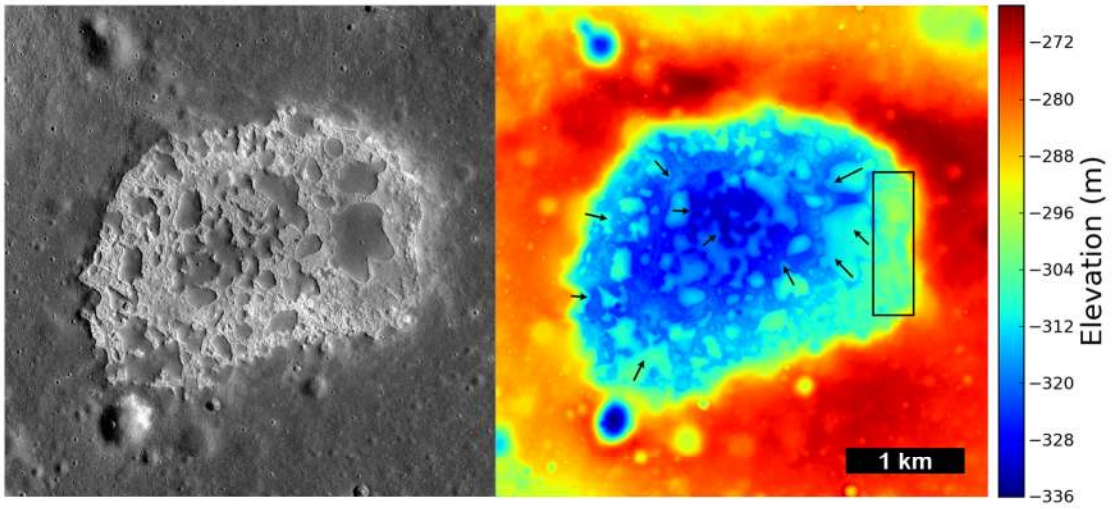

Figure 5.6: Colorized topography of Ina (2 m/px DTM). The black rectangle outlines an area where the uneven unit is topographically higher than the smooth unit. On the eastern rim, this section of uneven unit blocked the flow in mare basalt into the topographic depression caused by the collapse event. On the western rim, the uneven unit is lower in elevation, allowing mare basalt flows from the rim to drain back into the caldera. The small black arrows mark the direction of flow for the smooth unit in select places. Overall, the flow direction is dominantly towards the lowest topographic point at the approximate center of the depression, except for cases where the preexisting topography of the uneven unit acts as a barrier and redirects the flow.

Aristarchus impact. Age estimates for Aristarchus crater ranged from ∼1 Ga (Hartmann, 1968; Strom and Fielder, 1970), ∼450 Ma (Zisk et al., 1977), and ∼130 to 180 Ma (König et al., 1977), all based on crater counts from the continuous ejecta blanket. Recent counts of the entire proximal ejecta blanket of Aristarchus crater using craters D>60 m gave a model age of ∼189 Ma, and a model age of ∼150 Ma for D>200 m (Zanetti et al., 2013). Thus we interpret that the Aristarchus IMP is younger than 200 Ma.

5.4.5 Morphology

The sharp, meter-scale morphology of the IMPs was compared to very young Copernican craters (estimated ages from ∼10 to ∼100 Ma old), impact melt flow

fronts from the crater Tycho, and the volcanically emplaced, Eratosthenian-aged (2.5 ± 0.3 By old) Imbrium flows studied by Schaber (1973) (located at 28.94°N, -26.10°E, just north of Mons La Hire). Comparing the morphology of the IMPs to other young lunar features provided another constraint on age, in addition to the age estimates from the CSFDs. While the Imbrium basalt flows were not Copernican in age, they provided a reference for the morphology of older lava flows.

IMP Slopes and Smooth Unit Thickness

Elevation profiles from the NAC DTMs were used to calculate the flank slope and smooth unit thickness near the edges of the contacts between the smooth unit and the uneven unit (Table 5.2). In Ina, the slopes along the edges of the smooth unit were on average 26° (range 14-39°). The Hyginus IMP had the next steepest slopes, with an average of 22° (range 13-30°). The Sosigenes Graben and Tranquillitatis Whale IMPs had average flank slopes of 16° with a range of 8-32° at Sosigenes and a range of 5-37° at the Tranquillitatis Whale. The Manilus-1 IMP had an average flank slope of 14° (range 9-24°). The IMPs on the Cauchy-5 dome had the shallowest slopes with an average of 8° (range 3-12°). Elevation profiles (n=143) of unit boundaries within six IMPs (Ina, Sosigenes, Tranq. Whale, Cauchy-5, Hyginus, and Manilus-1) yielded smooth unit thickness measurements between 2-20 meters, with an average of 8 m (Figure 5.7).

Copernican Crater Slopes

Interior crater wall slopes of 35° were common within 20-km diameter Copernican craters such as Giordano Bruno, Moore F, and Larmor Q (Wagner et al., 2013). The age of Giordano Bruno formation event was estimated to be between 1-10 Ma (Morota et al., 2009; Williams et al., 2013), Moore F between 10-58 My, and between 58-100

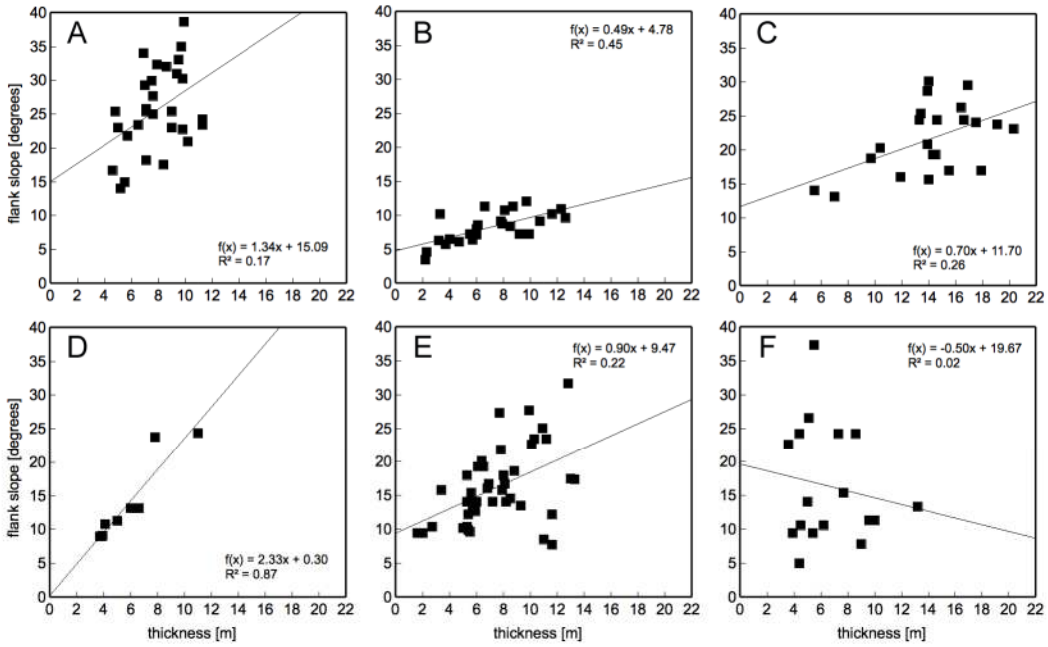

Figure 5.7: Scatter plots showing measurements of the elevation difference of the smooth unit surface (thickness of flow) above the stratigraphically lower uneven unit (x-axis) and the flank slope of the edge of the smooth units (y-axis). A) Ina, B) Cauchy-5, C) Hyginus, D) Manilus-1, E) Sosigenes, F) Tranq. Whale.

My for Larmor Q (Williams et al., 2013). The Eratosthenian crater Lichtenberg (20 km diameter), estimated to be >1.7 Ga old (Hawke et al., 2004), had average crater wall slopes from 28-32° (Wagner et al., 2013). Tycho crater had slopes from 26-32° on the upper crater wall based on LROC 100 m/px topography data. A NAC DTM containing a portion of the upper wall showed slopes from 31-34°. These slopes were not from the original crater wall, since Tycho was ∼86.2 km in diameter and has many inner terraces due to slumping. Age-dating using the duration of exposure to cosmic rays of previously shielded secondary material from the Tycho impact gave an age of 109±4 Ma (Drozd et al., 1977). Crater counts using LROC NAC images gave ages of ∼85 (+15/-18) Ma and counts using LROC WAC images gave ages of ∼124 Ma (+12/-12) (Hiesinger et al., 2012).

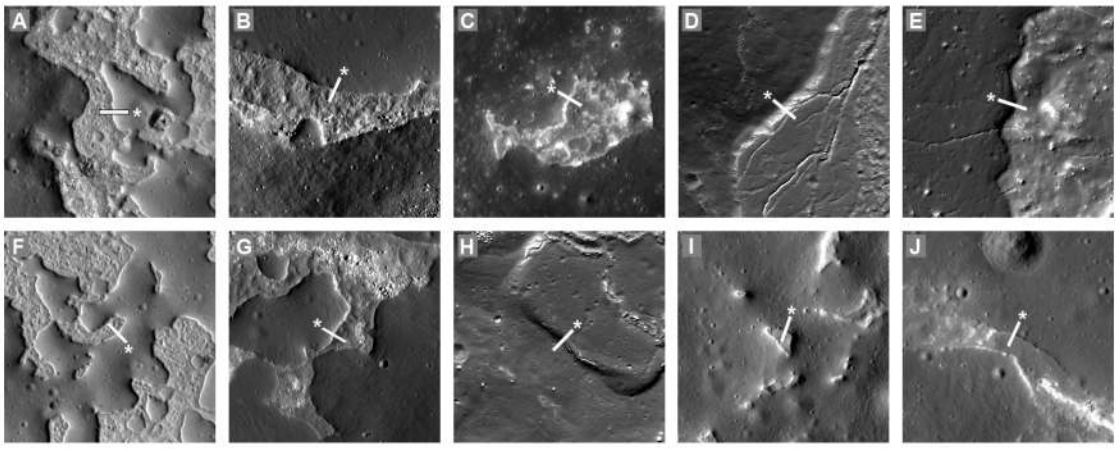

Figure 5.8: Series of 600 m wide images from four IMPs and Tycho crater impact melt. White lines indicate the location of the profiles in Figure 5.9 and asterisks mark the beginning of each profile. A) Ina, B) Sosigenes, C) Tranq. Whale, D) Tycho impact melt flow, E) Tycho impact melt flow (crater floor), F) Ina, G) Sosigenes, H) Hyginus, J) Cauchy-5.

Tycho Impact Melt Flow Fronts

NAC DTM elevation profiles across the boundaries of the smooth and uneven units were compared to profiles across Tycho impact melt flow fronts (Figure 5.8, 5.9). The contacts between the smooth and uneven units in the IMPs were as sharp as the flow fronts of impact melt, and the slopes on the flow fronts ranged from 10-31°. This range of slopes emphasized that while a young feature like Tycho may have areas with shallow slopes, some areas will have steeper slopes above the angle of repose.

Imbrium Lava Flow Topography

The topography of each IMP in NAC DTM data was compared to the topography of the older, Eratosthenian-aged Imbrium flows (Schaber, 1973). Within the extent of the Imbrium flows, there was a range of slopes (2-13°) and flow thickness (12-36 m), as well as a positive correlation between flow thickness and the flank slope (Figure 5.10). The plot showed that for a given age, a lava flow exhibited a range of thickness

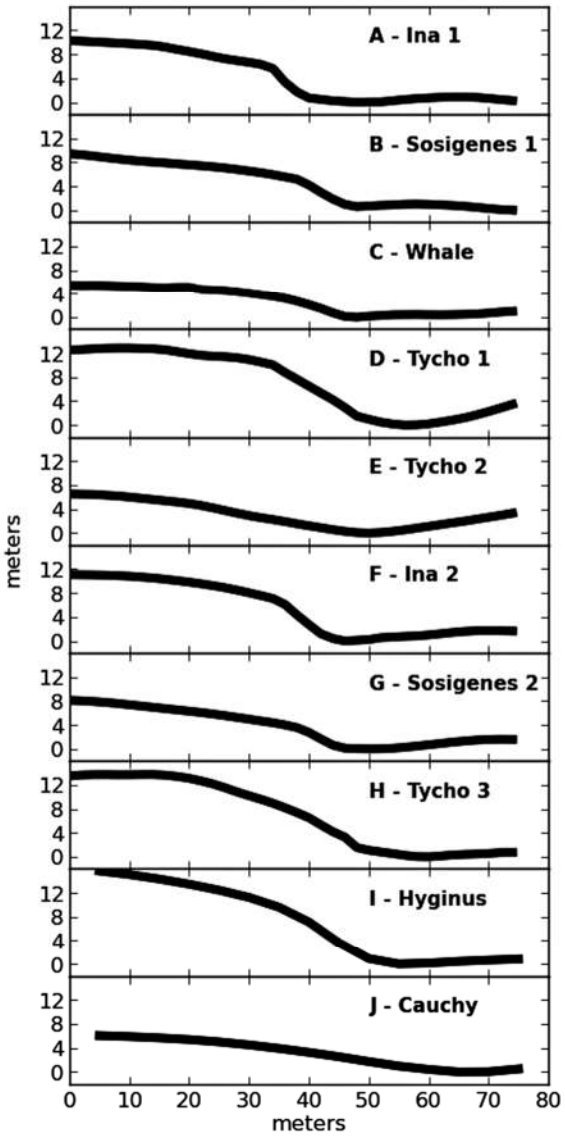

Figure 5.9: Elevation profiles across smooth and uneven unit boundaries from five different IMPs compared to profiles across impact melt flow fronts from Tycho crater. Vertical axis is elevation in meters (no vertical exaggeration). Letters for each profile correspond to the images in Figure 5.8.

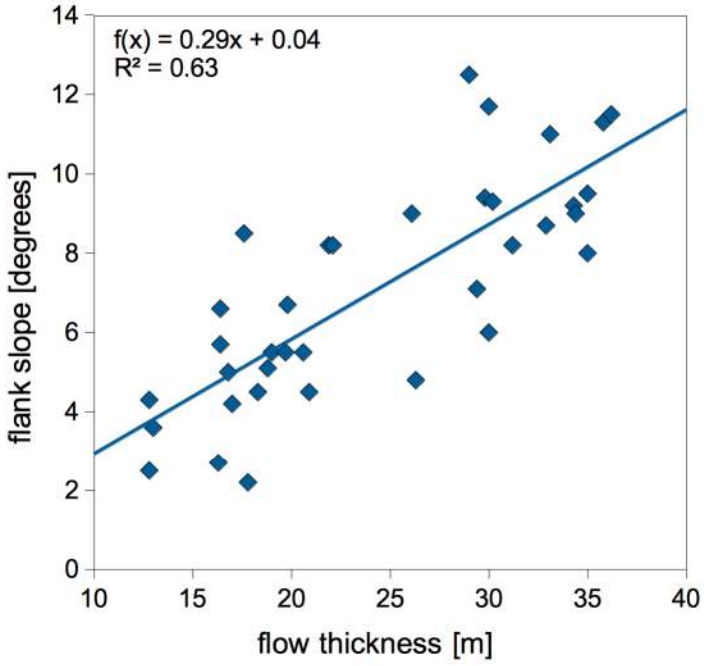

Figure 5.10: Measurements of thickness and flank slope from the edge of Imbrium lava flows. The best fit line (linear regression) indicates a positive correlation between flow thickness and the flank slope. Table 5.1 compares the average slope and thickness of the Imbrium flows to the IMPs with NAC DTMs.

and flow front slopes. Overall, the Imbrium flows were significantly thicker (Figure 5.12) than the smooth units within IMPs, and the slopes at the edge of the flows were shallower than all IMPs, with the exception of the IMP on the Cauchy-5 dome.

5.4.6 Multispectral Observations

Color ratios of units within and immediately surrounding a subset of seven IMPs were compared with other lunar terrains including large pyroclastic deposits, mare units, and average highlands material (Figure 5.11). The two ratios used were the Clementine 950/750 nm, which corresponds to mafic band strength (Lucey et al., 1998), and the 320/415 nm WAC ratio (Denevi et al., 2011; Denevi et al., submitted). The mare units immediately surrounding the IMPs had a distinct spectral signal. These areas were most similar to the spectral ratios of very large pyroclastic deposits

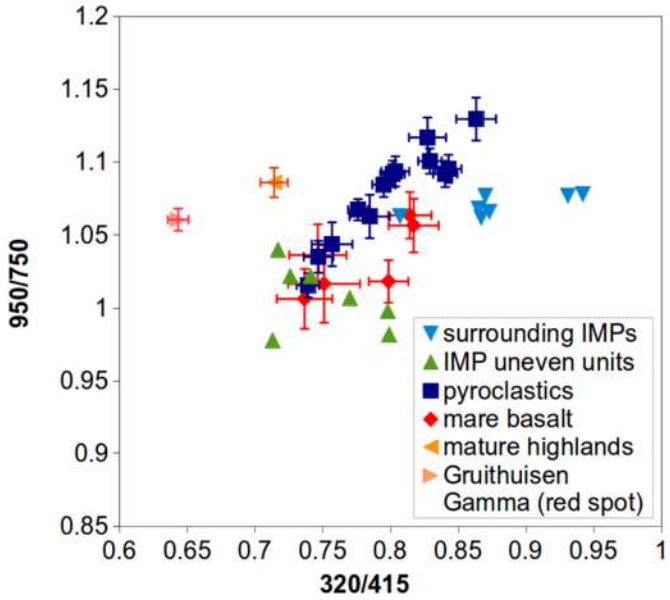

Figure 5.11: Color ratios of units within and immediately surrounding a subset of seven IMPs compared with color ratios of other lunar units including large pyroclastic deposits, mare units, and average highlands material. The horizontal axis is the 320/415 nm WAC ratio and the vertical axis is the 950/750 Clementine ratio. The mare units immediately surrounding the IMPs (filled-in squares) are most similar to the spectral ratios of large pyroclastic deposits. The uneven units within the IMPs (filled in circles) have spectral ratios consistent with mare basalt. The uncertainty bars are the standard deviation of the pixels within the region of interest.

such as Sulpicious Gallus, Mare Vaporum, Rima Bode, Harbinger, Aristarchus, southwestern Mare Humorum, Sinus Aestuum, and Taurus Littrow (Gaddis et al., 1998; Gaddis et al., 2003). The uneven units within the IMPs typically have spectral ratios consistent with mare basalt. Ina plots away from the other IMPs for both the uneven unit and surrounding mare units, with lower 320/415 nm WAC ratios.

5.5 Discussion

5.5.1 Crater density and age

Due to the small area of each IMP and the small diameters of the impact craters within those areas, a few caveats should be addressed when interpreting the model ages presented here. First, CSFDs formed from D <1 km craters have a high likelihood of contamination by secondary craters (McEwen and Bierhaus, 2006) since secondary craters are on average smaller than primary craters. All of the craters in CSFDs reported here are D <1 km, which means all craters are within the size the regime of secondaries. While secondary contamination is a concern, Ivanov (2006) interpreted that most small craters (D <200 m) on young lunar surfaces (<100 Ma) are primaries. In addition, the sample areas investigated here are small, and currently the minimum area required to accurately date a surface is not well constrained. However, recent models of the size distribution of terrestrial fireballs scaled to the Moon successfully reproduced the CSFD (area=0.1 km^2, D $\leq$22 m) for North Ray crater (Williams and Pathare, 2013), the age of which is constrained to 48.9±1.7 Ma and 50±0.8 Ma through cosmic ray exposure ages of Apollo 16 samples (Marti et al., 1973; Drozd et al., 1974; 1977) and 50.6±3.8 Ma through radiometric age dating (Behrmann et al., 1973). Previous crater counts of the area around North Ray crater give model ages of 48.9±1.7 (König, 1977), 50±1.4 (Neukum, 1983), 50±0.8 (Moore et al., 1980), 92.1 (Plescia and Robinson, 2011), and ~46-47 (Hiesinger et al., 2012) Ma. Williams and Pathare (2013) reproduced two ages for North Ray crater: 58.9±11 Ma through crater counting and 57.2±11 Ma using the model based on the terrestrial fireballs. The similarity of both methods of age estimation demonstrates that crater density chronometry systems can be applied to date young surfaces on the Moon using small diameter craters and small areas (Williams and Pathare, 2013).

Another approach to estimate the upper bound on the ages of the IMPs is to make comparisons with the onset diameters of equilibrium (Gault, 1970; Soderblom, 1970) for surfaces with constrained ages. The CSFDs of older surfaces have equilibrium populations at larger diameters. For example, the CSFD for Mare Tranquillitatis near the Sosigenes IMP is in equilibrium at D <290 m (model age ~3.5 Ga) (Hiesinger et al., 2003). Crater counts of Tycho ejecta (area=1.65 km^2) show a model age of ~85 Ma with the equilibrium population at crater diameters of <12 m, while CSFDs of the older Copernicus ejecta blanket (area=121 km^2) produce a model age of ~797 Ma and are in equilibrium at D <70 m (Hiesinger et al., 2012). No clear equilibrium population is visible within the IMP smooth unit CSFDs measured down to the limit of crater resolution (8 m). This indicates that for craters at D >10 m the smooth units of the IMPs are still in production (new impact craters do not destroy older craters). The IMPs are still in production while Tycho ejecta is in equilibrium at D<12 m, thus the approximate age of Tycho (~85 +15/-18, ~124 Ma +12/-12 (Hiesinger et al., 2012), 109±4 Ma (Drozd et al., 1977)) thus we adopt an upper bound on the age of the IMP smooth units of ~100 Ma.

The CSFDs of the uneven units compared to the smooth units show a deficiency of <20-25 m craters, which suggests a difference in crater retention between the smooth and uneven units. This difference is possibly due to varying target properties (Schultz et al., 1977; van der Bogert et al., 2013) since the uneven unit is made up of more bouldery, fragmented material. The craters on the IMPs have diameters that likely depend on strength-scaling, rather than gravity-scaling (van der Bogert et al., 2013) that may cause a difference in the CSFDs between the smooth and uneven units. For instance, the same size bolide may cause a different sized impact depending on the target properties. If the target properties of the uneven unit are biasing the CSFDs, then the uneven units are likely the same age as the smooth units. A similar age

between the smooth and uneven units was previously suggested by El-Baz (1972) and Garry et al. (2012).

5.5.2 Interpretation of smooth unit as lava flows

Measured smooth unit thickness (n=143, average=8 meters, range=2-20 m) were compared to mare basalt flow thickness recorded in the literature. While LROC DTMs were available for measuring elevation differences in this work, previous studies used a variety of methods to estimate mare basalt flow unit thickness. Howard et al. (1972) measured layering interpreted as basalt flows 10-20 m in thickness (from Apollo 15 surface images) in small outcrops along the west wall of Hadley Rille. Schaber (1973) used orbital images to estimate the average thickness of the surface flows in Mare Imbrium at 30-35 m with a range of 10-63 m. Brett (1975) performed chemical kinetic calculations for 14 Apollo basalts to estimate a thickness of <8 m for cooling units. Gifford and El-Baz (1981) measured 19 flow scarps <20 m thick from near-terminator Lunar Orbiter and Apollo orbital photographs. Robinson et al. (2012) identified and measured layers in lunar mare pits and impact craters to be ~10 m thick (range 2-14 m) and interpreted the layers to be single lava flow thicknesses. Enns and Robinson (2013) measured the thickness of exposures interpreted as lava flows in 50 fresh craters visible in high-resolution (~0.5 meters pixel scale) LROC images to be between 6-25 m with an average of 15 ± 5m. The average smooth unit thickness from IMPs (8 m) was more consistent with the work of Brett (1975), Robinson et al. (2012), and Enns and Robinson (2013) than the larger average thickness measurements from Howard et al. (1972), Schaber (1973), and Gifford and El-Baz (1981). However, the range of IMP smooth unit thickness (2-20 m) overlapped with the range of measurements reported by Schaber (1973) and Howard et al. (1972). Overall, the smooth unit thickness measurements from IMPs were consistent with the

range of thickness reported in the literature for single layers of lunar mare basalt flows. Based on the morphology, reflectance, and thickness measurements, the smooth units are interpreted here as mare basalt flows.

5.5.3 Topography and Age

Previous studies investigated the relationship between surface age and slope, usually in the context of the degradation of impact craters over time (e.g. Arvidson et al., 1975; Craddock and Howard, 2000; Rosenburg et al., 2011; Fassett, 2013). Two main processes contribute to degradation of slopes on the lunar surface: steady erosion through meteorite bombardment and downslope movement caused by gravity. Overall, younger impact crater walls should have steeper slopes (>30-35°) than older crater walls due to erosion. At the time of emplacement, the impact crater wall has an initial slope at or above the angle of repose (if the impact crater formed in solid rock). The angle of repose (30°-35°) of a granular material is the steepest angle (relative to a horizontal plane) at which the material is at rest (stable) and is primarily a function of grain roughness, angularity, and sorting (Allen, 1969, 1970; Carrigy, 1970) and is independent of gravity (Carson and Kirkby, 1972; Melosh, 2011, p.327; Atwood-Stone and McEwen, 2013). Slopes significantly greater than 36° are associated with blocky outcrops and not granular material, so it is thought that the angle of repose is close to 35° on the Moon (Wagner et al., 2013).

Observations of slopes within six IMPs indicate that four out of six IMPs have slopes comparable to those observed in the young Copernican (ranging from ~100 Myr to ~10 Myr in age) impact crater walls, which is consistent with the CSFD model ages showing that the IMPs are <100 My old. However, the IMPs at the Cauchy-5 dome and Manilus-1 have smooth unit flow margins with slopes <30°. The model age of the IMP at the Cauchy-5 dome is older (58±3.6 Ma) than Ina and the Sosigenes

IMP (Figure 5.5), which may account for the lower slopes, however it is unlikely that more degradation of the slopes would occur over a small period of time. Alternatively, the lower spatial resolution of the DTM may result in shallower measured slopes since steeper slopes at scales below the resolution would not be resolved. While slopes from 30-35° are indicative of a young (Copernican) age, shallow slopes do not rule out a young age since lava flows may in some cases initially be emplaced with shallower flow margins. An alternative interpretation is that the Cauchy-5 IMP is >100 My old, however it is likely still Copernican in age since the surface has not been heavily disrupted by impact craters. Appropriate NAC images (incidence angle >70°) for crater counting at the Manilus-1 IMP were not available at the time of this study.

The Imbrium slope and thickness data provide an example of a basaltic flow front for comparison to the IMPs, however the Imbrium flows are Eratosthenian, not Copernican, in age. The Imbrium flows are 2.5 +/- 0.3 Ga old (Schaber, 1973), thus the slopes on the flow fronts were expected to be <30° due to slope degradation over time. The Imbrium flow fronts have slopes from 2-13° and flow thickness from 12-36 m. The range of slopes and thickness indicates local variation within the same flow, and the data also showed a correlation between flow thickness and flank slope (Figure 5.10). The relatively shallow slopes on the Imbrium flows are consistent with an age much older than the IMPs. The extent (height and thickness) of the Imbrium flows is much larger than the flows within the IMPs, thus it will take longer for degradational processes to erode the flow, allowing the Imbrium flows to be visible from orbit for much longer timescales (Figure 5.12). The larger volume of the Imbrium flows also suggests that the emplacement conditions were significantly different at the Imbrium flows compared to the IMPs, implying that the initial slopes were created under different eruption conditions.

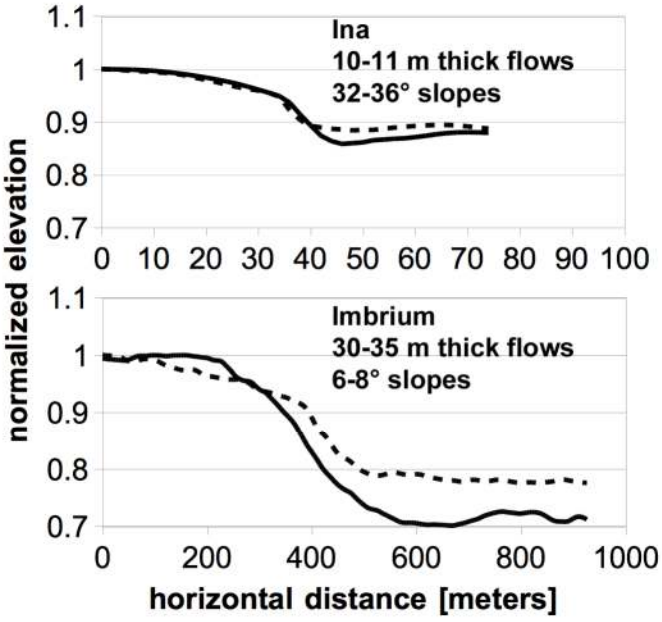

Figure 5.12: A comparison of the smooth unit margins from Ina compared to the Imbrium flows. Each profile is normalized to the maximum elevation. Note that the distance in horizontal axis is 10× greater for the Imbrium plot than the Ina plot. While the smooth units in Ina are three times thinner than the Imbrium flows, however the slopes are more than three times steeper than the Imbrium flows. This is consistent with a younger age for Ina than for the Imbrium flows.

5.5.4 Formation mechanism

For Ina we propose sequence of events that accounts for its formation and is applicable to the other IMPs. Initially a vent was extruding magma onto the surrounding area, forming the observed low-relief shield. Then drainage of the vent occurred, causing the level of magma to decrease in elevation, fracturing and disrupting the crust of lava ponded in the vent. This disrupted crust of mare basalt formed the uneven unit. This interpretation of the uneven unit is consistent with the units spectral signal, which is similar to lunar mare basalt units (Figure 5.11). Magma near the current rim flowed back, draining into the new depression, creating the sections of smooth unit flows connected to the rim (Figure 5.13). Next, the interior smooth unit

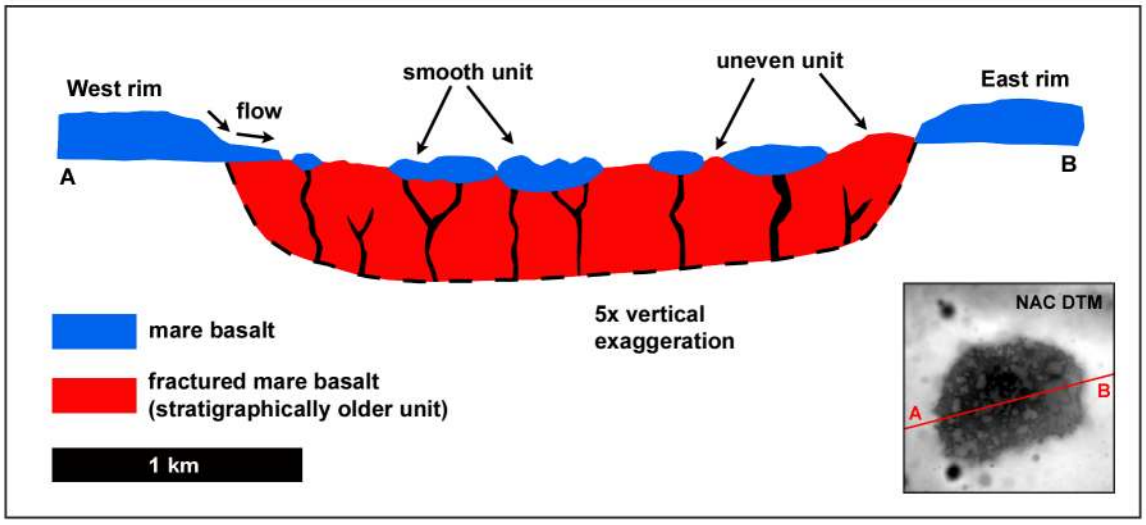

Figure 5.13: Cross section of Ina. Based on the elevation profile across the caldera as seen in the inset (NAC DTM).

flows formed as small volumes of magma extruded through the fractured uneven unit (Figure 5.13). The collapse depression decreases in elevation toward the center, and the flow direction of the smooth unit flows is generally towards the center (Figure 5.6). There are many locations where the topography of the uneven unit provided a topographic barrier to the flow of the smooth unit extrusions (Figure 5.6). Timing of the collapse and final stage eruption of the smooth unit flows was likely on the order hours or days.

This formation sequence is most consistent with the stratigraphic interpretation of El-Baz (1973), who proposed a formation due to collapse in the center of the low shield, with the subsequent extrusion of the "bulbous structures in the caldera floor." El-Baz (1973) suggested that the structures in the floor of Ina were domes with individual volcanic collapse craters; the formation of flows connected to Inas rim were not discussed. Images of Ina at scales of 25 cm/pixel were examined for inflation cracks, and no inflation cracks are seen on any of the other smooth units within the other IMPs studied in this paper suggesting that lava flow inflation (as described in

Garry et al., 2012) may not have been the primary mechanism for the formation of the IMPs.

The uneven unit formed from disruption of a lava pond basalt crust due to collapse, producing a blocky, broken layer. The scale of collapse at the vent (as in the cases of Ina, the Sosigenes IMP, and Hyginus) likely varies from vent-to-vent depending on local conditions thus the local caldera relief, size and planform for each IMP varies. At the Carrel-1 IMP (Figure 5.2d) the final extrusion of mare basalt covered most of the vent (and the uneven unit), however the relatively small section of uneven unit (a previous topographic high) remained uncovered. Lobate flow fronts are visible where the smooth unit flows contact the uneven unit, marking the stratigraphic relationship between the mostly covered uneven unit and mare basalt flows (Figure 5.2d).

Some of the IMPs are associated with pyroclastic deposits caused by explosive volcanism such as those found within the floor of the Hyginus caldera (7.73°N, 6.35°E) (Schultz, 1976; Hawke and Coombs, 1987; Wilson et al., 2011). Explosive volcanism is not a requirement for the formation of the IMPs in the model presented here although associated pyroclastic eruptions may have occurred at some or all of the IMPs. The excavation of a thick layer of regolith or pyroclastic material through explosive volcanism proposed by Schultz et al. (2006) as a hypothesis for the morphology of the Ina uneven unit is not consistent with the observations presented here. The uneven unit is stratigraphically older than the smooth units, while the explosive volcanism model from Schultz et al. (2006) implies the uneven unit is younger than the smooth units. The smooth unit does not appear to be modified by an explosive event since there are no blocks or signs of pyroclastic blanketing on any of the smooth unit flows.

The formation mechanism of the IMPs is fundamentally different from that of the mercurian hollows. Evidence suggests that mercurian hollows form as volatiles were released from the regolith due to either space weathering and solar heating or

perhaps contact heating by intrusions (Blewett et al., 2013). The volatiles may have originated as volcanic material that condensed onto the surface or in the subsurface and then were buried by volcanic deposits (Blewett et al., 2013). Later impact events then exposed the buried volatile material (Blewett et al., 2013). There is no evidence that a similar mechanism was responsible for the lunar IMPs.

5.5.5 Implications for lunar thermal evolution

We interpret the IMPs as late-stage mare volcanic vents (<100 Ma), occurring significantly after the majority of mare basalt eruptions thus providing an important constraint for the cooling rate of the lunar mantle. Shearer et al., 2006 stated that uncertainties in the duration and volume of mare magmatism made it difficult to use the range of mare basalt ages as a constraint on thermal models. Here we suggest that any valid thermal model must account for small volume eruptions through the Copernican period. This assumes that all the IMPs are contemporaneous with the subset of IMPs for which CSFD-derived model ages were caluclated. The IMPs are not extensive in terms of volume, but they are widely spread across the nearside maria (Figure 5.1). This distribution implies a significant source of heating persistent through the Copernican period for the central nearside coincident with the PKT. The high abundance of heat-producing elements (Th, U, and K) in the KREEP-rich material beneath the PKT could provide heating through radioactive decay required to produce partial melt in the lunar interior (Wieczorek and Phillips, 2000). The Tranquillitatis IMPs are outside the boundaries of the PKT (Jolliff et al., 2000) and may thus show that the materials at depth responsible for the surface expression of the PKT actually extend further to the southeast. The characteristic >3.5 ppm thorium signal of the PKT (Jolliff et al., 200) is likely masked by the Tranquillitatis mare, including the large shield volcano proposed in Spudis et al. (2013).

5.6 Conclusions

The discovery of Ina (Whitaker, 1972; El-Baz, 1972) and other IMPs (Schultz, 1976, 2006) indicated the possibility of Copernican volcanism. With new data from recent lunar orbiters the investigation into the origins and characteristics of young mare basalt volcanism has continued (e.g. Stooke, 2012). The morphology and units found in Ina are much more common than previously thought, now with 75 documented IMPs (from 100 to 5000 meters in the largest dimension) in the nearside lunar maria. Data used in this study of IMPs includes NAC nadir-pointing images with large and small incidence angles, WAC multispectral observations, and DTMs derived from NAC stereo pairs. Methods used within this work include crater age-dating using CSFDs to calculate model ages, comparisons of slopes with young terrains and other lunar basalt flows, and multispectral analysis. The following properties of the IMPs were determined from these analyses:

1. Newly discovered Ina-style volcanic features known as IMPs are dispersed across the central nearside, with occurrences in Mare Tranquillitatis over to Aristarchus crater and up to the Gruithuisen region and may represent the extent of the KREEP source regions.

2. The uneven units are stratigraphically older than the smooth units and formed as the Ina caldera collapsed and fractured the preexisting basalt.

3. The smooth units within the IMPs are volcanic in origin based on their occurrence in mare basalt, spectral signature, association with volcanic structures and effusive deposits (such as mare domes and shield volcanoes), and the interpretation of the smooth unit topography as evidence for single layer smooth unit mare flows.

4. Crater counts of smooth units at three locations give model ages ranging from 18-58 Ma, which are interpreted as a range of minimum ages, consistent with the sharp morphologic contacts between the smooth and uneven units.

5. Comparisons with small crater equilibrium populations for Tycho and Copernicus ejecta blankets suggest that the smooth units are younger than ∼100 Ma.

6. Topographic comparisons with Tycho, Giordano Bruno, Larmor Q, Moore F, and Lichtenberg crater suggest that Ina, Hyginus, and the Sosigenes Depression are <100 Ma old.

7. While the uneven units have fewer craters per unit area compared to the smooth units, the CSFDs overlap at crater diameters >20-25 m, which indicates the discrepancy at smaller diameters is simply a difference in target properties and not age.

The IMPs were formed as small basaltic eruptions and are estimated to be <100 Ma in age, which is significantly younger than previous estimates for the end of lunar mare basalt volcanism (∼1-1.2 Ga (e.g. Schultz and Spudis, 1983; Hiesinger et al., 2003, 2011; Borg et al., 2004). The young ages have implications for the models of lunar thermal evolution, which must provide enough heat to account for small volume eruptions late into the Copernican period. No samples of volcanic material with comparable age have been radiometrically age-dated. The youngest lunar basalts measured through radiometric age dating to-date are Apollo mare basalts ∼3.1 Ba (e.g. Ryder and Taylor, 1976; Ryder and Spudis, 1980; BVSP, 1989), and the lunar meteorite NWA 773, at ∼2.8 Ma (Borg et al., 2004). Sample return from Ina or one of the other major IMPs should be added to the list of critical materials to be returned from the Moon for radiometric age dating.

Chapter 6

CONCLUSION

The chapters of this dissertation had a common goal: to use recent spacecraft data to expand upon the current knowledge of lunar volcanisms diversity and the fundamental difference between the surface environments on the Moon and Mercury. This study of diverse lunar volcanism and regolith optical maturation rates on the Moon and Mercury leveraged new data from the LROC and MESSENGER missions to both confirm and challenge previously held hypotheses in planetary science.

Chapter 2 described the process and datasets used in the absolute radiometric calibration of the LROC WAC and NAC cameras. While the in-flight radiometric calibration is only a small portion of the entire image calibration process, it is an important contribution and an improvement on the pre-flight, laboratory-derived calibration coefficients. Absolute radiometric calibration of the two cameras was essential before the WAC and NAC images could be compared to other datasets, such as images from the MESSENGER WAC in orbit around Mercury.

Chapter 3, Relative Optical Maturation Rates of Regolith on Mercury and the Moon, took the next step and compared data from the LROC WAC (565 nm band) and the MESSENGER WAC (560 nm band) to observe young crater populations in an effort to quantify differences in space weathering rates on both bodies. Previous studies modeled that the rate of space weathering and therefore regolith optical maturation should be higher on Mercury than on the Moon (Hapke, 1977; Cintala, 1992; Hapke, 2001; Noble and Pieters, 2003). How could models of faster regolith maturation on Mercury compared to the Moon be tested using remote sensing observations from LROC and MESSENGER? The similar wavelengths of the two WAC cameras

provided the required observations to measure the areal density of the youngest crater populations, the reflectance of the ejecta materials, and the length of the crater rays relative to the crater diameter. A combination of three additional ideas yielded a quantitative estimate of the relative regolith optical maturation rate on Mercury compared to the Moon: 1) crater maturity rays decrease in reflectance over time due to space weathering, 2) the inherent link between the degradation state of craters and chronostratigraphic periods, and 3) the connection between the modeled impact flux rate over the past ∼3 Ga and the crater populations on the surface. Using the new empirical measurements of crater density, the chapter presented the following narrative and primary conclusions. There are 2 times fewer Kuiperian craters per unit area on Mercury than Copernican craters per unit area on the Moon. Initially equating the duration of the Copernican and Kuiperian periods, models for the impact flux of near-Earth objects (Le Feuvre and Wieczorek, 2008, 2011; Greenstreet et al., 2012) and the observed counts of Kuiperian and Copernican impact craters disagreed by a factor of ∼4. A faster rate of optical maturation on Mercury than on the Moon accounted for the deficit of Kuiperian craters on Mercury since faster regolith maturation on Mercury causes maturity rays to fade faster than they would on the Moon. A consequence of this explanation is that optical maturation on Mercury is up to 4 times faster than on the Moon. This faster rate of optical maturation shortened the duration of the Kuiperian period relative to the Copernican, based on the definition of the youngest chronostratigraphic periods from the persistence of crater maturity rays (Shoemaker and Hackman, 1962; Spudis and Guest, 1988). The average photometrically normalized reflectance of immature lunar highland material is a factor of 1.9±0.4 higher than the reflectance of immature material on Mercury. The average mercurian surface reflectance was known to be less than the average lunar highlands reflectance, however prior to the MESSENGER mission it was not known if this was

due primarily to an increased space weathering environment at Mercury (causing an increase in the amount of regolith maturation) or compositional differences between the lunar highlands and Mercury. Assuming that the immature materials have a minimal amount of exposure to space weathering, the difference in reflectance of immature materials is likely primarily caused by differences in composition between the lunar highlands and average Mercury surface material, a finding consistent with those of previous work (Denevi and Robinson, 2008; Nittler et al., 2011; Weider et al., 2012). The chapter also presented measurements of the length and number of immature crater rays on Mercury and the Moon. Differences in the ratio of ray length to crater diameter between Mercury and the Moon might be expected due to faster optical maturation on Mercury, but no significant differences were detected. There were five craters with higher ratios of ray length to crater diameter than the rest of the rayed crater populations: Giordano Bruno and Byrgius A on the Moon, and Debussy, Xiao Zhao, and Qi Baishi on Mercury. Previous work on the properties of crater rays and ejecta suggests that the youngest craters should have higher ratios of ray length to diameter, assuming ray thickness decreases with the distance from the crater rim (Melosh, 1989; Hörz et al., 1991; Grier et al., 2001). Thus, Qi Baishi, Xiao Zhao, and Debussy are among the youngest rayed craters on Mercury. The rays of these craters can be used as stratigraphic clues to determine the relative ages of surrounding geologic units. Future observations from MESSENGER will provide data from MASCS (Mercury Atmospheric and Surface Composition Spectrometer) to examine the spectra of Kuiperian crater rays and ejecta, and 10-band MDIS WAC observations of the most immature craters specifically targeted in an effort to detect a 1-micron iron feature.

Chapter 4, The Gruithuisen Domes: Age and Morphology of Silicic Nonmare Volcanism, returned the focus of the dissertation to the Moon through the examination of

relatively rare ancient silicic lunar volcanism. The Gruithuisen Domes were confirmed to be silicic in composition by recent Diviner data (Greenhagen et al., 2010), although some studies previously suggested that the domes were silicic based on morphology alone (Smith, 1973; Malin, 1974; Head and McCord, 1978; Wagner et al., 2002; Wilson and Head, 2003). Fragments of silcic, nonmare rock types exist in the Apollo sample collection and the Gruithuisen Domes are a candidate source region for these fragments (e.g. Jolliff et al., 1991, 1998; Korotev, 1998; Papike et al., 1998). Ancient silicic lunar rock types, which make up nonmare domes like the Gruithuisen Domes, may have been more prevalent in lunar history (Chevrel, 1999). The chapter focused on understanding the detailed morphology of the domes to determine eruption properties of the magma, the composition of the domes, and explaining the distribution of the high-silica signal in the Diviner data. The chapter included a combination of methods using LROC data (NAC and DTMs) and quantitative comparisons with terrestrial silicic dome morphologies, leveraging extensive previous work on the eruption behavior of viscoplastic silicic magmas on Earth (Blake, 1990; Griffiths and Fink, 1997; Fink and Griffiths, 1998). Data from Diviner, the Lunar Prospector Gamma Ray Spectrometer, Clementine, and the LROC WAC were also used to answer questions about the age, composition and morphology of the Gruithuisen Domes. Crater size-frequency distributions gave a model age of 3.60 +0.06/-0.09 Ga for all summit plateau areas on the Gamma and Delta domes, which was at the younger end of the age estimates from Wagner et al. (2002). The model ages presented here are an improvement upon the work of Wagner et al. (2002) since the 2 m/px DTM enabled for a more restrictive selection of the count area to only areas on the summit plateaus with shallow slopes ($< 2°$), and an increase in image resolution (Wagner et al. (2002) used $\sim$60 m/px Lunar Orbiter data). Areas indicating high silica in the Diviner data are associated with relatively fresh craters and steep slopes, which is consistent with

immature dome material being uncovered or excavated in those areas. The Gamma and Delta domes are at the critical height expected for domes with a rhyolitic composition (versus an andesitic or dacitic composition). The NW dome has a higher aspect ratio compared to the other two domes, and a smaller areal extent, which suggests that the magma had a higher viscosity and possibly a higher crystal content at the time of eruption. The domes formed through effusive volcanic processes as indicated by the original volcanic topography of ridges parallel to the flow direction (radial from the center of the domes, not compressional). Sample return is required to determine the lithology of the Gruithuisen Domes, understand the composition of the domes in relation to the magmatic evolution on the Moon. Obtaining samples of the Gruithuisen Domes is key to understanding the full suite of lunar volcanic material.

Chapter 5 introduced a new kind of lunar feature: the small, morphologically sharp irregular mare patches (IMPs) which are consistent with recent lunar volcanism widely distributed across the nearside lunar maria. The existence of Copernican, <100 Ma basaltic volcanism has implications for long-lived nearside magmatism and models of lunar thermal evolution. Enough heat must be produced in the lunar mantle for a long enough period of time, likely through the radiogenic heating, to account for small volume eruptions late into the Copernican period. No samples of volcanic material with comparable ages have been radiometrically age-dated. The youngest lunar basalts measured through radiometric age dating to-date are Apollo mare basalts ~3.1 Ga (e.g. Ryder and Taylor, 1976; Ryder and Spudis, 1980; BVTP, 1989), and the lunar meteorite NWA 773, at ~2.8 Ma (Borg et al., 2004). Reported ages based on both sample ages and remote sensing studies have lunar mare basalt volcanism starting at ~3.9-4.0 Ga and ceasing at ~1-1.2 Ga (e.g. Schultz and Spudis, 1983; Hiesinger et al., 2011; BVTP, 1989). Crater counts of IMP smooth units at three locations gave model ages ranging from 18-58 Ma, which is significantly more

recent than previous estimates for the end of lunar basaltic volcanism. Comparisons with small crater equilibrium populations for Tycho and Copernicus ejecta blankets suggest that the smooth units are <100 Ma. Additional topographic comparisons with Copernican impact crater morphologies crater suggest that a subset of the IMPs (for which topographic data is available) are <100 Ma old. These model ages are consistent with the sharp morphologic contacts between the smooth and uneven units at each of the IMPs. The topography of the smooth units was consistent with single layer mare flows, and the stratigraphically older uneven units (a stratigraphic relationship common to all IMPs) are interpreted as fractured mare basalt. 75 IMPs between 100-5000 meters in the largest dimension were documented in NAC images and digital topographic models. Further study of a subset of the larger IMPs which are visible in the multispectral Wide Angle Camera determined that the smooth and uneven units were both consistent with basaltic material. A model of vent collapse, basaltic crust fracturing, magma backflow into the vent collapse depression, and the subsequent extrusion of small-volume flows summarizes the formation mechanism for the IMPs. Future work on the IMPs includes continuing LROC targeting efforts to collect an ever increasing set of observations for each IMP. While the initial identification of an IMP within a NAC image frame is excellent, other analyses are enabled by targeting observations with large incidence angles ($> 70°$) for crater counting, NAC stereo pairs for creating digital topographic models, and low incidence angle images for measuring surface reflectance. A high priority is crater counting at additional IMPs to better estimate ages and understand the range of ages within the population. Eventually, a sample return from one of the larger IMPs is required for radiometric age dating to confirm the age estimates determined in this dissertation.

From comparing reflectance measurements of various lunar observations for calibrating in-flight cameras to cross-planet studies of young impacts and silicic volca-

noes, this dissertation was built upon the principles of comparative planetology and the spirit of discovery. The identification of new and widely spatially distributed IMPs through the NAC images was a great opportunity to look at the Moon and lunar geologic history with renewed perspective. The IMPs' young age proposed here refined the understanding of lunar thermal history and confirmed that lunar volcanism did not end abruptly with the end of the eruption of the maria, but rather decreased gradually over time. Our view of the Moon has changed once again.

> We shall not cease from exploration
> And the end of all our exploring
> Will be to arrive where we started
> And know the place for the first time.

- T.S. Eliot, Four Quartets

REFERENCES

Adams, J.B., Jones, R.L., 1970. Spectral reflectivity of lunar samples. Science 167, 737-739, doi:10.1126/science.167.3918.737.

Adams, J.B., McCord, T.B., 1971. Optical properties of mineral separates, glass, and anorthositic fragments from Apollo mare samples. Proc. Lunar Sci. Conf. 2, 2183-2195.

Adams, J.B., McCord, T.B., 1977. Mercury: Evidence for an anorthositic crust from reflectance spectra. Bull. Amer. Astron. Soc. 9, 457.

Alhajjah, A., Pandey, D.K., Paden, J., Priestley, K.J., Lee, R.B., Wilson, R.S., Thomas, S., 2004. Calibrations of the Clouds and the Earth's Radiant Energy System (CERES) instruments on the Terra and Aqua spacecrafts. Proc. SPIE, 5232, 604. Remote Sensing for Agriculture, Ecosystems, and Hydrology V. Edited by Owe, Manfred; D'Urso, Guido; Moreno, Jose F.; Calera, Alfonso. Proceedings of the SPIE, Volume 5232, pp. 604-615 (2004).

Allen, J.R.L., 1969. The maximum slope-angle attainable by surfaces underlain by bulked equal spheroids with variable dimensional ordering. Geol. Soc. Am. Bull. 80, 1923-1930, doi: 10.1130/0016-7606(1969)80[1923:TMSABS]2.0.CO;2.

Allen, J.R.L., 1970. The avalanching of granular solids on dune and similar slopes. J. Geol. 78, 326-351.

Allen, C.C., Morris, R.V., Lauer Jr., H.V., McKay, D.S., 1993. Microscopic iron metal on glass and minerals - A tool for studying regolith maturity. Icarus 104, 291-300, doi:10.1006/icar.1993.1102.

Anderson, J.M., Becker, K.J., Kieffer, H.H., Dodd., D.N., 1999. Real Time Control of the Robotic Lunar Observatory Telescope. Publications of the Astronomical Society of the Pacific 111, 737-749.

Anderson, J.A., Sides, S.C., Soltesz, D.L., Sucharski, T.L., Becker, K.J., 2004. Modernization of the integrated software for imagers and spectrometers. Lunar Planet. Sci. 35, abstract 2039.

Archinal, B.A., Rosiek, M.R., Kirk, R.L., Redding, B.L., 2006. The Unified Lunar Control Network 2005, U.S. Geological Survey Open-File Report 2006-1367, URL: http://pubs.usgs.gov/of/2006/1367/

Arvidson, R., Drozd, R.J., Hohenberg, C.M., Morgan, C.J., Poupeau, G., 1975. Horizontal transport of the regolith, modification of features, and erosion rates on the lunar surface. The Moon 13, 67-79.

Ashley, J.W., et al., 2012. Geology of the King crater region: New insights

into impact melt dynamics on the Moon. J. Geophys. Res. 117, E00H29, doi:10.1029/2011JE003990.

Atwood-Stone, C., McEwen, A.S., 2013. Avalanche slope angles in low-gravity environments from active martian sand dunes. Geophys. Res. Lett. 40, 2929-2934, doi:10.1002/grl.50586.

Basaltic Volcanism Study Project, 1981. Basaltic Volcanism on the Terrestrial Planets. Pergamon Press, Inc., New York. 1286 pp.

Basilevsky, A.T., 1976. On the rate of evolution of small lunar craters. Proc. Lunar Sci. Conf. 7, 32-34.

Behrmann, C., Grozaz, G., Drozd, R., Hohenberg, C., Ralston, C., Walker, R., Yuhas, D., 1973. Cosmic-ray exposure history of North Ray and South Ray material. Proc. Lunar Sci. Conf. 4, 1957-1974.

Bell, J.F., III, Wolff, M.J., James, P.B., Clancy, R.T., Lee, S.W., Martin, L.J., 1997. Mars surface mineralogy from Hubble Space Telescope imaging during 1994-1995: Observations, calibration, and initial results. J. Geophys. Res. 102, 9109-9123.

Bingham, E.C., 1916. An Investigation of the Laws of Plastic Flow. U.S. Bureau of Standards Bulletin 13, 309-353.

Blake, S., 1990. Viscoplastic models of lava domes. In: Fink, J.H. (Ed.), Lava Flows and Domes: Emplacement Mechanisms and Hazard Implications. IAVCEI Proc. Volcanology, vol. 2. Springer., pp. 88-128.

Blewett, D.T., Lucey, P.G., Hawke, B.R., Jolliff, B.L., 1997a. Clementine images of the lunar sample-return stations: Refinement of FeO and TiO_2 mapping techniques. J. Geophys. Res. 102, 16319-16325, doi:10.1029/97JE01505

Blewett, D.T., Lucey, P.G., Hawke, B.R., Ling, G.G., Robinson, M.S., 1997b. A comparison of mercurian reflectance and spectral quantities with those of the Moon. Icarus 129, 217-231, doi:10.1006/icar.1997.5785.

Blewett, D.T., Hawke, B.R., Lucey, P.G., 2002. Lunar pure anorthosite as a spectral analog for Mercury. Meteorit. Planet. Sci. 37, 1245-1254, doi:10.1111/j.1945-5100.2002.tb00893.x.

Blewett, D.T., et al., 2009. Multispectral images of Mercury from the first MESSENGER flyby: Analysis of global and regional color trends. Earth Planet. Sci. Lett. 285, 272-282, doi:10.1016/j.epsl.2009.02.021.

Blewett, D.T., et al., 2011. Hollows on Mercury: MESSENGER evidence for geologically recent volatile-related activity. Science 333, 1856-1859,

doi:10.1126/science.1211681.

Blewett, D. T., et al., 2013. Mercury's hollows: Constraints on formation and composition from analysis of geological setting and spectral reflectance. J. Geophys. Res. 118, 1013-1032, doi:10.1029/2012JE004174.

Boardman, J.W., et al., 2011. Measuring moonlight: An overview of the spatial properties, lunar coverage, selenolocation, and related Level 1B products of the Moon Mineralogy Mapper. J. Geophys. Res. 116, doi:10.1029/2010JE003730.

Borg L.E., Shearer, C.K., Asmerom, Y., Papike, J.J., 2004. Prolonged KREEP magmatism on the Moon indicated by the youngest dated lunar igneous rock. Nature 432, 209-211, doi:10.1038/nature03070.

Bottke, W.F. Jr., Morbidelli, A., Jedicke, R., Petit, J., Levison, H.F., Michel, P., Metcalfe, T.S., 2002. Debiased orbital and absolute magnitude distribution of the Near-Earth objects. Icarus 156, 399-433, doi:10.1006/icar.2001.6788.

Boyd A.K., Robinson, M.S., Sato, H., 2012. Lunar Reconnaissance Orbiter Wide Angle Camera Photometry: An empirical solution. Lunar Planet. Sci. 43, abstract 2795.

Braden, S.E., Robinson, M.S., 2011. Human exploration of the Gruithuisen Domes. GSA Special Papers 483, 507-518, doi: 10.1130/2011.2483(30).

Bray, V.J., et al., 2010. New insight into lunar impact melt mobility from the LRO camera. Geophys. Res. Lett. 37, L21202, doi: 10.1029/2010GL044666.

Brett, R., 1975. Thicknesses of some lunar mare basalt flows and ejecta blankets based on chemical kinetic data, Proc. Lunar Sci. Conf. 6, 1135-1141.

Bruno, B.C., Lucey, P.G., Hawke, B.R., 1991. High resolution UV-visible spectroscopy of lunar red spots, Lunar Planet. Sci. 21, 405-415.

Burns, K., Robinson, M.S., Speyerer, E., the LROC Science Team, 2011. Two years of digital terrain model production using the Lunar Reconnaissance Orbiter Narrow Angle Camera. American Geophysical Union, Fall Meeting, abstract P43D-1706.

Carrigy, M.A., 1970. Experiments on the angles of repose of granular materials. Sedimentology 14, 147-158, doi: 10.1111/j.1365-3091.1970.tb00189.x.

Carson, M.A., Kiriby, M.J., 1972. Hillslope Form and Process. Cambridge University Press, New York, 476 pp., Cambridge Geographical Studies.

Charette, M., McCord, T., Pieters, C., Adams, J., 1974. Application of remote spectral reflectance measurements to lunar geology and determination of Ti

content of lunar soils. J. Geophys. Res. 79, 1605-1613.

Chevrel, S.D., Pinet, P.C., Head, J.W., 1999. Gruithuisen domes region: A candidate for an extended nonmare volcanism unit on the Moon. J. Geophys. Res. 104, 16515-16529, doi:10.1029/1998JE900007.

Cintala, M.J., 1992. Impact-induced thermal effects in the lunar and mercurian regoliths. J. Geophys. Res. 97, 947, doi:10.1029/917JE0220.

Cloutis, E.A., Sunshine, J.M., Morris, R.V., 2004. Spectral reflectance compositional properties of spinels and chromites: Implications for planetary remote sensing and geothermometry. Meteorit. Planet. Sci. 39, 545-565, doi:10.1111/j.1945-5100.2004.tb00918.x.

Cloutis, E.A., McCormack, K.A., Bell III, J.F., Hendrix, A.R., Bailey, D.T., Craig, M.A., Mertzman, S.A., Robinson, M.S., Riner, M.A., 2008. Ultraviolet spectral reflectance properties of common planetary minerals. Icarus 197, 321-347.

Conel, J.E., 1969. Infrared emissivities of silicates: Experimental results and a cloudy atmosphere model of spectral emission from condensed particulate mediums. J. Geophys. Res. 74, 1614-1634.

Crisp, D. 2000. Atmospheric Scattering and Continuum Absorption. In Allen's Astrophysical Quantities. p.265

Davies, M.E., Dwornik, S.E., Gault, D.E., Strom, R.G., 1978. Atlas of Mercury, U.S. Govemment Printing Office, NASA SP-423, Washington, D.C., 128 pp.

Denevi, B.W., Robinson, M.S., 2008. Mercury's albedo from Mariner 10: Implications for the presence of ferrous iron. Icarus 197, 239-246, doi:10.1016/j.icarus.2008.04.021.

Denevi, B.W., et al., 2009. The evolution of Mercury's crust: A global perspective from MESSENGER. Science 324, 613-618, doi:10.1126/science.1172226.

Denevi, B.W., Robinson, M.S., Sato, H., McEwen, A.S., Hapkie, B.W., 2011. LROC WAC Ultraviolet Reflectance of the Moon, Lunar Planet. Sci. 42, abstract 2304.

Denevi, B.W., et al., 2012. Physical constraints on impact melt properties from Lunar Reconnaissance Orbiter Camera images. Icarus 219, 665-675, doi: 10.1016/j.icarus.2012.03.020.

Denevi, B.W., Robinson, M.S., Boyd, A.K., Sato, H., Hapke, B.W., Hawke, B.R., 2013. Characterization of space weathering from Lunar Reconnaissance Orbiter Camera ultraviolet observations of the Moon. submitted for publication.

de Silva, S.L., Self, S., Francis, P.W., Drake, R.E., Ramirez, R.C., 1994. Effusive silicic volcanism in the central Andes: The Chao dacite and other young lavas of the Altiplano-Puna volcanic complex. J. Geophys. Res. 99, 17805-17826, doi:10.1029/94JB00652.

Domingue, D.L., et al., 2011. Photometric correction of Mercury's global color mosaic. Planet. Space Sci. 59, 1873-1887, doi:10.1016/j.pss.2011.03.014.

Domingue, D.L., Murchie, S.L., Denevi, B.W., Chabot, N.L., 2013. MESSENGER's Mercury Global Color Mosaic: Photometric Update. Lunar Planet. Sci. MMXIII, Abstract 1324.

Drozd, R.J., Hohenberg, C.M., Morgan, C.J., Ralston, C.E., 1974. Cosmic-ray exposure history at the Apollo 16 and other lunar sites: Lunar surface dynamics, Geochim. Cosmochim. Acta 38, 1625-1642, doi:10.1016/0016-7037(74)90178-1.

Drozd, R.J., Hohenberg, C.M., Morgan, C.J., Podosek, F.A., Wroge, M.L., 1977. Cosmic-ray Exposure History at Taurus-Littrow, Proc. Lunar Sci. Conf. 8, pp. 3027-3043.

El-Baz, F., 1972. New geological findings in Apollo 15 photography. Proc. Lunar Sci. Conf. 3, pp. 39-61.

El-Baz, F., 1973. Apollo 17 Preliminary Science Report, NASA SP-330, p. 30-13 to 30-17.

Eliason, E., Isbell, C., Lee, E., Becker, T., Gaddis, L., McEwen, A.S., Robinson, M.S., 1999. Mission to the Moon: The Clementine UVVIS global lunar mosaic, PDS Volumes USA_NASA_PDS_CL_4001 through 4078, produced by the U.S. Geological Survey and distributed on CD media by the Planetary Data System.

Elphic, R.C., Lawrence, D.J., Feldman, W.C., Barraclough, B.L., Maurice, S., Binder, A.B., Lucey, P.G., 1998. Lunar Fe and Ti Abundances: Comparison of Lunar Prospector and Clementine Data. Science 281, 1493-1496.

Elphic, R.C., et al., 2002. Lunar Prospector neutron spectrometer constraints on TiO_2. J. Geophys. Res. 107(E4).

Enns, A.C., Robinson, M.S., 2013. Basaltic layers exposed in lunar mare craters, Lunar Planet. Sci. 44, abstract 2751.

Evans, L.G., et al., 2012. Major-element abundances on Mercury: Results from the MESSENGER gamma-ray spectrometer. J. Geophys. Res. 117, E00L07, doi:10.1029/2012JE004178.

Fink, J.H., Griffiths, R.W., 1998. Morphology, eruption rates, and rheology of lava domes: Insights from laboratory models. J. Geophys. Res. 103, 527-545,

doi:10.1029/97JB02838.

Fischer, E.M., Pieters, C.M., 1994. Remote determination of exposure degree and iron concentration of lunar soils using VIS-NIR spectroscopic methods. Icarus 111, 475-488, doi:10.1006/icar.1994.1158.

Fischer, E.M., Pieters, C.M., 1996. Composition and exposure age of the Apollo 16 Cayley and Descartes regions from Clementine data: Normalizing the optical effects of space weathering. J. Geophys. Res. 101, 2225-2234, doi:10.1029/95JE02983.

Folguera, A., et al., 2009. Retroarc volcanism in the northern San Rafael Block (34° – 35°30'S) southern Central Andes: occurrence, age, and tectonic setting. J. Volcanol. Geotherm. Res. 186, 169-185.

Gaddis, L.R., Rosanova, C., Hawke, B.R., Coombs, C., Robinson, M.S., 1998. Small lunar pyroclastic deposits: A new global perspective. Lunar Planet. Sci. 29, abstract 1807.

Gaddis, L.R., Staid, M.I., Tyburczy, J.A., Hawke, B.R., Petro, N.E., 2003. Compositional analyses of lunar pyroclastic deposits. Icarus 161, 262-280.

Garry, W.B., et al., 2012. The origin of Ina: Evidence for inflated lava flows on the Moon. J. Geophys. Res., 117, E00H31, doi:10.1029/2011JE003981.

Gault, D.E., 1970. Saturation and equilibrium conditions for impact cratering on the lunar surface: Criteria and implications. Radio Science 5, 273-291, doi:10.1029/RS005i002p00273.

Gault, D.E., Guest, J.E., Murray, J.B., Dzurisin, D., Malin, M.C., 1975. Some comparisons of impact craters on Mercury and the Moon. J. Geophys. Res. 80, 2444-2460, doi:10.1029/JB080i017p02444.

Gellman, D.I., et al., 1993. Review of SPOT-1 and -2 calibrations at White Sands from launch to the present. Proc. SPIE, 1938, 118-125.

Gifford, A.W., F. El-Baz, 1981. Thicknesses of lunar mare flow fronts. Moon and the Planets 24, 391-398.

Giguere, T., Taylor, G.J., Hawke, B.R., Lucey, P.G., 2000. The titanium contents of lunar mare basalts. Meteoritics and Planetary Science 35, 193-200, doi:10.1111/j.1945-5100.2000.tb01985.x.

Gleiter, H., 1989. Nanocrystalline materials, Prog. Mater. Sci. 33, 223-315.

Glotch, T.D., et al., 2010. Highly silicic compositions on the Moon. Science 329, doi:10.1126/science.1192148.

Glotch, T.D., et al., 2011. The Mairan Domes: Silicic volcanic constructs on the Moon. Geophysical Research Letters, 38, doi:10.1029/2011GL049548.

Gold, T., 1955. The lunar surface. Mon. Not. R. Astron. Soc. 115, 585-604.

Green, R.O., et al., 2007. The Moon Mineralogy Mapper: Characteristics and early laboratory calibration results. Lunar Planet. Sci. 38, abstract 2354.

Greenhagen, B.T., et al., 2010. Global Silicate Mineralogy of the Moon from the Diviner Lunar Radiometer. Science 329, 1507-1509, doi:10.1126/science.1192196.

Gregg, T.K.P., Fink, J.H., 1996. Quantification of extraterrestrial lava flow effusion rates through laboratory simulations. J. Geophys. Res. 101, 16891-16900.

Greenstreet, S., Ngo, H., Gladman, B., 2012. The orbital distribution of Near-Earth objects inside Earth's orbit. Icarus 217, 355-366, doi:10.1016/j.icarus.2011.11.010.

Greig, J. W., 1927. Immiscibility in silicate melts. American Journal of Science 5, 13, 1-44.

Grier, J.A., McEwen, A.S., Lucey, P.G., Milazzo, M., Strom, R.G., 2001. Optical maturity of ejecta from large rayed lunar craters. J. Geophys. Res. 106, 32847-32862, doi:10.1029/1999JE001160.

Griffiths, R.W., Fink, J.H., 1993. Effects of surface cooling on the spreading of lava flows and domes. J. Fluid Mech. 252, 667-702.

Griffiths, R.W., Fink, J.H., 1997. Solidifying Bingham extrusions: a model for the growth of silicic lava domes. J. Fluid Mech. 347, 13-36, doi:10.1017/S0022112097006344.

Guenther, B., et al. 1996. MODIS calibration: A brief review of the strategy for the at-launch calibration approach. J. Atmos. Oceanic Tech. 13, 274, doi: 10.1175/1520-0426(1996)013<0274:MCABRO>2.0.CO;2.

Hagerty, J.J., Lawrence, D.J., Hawke, B.R., Vaniman, D.T., Elphic, R.C., Feldman, W.C., 2006. Refined thorium abundances for lunar red spots: Implications for evolved, nonmare volcanism on the Moon. J. Geophys. Res. 111, E06002, doi:10.1029/2005JE002592.

Hapke, B., Cohen, A., Cassidy, W., Wells, E., 1970. Solar radiation effects on the optical properties of Apollo 11 lunar samples. Proc. Apollo 11 Lunar Sci. Conf., 2199-2212.

Hapke, B., Cassidy, W., Wells, E., 1975a. Effects of vapor-phase deposition processes on the optical, chemical, and magnetic properties of the lunar regolith. The Moon 13, 339-353, doi:10.1007/BF00567525.

Hapke, B., Danielson, J., Klaasen, K., Wilson, L., 1975b. Photometric observations of Mercury from Mariner 10. J. Geophys. Res. 80, 2431-2443, doi:10.1029/JB080i017p02431.

Hapke, B., 1977. Interpretations of optical observations of Mercury and the Moon. Phys. Earth Planet. Inter. 15, 164-274, doi:10.1016/0031-9201(77)90035-8.

Hapke, B., 1993. Theory of Reflectance and Emittance Spectroscopy. Cambridge University Press, New York. 455pp.

Hapke, B., 2001. Space weathering from Mercury to the asteroid belt. J. Geophys. Res. 106, 10039-10073, doi:10.1029/2000JE001338.

Harris, D.L., 1961. Photometry and colorimetry of planets and satellites, in Planets and Satellites, edited by G. P. Kuiper and B. M. Middlehurst, pp. 272-342, University of Chicago Press, Chicago.

Hartmann, W.K., 1968. Lunar Crater Counts. VI: The Young Craters Tycho, Aristarchus, and Copernicus. Communications of the Lunar and Planetary Laboratory 7, 3, 145-156.

Haruyama, J., et al., 2008. Global lunar-surface mapping experiment using the Lunar Imager/Spectrometer on SELENE. Earth Planets Space 60, 243-255.

Haruyama, J., Ohtake, M., Matunaga, T., Morota, T., Honda, C., Yokota, Y., Ogawa, Y., LISM working group, 2009. SELENE (Kaguya) Terrain Camera observation results of nominal mission period. Lunar Planet. Sci. 40, abstract 1553.

Hawke, B.R., Coombs, C.R., 1987. Remote sensing studies of the Rima Hyginus region of the Moon. Lunar Planet. Sci. 18, p. 407.

Hawke, B.R., et al., 2004. The origin of lunar crater rays. Icarus 170, 1-16, doi:10.1016/j.icarus.2004.02.013.

Hawkins, S.E., et al., 2007. The Mercury Dual Imaging System on the MESSENGER spacecraft. Space Sci. Rev. 131, 247-338, doi:10.1007/s11214-007-9266-3.

Head J.W., 1976. Lunar volcanism in space and time. Rev. Geophys. Space Phys. 14, 265-300.

Head, J.W., Hess, P.C., McCord, T.B., 1978. Geologic characteristics of lunar highland volcanic domes (Gruithuisen and Mairan Region) and possible eruption conditions. Lunar Planet. Sci. IX, 488-490.

Head, J.W., McCord, T.B., 1978. Imbrian-Age highland volcanism on

the Moon: The Gruithuisen and Mairan domes. Science 199, 1433-1436, doi:10.1126/science.199.4336.1433.

Head, J.W., Gifford, A., 1980. Lunar mare domes: Classification and modes of origin. The Moon and the Planets 22, 235-258, doi:10.1007/BF00898434.

Head, J.W., Wilson, L., 1992. Lunar mare volcanism: Stratigraphy, eruption conditions, and the evolution of secondary crusts. Geochim. Cosmochim. Acta 56, 2155-2175.

Herrick, R.R., Curran, L.L., Baer, A.T., 2011. A Mariner/MESSENGER global catalog of mercurian craters. Icarus 215, 452-545, doi:10.1016/j.icarus.2011.06.021.

Hiesinger, H., Head, J.W., Wolf, U., Jaumann, R., Neukum, G., 2002. Lunar mare basalt flow units: Thicknesses determined from crater size-frequency distributions. Geophys. Res. Lett. 29, 89-1-89-4, doi:10.1029/2002GL014847.

Hiesinger H., Head, J.W., III, Wolf, U., Jaumann, R., Neukum, G., 2003. Ages and stratigraphy of mare basalts in Oceanus Procellarum, Mare Nubium, Mare Cognitum, and Mare Insularum. J. Geophys. Res. 108, 5065, doi:10.1029/2002JE001985.

Hiesinger, H., Head, J.W., Wolf, U., Jaumann, R., Neukum, G., 2011. Ages and stratigraphy of lunar mare basalts: A synthesis. GSA Special Papers 477, 1-51, doi:10.1130/2011.2477(01).

Hiesinger, H., van der Bogert, C.H., Pasckert, J.H., Funke, L., Gicomini, L., Ostrach, L.R., Robinson, M.S., 2012. How old are young lunar craters? J. Geophys. Res. 117, E00H10, doi:10.1029/2011JE003935.

Holsclaw, G.M., McClintock, W.E., Domingue, D.L., Izenberg, N.R., Blewett, D.T., Sprague, A.L., 2010. A comparison of the ultraviolet to near-infrared spectral properties of Mercury and the Moon as observed by MESSENGER. Icarus 209, 179-194, doi:10.1016/j.icarus.2010.05.001.

Hörz, F., Grieve, R., Heiken, G., Spudis, P., Binder, A., 1991. Lunar surface processes, in The Lunar Sourcebook: A User's Guide to the Moon, edited by G. Heiken, D. Vaniman, and B. French, pp. 61-120, Cambridge University Press, New York.

Housley, R., Grant, R., Paton, N., 1973. Origin and characteristics of excess Fe metal in lunar glass welded aggregates. Proc. Lunar Sci. Conf. 4, 2737-2741.

Howard, K.A., Head, J.W., Swann, G.A., 1972. Geology of Hadley Rille. Proc. Lunar Sci. Conf. 3, pp. 399-400.

Huppert, H.E., 1982. The propagation of two-dimensional and axisymmetric

viscous gravity currents over a rigid horizontal surface. J. Fluid Mech. 121, 43-58.

Huppert H.E., Shepherd, J.B., Sigurdsson, H., Sparks, R.S.J., 1982. On lava dome growth, with application to the 1979 lava extrusion of the Soufriére of St. Vincent. J. Volcanol. Geotherm. Res. 14, 199-222.

Ivanov, B.A., 2006. Earth/Moon impact rate comparison: Searching constraints for lunar secondary/primary cratering proportion. Icarus 183, 504-507, doi: 10.1016/j.icarus.2006.04.004.

James, O.B., Lindstrom, M.M., Flohr, M.K., 1987. Petrology and geochemistry of alkali gabbronorites from lunar breccia 67975. J. Geophys. Res. 92, 314-330.

Jolliff, B.L., 1991. Fragments of quartz monzodiorite and felsite in Apollo 14 soil particles. Lunar Planet. Sci. 21, 101-118.

Jolliff, B.L., 1998. Large-scale separation of K-frac and REEP-frac in the source regions of Apollo impact-melt breccias and a revised estimate of the KREEP composition. Int. Geol. Rev. 40, 916-935.

Jolliff, B.L., Floss, C., McCallum, I. S., Schwartz, J. M., 1999. Geochemistry, petrology, and cooling history of 14161,7373: A plutonic lunar sample with textural evidence of graniticfraction separation by silicateliquid immiscibility. Am. Mineral. 84, 821-837.

Jolliff, B.L., Gillis, J.J., Haskin, L.A., Korotev, R.L., Wieczorek, M.A., 2000. Major lunar crustal terranes: Surface expressions and crust-mantle origins. J. Geophys. Res. 105, 4197-4216.

Jolliff, B.L., et al., 2011. Non-mare silicic volcanism on the lunar farside at Compton-Belkovich. Nature Geoscience 4, 566-571, doi:10.1038/NGEO1212.

Jolliff, B.L., Stopar, J.D., Lawrence, S.J., Robinson, M.S., Hawke, B.R., 2012. New Views of Silicic Volcanism on the Moon, Second Conference on the Lunar Highlands Crust. abstract. 1677, p. 27-28.

Keller, M.R., et al., 2013. Time-dependent calibration of Messenger's Wide-Angle Camera following a contamination event. Lunar Planet. Sci. MMXIII, Abstract 2489.

Keller, L., McKay, D.,1993. Discovery of vapor deposits in the lunar regolith. Science 261, 1305-1307, doi:10.1126/science.261.5126.1305.

Kieffer, H.H., Anderson, J.A., 1998. Use of the moon for spacecraft calibration over 350 to 2500 nm. Proc. SPIE, 3498, 325-336.

Kieffer, H.H., Stone, T.C., 2005. The spectral irradiance of the Moon. As-

tron. J. 129, 2887-2901. doi:10.1086/430185.

Kneissl, T., van Gasselt, S., Neukum, G., 2011. Map-projection-independent crater size-frequency determination in GIS environments-New software tool for ArcGIS. Planet. Space Sci. 59, 1243-1254, doi:10.1016/j.pss.2010.03.015.

König, B., 1977. Untersuchungen von primären und sekundären Einschlagsstrukturen auf dem Mond und Laborexperimente zum Studium des Auswurfs von Sekundärteilchen, Ph.D. thesis, Univ. Heidelberg, Heidelberg, Germany.

König, B., Neukum, G., Fechtig, H., 1977. Recent Lunar Cratering: Absolute Ages of Kepler, Aristarchus, Tycho, Proc. Lunar Sci. Conf. 8, 555-557.

Korotev, R.L. 1998. Concentration of radioactive elements in lunar materials. J. Geophys. Res. 103, 1691-1701.

Kusuma, K.N., Sebastian, N., Murty, S.V.S., 2012. Geochemical and mineralogical analysis of Gruithuisen region on Moon using M3 and DIVINER images. Planet. Space Sci. 67, 46-56, doi:10.1016/j.pss.2012.02.012.

Lawrence, D.J., Feldman, W.C., Barraclough, B.L., Binder, A.B., Elphic, R.C., Maurice, S., Thomsen, D.R., 1998. Global Elemental Maps of the Moon: The Lunar Prospector Gamma-Ray Spectrometer. Science 281, 1484-1489, doi:10.1126/science.281.5382.1484.

Lawrence, D.J., Elphic, R.C., Feldman, W.C., Prettyman, T.H., Gasnault, O., Maurice, S., 2003. Small area thorium features on the lunar surface. J. Geophys. Res. 108(E9), 5102, doi:10.1029/2003JE002050.

Lawrence, D.J., et al., 2005. Evidence for a high-Th evolved lithology on the Moon at Hansteen Alpha. Geophys. Res. Lett. 32, L07201, doi:10.1029/2004GL022022.

Lawrence, S.J., Hawke, B.R., Gillis-Davis, J.J., Taylor, G.J., Lawrence, D.J., Cahill, J.T., Hagerty, J.J., Lucey, P.G., Smith, G.A., Keil, K., 2008. Composition and Origin of the Dewar Geochemical Anomaly. J. Geophys. Res. 113(E02001), doi: 10.1029/2007JE002904.

Lawrence, S.J., et al., 2013. LRO observations of morphology and surface roughness of volcanic cones and lobate lava flows in the Marius Hills. J. Geophys. Res. Planets 118, 615-634, doi:10.1002/jgre.20060.

Le Feuvre, M., Wieczorek, M.A., 2008. Nonuniform cratering of the terrestrial planets. Icarus 197, 291-306, doi:10.1016/j.icarus.2008.04.011.

Le Feuvre, M., Wieczorek, M.A., 2011. Nonuniform cratering of the Moon and a revised crater chronology of the inner Solar System. Icarus 214, 1-20, doi:10.1016/j.icarus.2011.03.010.

Lindstrom, M.M., 1984. Alkali gabbronorite, ultra-KREEPy melt rock and the diverse suite of clasts in North Ray crater feldspathic fragmental breccia 67975. Lunar Planet. Sci. 15, 50-62.

Logan, L.M., Hunt, G.R., Salisbury, J.W., Balsamo, S.R., 1973. Compositional implications of Christansen frequency maximums for infrared remote sensing applications. J. Geophys. Res. 78, 4983-5003.

Lucas, J.W., Conel, J.E., Hagemeyer, W.A., Garipay, R.R., Saari, J.M., 1967. Lunar surface thermal characteristics from Surveyor 1. J. Geophys. Res. 72, 779-789, doi:10.1029/JZ072i002p00779.

Lucas, J.W., Garipay, R.R., Hagemeyer, W.A., Saari, J.M., Smith, J.W., Vitkus, G., 1968. Lunar surface temperatures and thermal characteristics: Surveyor 5 science results. J. Geophys. Res. 73, 7209-7218, doi:10.1029/JB073i022p07209.

Lucey, P.G., Taylor, G.J., Malaret, E., 1995. Abundance and distribution of iron on the Moon. Science 268, 1150-1153, doi:10.1126/science.268.5214.1150.

Lucey, P.G., Blewett, D.T., Hawke, B.R., 1998. Mapping the FeO and TiO_2 content of the lunar surface with multispectral imagery. J. Geophys. Res. 103, 3679-3700.

Lucey, P.G., Blewett, D.T., Taylor, G.J., Hawke, B.R., 2000a. Imaging of lunar surface maturity. J. Geophys. Res. 105, 20377-20386, doi:10.1029/1999JE001110.

Lucey, P.G., Blewett, D.T., Jolliff, B.L., 2000b. Lunar iron and titanium abundance algorithms based on final processing of Clementine ultraviolet-visible images. J. Geophys. Res. 105, 20297-20306, doi:10.1029/1999JE001117.

Lucey, P.G., 2006. Radiative transfer modeling of the effect of mineralogy on some empirical methods for estimating iron concentration from multispectral imaging of the Moon. J. Geophys. Res. 111, E08003, doi:10.1029/2005JE002661.

Lucey, P.G., Riner, M.A., 2011. The optical effects of small iron particles that darken but do not redden: Evidence of intense space weathering on Mercury. Icarus 212, 451-462, doi:10.1016/j.icarus.2011.01.022.

Mahanti, P., Robinson, M.S., Humm, D., Boyd, A., Braden, S.E., 2012. In-flight absolute radiometric calibration of Lunar Reconnaissance Orbiter Wide Angle Camera. NASA Lunar Science Forum, abstract.

Malin, M.C., 1974. Lunar red spots: Possible pre-mare materials. Earth Planet. Sci. Lett. 21, 331-341.

Mallama, A., 2002. Photometry of Mercury from SOHO/LASCO and Earth. The

phase function from 2 to 170 deg. Icarus 155, 253-264, doi: 10.1006/icar.2001.6723.

Marti, K., Lightner, B.D., Osborn, T.W., 1973. Krypton and xenon in some lunar samples and the age of North Ray crater. Proc. Lunar Sci. Conf. 4, 2037-2048.

McClintock, W.E., et al., 2008. Spectroscopic observations of Mercurys surface reflectance during MESSENGERs first Mercury flyby. Science 321, 62-65, doi:10.1126/science.1159933.

McEwen, A.S., Bierhaus, E.B., 2006. The importance of secondary cratering to age constraints on planetary surfaces. Annu. Rev. Earth Planet. Sci. 34, 535-567.

McKay, D.S., Fruland, R.M., Heiken, G.H., 1974. Grain size and the evolution of lunar soils. Lunar Sci. Conf. 5, 887-906.

Mekhontsev, S. Hanssen, L., 2007. NIST thermal emission metrology in support of climate benchmarks traceability. American Geophysical Union, Fall Meeting, abstract A31B-0307.

Melosh, H.J., 1989. Impact Cratering: A Geologic Process, 245 pp., Oxford University Press, New York.

Melosh, H.J., 2011. Planetary Surface Processes, Cambridge. Univ. Press, Cambridge, U. K.

Meyer C., 1977. Petrology, mineralogy and chemistry of KREEP basalt. Phys. Chem. Earth 10, 239-260.

Michael, G.G., Neukum, G., 2010. Planetary surface dating from crater size-frequency distribution measurements: Partial resurfacing events and statistical age uncertainty. Earth Planet. Sci. Lett. 294, 223-229, doi:10.1016/j.epsl.2009.12.041.

Miller, C.D., 1985. Holocene eruptions at the Inyo volcanic chain, California: Implications for possible eruptions in Long Valley caldera. Geology 13, 14-17, doi: 10.1130/0091-7613(1985)13<14:HEATIV>2.0.CO;2.

Minnaert, M., 1961. Photometry of the Moon. In: Kuiper, G.P., Middlehurst, B.M. (Eds.), Planets and Satellites, The Solar System, vol. 3. University of Chicago Press, pp. 213-248.

Moore, H.J., Boyce, J.M., Hahn, D.A., 1980. Small impact craters in the lunar regolith: Their morphologies, relative ages, and rates of formation. Moon 23, 231-252, doi:10.1007/BF00899820.

Morota, T., et al., 2009. Formation age of the lunar crater Giordano Bruno. Meteoritics and Planetary Science 44, 1115-1120, doi:10.1111/j.1945-5100.2009.tb01211.x

Morris, R., 1976. Surface exposure indices of lunar soils: A comparative FMR study. Lunar Sci. Conf. 7, 315-335.

Morris, R., 1980. Origin and size distribution of metallic iron particles in the lunar regolith. Lunar Sci. Conf. 11, 1697-1712.

Morrison, D., 1970. Thermophysics of the planet Mercury. Space Sci. Rev. 11, 271-307, doi:10.1007/BF00241524.

Murase and McBirney, 1973. Properties of some common igneous rocks and their melts at high temperatures. Geol. Soc. Am. Bull. 84, 3653-3592, doi: 10.1130/0016-7606(1973)84<3563:POSCIR>2.0.CO;2.

Nagao, K., et al., 2011. Irradiation history of Itokawa regolith material deduced from noble gases in the Hayabusa samples. Science 333, 1125-1128, doi:10.1126/science.1207785.

National Research Council, 2007. The Scientific Context for Exploration of the Moon: Final Report. Washington, DC: The National Academies Press, 120 pp.

Neukum, G., 1983. Meteoritenbombardement und Datierung planetarer Oberflchen, Habilitation Thesis, Univ. Mnchen, Munich, Germany.

Neukum G., Ivanov, B.A., Hartmann, W.K., 2001. Cratering records in the inner solar system in relation to the lunar reference system. Space Sci. Rev. 96, 55-86, doi: 10.1023/A:1011989004263.

Nittler, L. R., et al., 2011. The major-element composition of Mercury's surface from MESSENGER x-ray spectrometry. Science 333, 1847-1850, doi:10.1126/science.1211567.

Noble, S.K., Pieters, C.M., Taylor, L.A., Morris, R.V., Allen, C.C., McKay, D.S., Keller, L.P., 2001. The optical properties of the finest fraction of lunar soil: Implications for space weathering. Meteorit. Planet. Sci. 36, 31-42, doi:10.1111/j.1945-5100.2001.tb01808.x.

Noble, S.K., Pieters, C.M., 2003. Space weathering on Mercury: Implications for remote sensing. Sol. Syst. Res. 37, 34-39.

Noble, S.K., Pieters, C.M., Keller, L.P., 2007. An experimental approach to understanding the optical effects of space weathering. Icarus 192, 629-642, doi:10.1016/j.icarus.2007.07.021.

Noguchi, T., et al., 2011. Incipient space weathering observed on the surface of Itokawa dust particles. Science 333, 1121-1125, doi:10.1126/science.1207794.

Nozette, S., et al., 1994. The Clementine mission to the Moon: Scientific overview. Science 266, 1835-1839.

Oberbeck, V.R., 1975. The role of ballistic erosion and sedimentation in lunar stratigraphy. Rev. Geophys. Space Phys. 13, 337-362, doi:10.1029/RG013i002p00337.

Paige, D.A., et al., 2010. The Lunar Reconnaissance Orbiter Diviner Lunar Radiometer Experiment. Space Science Reviews 150, 125-160, doi:10.1007/s11214-009-9529-2.

Papike, J.J., Vaniman, D.T., 1978. The lunar mare basalt suite. Geophys. Res. Lett. 5, 433-436, doi: 10.1029/GL005i006p00433.

Papike, J.J., Ryder, G., Shearer, C.K., 1998. Lunar samples. Rev. Mineral. 36, 5-1-5-189.

Pavlovsky, C., et al., 2002. ACS instrument handbook, version 3.0, public document, Space Telesc. Sci. Inst., Baltimore, Md.

Pieters, C.M., 1978. Mare basalt types on the front side of the Moon: A summary of spectral reflectance data. Proc. Lunar Sci. Conf. IX, 2825-2849.

Pieters, C.M., Fischer, E.M., Rode, O., Basu, A., 1993. Optical effects of space weathering: The role of the finest fraction. J. Geophys. Res. 98, 20817-20824, doi:10.1029/93JE02467.

Pieters, C.M., et al., 2009. The Moon Mineralogy Mapper (M3) on Chandrayaan-1. Indian Academy of Sciences, Current Science 96, 500-505.

Pike, R.J., 1978. Volcanoes on the inner planets: Some preliminary comparisons of gross topography. Lunar Planet. Sci. 9, 3239-3273.

Plescia, J.B., Robinson, M.S., 2011. New constraints on the absolute lunar crater chronology. Lunar Planet Sci. 42, 1839.

Raitala, J., Kreslavsky, M.A., Shkuratov, Y.G., Starukhina, L.V., Kaydash, V.G., 1999. Nonmare volcanism on the Moon: Characteristics from the Clementine data. Lunar Planet. Sci. XXX, abstract 1457.

Rava, B., Hapke, B., 1987. An analysis of the Mariner 10 color ratio map of Mercury. Icarus 71, 397-429, doi:10.1016/0019-1035(87)90037-6.

Riner, M.A., Lucey, P.G., Desch, S.J., McCubbin, F.M., 2009. Nature of opaque components on Mercury: Insights into a Mercurian magma ocean. Geophys. Res. Lett. 36, L02201, doi:10.1029/2008GL036128.

Riner, M.A., McCubbin, F.M., Lucey, P.G., Talyor, G.J., GillisDavis, J.J., 2010. Mercury surface composition: Integrating petrologic modeling and remote sensing data to place constraints on FeO abundance. Icarus 209, 301-313, doi:10.1016/j.icarus.2010.05.018.

Riner, M.A., Lucey, P.G., 2012. Spectral effects of space weathering on Mercury: The role of composition and environment. Geophys. Res. Lett. 39, L12201, doi:10.1029/2012GL052065.

Robinson, M.S., Lucey, P.G., 1997. Recalibrated Mariner 10 color mosaics: Implications for mercurian volcanism. Science 275, 197-200, doi:10.1126/science.275.5297.197.

Robinson, M.S., Taylor, G.J., 2001. Ferrous oxide in Mercurys crust and mantle. Meteorit. Planet. Sci. 36, 841-847, doi:10.1111/j.1945-5100.2001.tb01921.x.

Robinson, M.S., Hapke, B.W., Garvin, J.B., Skillman, D., Bell, J.F., III, Ulmer, M.P., Pieters, C.M., 2007. High resolution mapping of TiO_2 abundances on the Moon using the Hubble Space Telescope. Geophys. Res. Lett. 34, L13203, doi:10.1029/2007GL029754.

Robinson, M.S., et al., 2008. Reflectance and color variations on Mercury: Regolith processes and compositional heterogeneity. Science 321, 66-69, doi:10.1126/science.1160080.

Robinson, M.S., et al., 2010. Lunar Reconnaissance Orbiter Camera (LROC) instrument overview. Space Sci. Rev. 150, 81-124, doi:10.1007/s11214-010-9634-2.

Robinson, M.S., Thomas, P.C., Braden, S.E., Lawrence, S.J., Garry, W.B., the LROC Team, 2010. High resolution imaging of Ina: Morphology, relative ages, formation. Lunar Planet. Sci. 41, abstract 2592.

Robinson, M.S., Ashley, J.W., Boyd, A.K., Wagner, R.V., Speyerer, E.J., Hawke, B.R., Hiesinger, H., van der Bogert, C.H., 2012. Confirmation of sublunarean voids and thin layering in mare deposits. Planetary and Space Science 69, 18-27, doi: 10.1016/j.pss.2012.05.008.

Robinson, K.L., Taylor, G.J., 2011. Intrusive and extrusive lunar felsites. Lunar Planet. Sci. XLII, abstract 1257.

Roedder, E., 1951. Low temperature liquid immiscibility in the system K_2O-FeO-Al_2O_a-SiO_2, American Mineralogoist, 36, 282-286.

Roedder, E., 1953. High silica portion of the system K_2O-FeO-Al_2O_a-SiO_2, Geological Society of America Bulletin 64, 1554.

Roedder, E., Weiblen, P.W., 1970. Silicate liquid immiscibility found in lu-

nar rocks, Geotimes, 10-13.

Ryder, G., Taylor, G.J., 1976. Did mare-type volcanism commence early in lunar history? Proc. Lunar Sci. Conf., 7, pp. 1741-1755.

Ryder, G., Spudis, P.D., 1980. Volcanic rocks in the lunar highlands. Proc. Conf. on the Lunar Highlands Crust, pp. 353-375.

Sarantos, M., Slavin, J.A., Benna, M., Boardsen, S.A., Killen, R.M., Schriver, D., Trávníček, P., 2009. Sodium-ion pickup observed above the magnetopause during MESSENGER's first Mercury flyby: Constraints on neutral exospheric models. Geophys. Res. Lett. 36, L04106, doi:10.1029/2008GL036207.

Sato, H., Denevi, B.W., Robinson, M.S., Hapke, B.W., McEwen, A.S., 2011. Photometric normalization of LROC WAC global color mosaic. Lunar Planet. Sci. XLII, Abstract 1608.

Schaber, G.G., 1973. Lava flows in Mare Imbrium: Geologic evaluation from Apollo orbital photography. Proc. Lunar Sci. Conf. 4, 73-92.

Schultz, P.H., 1976. Moon Morphology, University of Texas Press, Austin, Texas, 626 pp.

Schultz, P.H., Gault, D., Greeley, R., 1977. Interpreting statistics of small lunar craters, Proc. Lunar Sci. Conf. 8, pp. 3539-3564.

Schultz, P.H., Spudis, P.D., 1983. Beginning and end of lunar mare volcanism. Nature 302, 233-236, doi:10.1038/302233a0.

Schultz, P.H., Gault, D.E., 1985. Clustered impacts - Experiments and implications. J. Geophys. Res. 90, 3701-3732, doi: 10.1029/JB090iB05p03701.

Schultz, P.H., Staid, M.I., Pieters, C.M., 2006. Lunar activity from recent gas release. Nature 444, 184-186, doi:10.1038/nature05303.

Scott, D.H., Eggleton, R.E., 1973. Geologic map of the Ruemker Quadrangle of the Moon. Map I-805 (LAC 23), U.S. Geol. Surv., Washington, D.C., 1973.

Seddio, S.M., Jolliff, B.L., Korotev, R.L., Zeigler, R.A., 2011. Fragments of Granite in Apollo 12 Regolith: Pieces of 12013? Lunar Planet. Sci. 42, abstract 2381.

Shearer C.K., Papike, J.J., 1999. Magmatic evolution of the Moon. Am Mineral 84, 1469-1494.

Shearer, C.K. et al., 2006. Thermal and Magmatic Evolution of the Moon. Chapter 4, pages 365-518. In: Jolliff, B.L., et al., eds. (2006), New Views of the

Moon, Rev. Min. Geochem., 60, 1-704.

Shepherd, J.B., et al., 1979. The eruption of Soufriére Volcano, St. Vincent, April-June, 1979. Nature 282, 24-28.

Shoemaker, E.M., Hackman, R.J., 1962. Stratigraphic basis for a lunar time scale, in The Moon: Symposium 14 of the International Astronomical Union, edited by Z. Kopal and Z. K. Mikhailov, pp. 289-300, Academic, San Diego, Calif.

Slater, P.N., Biggar, S.F., Thome, K.J., Gellman, D.I., Spyak, P.R., 1995. In-flight radiometric calibration of ASTER by reference to well-characterized scenes. Proc. SPIE Vol. 2317, p. 49-60.

Slavin, J.A, et al., 2010. MESSENGER observations of extreme loading and unloading of Mercury's magnetic tail. Science 329, 665-668, doi:10.1126/science.1188067.

Smith, E. I., 1973. Identification, distribution and significance of lunar volcanic domes. The Moon 6, 3-31.

Soderblom, L.A., 1970. A Model for Small-Impact Erosion Applied to the Lunar Surface. J. Geophys. Res. 75, 2655, doi:10.1029/JB075i014p02655.

Soderblom, L.A., 1972. The process of crater removal in the lunar maria. In Apollo 15 preliminary science report, NASA Special Paper 289. Washington, D.C.: U.S. Government Printing Office, pp. 25-87-25-91.

Speyerer, E., Robinson, M.S., Denevi, B.W., 2011. Lunar Reconnaissance Orbiter Camera Global Morphological Map of the Moon. Lunar Planet. Sci. XLII, Abstract 2387.

Sprague, A.L., et al., 2009. Spectral emissivity measurements of Mercurys surface indicate Mg- and Ca-rich mineralogy, K-spar, Na-rich plagioclase, rutile, with possible perovskite, and garnet. Planet. Space Sci. 57, 364-383, doi:10.1016/j.pss.2009.01.006.

Spudis, P.D., Guest, J.E., 1988. Stratigraphy and geologic history of Mercury, in Mercury, edited by F. Vilas, C. Chapman, and M. S. Matthews, pp. 118-164, University of Arizona Press, Tucson, Arizona.

Spudis, P.D., McGovern, P.J., Kiefer, W.S., 2013. Large shield volcanoes on the Moon. J. Geophys. Res. Planets 118, 1063-1081, doi:10.1002/jgre.20059.

Staid, M.I., et al., 2011. The spectral properties of Ina: New observations from the Moon Mineralogy Mapper. Lunar Planet. Sci. 42, abstract 2499.

Stockstill-Cahill, K.R., McCoy, T.J., Nittler, L.R., Weider, S.Z., Hauck, S.A. II, 2012. Magnesium-rich crustal compositions on Mercury: Implications

for magmatism from petrologic modeling. J. Geophys. Res. 117, E00L15, doi:10.1029/2012JE004140.

Stone, T.C., Kieffer, H.H., 2002. Absolute irradiance of the Moon for on-orbit calibration. In: Barnes, W.L. (Ed.), Earth Observing Systems VII. Proc. SPIE, vol. 4814, pp. 211-221.

Stone, T.C., Kieffer, H.H., 2006. Use of the Moon to support on-orbit sensor calibration for climate change measurements. In: Butler, J. (Ed.), Earth Observing Systems XI. Proc. SPIE, vol. 6296. doi:10.1117/12.678605.

Stooke, P.J., 2012. Lunar Meniscus Hollows. Lunar Planet. Sci. 43, abstract 1011.

Strain, P.L., El-Baz, F., 1980. The geology and morphology of Ina. Proc. Lunar Sci. 11, 2437-2446.

Strazzulla, G., Dotto, E., Binzel, R., Brunetto, R., Barucci, M.A., Blanco, A., Orofino V., 2005. Spectral alteration of the Meteorite Epinal (H5) induced by heavy ion irradiation: a simulation of space weathering effects on near-Earth asteroids. Icarus 174, 31-35, doi: 10.1016/j.icarus.2004.09.013.

Strom, R.G., Fielder, G., 1970. Multiphase eruptions associated with the lunar craters Tycho and Aristarchus. Communications of the Lunar and Planetary Laboratory 8, 4, 235-288.

Strom, R.G., Neukum, G., 1988. The cratering record on Mercury and the origin of impacting objects, in Mercury, edited by F. Vilas, C. R. Chapman, and M. S. Matthews, pp. 336-373, Univ. of Ariz. Press, Tucson.

Strom, R.G., Malhotra, R., Ito, T., Yoshida, F., Kring, D.A., 2005. The origin of planetary impactors in the inner solar system. Science 309, 1847-50, doi:10.1126/science.1113544.

Strom, R.G., Chapman, C.R., Merline, W.J., Solomon, S.C., Head, J.W., 2008. Mercury cratering record viewed from MESSENGER's first flyby. Science 321, 79-81, doi:10.1126/science.1159317.

Stuart-Alexander, D.E., Wilhelms, D.E., 1975. The Nectarian system, a new lunar time-stratigraphic unit. J. Res. U.S. Geol. Surv. 3, 53-58.

Sun, J., Xiong, X., Barnes, W.L., 2006. MODIS Reflective Solar Bands Radiometric Stability Monitoring Using the Moon. American Geophysical Union, Fall Meeting 2007, abstract B51A-06.

Talboys, D.L., et al., 2009. In situ radiometric dating on mars: Investigation of the feasibility of K-Ar dating using flight-type mass and X-ray spectrome-

ters. Planetary and Space Science 57(11), 1237-1245, doi:10.1016/j.pss.2009.02.012.

Thome, K.J., Gellman, D.I., Parada, R.J., Biggar, S.F., Slater, P.N., Moran, M.S., 1993. In-flight radiometric calibration of Landsat-5 Thematic Mapper from 1984 to the present. Proc. SPIE Vol. 1938, p. 126-130.

Tran, T., et al., 2011. Morphometry of Lunar Volcanic Domes from LROC. Lunar Planet. Sci. 42, abstract 2228.

van der Bogert, C.H., Hiesinger, H., Krüger, T., McEwen, A.S., Dundas, C., 2013. New evidence for target property influence on crater size-frequency distributions. Lunar Planet. Sci. 44, abstract 1962.

Vaniman, D.T., Papike, J.J., 1978. The lunar highland melt-rock suite. Geophys. Res. Lett. 5, 429-432, doi: 10.1029/GL005i006p00429.

Vaniman, D.T., Dietrich, J., Taylor, G.J., Heiken, G.H., 1991a. Exploration, samples, and recent concepts of the Moon, in The Lunar Sourcebook, edited by G.H. Heiken, D.T. Vaniman, and B.M. French, pp. 5-26, Cambridge University Press, Cambridge.

Vaniman, D.T., Reedy, R., Heiken, G.H., Olhoeft, G., Mendell, W., 1991b. The lunar environment, in The Lunar Sourcebook, edited by G.H. Heiken, D.T. Vaniman, and B.M. French, pp. 27-60, Cambridge University Press, Cambridge.

Vasavada, A.R., Paige, D.A., Wood, S.E., 1999. Near-surface temperatures on Mercury and the Moon and the stability of polar ice deposits. Icarus 141, 179-193, doi:10.1006/icar.1999.6175.

Vernazza, P., Binzel, R.P., Rossi, A., Fulchignoni, M., Birlan, M., 2009. Solar wind as the origin of rapid reddening of asteroid surfaces. Nature 458, 993-995, doi:10.1038/nature07956.

Veverka, J., Helfenstein, P., Hapke, B., Goguen, J.D., 1988. Photometry and polarimetry of Mercury, in Mercury, edited by F. Vilas, C. Chapman, and M. S. Matthews, pp. 37-58, University of Arizona Press, Tucson, Arizona.

Vilas, F., 1985. Mercury: Absence of crystalline Fe2+ in the regolith. Icarus 64, 133-138, doi:10.1016/0019-1035(85)90044-2.

Vilas, F., 1988. Surface composition of Mercury from reflectance spectrophotometry, in Mercury, edited by F. Vilas, C. Chapman, and M.S. Matthews, pp. 59-76, University of Arizona Press, Tucson, Arizona.

Vilas, F., McCord, T.B., 1976. Mercury: Spectral reflectance measurements (0.33-1.06 μm) 1974/1975. Icarus 28, 593-599, doi:10.1016/0019-1035(76)90132-9.

Vilas, F., Leake, M.A., Mendell, W.W., 1984. The dependence of reflectance spectra of Mercury on surface terrain. Icarus 59, 60-68, doi:10.1016/0019-1035(84)90055-1.

Wagner, J.K., Hapke, B.W., Wells, E.N., 1987. Atlas of reflectance spectra of terrestrial, lunar, and meteoritic powders and frosts from 92 to 1800 nm. Icarus 69, 14-28, doi:10.1016/0019-1035(87)90003-0.

Wagner, R., Head, J.W., Wolf, U., Neukum, G., 2002. Stratigraphic sequences and ages of volcanic units in the Gruithuisen region of the Moon. J. Geophys. Res. 107, 5104, doi:10.1029/2002JE001844.

Wagner, R.V., M. S. Robinson, E. J. Speyerer, and P. Mahanti (2013), Topography of 20-km diameter craters on the Moon, Lunar Planet. Sci., 44, abstract 2924.

Warell, J., 2004. Properties of the Hermean regolith: IV. Photometric parameters of Mercury and the Moon contrasted with Hapke modelling. Icarus 167, 271-286, doi:10.1016/j.icarus.2003.10.010.

Warren, P.H., 1985. The magma ocean concept and lunar evolution. Annu. Rev. Earth Planet. Sci. 13, 201-240.

Weider, S.Z., Crawford, I.A., Joy, K.H., 2010. Individual lava flow thicknesses in Oceanus Procellarum and Mare Serenitatis determined from Clementine multispectral data. Icarus 209, 323-336, doi:10.1016/j.icarus.2010.05.010.

Weider, S.Z., et al., 2012. Chemical heterogeneity on Mercurys surface revealed by the MESSENGER X-Ray Spectrometer. J. Geophys. Res. 117, E00L05, doi:10.1029/2012JE004153.

Whitaker, E.A., 1972. Lunar color boundaries and their relationship to topographic features: A preliminary survey. Moon 4, 348-355.

Whitaker, E.A., 1972. Apollo 15 Preliminary Science Report. NASA SP-289, p.25-84 to 25-85.

Whitford-Stark, J.L., 1982. Factors influencing the morphology of volcanic landforms: An Earth-Moon comparison. Earth Sci. Reviews 18, 109-168, doi: 10.1016/0012-8252(82)90050-2.

Wieczorek, M.A., Phillips, R.J., 2000. The "Procellarum KREEP Terrane": Implications for mare volcanism and lunar evolution. J. Geophys. Res. 105, 20417-20430, doi:10.1029/1999JE001092.

Wilcox, B.B., Robinson, M.S., Thomas, P.C., Hawke, B.R., 2005. Constraints on the depth and variability of the lunar regolith. Meteoritics & Planetary Science

40, 695-710, doi:10.1111/j.1945-5100.2005.tb00974.x.

Wilhelms, D.E., 1987. The Geologic History of the Moon. Professional Paper 1348, US Geological Survey, Boulder, CO, 302pp.

Wilhelms, D.E., Byrne, C.J., 2009. Stratigraphy of Lunar Craters, Available at http://www.imageagain.com/Strata/StratigraphyCraters.2.0.htm

Williams, J-P., Pathare, A.V., 2013. The size-frequency distribution of small craters on the Moon and Mars. Lunar Planet. Sci. 44, abstract 2832.

Williams, J-P., Hayne, P.O., Ghent, R.R., Paige, D.A., 2013. Dating young impact craters on the Moon, Lunar Science Institute Virtual Forum, July 16-18.

Williams, H., McBirney, A.R., 1979. Volcanology, 397 pp., Freeman, Cooper, San Francisco, California.

Wilson, L., Head, J.W., 2003. Lunar Gruithuisen and Mairan domes: Rheology and mode of emplacement. J. Geophys. Res. 108, 5012, doi:10.1029/2002JE001909.

Wilson, L., Hawke, B.R., Giguere, T.A., Petrycki, E.R., 2011. An igneous origin for Rima Hyginus and Hyginus crater on the Moon. Icarus 215, 584-595, doi:10.1016/j.icarus.2011.07.003.

Wood, J.A., Dickey, J.S., Jr., Marvin, U.B., Powell, B.N., 1970. Lunar Anorthosites. Science 167, 602-604, doi:10.1126/science.167.3918.602.

Wood, J.A., 1975. Lunar Petrogenesis in A Well-Stirred Magma Ocean. Abstracts of the Lunar and Planetary Science Conference, 6, page 881.

Wood, C.A., Head, J.W., 1975. Geologic setting and provenance of spectrally distinct pre-mare material of possible volcanic origin. paper presented at Conference on Origins of Mare Basalts, Lunar Sci. Inst., Houston, Tex.

Young, R.A., 1975. Mare crater size-frequency distributions: implications for relative surface ages and regolith development. Proc. Lunar Sci. Conf. 6, 2645-2662.

Zanetti, M., Jolliff, B., van der Bogert, C.H., Hiesinger, H., 2013. New determination of crater size-frequency distribution variation on continuous ejecta deposits: Results from Aristarchus crater. Lunar Planet. Sci. 44, abstract 1842.

Zisk, S.H., Hodges, C.A., Moore, H.J., Wilhelms, D.E., Shorthill, R.W., Thompson, T.W., Whitaker, E.A., 1977. The Aristarchus-Harbinger region of the Moon - Surface geology and history from recent remote-sensing observations. The Moon 17, 59-99, doi:10.1007/BF00566853.

APPENDIX A

LUNAR AND MERCURIAN CRATER DATA

This appendix contains four table which contain the data for craters with diameter D $\geq$ 10 km from 40°S to 40°N latitude on Mercury and the Moon classified into the four relative age groups discussed in chapter 3. These four groups are 1) Kuiperian, 2) Copernican (craters with high-reflectance ejecta), and 3) Mansurian, 4) Eratosthenian (craters with sharp rims but no high-reflectance ejecta) on Mercury and the Moon. Only lunar craters in the highlands terrain were included (craters in the maria). Crater data were collected using four orbital mosaics from the Mercury Dual Imaging System Wide Angle Camera (WAC) and the Lunar Reconnaissance Orbiter Camera WAC. Two mosaics were 1 kilometer per pixel scale comprised of images with incidence angles less than 45° (relatively high sun). Two mosaics were 200 meter per pixel scale comprised of low sun angle images for morphologic classifications. The areal coverage of the mercurian high sun and low sun mosaics was not continuous between 40°S to 40°N latitude at the time of data collection, and some areas covered in one mosaic may not be in the other. Latitude and longitude values for the lunar craters are in the Unified Lunar Control Network (UCLN) 2005 (Archinal et al., 2006). A preexisting database of mercurian craters (with diameters D > 10 km) derived from Mariner 10 and MESSENGER flyby data was used as a starting point for crater documentation (Herrick et al., 2011). A database of lunar craters with diameters D $\geq$ 30 km including relative age determinations (Wilhelms and Byrne, 2009) and the United States Geological Survey lunar shapefiles for named features were starting points for lunar crater documentation.

An explanation of the columns in the following four tables:

1. Column FEATURE_NAME, the crater name. If no name exists, then the entry reads "Unnamed".

2. Column DIAMETER [km], the approximate diameter of the crater in kilometers.

3. Column CENTER_LAT, the latitude (in degrees) of the crater center.

4. Column CENTER_LON, the longitude (in positive east 360 east degrees) of the crater center.

5. Column EJECTA_TYPE, which describes whether the high-reflectance ejecta surrounding the crater rim has "distinct" rays, or it forms a high-reflectance "halo" without any discernable rays. If the entry says "intermediate" then the crater has high-reflectance ejecta, but the rays are hard to distinguish. If the entry says "unclear" then no classification could be made based on the available data.

6. Column UNCERTAINTY, the uncertainty of the classification of the crater into the group. Entry is "high" or "low". "Low" means that the crater has all the characteristics of the group. "High" means that the crater appears more degraded than the rest of the group, or that identification of one of the characteristics was ambiguous.

Table A.1: Mercurian craters with high-reflectance ejecta (Kuiperian group)

Name	D [km]	Lat	Lon	Ejecta	Uncertainty
Unnamed	15.4	-36.43	183.3	distinct	low
Unnamed	24	-10.2	184.6	halo	low
Nureyev	16.2	11.61	186.9	distinct	low
Unnamed	26	-7.1	187.96	halo	low
Unnamed	13	0.5	189	distinct	low
Basho	74.6	-32.43	189.56	distinct	low
Unnamed	13	30.51	191.14	halo	low
Unnamed	14	20.8	193.9	halo	low
Unnamed	10	34.8	193.9	unclear	low
Unnamed	11	-20.34	194.99	halo	low
Unnamed	23.1	-13.8	196.6	halo	low
Unnamed	14	-14.7	199.6	halo	low
Unnamed	11	-2.09	200.41	halo	low
Unnamed	19	-16.78	203.27	distinct	low
Unnamed	11	-22.62	208.15	distinct	low
Unnamed	16	-16.94	213.38	intermediate	low
Balzac	67	10.58	215.41	intermediate	high
Theophanes	46.4	-5.07	217.32	halo	high
Unnamed	12	-34.01	220.71	distinct	low
Unnamed	17.1	-38.1	222	halo	high
Unnamed	10	-29.5	223.2	halo	low
Schoenberg	27.6	-16.11	224.01	intermediate	low
Unnamed	30	16.9	224.3	halo	low
Bartok	116.7	-29.28	225.03	intermediate	low
Mena	15.2	-0.15	235.37	distinct	low
Unnamed	10	-24.19	237.05	halo	low
Unnamed	16	-21	237.89	halo	low
Waters	13.6	-8.96	254.58	distinct	low
Unnamed	28	-5.79	259.02	halo	low
Unnamed	16	-13.8	259.2	intermediate	low
Unnamed	21.4	-10.7	260.1	distinct	low
Unnamed	10.5	-32.35	260.92	halo	low
Unnamed	11.5	12.2	262.5	halo	low
Copley	34.9	-38.56	274.05	distinct	low
Unnamed	10	-4.21	274.78	halo	low
Futabatei	57.3	-16.08	276.47	distinct	low
Snorri	21.3	-9.15	276.77	distinct	low
Unnamed	10	-17.33	277.75	halo	low
Unnamed	12.3	-17.22	279.2	halo	low
Unnamed	13.9	5.02	279.62	halo	high
Unnamed	10	-30.76	280.55	halo	low
Unnamed	31	-18.89	287.83	halo	low
Tansen	27.1	4.13	288.36	distinct	low

Unnamed	21	8.39	292.08	halo	low
Unnamed	34	-34.74	293.31	intermediate	low
Unnamed	48	0.79	294.78	distinct	low
Unnamed	23	-9.5	298.5	intermediate	low
Unnamed	31	10.8	299.1	halo	low
Unnamed	10	20.32	299.32	distinct	low
Unnamed	13	-32.38	308.88	halo	low
Bek	32.2	21.18	309.08	distinct	low
Unnamed	25	-29.95	310.83	distinct	low
Unnamed	15	-2.03	314.24	halo	low
Unnamed	18.5	22.48	315.11	halo	low
Unnamed	11.8	-24	316.3	halo	low
Unnamed	14	26.1	317	halo	low
Unnamed	22	7.48	319.16	intermediate	low
Unnamed	40	-33.67	320.46	intermediate	low
Dominici	20	1.32	323.55	distinct	low
Kuiper	62.3	-11.32	328.6	distinct	low
Unnamed	10	12.67	330.37	unclear	low
Unnamed	11	31.2	331.31	halo	low
Unnamed	12	34.74	331.73	halo	high
Unnamed	20	29.56	332.85	halo	low
Unnamed	17	-3.86	335.7	halo	high
Unnamed	19.4	-0.26	339.91	halo	low
Unnamed	10	-37.36	339.99	unclear	low
Unnamed	12.5	24.43	340.33	halo	low
Unnamed	16	31.3	344.28	halo	high
Unnamed	12	-35.59	345.55	distinct	low
Unnamed	29	-28.3	348.09	intermediate	low
Unnamed	20.6	-11.72	349.07	halo	low
Unnamed	12	0.96	353.24	distinct	low
Unnamed	23.5	-1.01	355.92	distinct	low
Unnamed	12.4	-5.45	1.69	halo	low
Unnamed	12	-28.87	3.95	distinct	low
Debussy	80.2	-33.97	12.69	distinct	low
Unnamed	25	19.43	13.87	halo	low
Hodgkins	19.2	29.04	18.01	distinct	low
Unnamed	26	24.39	20.2	halo	low
Petipa	12	11.52	20.98	distinct	low
Unnamed	15.7	-3.91	21.76	halo	low
Unnamed	12	24.52	22.07	halo	low
Berkel	22.4	-13.7	26.77	distinct	low
Unnamed	29	-10.3	29.98	intermediate	low
Seuss	63.5	7.73	33.24	intermediate	low
Unnamed	11.3	-1.52	43.76	halo	low
Unnamed	15	-28.87	51.71	halo	low
Unnamed	10	-2.2	54.22	distinct	low
Unnamed	12.9	-36.22	58.11	halo	low

Unnamed	12	-29.92	59.14	halo	low
Unnamed	23	-17.65	67.98	distinct	low
Unnamed	11	0.69	78.3	distinct	low
Unnamed	12.5	10.62	80.54	halo	low
Unnamed	24	19.6	81.29	intermediate	low
Unnamed	12	-35.2	86.15	halo	low
Unnamed	10	-19.95	95.86	halo	high
Unnamed	14	-0.72	96.1	distinct	low
Unnamed	15	-8.86	103.29	distinct	low
Unnamed	42.3	-29.5	106	halo	low
Unnamed	16	-35.68	107.32	distinct	low
Eminescu	129.8	10.7	114.3	intermediate	low
Amaral	108.5	-26.54	117.8	intermediate	low
Unnamed	50	-36.58	118.65	halo	low
Unnamed	13	-4.59	119.29	distinct	low
Unnamed	19	-20.42	120.69	distinct	low
Enwonwu	37.8	-9.99	121.97	distinct	low
Xiao Zhao	24.1	10.57	123.91	distinct	low
Unnamed	13	-19.55	125.09	intermediate	low
Unnamed	12	-25.27	126.52	halo	low
Unnamed	17	-38.64	128.07	distinct	low
Unnamed	27	-34.39	133.7	halo	low
Unnamed	13	-8.56	136.19	distinct	low
Unnamed	13.6	-18.89	138.23	halo	low
Unnamed	34	-23	140.63	intermediate	low
Unnamed	16	-15.06	142.42	halo	low
Unnamed	11	-29.9	143.44	halo	low
Unnamed	10	6.16	149.79	halo	low
Unnamed	10	-6.02	151.12	distinct	low
Unnamed	18.6	-19.21	154.94	halo	low
Cunningham	37.6	30.37	157.16	distinct	low
Raden Saleh	22.6	2.06	158.93	distinct	low
Unnamed	12	-22	162.71	halo	low
Unnamed	26	-24.46	162.88	halo	low
Qi Baishi	14.9	-4.3	164.47	distinct	low
Unnamed	14.6	-17.47	165.51	halo	low
Unnamed	12	28.33	168.44	halo	low
Unnamed	10	17.78	169.66	halo	low
Unnamed	15	19.01	172.49	distinct	low
Hovnatanian	34.4	-7.73	172.83	distinct	low
Unnamed	18.5	22.74	174.36	intermediate	low
Balanchine	40.9	38.53	175.72	distinct	low

Table A.2: Mercurian craters with sharp rims and no high-reflectance ejecta (Mansurian group)

Name	D [km]	Lat	Lon	Uncertainty

Unnamed	21.4	19.06	180.28	low
Unnamed	14.5	-23.6	180.4	low
Unnamed	20.3	-35.8	180.45	low
Unnamed	13.4	27	180.5	low
Unnamed	17.1	29.33	180.68	low
Unnamed	14	-7.4	181.2	low
Unnamed	46.6	36.3	182.1	low
Unnamed	29.5	0.41	182.49	low
Unnamed	13	-36.2	182.5	low
Unnamed	10	-8.1	183.1	low
Unnamed	30.9	10.3	183.1	low
Unnamed	10	12.39	183.29	low
Unnamed	14	-36.36	183.3	low
Unnamed	10	37.87	183.48	low
Unnamed	19.1	-21.6	183.6	low
Unnamed	32	32.25	183.61	high
Unnamed	13	14.1	184.2	low
Unnamed	15.2	-31.4	184.4	low
Unnamed	14	7.3	184.6	low
Unnamed	16.5	0.7	184.6	low
Unnamed	14	0.5	185.1	low
Unnamed	11	-30.97	185.2	low
Unnamed	22.9	19.2	185.4	low
Unnamed	13	-31.65	185.57	low
Unnamed	52.3	-20.1	185.6	low
Unnamed	17.1	-24.61	185.67	low
Unnamed	35.9	12.1	186.2	low
Unnamed	10	-5.9	186.7	low
Unnamed	20.5	4.91	187.61	low
Unnamed	30.5	27.72	187.79	low
Unnamed	26	-7.2	187.9	low
Unnamed	11	15	188.1	low
Unnamed	30.4	-38.1	188.4	low
Unnamed	10.2	14.85	188.52	low
Unnamed	12	-8.56	189.32	low
Unnamed	10.1	20.9	189.36	low
Unnamed	15.1	-23	190	low
Unnamed	46.5	9.3	190.2	low
Unnamed	11.3	-3.55	190.24	low
Unnamed	10	-8.7	190.4	low
Unnamed	19.1	-17.5	190.5	high
Unnamed	27.8	29.4	190.7	low
Unnamed	11	-0.3	190.8	low
Unnamed	14.9	15.7	190.8	low
Unnamed	20.1	-24.2	191	low
Unnamed	11.9	30.5	191.1	low
Unnamed	10.5	35	191.2	low

Unnamed	15	13.8	191.2	low
Unnamed	32.8	32.5	191.2	low
Unnamed	11.3	-7.1	191.3	low
Unnamed	10.5	9.4	191.7	low
Unnamed	26.1	-10.1	191.7	low
Unnamed	12.2	18.6	191.8	low
Unnamed	10	-24.2	191.9	low
Unnamed	10.5	-12.2	192.5	low
Unnamed	20	1.9	192.6	low
Unnamed	13.2	-11.9	192.8	low
Unnamed	10.1	-29.1	193	low
Unnamed	12.2	35.9	193.3	low
Unnamed	11.5	18.3	193.5	low
Unnamed	14	24	193.8	low
Unnamed	12.2	9.5	193.9	low
Unnamed	10	-27.3	194.1	low
Unnamed	23.5	18.4	194.3	low
Unnamed	11	19.9	194.7	low
Unnamed	15.9	26.9	194.7	low
Unnamed	10	-20.4	195	low
Unnamed	20.1	-21.7	195.2	high
Unnamed	40.7	36.1	195.6	low
Unnamed	45.2	-19.7	195.8	low
Unnamed	16	2	196	low
Unnamed	12	28.3	196.4	low
Unnamed	10.5	14	196.5	low
Unnamed	12.4	31.2	196.6	low
Unnamed	17	6.5	196.7	low
Unnamed	10	5.6	196.9	low
Unnamed	23.3	-35.3	197	low
Unnamed	10.1	-12.3	197.3	low
Unnamed	13.5	4.7	197.3	low
Unnamed	13.9	16.5	197.6	low
Unnamed	25.2	27.2	197.6	low
Unnamed	10.5	-9.4	198.2	low
Unnamed	11	5.7	198.2	low
Unnamed	18.3	18.8	198.9	low
Unnamed	19.9	11.9	198.9	low
Unnamed	21.2	14.4	198.9	low
Unnamed	56	-3.2	199	low
Unnamed	64	11.7	199.42	high
Unnamed	18.5	6.4	199.5	low
Unnamed	11	-25	199.6	low
Unnamed	10.5	-18.5	200.2	low
Unnamed	12.7	16.9	200.2	low
Unnamed	10	-2.1	200.4	low
Unnamed	13.1	1.3	200.5	low

Unnamed	13.9	38.6	201	low
Unnamed	10.1	1	201.1	low
Unnamed	11.5	-34.4	201.2	low
Unnamed	10	18.7	201.3	low
Unnamed	19.8	32.3	201.4	low
Unnamed	12.4	32.9	201.5	low
Unnamed	37	4.8	202.5	low
Unnamed	11	-7	202.6	low
Unnamed	28.5	-18.4	202.6	low
Unnamed	10.7	32.8	202.7	low
Unnamed	11.5	25.4	202.7	low
Unnamed	15	-0.9	202.8	low
Unnamed	16.8	35.7	203.4	low
Unnamed	11	7.3	203.7	low
Unnamed	47	-27.93	203.75	low
Unnamed	10.5	23.6	203.8	low
Unnamed	12.2	8.6	204	low
Unnamed	51.2	-25.2	204	low
Unnamed	11.2	31.6	204.1	low
Unnamed	12	20.9	204.5	low
Unnamed	31	-1.94	204.69	low
Unnamed	14.2	-36.4	204.7	low
Unnamed	32.9	19.8	204.7	low
Unnamed	10.6	10.3	205.8	low
Unnamed	33.8	26.6	206.3	low
Unnamed	10.8	37.46	206.34	low
Unnamed	33	9.73	206.4	low
Unnamed	10.2	-26.3	206.7	low
Unnamed	11.5	-32.6	206.7	low
Unnamed	12.6	-31.2	206.7	low
Unnamed	11	20.9	208.1	low
Unnamed	31.8	31	208.1	low
Couperin	79.44	29.74	208.1	low
Unnamed	12.6	-26.45	208.2	low
Unnamed	17.8	-11.4	208.7	low
Unnamed	16.5	-31.73	209	low
Unnamed	10.5	31	209.3	low
Unnamed	12.5	16.2	209.3	low
Unnamed	13.1	-23.4	210.1	low
Unnamed	12.3	-38	210.2	low
Unnamed	10	35.6	210.3	low
Unnamed	10	21.2	210.7	low
Unnamed	11.4	26.3	211	low
Unnamed	12	-23.3	211	low
Tyagaraya	107.9	3.8	211.2	low
Unnamed	13.5	-19.5	211.5	low
Unnamed	11	-20	211.9	low

Unnamed	12	36.5	212	low
Unnamed	31.9	16.3	212.3	low
Unnamed	14.3	-34.1	212.6	low
Zeami	120	-3.1	212.6	low
Unnamed	37	35.42	212.7	high
Unnamed	15	-5.1	212.8	low
Unnamed	10	18.5	214.1	low
Unnamed	53.8	27.9	214.1	low
Unnamed	12	29	214.3	low
Unnamed	10	-19.2	214.5	low
Unnamed	35.2	-7.9	214.6	low
Unnamed	10.1	-28.2	214.8	low
Unnamed	10	-19.1	214.9	low
Unnamed	25.8	38	215.1	low
Unnamed	10.1	14.7	215.7	low
Unnamed	18.9	35.6	217	low
Unnamed	10.5	-39.4	217.1	low
Unnamed	12	-34.8	217.2	low
Unnamed	10.5	-24.7	217.3	low
Unnamed	13.2	22.5	217.3	low
Unnamed	22.5	15.1	218.2	low
Unnamed	20.1	-19.1	218.3	low
Unnamed	12	31.8	219.3	low
Unnamed	10.5	0.5	219.4	low
Unnamed	13.2	19.2	219.6	low
Unnamed	12	1.9	219.7	low
Unnamed	13	3.6	219.9	low
Unnamed	11.3	3	220	low
Unnamed	11.3	21.3	220.4	high
Unnamed	11.8	17.9	220.5	low
Unnamed	41.7	22.6	220.7	low
Unnamed	15.7	33.18	220.89	low
Unnamed	15.8	6.4	221.4	low
Unnamed	20.9	37.9	221.4	low
Unnamed	16	-5.3	221.7	low
Unnamed	13.2	-11.2	222	low
Unnamed	34	1.9	222	low
Unnamed	12	15.8	222.4	low
Unnamed	11	-23.5	222.7	low
Unnamed	16.1	-27.9	222.9	low
Unnamed	10	-11.6	223.1	low
Unnamed	20.5	39.5	223.3	low
Unnamed	14.7	-34.7	223.4	low
Unnamed	10.2	-18	223.6	low
Unnamed	10	-12.1	223.9	low
Unnamed	11.5	-12.7	223.9	low
Unnamed	15.1	14.2	223.9	low

Unnamed	13.1	13.4	224	low
Unnamed	30	-16.05	224.05	low
Unnamed	16	-34.6	224.1	low
Unnamed	10	27.5	224.5	low
Unnamed	14.1	2.6	224.5	low
Unnamed	14.5	-23.4	224.9	low
Bartok	116.7	-29.4	224.9	low
Unnamed	12.3	-16.5	225.1	low
Unnamed	10.2	-18	225.2	low
Unnamed	13	-5.7	225.3	low
Unnamed	20	-16.9	225.3	high
Unnamed	10	-0.9	225.4	low
Unnamed	11.6	-26.5	225.7	low
Unnamed	16	-2.5	225.9	low
Unnamed	49.1	-17.2	226	low
Unnamed	16.5	14.4	226.2	low
Unnamed	12.3	23.9	228.18	low
Unnamed	12.5	-21.5	228.2	low
Unnamed	12.8	-38.4	228.7	low
Unnamed	16.5	-17.5	228.7	low
Unnamed	20.5	18.4	228.8	low
Unnamed	26.1	15.32	228.95	low
Unnamed	10.2	36.84	228.97	low
Unnamed	13.5	20.7	229	low
Unnamed	12	2	229.3	low
Unnamed	10	-24.5	229.5	low
Unnamed	13.2	-1.7	229.5	low
Unnamed	40.1	38	229.5	low
Unnamed	79.8	23.4	229.5	low
Unnamed	18	30.54	229.98	low
Unnamed	10	10.95	229.99	low
Unnamed	21.5	11.9	230	high
Unnamed	34	-20.6	230.7	low
Unnamed	10.7	-10.6	230.8	low
Unnamed	11.5	18.47	231.72	low
Unnamed	60.1	-25	231.9	low
Unnamed	13.5	-14.6	232.2	low
Unnamed	63	23.62	232.56	low
Unnamed	10	3.9	232.6	low
Unnamed	14.1	-26.4	233.3	low
Unnamed	29	7.5	234.2	low
Unnamed	10	-29.8	234.4	low
Unnamed	13.1	37.34	234.61	high
Unnamed	13.3	13.61	235.01	low
Unnamed	16	-11.4	235.1	low
Unnamed	25.5	9.3	235.2	low
Unnamed	11	-30.6	235.3	low

Unnamed	10	33.56	235.48	low
Unnamed	20.8	-18	235.5	low
Unnamed	60	-21.8	235.7	low
Unnamed	20	6.5	235.8	low
Unnamed	36.1	-33.1	236.2	low
Unnamed	15.3	5.9	236.3	low
Unnamed	10.5	13.9	236.31	low
Cezanne	70	-8.5	236.4	low
Unnamed	24.1	-13.26	236.49	low
Unnamed	12.3	-3.9	236.7	low
Unnamed	10	-20.8	237	low
Unnamed	10.5	-4.3	237.3	low
Unnamed	60	9	237.3	low
Unnamed	13.1	24.1	237.5	low
Unnamed	11	-18.8	237.9	low
Unnamed	16.3	17.11	237.93	low
Unnamed	16	-21.03	238	low
Unnamed	12.4	-6	238.5	low
Unnamed	30.9	22.5	238.6	high
Unnamed	14.1	-15.5	239.1	low
Unnamed	14	-12.2	239.3	low
Unnamed	14	-32.8	239.4	low
Unnamed	12.3	-38.3	239.9	low
Unnamed	10	-26.9	240	low
Unnamed	16	9.52	240.63	low
Unnamed	11.2	-25.1	240.7	low
Unnamed	33.5	1.56	240.98	low
Unnamed	10.4	-35	241.2	low
Unnamed	14	21.9	241.6	high
Unnamed	16.7	8.05	241.91	low
Unnamed	55	5.5	242.5	low
Unnamed	10	-14.9	242.6	low
Unnamed	10	12.8	242.8	low
Unnamed	19.5	-13.1	243.3	low
Unnamed	64.9	36.3	244	low
Unnamed	13	-27.4	244.1	low
Unnamed	17.2	-5.6	245.3	low
Unnamed	54	11.7	245.3	low
Unnamed	20.1	12.9	245.5	low
Unnamed	10.4	-10.1	246	low
Unnamed	21.1	8.7	246	low
Unnamed	16.3	-8	246.1	low
Unnamed	14.5	11.7	246.2	low
Unnamed	21	-39.4	246.2	low
Unnamed	26.5	26.2	246.4	low
Unnamed	12	22.3	246.9	low
Unnamed	11.2	-37	247.2	low

Unnamed	10	4.9	247.6	low
Unnamed	17.5	-4.1	247.7	low
Unnamed	10.5	12.5	247.9	low
Unnamed	10	18.1	249.3	low
Unnamed	27.5	-36.62	249.45	low
Unnamed	18	16.04	250	low
Unnamed	12	-31.9	250.1	low
Unnamed	11	-24.9	250.2	low
Unnamed	17	16.6	250.3	low
Unnamed	10	10.3	250.9	low
Unnamed	25	34.09	251.08	high
Unnamed	10	17.2	251.2	low
Unnamed	10.2	-12	251.4	low
Unnamed	13	19.4	251.6	low
Unnamed	64	-0.69	251.69	low
Unnamed	11	16	251.9	low
Unnamed	10.5	-31.1	252.4	low
Unnamed	13	-34.8	252.5	low
Unnamed	21.5	-23.8	252.9	low
Unnamed	11	-2.4	254.1	low
Unnamed	22.2	19.5	254.2	low
Unnamed	14.2	-36.6	254.4	low
Unnamed	44.1	13.3	254.9	low
Unnamed	58.9	-16.9	254.9	low
Unnamed	10	37.2	255.3	low
Unnamed	10	-31.5	255.4	low
Unnamed	27.9	17.9	256.1	low
Unnamed	15.9	-35.9	256.2	low
Unnamed	10.3	-38.1	256.4	low
Unnamed	10	35	256.5	low
Unnamed	14.5	-39.4	257.1	low
Unnamed	12.1	-38.8	257.2	low
Unnamed	54.9	-18.8	257.3	low
Unnamed	10	-6.5	257.4	low
Unnamed	10	16.6	257.4	low
Unnamed	11.9	22.4	257.7	low
Unnamed	12.5	1.4	257.8	low
Unnamed	10	35.3	258.1	low
Unnamed	12.1	-6.4	258.1	low
Unnamed	16.4	-11.9	258.3	low
Unnamed	10	-9.9	259	low
Unnamed	11.5	18.9	259	low
Unnamed	16.5	25.5	259.2	low
Unnamed	10.4	26.6	259.3	low
Unnamed	11.2	8.8	259.3	low
Unnamed	22.5	37.4	260.3	low
Unnamed	12.2	1.6	260.7	low

Unnamed	10.5	-20	260.8	low
Unnamed	10	-32.4	261	low
Unnamed	10.1	8.6	261.4	low
Unnamed	32.9	24.1	261.9	low
Unnamed	11.7	33.8	262.2	low
Unnamed	12.5	-1.8	262.8	low
Unnamed	20	2.1	262.8	high
Unnamed	32	34.1	263	low
Unnamed	60	0	263.9	low
Unnamed	20	-2.6	264	low
Unnamed	24	10.3	264.9	low
Unnamed	11	32.6	265	low
Unnamed	15.1	-7.1	265.8	low
Unnamed	10	-17.7	266.4	low
Unnamed	35.3	25	266.4	low
Unnamed	18.5	38.8	266.7	low
Unnamed	32.1	15.4	266.8	low
Unnamed	13	0.7	268.7	low
Unnamed	13.4	18	269.2	low
Unnamed	21.8	-36.4	269.2	low
Unnamed	10.2	-4.7	269.8	low
Unnamed	10.6	5.9	270.9	low
Unnamed	13.2	-11.3	271.2	low
Unnamed	10	-3.3	271.3	low
Unnamed	11.3	-38	271.3	low
Unnamed	17	35.4	271.6	low
Unnamed	14.3	18.1	271.8	low
Unnamed	12.9	-15.3	273.1	low
Unnamed	10.6	20	273.2	low
Unnamed	12	-35.9	273.2	low
Unnamed	17	22.3	273.2	low
Unnamed	18.2	8.9	273.5	low
Unnamed	39.8	-19.5	273.5	high
Unnamed	11	30.8	273.9	low
Unnamed	26.9	39.4	274.3	low
Unnamed	11.5	-10.3	274.5	low
Unnamed	32.5	-35.28	274.5	low
Unnamed	13.6	38.7	274.6	low
Unnamed	10	-4.2	274.8	low
Unnamed	12.3	17	275.5	low
Unnamed	17	-4.3	275.5	low
Unnamed	10	-6.7	275.9	low
Unnamed	14	21	276	low
Unnamed	30.5	36.6	276.1	low
Unnamed	10.7	19.9	276.2	low
Unnamed	36.6	-29	276.3	high
Unnamed	49.8	-11.6	276.3	low

Unnamed	10.4	15.6	276.5	low
Unnamed	29.9	-14.7	276.5	low
Unnamed	30.1	15.2	277.4	low
Unnamed	12.6	-2	277.6	low
Unnamed	10	-17.3	277.8	low
Unnamed	10	1.2	277.8	low
Unnamed	12	-4.9	278.1	low
Unnamed	56.6	38.3	278.1	low
Unnamed	18.2	21.5	278.5	low
Unnamed	10	2.7	278.6	low
Unnamed	10	-25.8	278.9	low
Unnamed	10.5	26.3	279	low
Unnamed	11.7	-17.2	279.2	low
Unnamed	14.3	8.7	279.5	low
Unnamed	14.2	5	279.6	low
Unnamed	11	-1.4	279.9	low
Unnamed	13.8	12.7	279.9	low
Unnamed	21.8	-26.3	280.5	low
Unnamed	37	35	280.6	low
Unnamed	10.5	4.1	280.7	low
Unnamed	12	-5.9	280.9	low
Unnamed	14.5	-32.9	280.9	low
Unnamed	10.1	30.4	281.2	low
Unnamed	21.9	-19.9	281.2	low
Unnamed	14.5	-16.2	281.3	low
Unnamed	10	32.45	281.83	low
Unnamed	24	7.9	281.9	low
Unnamed	25	-3.1	281.9	low
Unnamed	10.9	-27.4	282.7	low
Unnamed	12.2	17.7	282.8	low
Unnamed	31.5	4.9	282.8	low
Unnamed	11.9	-20	283	low
Unnamed	16	3.2	283	low
Unnamed	37.8	-18.4	283	low
Unnamed	14.1	-24	283.5	low
Unnamed	15	-35.8	283.6	low
Unnamed	31	-2.3	283.7	low
Unnamed	16.1	-35.4	284.2	low
Unnamed	11	-39.4	284.7	low
Unnamed	36.9	27.2	284.8	low
Unnamed	13.3	-23	285.2	low
Unnamed	23.7	-25.6	285.4	low
Unnamed	11.3	-7.6	286	low
Unnamed	11	24.9	286.3	low
Unnamed	20	-7.4	286.8	low
Unnamed	12.7	7.5	287.1	low
Unnamed	10.1	20.3	287.3	low

Unnamed	28.6	-28.9	287.3	low
Unnamed	18.3	-16.9	287.5	low
Unnamed	10.5	-2	287.6	low
Unnamed	21.3	12	287.7	high
Unnamed	41	-3.4	287.7	low
Unnamed	29.8	-18.9	287.8	low
Unnamed	13	-37.8	288.1	low
Unnamed	20	-6.5	288.1	low
Unnamed	18.1	-1.7	288.3	low
Unnamed	11.4	22.8	288.4	low
Unnamed	11.1	-4.2	288.5	low
Unnamed	16.1	18.8	288.6	low
Unnamed	20	-38	288.7	low
Unnamed	26.5	-13.2	288.7	low
Unnamed	13.3	-23.4	288.8	low
Unnamed	18	39.8	289	low
Unnamed	20.5	-39.9	289	low
Unnamed	11	32.8	289.15	low
Unnamed	10	-12.6	289.3	low
Unnamed	10	-36.7	289.6	low
Unnamed	11	32.3	289.8	low
Unnamed	11	29.3	290	low
Unnamed	10.5	26.1	290.1	low
Unnamed	16.2	-0.6	290.4	low
Unnamed	13.7	4.4	290.5	low
Unnamed	14	12.6	290.6	low
Unnamed	19.2	18.6	290.6	low
Unnamed	11.2	-37	291.5	low
Unnamed	28.5	23.2	291.5	low
Unnamed	17.3	-14.3	291.9	low
Unnamed	13.2	-29.9	292	low
Unnamed	31.6	-24.9	292	low
Unnamed	29.6	-28.8	292.2	low
Unnamed	17.5	30.94	292.35	low
Unnamed	38.4	-32.8	293	low
Unnamed	13.8	31.4	293.1	low
Unnamed	19.9	-10.3	293.2	low
Unnamed	36.5	-28.8	293.6	low
Unnamed	14.5	-11.9	293.7	low
Unnamed	48.2	33.5	293.8	low
Unnamed	10.7	-38	294	low
Unnamed	12	-17.2	294.1	low
Unnamed	10	23.5	294.5	low
Unnamed	11	17.8	294.8	low
Unnamed	14.4	36.6	294.8	low
Unnamed	10	-18.6	294.9	low
Unnamed	11.5	-14	294.9	low

Unnamed	16	24.1	295.2	low
Unnamed	12.4	26.9	295.5	low
Unnamed	13.6	28.5	295.6	low
Unnamed	47	25.6	295.61	low
Unnamed	13.1	9	296.1	low
Unnamed	12	-37.9	296.2	low
Unnamed	30.1	-6.2	296.2	low
Unnamed	10.4	13.5	296.3	low
Unnamed	19.7	-30.4	296.5	low
Unnamed	23.6	-33	296.7	low
Unnamed	17.8	-26.3	296.8	low
Unnamed	10.1	-34.3	296.9	low
Unnamed	12.9	-12.2	296.9	low
Unnamed	50.4	30.7	297.3	low
Unnamed	17	25.3	297.6	low
Unnamed	19.5	13	297.7	low
Unnamed	17.5	7	297.9	low
Unnamed	14.6	-34.5	298	low
Unnamed	11.8	36.7	298.1	low
Unnamed	10	10	298.2	low
Unnamed	10.5	-7.8	298.5	low
Unnamed	10	-19.5	298.6	low
Unnamed	10	27.3	298.6	low
Unnamed	15.5	20.9	299	low
Unnamed	11	28.5	299.2	low
Unnamed	10.2	0.8	299.8	low
Unnamed	10	12.6	300.1	low
Unnamed	29.3	-38	300.2	low
Unnamed	111.9	6.7	300.5	low
Unnamed	13.6	-9.8	300.8	low
Unnamed	10.1	3.9	300.9	low
Unnamed	37.9	-4.1	301.1	low
Unnamed	19.5	-39.1	301.3	low
Unnamed	10.4	-32.5	301.6	low
Unnamed	11.2	9.4	301.6	low
Unnamed	33.2	36.9	301.6	low
Unnamed	14.1	20.3	302.1	low
Unnamed	15.5	-4.8	302.1	low
Unnamed	11	-0.6	302.4	low
Unnamed	11	25.3	302.5	low
Unnamed	21.7	-25.9	302.6	low
Unnamed	10	27.7	302.7	low
Unnamed	28.2	28.9	302.8	low
Unnamed	11	25.7	303	low
Unnamed	10.2	38	303.1	low
Unnamed	10.2	-35.3	303.2	low
Unnamed	13.9	-20.1	303.2	low

Unnamed	13.2	35.7	303.4	low
Unnamed	10	39.3	303.5	low
Unnamed	21.5	-27	303.5	low
Calvino	68.9	-4	304	low
Hopper	35.6	-12.4	304.1	low
Unnamed	10.5	0.7	304.2	low
Unnamed	15.8	-26	304.4	low
Unnamed	12.1	-22.5	304.5	low
Unnamed	10.1	30.1	305.1	low
Unnamed	20.1	28.4	305.1	high
Unnamed	10	-33.2	305.2	low
Unnamed	14.2	-24.6	305.2	low
Unnamed	21.1	5.8	305.3	low
Unnamed	20	-23.2	305.6	low
Unnamed	12	33.1	305.8	low
Unnamed	16.1	-9.2	305.8	low
Unnamed	56.4	22.1	306.1	low
Unnamed	13.1	30.1	306.2	low
Unnamed	21.9	14.8	306.6	low
Unnamed	17	-8.1	306.9	low
Unnamed	18.9	-13.9	307	low
Unnamed	10	-12.2	308.2	low
Unnamed	10.5	3	308.3	low
Unnamed	10.4	-21.6	308.5	low
Unnamed	13.3	7.2	308.8	low
Unnamed	11.8	-32.3	308.9	low
Unnamed	110.1	13.2	308.9	low
Unnamed	10.5	-37.9	309.2	low
Unnamed	10	1	309.3	low
Unnamed	41.3	23.2	309.6	low
Unnamed	10	-2.2	309.8	low
Unnamed	27.2	34	309.8	low
Unnamed	17.5	-28.9	309.9	low
Unnamed	24.1	11.6	309.9	low
Unnamed	11	-24.2	310.1	low
Unnamed	10.4	-20.7	310.2	low
Unnamed	11.7	-38.9	310.2	low
Unnamed	13.7	-26.6	310.3	low
Unnamed	11.1	-1.7	310.4	low
Unnamed	16	0.6	310.6	low
Unnamed	16.5	-25.3	310.6	low
Unnamed	11.3	-6.3	310.7	low
Unnamed	10	-1	310.9	low
Unnamed	14.5	27.9	310.9	low
Unnamed	10	-2.8	311.1	low
Unnamed	16.1	-36.4	311.1	low
Lermontov	161.9	15.4	311.1	low

Unnamed	21.2	22.9	311.2	low
Unnamed	12.2	11.7	311.5	low
Unnamed	10.5	12.4	311.7	low
Unnamed	12.2	5.2	312	low
Unnamed	34.6	-23.1	312	low
Unnamed	12	0.7	312.3	low
Unnamed	12.2	-34.7	312.6	low
Unnamed	55.1	3	312.6	low
Unnamed	11	-15.1	312.9	low
Unnamed	10.2	13.5	313	low
Unnamed	27.2	29.9	313.1	low
Unnamed	14.6	-21.8	313.6	low
Unnamed	25.8	-13.7	313.9	low
Unnamed	10.1	27.7	314.4	low
Unnamed	10	-34.9	314.6	low
Unnamed	17	-7.8	314.6	low
Unnamed	10.2	35.9	314.7	low
Unnamed	18.5	-22.8	314.7	low
Unnamed	30.8	-16.5	314.7	low
Unnamed	14.5	17.7	314.8	low
Unnamed	31.1	9.7	315	low
Unnamed	10	38.7	315.1	low
Unnamed	11.9	-13.1	315.1	low
Unnamed	12.7	28.7	315.1	low
Unnamed	22.1	-26.7	315.4	low
Unnamed	29.2	24.5	315.6	high
Unnamed	10	26.8	315.8	low
Unnamed	10.1	33.5	315.9	low
Unnamed	10	-8.6	316	low
Unnamed	10.2	3.3	316.3	low
Unnamed	10.1	-32.5	316.5	low
Unnamed	10.4	-23.4	317.1	low
Unnamed	12	-7.4	317.1	low
Unnamed	11.7	-12.4	317.3	low
Unnamed	10.3	-14.5	317.7	low
Unnamed	13.1	32.3	317.7	low
Unnamed	10.7	-38.2	317.8	low
Unnamed	11.5	-3.5	318.3	low
Unnamed	11	15.7	318.6	low
Unnamed	15.2	30.6	318.8	low
Unnamed	19.2	-12.7	318.9	low
Unnamed	15.2	8.8	319	low
Unnamed	22.2	36.4	319.2	low
Unnamed	41.3	20.5	319.4	low
Unnamed	10.1	2	319.5	low
Unnamed	12.2	32	319.6	low
Unnamed	13	-35.6	319.8	low

Unnamed	13.7	-7.1	319.8	low
Unnamed	13.1	-30.4	319.9	low
Unnamed	27.5	25.7	319.9	low
Unnamed	10.5	35.3	320.2	low
Unnamed	19.5	31.1	320.2	low
Unnamed	10	-11.2	320.4	low
Unnamed	10.5	-21.6	320.4	low
Unnamed	44	-33.5	320.4	low
Unnamed	16.6	0.2	320.5	low
Unnamed	14.1	33.5	320.7	low
Unnamed	10	26.6	320.9	low
Unnamed	11.5	29.3	321.1	low
Unnamed	14.1	-26	321.2	low
Unnamed	10.1	30.5	321.3	low
Unnamed	40.4	37.9	321.3	low
Unnamed	11.5	-2.5	321.4	low
Unnamed	11.5	-22.5	321.5	low
Unnamed	55.4	15.7	321.6	low
Unnamed	12.4	-14.6	321.9	low
Unnamed	25.2	35.1	322.4	low
Unnamed	47.3	17.2	322.5	low
Unnamed	46.5	22.5	322.6	low
Unnamed	24.7	-22.1	322.7	low
Unnamed	10.1	-31.5	323.4	low
Unnamed	47.2	-28.5	323.5	high
Unnamed	17.5	-18.2	323.6	low
Unnamed	20.6	-29.7	323.8	low
Unnamed	12	-17	323.9	low
Unnamed	10.1	37.8	324	low
Unnamed	14.9	23.5	324.1	low
Unnamed	18	35.7	324.1	low
Unnamed	10.1	25.5	324.2	low
Unnamed	12	-8.2	324.3	low
Unnamed	13.6	-36.5	324.4	low
Unnamed	47.3	12.4	324.4	low
Unnamed	28.5	24.4	324.5	low
Unnamed	14.5	-0.3	324.8	low
Unnamed	15.7	-31.7	324.8	low
Unnamed	23.2	34.9	324.9	high
Unnamed	12.1	-35.3	325.1	low
Unnamed	13.4	-1.6	325.1	low
Unnamed	10	36.8	325.2	low
Unnamed	39.6	-18.9	325.2	low
Unnamed	10.3	-10.8	325.6	low
Unnamed	11.4	3.7	325.8	low
Unnamed	10	-0.2	326.2	low
Unnamed	34.2	39.1	326.2	low

Unnamed	23.1	12.4	326.3	low
Unnamed	10.2	1.8	326.4	low
Unnamed	30.5	30.6	326.5	low
Unnamed	13	-15	326.6	low
Unnamed	16.4	32.3	326.7	low
Unnamed	11.4	-23.5	326.9	low
Unnamed	14.8	16.9	326.9	low
Unnamed	11.1	4.7	326.96	low
Unnamed	10	22.3	327	low
Unnamed	18.9	-12.1	327	high
Unnamed	26.1	4.9	327.2	high
Unnamed	14.1	22.9	327.3	low
Unnamed	11.1	3.6	327.7	low
Unnamed	11.3	9.2	327.9	low
Unnamed	27.2	14.5	328.3	low
Unnamed	10	17.3	328.5	low
Unnamed	16.2	8.5	328.8	low
Unnamed	18.2	-5.3	328.9	high
Unnamed	12.1	14.8	329	low
Unnamed	12.1	31.9	329.2	low
Unnamed	19	-1.3	329.3	low
Unnamed	17.5	39.7	329.4	low
Unnamed	13.4	-22	330	low
Unnamed	12	-33.4	330.4	low
Unnamed	18.9	-8.7	330.6	high
Unnamed	19.7	-0.5	331	low
Unnamed	10	23	331.4	low
Unnamed	10.8	-3.4	331.4	low
Unnamed	13.5	-2	331.4	low
Unnamed	11.3	34.8	331.7	low
Unnamed	10.1	13.4	332.1	low
Unnamed	14.9	-17.1	332.1	low
Unnamed	18.7	-27.7	332.3	low
Unnamed	10	23.2	332.6	low
Unnamed	20.1	15.6	332.6	low
Unnamed	16.6	10.7	332.7	low
Unnamed	11	17.4	332.8	low
Unnamed	12	-31.4	332.8	low
Unnamed	12.2	-34.2	332.8	low
Unnamed	20.2	29.6	332.8	low
Unnamed	14.1	32.3	333	low
Unnamed	11.1	34.8	333.1	low
Unnamed	17.5	-3	333.5	low
Unnamed	10.6	23.3	333.9	low
Unnamed	14.5	-25.4	334	low
Unnamed	10.5	10.2	334.4	low
Unnamed	11.6	13.7	334.6	low

Unnamed	13	-18.7	334.6	low
Unnamed	12	-31.4	334.7	low
Unnamed	20.2	31.5	335.1	low
Unnamed	10	-25.1	335.5	low
Unnamed	17	-3.8	335.7	low
Unnamed	25.8	4.7	335.9	low
Unnamed	12.1	20.6	336.1	low
Unnamed	14	12.7	336.1	low
Unnamed	11.1	5.3	336.3	low
Unnamed	10.1	-27.9	336.4	low
Unnamed	10	-8.9	336.6	low
Unnamed	10	-3.5	336.6	low
Unnamed	14.1	10	336.7	low
Unnamed	10.1	-3.6	337.3	low
Unnamed	16.5	28.1	337.3	low
Unnamed	30.5	15.5	337.4	low
Unnamed	10.5	-32.9	337.5	low
Unnamed	12.3	29	337.6	low
Unnamed	10	27.2	337.9	low
Unnamed	11.2	22.2	338.1	low
Unnamed	13.1	-9.1	338.1	low
Unnamed	12.7	-32.1	338.2	low
Unnamed	10.1	33	338.3	low
Unnamed	11.2	-21	339.7	low
Unnamed	13.4	4.2	339.8	low
Unnamed	18.8	-0.1	339.9	low
Unnamed	35.5	-23	339.9	low
Unnamed	10.2	-37.3	340	low
Unnamed	14.8	27.9	340.2	low
Unnamed	10	-6.9	340.6	low
Unnamed	11.2	17.4	340.9	low
Unnamed	14.1	22.7	341.3	low
Unnamed	10.5	-39.9	341.4	low
Unnamed	12.7	-9.1	341.6	low
Unnamed	11	21.8	341.7	low
Unnamed	11.5	35.6	342	low
Unnamed	10.3	-13.1	342.2	low
Unnamed	14.2	10.2	342.2	low
Unnamed	14.2	-22.6	342.5	low
Unnamed	11.2	32.7	342.8	low
Unnamed	20.8	-23.6	343	low
Unnamed	10.5	26.6	343.1	low
Unnamed	10	39.9	343.3	low
Unnamed	11.2	-11.4	343.3	low
Unnamed	10.1	-29.5	343.4	low
Unnamed	18.1	6.5	343.5	low
Unnamed	13.6	38.5	343.8	low

Unnamed	24.2	34	344.1	high
Unnamed	14.1	31.5	344.3	low
Unnamed	15.4	24.2	344.3	low
Unnamed	10.6	36.8	344.4	low
Unnamed	29.2	15.1	344.4	low
Unnamed	10.9	-38.8	344.9	low
Unnamed	10.4	2.3	345.2	low
Unnamed	18.4	-39.7	345.3	low
Unnamed	21.5	-1.4	345.4	low
Unnamed	10	27.6	346.2	low
Unnamed	17.4	-0.4	346.3	low
Unnamed	12.6	11.4	346.8	low
Unnamed	15.6	37.6	346.9	low
Unnamed	10	-23.1	347	low
Unnamed	42.9	-4.7	347.3	low
Unnamed	10	-18.9	347.8	low
Unnamed	37.3	29.1	347.8	low
Unnamed	13.1	-22	347.9	low
Unnamed	21.5	24.1	348.1	low
Unnamed	29.5	-28.2	348.1	low
Unnamed	20.1	13.3	348.6	low
Unnamed	10.3	-39.8	349.1	low
Unnamed	11	16.7	349.1	high
Unnamed	19.2	-11.6	349.1	low
Unnamed	16.7	6.1	349.2	high
Unnamed	10.8	11.1	349.5	low
Unnamed	16.4	14.5	350.1	low
Unnamed	11	31.6	350.4	low
Unnamed	19.2	32.3	350.4	low
Unnamed	16.9	-28.8	350.5	low
Unnamed	16.7	-21.6	350.6	low
Unnamed	10	-15.4	350.7	low
Unnamed	20	5.3	350.7	low
Unnamed	14	29.5	350.9	low
Unnamed	28.2	27	350.9	low
Unnamed	24.1	25.6	351.1	low
Unnamed	16.8	36.9	351.2	low
Unnamed	14.5	2.5	351.8	low
Unnamed	21.5	11.9	352.2	low
Unnamed	12	28.8	352.3	low
Unnamed	12.5	21.6	352.4	low
Unnamed	15	25.3	352.4	low
Unnamed	17.5	-0.9	352.4	low
Unnamed	33.7	38.1	352.8	low
Unnamed	10	7.8	353	low
Unnamed	11.3	15.9	353.1	low
Unnamed	12	23.3	353.2	low

Unnamed	15.8	15.8	353.6	low
Unnamed	21.9	-18	353.6	low
Unnamed	21.9	-32.7	353.9	high
Unnamed	37.3	32.4	354	low
Unnamed	16.9	28.7	354.1	low
Unnamed	11	11.8	354.7	low
Unnamed	13.8	19.5	354.8	low
Unnamed	12.3	-30.4	355	low
Unnamed	13.4	-12.1	355.5	low
Unnamed	13.4	4.2	355.6	low
Unnamed	10	-31.6	355.7	low
Unnamed	10	9.4	355.7	low
Unnamed	22.5	36.1	355.7	low
Unnamed	10	-15.8	355.8	low
Unnamed	23.2	-22.2	355.8	low
Unnamed	10	-30	355.9	low
Unnamed	11.2	-5.6	356.3	low
Unnamed	11.8	-30.8	356.4	low
Unnamed	12.9	-23.9	357.2	low
Unnamed	16.2	30.2	357.2	low
Unnamed	13.5	-24.2	357.4	low
Unnamed	15	-23	357.4	low
Unnamed	14.5	-18	357.8	low
Unnamed	13.1	-26.9	357.9	low
Unnamed	14.3	-9.3	359.1	low
Unnamed	13.6	-12.4	359.3	low
Unnamed	20.7	-14	359.3	low
Unnamed	14.7	9.2	359.5	low
Unnamed	16.6	26.5	359.6	low
Unnamed	37.2	34.4	359.6	low
Unnamed	17	0.2	359.7	high
Unnamed	34.9	11.3	0	low
Unnamed	12.5	-26.4	0.1	low
Unnamed	19.5	-36.4	0.4	low
Unnamed	10.1	-10.9	0.9	low
Unnamed	15.5	-32.7	1.1	low
Unnamed	10.8	-27.6	1.2	low
Unnamed	14.2	-21.1	1.3	low
Unnamed	17	30.5	1.5	low
Unnamed	12	14.6	2.1	low
Unnamed	13	37.8	2.1	low
Unnamed	13.8	-21	2.7	low
Unnamed	19.3	34.2	2.7	low
Unnamed	10	-9.3	2.9	low
Unnamed	14.1	-23	3	low
Unnamed	12.4	18.4	3.1	low
Unnamed	11.4	-32.4	3.2	low

Unnamed	11.6	24.8	3.3	low
Unnamed	10.5	39	4	low
Unnamed	17.8	-18.3	4.1	low
Unnamed	12	16.4	4.2	low
Unnamed	12.8	-12.4	4.3	low
Unnamed	20	39.3	4.8	low
Unnamed	10	29	5	low
Kyosai	38.9	25.2	5	low
Unnamed	10.4	-24.7	5.2	low
Unnamed	13.2	13	5.6	low
Unnamed	13.5	6.8	5.6	low
Unnamed	17	37.9	5.6	low
Unnamed	10.2	-3.3	5.7	low
Unnamed	13.4	-11.1	6.1	low
Unnamed	23.7	-20.3	6.1	high
Unnamed	14.6	36.7	6.8	low
Unnamed	18.5	-24	6.8	low
Unnamed	15	-22.4	6.9	low
Unnamed	20.3	13.2	6.9	low
Unnamed	23.2	15.3	6.9	low
Unnamed	10.5	-2.5	7.2	low
Unnamed	13.7	15.7	7.2	low
Unnamed	14.9	-5.9	7.2	low
Unnamed	13.7	-8	7.3	low
Unnamed	14	17.3	7.3	low
Unnamed	31.7	34.7	7.3	low
Unnamed	11.1	-9.4	7.6	low
Unnamed	17.4	-18.8	7.8	low
Unnamed	28.5	-25.6	7.8	low
Unnamed	12	-36.6	8.1	low
Unnamed	23.1	7.6	8.1	low
Unnamed	15.2	-9.7	8.7	low
Unnamed	10.7	-23.9	8.8	low
Unnamed	10.7	-19.8	9.1	low
Unnamed	15	23.8	9.3	low
Unnamed	14.4	33.2	9.4	low
Unnamed	24.1	39.2	9.4	low
Unnamed	11.4	10.7	9.5	low
Unnamed	10.4	-24	9.7	low
Unnamed	11.8	15.9	10.1	low
Unnamed	12.8	30.3	10.5	low
Unnamed	10	35.2	10.7	low
Unnamed	16.7	-5.1	10.7	low
Unnamed	11.1	-6.9	11	low
Unnamed	13.1	-16.2	11.8	low
Unnamed	15	11.2	12	low
Unnamed	10.2	23.3	12.1	low

Unnamed	16.6	0.5	12.3	low
Unnamed	10	15.8	12.6	low
Unnamed	10.1	30.3	12.8	low
Unnamed	23.2	3.5	12.9	low
Unnamed	14	29.7	13.2	low
Unnamed	16.4	13.2	13.2	low
Unnamed	67.4	36	13.8	low
Unnamed	10.5	-6.1	14	low
Unnamed	12	-21.6	14.5	low
Unnamed	13.8	-27.7	14.9	low
Unnamed	26.2	-25.6	15.1	high
Unnamed	10.7	-31.1	15.2	low
Unnamed	13.9	25.1	15.3	low
Unnamed	15	-14.2	15.8	low
Unnamed	21.7	-24	15.8	low
Unnamed	20.5	25.3	16.2	low
Unnamed	11.1	4.8	16.5	low
Unnamed	16.3	27.7	16.5	low
Unnamed	16	27.2	16.7	low
Unnamed	15.7	-14.4	16.9	low
Unnamed	14.6	-23.6	17	low
Unnamed	14.8	15.6	17.1	low
Unnamed	10.2	11.2	17.4	low
Unnamed	12.2	-29.4	17.5	low
Unnamed	39.4	0.2	17.7	low
Unnamed	29	37.45	19.12	high
Unnamed	31.1	-20	19.2	low
Unnamed	28.1	25	19.3	low
Unnamed	12	6.3	19.5	low
Unnamed	10.8	2.6	19.6	low
Unnamed	12.1	28	20	low
Unnamed	11	-25.8	20.1	low
Unnamed	24.5	24.5	20.3	low
Unnamed	20.4	-1	20.4	low
Unnamed	11	20.9	20.5	low
Unnamed	22.7	8.4	20.6	high
Unnamed	12	-19.3	20.8	low
Unnamed	16.4	-3.9	21.7	low
Unnamed	11	-35	22	low
Unnamed	12	24.6	22	low
Unnamed	10.5	-28.8	22.1	low
Unnamed	11.5	35.62	22.61	low
Unnamed	19	8.1	22.9	low
Unnamed	14.1	20	23.5	low
Unnamed	14.1	-27.7	23.6	low
Unnamed	14.5	20.2	24.3	low
Unnamed	16	27	24.3	low

Unnamed	20.9	-30.5	24.3	low
Unnamed	10.6	11.89	24.43	low
Unnamed	10.7	24.11	24.68	low
Unnamed	17.2	36.3	24.9	low
Unnamed	16.2	39.7	25.61	low
Unnamed	27.5	6.68	25.63	low
Unnamed	12.1	29.3	26	low
Unnamed	17.5	20.6	26.1	low
Unnamed	31.2	17.1	26.1	low
Unnamed	20.5	-7.31	26.25	low
Unnamed	25.5	-4.9	26.5	low
Unnamed	42.4	-20.3	26.8	low
Unnamed	15	-11.87	27.48	low
Unnamed	24	12.72	28.37	low
Unnamed	10	26.69	28.39	low
Unnamed	12.2	25.2	28.9	low
Unnamed	11.2	-22.4	29.6	low
Unnamed	12.2	25.5	29.9	low
Unnamed	13.6	5.66	29.95	low
Unnamed	64	-36.52	30.2	low
Unnamed	17.8	23.8	30.6	low
Unnamed	21.1	22.3	30.6	low
Unnamed	13.6	-7.14	30.84	low
Unnamed	24.2	34.76	31.07	low
Unnamed	32.2	-23.4	31.5	low
Unnamed	45.9	14.8	31.5	low
Unnamed	11	-33.5	31.6	low
Unnamed	45	-6.27	31.85	low
Unnamed	11	-33.2	32.1	low
Unnamed	15.6	-11.27	32.61	low
Unnamed	40.7	-16.7	32.7	low
Unnamed	17	1.35	32.85	low
Unnamed	16.1	-31.3	32.9	low
Suess	64	7.67	33.22	low
Unnamed	31.5	22.3	33.3	low
Unnamed	20	11.71	33.44	low
Unnamed	10.1	-37.3	33.5	low
Unnamed	18.5	-34	34.3	low
Unnamed	21	2.8	34.3	low
Unnamed	15.5	-30.81	34.31	low
Unnamed	28.3	-5.6	35.2	low
Unnamed	19.7	9.4	35.6	low
Unnamed	72.3	35.5	35.6	low
Unnamed	10.4	16.1	35.72	low
Unnamed	28.5	16.2	36.4	low
Unnamed	19.9	-28.8	38.6	low
Unnamed	26.5	-3.7	38.6	low

Unnamed	10	36.35	39.65	low
Unnamed	15.5	24.55	39.69	low
Unnamed	14.9	-29.4	40	low
Unnamed	19.1	6.8	40.2	low
Unnamed	17.6	10.4	40.5	low
Unnamed	19.5	-29.2	40.9	low
Unnamed	90	-36.4	41.25	low
Unnamed	32.4	-21.9	41.6	low
Unnamed	52.5	9.8	41.8	low
Unnamed	13.6	-11	42.4	low
Unnamed	12.5	31.79	42.63	low
Unnamed	11	40.17	42.89	low
Unnamed	24.3	-34.6	43.1	low
Unnamed	31	37.02	43.19	low
Unnamed	28.5	-20.7	43.2	low
Unnamed	13.3	39.6	43.3	low
Unnamed	14.5	23.5	43.6	low
Unnamed	14	21	43.7	low
Unnamed	11.5	-1.4	43.8	low
Unnamed	33.3	34.8	43.8	low
Unnamed	15.5	-31.8	44.4	low
Unnamed	38	-22.82	44.48	high
Unnamed	13.1	-3	44.5	low
Unnamed	29.1	5.2	44.5	low
Unnamed	10	27.98	44.8	low
Unnamed	21.1	14.4	44.8	low
Unnamed	12.5	-39.71	44.98	low
Unnamed	26.2	-31.7	45.2	low
Unnamed	54	-37.6	45.5	low
Unnamed	15.8	40	45.6	low
Unnamed	11	-17.61	45.72	low
Unnamed	18.2	13.1	45.8	low
Unnamed	11	-29.6	45.9	low
Unnamed	13.4	27.26	45.93	low
Unnamed	22.5	29.24	46.05	low
Unnamed	26.2	7.7	46.2	low
Unnamed	14.1	34.55	46.21	low
Unnamed	18.5	19.4	46.3	low
Unnamed	11	-8	46.6	low
Unnamed	10	-31.2	47.5	low
Unnamed	10.5	-5	47.6	low
Unnamed	19	37.7	47.7	low
Unnamed	21.8	-0.4	47.9	low
Unnamed	12.7	-26.9	48.4	low
Unnamed	10.4	5.8	48.7	low
Unnamed	46	11.36	48.7	low
Unnamed	25.7	-32.2	49.2	low

Unnamed	10.1	-17.5	49.3	low
Unnamed	11.8	37.3	49.7	low
Unnamed	13.5	4	49.7	low
Unnamed	30.5	-25	49.9	low
Unnamed	12.5	9.1	50.1	low
Unnamed	13.9	-13.5	50.1	low
Unnamed	28.2	36	51	low
Unnamed	22.4	-2.5	51.3	low
Unnamed	13	22.9	51.4	low
Unnamed	13.8	-4.5	51.4	low
Unnamed	10	36.3	51.6	low
Unnamed	11.2	-39.5	52	low
Unnamed	12.2	38.1	52	low
Unnamed	14.4	1.1	52	low
Unnamed	17.4	12.5	52	low
Unnamed	13.2	-21.2	52.4	low
Unnamed	60	31.1	52.55	low
Unnamed	26.4	19.6	53.2	low
Unnamed	25.5	21.5	53.5	low
Unnamed	14.5	-30.1	53.7	low
Unnamed	27.5	18.93	53.87	high
Unnamed	37.2	-3.2	54.3	low
Unnamed	13.1	17.5	54.6	low
Unnamed	12.9	-8	55	low
Unnamed	21.3	10.2	55.9	low
Unnamed	12.3	-12.6	56	low
Unnamed	16.2	8.9	56.3	low
Unnamed	11.8	13.9	56.7	low
Unnamed	27.4	-2.6	57.4	low
Unnamed	10.4	0.3	57.6	low
Unnamed	10.5	36.6	57.9	low
Unnamed	47.6	17.1	57.9	low
Unnamed	10.2	-13.7	58.1	low
Unnamed	23	-24.4	58.2	low
Unnamed	24.5	0.9	58.2	low
Unnamed	18.8	37.2	58.3	low
Unnamed	20.1	8.5	58.4	low
Unnamed	10	-13.4	58.5	low
Unnamed	12.2	1.7	59	low
Unnamed	39.5	-29.1	59	low
Unnamed	11	-0.9	59.1	low
Unnamed	11.3	-29.9	59.1	low
Unnamed	39.6	15.2	59.2	low
Unnamed	21.2	-3.1	59.4	low
Unnamed	27.4	-11.7	59.8	low
Unnamed	11	-21.7	60.3	low
Unnamed	19.8	-27.4	60.3	low

Unnamed	16.8	9.4	60.7	low
Unnamed	16.8	35.7	60.7	low
Unnamed	26	1.9	61.3	low
Unnamed	12	-13.6	61.7	low
Unnamed	11.2	-17.3	62.3	low
Unnamed	18.2	-38.5	62.9	low
Unnamed	10.1	-35.3	64.2	low
Unnamed	10	-38.7	64.3	low
Unnamed	11.1	39.4	64.3	low
Unnamed	19.1	-25.8	64.3	low
Unnamed	10.8	39.8	64.5	low
Unnamed	12.2	13	64.5	low
Unnamed	13.1	-1	64.5	low
Unnamed	14.4	-25.3	64.9	low
Firdousi	101.4	3.5	65.4	low
Unnamed	35.3	-26.5	65.9	low
Unnamed	10.2	-34.6	66	low
Unnamed	35.1	-6	66	low
Unnamed	15.2	-9.9	66.1	high
Unnamed	19.8	6.2	66.4	low
Unnamed	10.3	-5.7	66.5	low
Unnamed	21.1	20.6	66.5	low
Unnamed	12.1	-32.3	66.9	low
Unnamed	10.9	21.8	67.2	low
Unnamed	11	16.8	67.3	low
Unnamed	10.2	39.7	67.6	low
Unnamed	17.5	-0.6	67.9	low
Unnamed	23.1	-17.7	68	low
Unnamed	15	-36.5	68.2	low
Unnamed	10	39.9	68.6	low
Unnamed	10.3	32.1	68.7	low
Unnamed	11	-12	68.7	low
Unnamed	12	-3.3	68.9	low
Unnamed	44.3	27.4	69.1	low
Unnamed	13.7	14.2	69.2	low
Unnamed	29.3	3.6	69.3	low
Unnamed	15.2	-20.8	69.4	low
Unnamed	10.3	10.3	69.8	low
Unnamed	14.8	11.5	69.8	low
Unnamed	10.8	-2.2	70.2	low
Unnamed	18	15.1	70.3	low
Unnamed	12.7	32.4	70.8	low
Unnamed	13.5	35.8	70.9	low
Unnamed	16.4	6.4	70.9	low
Unnamed	16.5	35.1	71.4	low
Unnamed	13.4	-3.9	71.7	low
Unnamed	10	19.8	72	low

Unnamed	11	-36.5	72	low
Unnamed	18.3	-35.5	72.2	low
Unnamed	11.2	-25.2	72.9	low
Unnamed	55.7	29.7	72.9	low
Unnamed	11.3	19.7	73.1	low
Unnamed	15.1	34.4	73.6	low
Unnamed	19.4	-27.4	73.8	low
Unnamed	10.1	-6.1	73.9	low
Unnamed	11	-15.6	74.2	low
Unnamed	21.1	13.3	74.3	low
Unnamed	12.1	-28.7	74.4	low
Unnamed	12	-6.7	74.5	low
Unnamed	10	19.7	75	low
Unnamed	21.5	29.6	75.1	low
Unnamed	15	32.4	75.2	low
Unnamed	17.5	19.4	75.3	low
Unnamed	10	3.2	75.8	low
Unnamed	11.2	-5.4	75.9	low
Unnamed	17	32.8	76.5	low
Unnamed	25	34.1	76.8	low
Unnamed	15.5	-8.4	77.3	low
Unnamed	21.3	38.4	77.5	low
Unnamed	10	11.6	77.9	low
Unnamed	10.3	37.4	78.2	low
Unnamed	11	-12.8	78.3	low
Unnamed	15	9.4	78.6	low
Unnamed	14.7	14.9	78.7	low
Unnamed	24.1	38.5	78.7	low
Unnamed	10.4	19	79	low
Unnamed	13.5	-25	79.1	low
Unnamed	26.6	29	79.1	high
Unnamed	14.3	24.4	79.2	low
Unnamed	23.1	39.7	79.7	low
Unnamed	23.7	-33.5	80	high
Unnamed	29.5	25.9	80.1	low
Unnamed	12.3	10.6	80.5	low
Unnamed	10.1	-16.6	80.7	low
Unnamed	10	25.5	81.2	low
Unnamed	25.1	31.5	81.5	low
Unnamed	17.6	-35	81.7	low
Unnamed	17.6	-34.7	82	low
Unnamed	10.4	7.7	82.1	low
Unnamed	39.8	-10.4	83	low
Unnamed	15.2	11.2	83.4	low
Unnamed	36.5	-5.1	83.4	low
Unnamed	10	6.9	83.5	low
Unnamed	20.7	-2.7	83.5	low

Unnamed	20.5	-35.5	83.8	low
Unnamed	13	25.3	84.1	low
Unnamed	19.5	2.5	84.5	low
Unnamed	12.5	15.4	84.6	low
Unnamed	10.6	24.9	85	low
Unnamed	60.7	-15.6	85	low
Unnamed	18.2	12.1	85.4	low
Unnamed	11.9	-12.8	85.9	low
Unnamed	10	30.7	86.3	low
Unnamed	10.8	-35.2	86.3	low
Unnamed	19.1	-1.1	86.3	low
Unnamed	16.2	32.6	87	low
Unnamed	44.4	-33.7	87.3	low
Unnamed	10.1	-28.3	87.6	low
Unnamed	20.4	5.2	88.6	low
Unnamed	11.3	37.6	88.7	low
Unnamed	34.2	-14.5	88.9	low
Unnamed	12.5	-0.2	89.4	low
Unnamed	28.3	7	89.8	low
Unnamed	10	24.4	90.4	low
Unnamed	14.2	26.8	90.4	low
Unnamed	11.6	18.7	90.9	low
Unnamed	12.5	-11.9	90.9	low
Unnamed	19.5	-5.1	91.3	low
Unnamed	13.2	-2.3	91.6	low
Unnamed	13.9	26.2	92	low
Unnamed	23.8	8.6	92	low
Unnamed	25.6	-19.7	92.2	low
Unnamed	12	28.5	92.3	low
Unnamed	11.4	35.9	93.3	low
Unnamed	10.1	-3.8	94.5	low
Unnamed	10.5	24.24	95.4	low
Fonteyn	29.4	32.8	95.6	low
Unnamed	14.5	4.4	95.7	low
Unnamed	16.5	6.5	95.8	low
Unnamed	25.8	-22.6	96.1	low
Unnamed	11.6	26.9	96.5	low
Unnamed	11.5	23.9	96.7	low
Unnamed	18.2	-19.7	96.8	low
Unnamed	10	21.9	97.5	low
Unnamed	16.5	-17.7	97.6	low
Unnamed	11.2	-12.5	98.2	low
Unnamed	21.3	-16.6	98.2	low
Unnamed	32.5	29.2	100.3	low
Unnamed	10	-38.2	102.3	low
Unnamed	10.3	-33.3	102.6	low
Unnamed	12.8	10.5	102.7	low

Unnamed	17.5	4.7	102.7	low
Unnamed	10	-18.3	102.8	low
Unnamed	13.6	7.8	103.1	low
Unnamed	19.1	-1.8	103.1	low
Unnamed	11.6	10.9	103.2	low
Unnamed	26.1	38.3	103.8	low
Unnamed	10.5	13.7	104.3	low
Unnamed	16	-35.6	104.3	low
Unnamed	15	23.7	104.9	low
Unnamed	10.3	30.2	105.1	low
Unnamed	12.8	-1.3	105.4	low
Unnamed	10.1	4.3	105.7	low
Unnamed	38.7	-5.5	106.1	low
Unnamed	10	-0.4	106.2	low
Unnamed	11.1	-1.1	106.2	low
Unnamed	11.5	14.6	106.3	low
Unnamed	24.6	31.3	106.9	low
Unnamed	10.1	29.1	107.4	low
Unnamed	22.8	20.4	107.7	low
Unnamed	35	23.3	108.3	low
Unnamed	13.6	4.6	108.9	low
Unnamed	10.4	5.3	109	low
Unnamed	12	-26.6	109.3	low
Unnamed	23.2	-11.2	110.4	low
Unnamed	20.7	32.2	110.9	low
Unnamed	12	-2.6	111.7	low
Unnamed	13.2	-9.3	112.8	low
Unnamed	14.5	-1.8	112.8	low
Unnamed	10.8	0.1	113.2	low
Unnamed	16.6	22	113.3	low
Unnamed	10	36.2	113.8	low
Unnamed	10.2	-36.5	114.1	low
Unnamed	16.9	-7.3	116	low
Unnamed	32.5	-9.9	116.4	low
Unnamed	10.3	-1	116.8	low
Unnamed	12.8	12	117.1	low
Unnamed	18.6	-25.6	117.5	low
Unnamed	10.7	-16	118.3	low
Unnamed	12.6	23.1	118.5	low
Unnamed	17.1	-15.7	118.5	low
Unnamed	40.4	-36.6	118.6	low
Unnamed	17	27	118.8	low
Unnamed	13.4	26	118.9	low
Raditladi	254.1	27.2	119.2	low
Unnamed	45	-7.22	120.51	low
Unnamed	10	24.8	121.2	low
Unnamed	10.8	-14.4	121.3	low

Unnamed	10.4	37.7	121.8	low
Unnamed	11.6	22.8	122.6	low
Unnamed	13.6	-4	122.9	low
Unnamed	10.1	-21.5	123.9	low
Unnamed	10.1	33.7	124.2	low
Unnamed	16.3	-11.1	124.9	low
Eastman	66.1	9.5	125.8	low
Unnamed	10	20.9	126.3	low
Unnamed	12	-7.5	126.5	low
Unnamed	13.2	26.7	127	low
Unnamed	18.3	-0.3	127.3	low
Unnamed	10.8	22.1	127.4	low
Unnamed	11.6	-34.3	127.6	low
Unnamed	13	25	127.6	low
Unnamed	15.4	7.9	127.6	low
Unnamed	24.5	-12.6	127.7	low
Unnamed	13.6	14.9	128.8	low
Unnamed	25.6	-18.2	128.9	low
Unnamed	10.6	32.2	129.1	low
Unnamed	14.5	18.7	129.8	low
Unnamed	14	-23.5	129.9	low
Unnamed	10.2	-1.6	130	low
Unnamed	10	21.3	130.1	low
Unnamed	12.2	-10.8	130.4	low
Unnamed	14.3	-13	130.4	low
Unnamed	24.5	17.7	130.5	low
Unnamed	14.5	34	130.6	low
Unnamed	11	36.8	130.8	low
Unnamed	10	1.9	131.2	low
Unnamed	13.5	20.1	131.3	low
Unnamed	12.7	-12.4	131.6	low
Unnamed	11.1	34.59	131.7	low
Unnamed	11.2	-7.8	131.8	low
Unnamed	12.2	6	131.8	low
Unnamed	10	-0.9	132	low
Unnamed	11.1	14.1	132.1	low
Unnamed	10.2	17.5	132.4	low
Unnamed	14.2	-1.5	133	low
Unnamed	45.5	12.4	133.4	low
Unnamed	10	-1.8	133.5	low
Unnamed	11.3	25.5	133.5	low
Unnamed	41.9	-2.1	133.5	high
Unnamed	10	15.85	133.65	low
Unnamed	14.4	16.1	134	low
Unnamed	33.1	-21.8	134	low
Unnamed	12.9	10.2	134.3	low
Unnamed	13.5	-4.7	134.4	low

Unnamed	11.1	-10.5	135.3	low
Unnamed	13.1	22.9	135.4	low
Unnamed	14.2	-18.9	135.4	low
Unnamed	11.5	0.3	136.4	low
Unnamed	14.3	-4.7	136.5	low
Unnamed	16.4	2.3	136.5	low
Unnamed	46.1	-12.3	136.6	low
Unnamed	15.1	6.3	136.7	low
Unnamed	10	-17.6	136.9	low
Unnamed	53	30.1	137	low
Unnamed	11	4.8	137.2	low
Unnamed	18.1	-18.9	137.3	low
Unnamed	25.9	5.7	137.3	low
Unnamed	13	15.9	137.7	low
Unnamed	27.4	18.9	137.7	low
Unnamed	20.1	19.3	138.1	low
Unnamed	13	-18.9	138.2	low
Unnamed	12	22.3	138.3	low
Unnamed	10.5	-25.6	138.5	low
Unnamed	15.5	-1.5	138.5	low
Unnamed	45.3	1.9	138.6	low
Unnamed	10	10.3	138.9	low
Unnamed	14.6	27.6	139.4	low
Unnamed	13.2	-39	139.7	low
Unnamed	10.8	25	140.1	low
Unnamed	26.1	-34.9	140.6	low
Unnamed	33.5	-23	140.7	low
Unnamed	11.5	-26	140.8	low
Unnamed	12.5	-15.9	141	low
Unnamed	15.7	-35.7	141	low
Unnamed	12.2	28.8	141.5	low
Unnamed	56	7.6	141.5	low
Unnamed	10.6	9.7	141.8	low
Unnamed	10.1	-32.6	141.9	low
Unnamed	10.2	13.7	141.9	low
Unnamed	15.1	-15	142.4	low
Unnamed	31.2	-10.8	142.4	low
Unnamed	24.2	23.8	142.5	low
Unnamed	11	-26.2	142.6	low
Unnamed	14.8	22.5	142.8	low
Unnamed	18.5	10.8	143.4	low
Unnamed	10.3	-29.9	143.5	low
Unnamed	11	19.5	144.2	low
Moody	76.8	-13.3	144.9	low
Unnamed	15.8	-24.9	145	low
Unnamed	11.5	-11.4	145.6	low
Unnamed	10.1	-32.2	145.9	low

Unnamed	10.5	29.1	146	low
Unnamed	11.6	-39.1	146.2	low
Unnamed	26.3	31.3	146.2	low
Kertesz	31.6	27.3	146.2	low
Unnamed	14	24.1	146.3	low
Unnamed	10.1	-18.6	146.5	low
Unnamed	11.1	4.6	146.6	low
Unnamed	26.1	-14.6	146.9	low
Unnamed	13.1	-18.5	147.3	low
Unnamed	37.4	8.7	147.3	low
Unnamed	18.7	24.1	147.4	low
Unnamed	21.7	29.1	147.6	low
Unnamed	10.6	-21.2	147.7	low
Unnamed	17.7	0.9	147.8	low
Unnamed	13.8	-16.1	148	low
Unnamed	15.9	6.6	148.1	low
Unnamed	15.5	31.9	148.6	low
Unnamed	13.8	24.6	148.7	low
Unnamed	19.9	-24.2	148.9	low
Unnamed	15	-1.4	149.2	low
Unnamed	21.2	-26.2	149.4	low
Unnamed	23.4	-30.6	149.4	low
Unnamed	10.5	3.8	149.5	low
Unnamed	16	-6.9	149.8	low
Unnamed	10.2	10.1	150	low
Unnamed	10	-20.8	150.1	low
Unnamed	12	11.9	150.1	low
Unnamed	13	16	150.1	low
Unnamed	10.8	8.7	150.2	low
Unnamed	13.2	-1.3	150.7	low
Unnamed	10	-11.3	150.8	low
Unnamed	10.3	-0.7	151.9	low
Unnamed	14.5	16.3	152.1	low
Unnamed	10	-10.6	152.3	low
Unnamed	26.5	-22.7	152.5	low
Unnamed	20	-25.6	153.1	low
Unnamed	38.3	27	153.1	low
Unnamed	10.5	-27.3	153.2	low
Unnamed	25.1	-21.8	153.2	low
Unnamed	10	20.3	153.4	low
Unnamed	10.6	34	153.5	low
Unnamed	13	-22.9	153.5	low
Unnamed	11	-32	153.6	low
Unnamed	10.4	-3.5	153.9	low
Unnamed	10.6	-13.8	154	low
Unnamed	14.6	1.4	154.4	low
Unnamed	11.6	17.9	154.6	low

Unnamed	21.8	38.3	154.7	low
Unnamed	11.6	-32.5	154.8	low
Unnamed	18.2	-19.2	155	low
Unnamed	16	31.8	155.1	low
Unnamed	12.9	-21.8	155.2	low
Unnamed	10.7	12.7	155.3	low
Unnamed	12.8	-20.1	155.9	low
Unnamed	54.4	4.7	155.9	low
Unnamed	18.5	6.7	156	low
Unnamed	10.2	-8	156.2	low
Unnamed	19	-25.5	156.4	low
Unnamed	15	-2.5	156.7	low
Unnamed	11.6	-13.8	156.8	low
Unnamed	12.2	15.4	156.8	low
Unnamed	10.7	20.9	157	low
Unnamed	18.2	19.8	157.7	low
Unnamed	17	-16.5	157.8	low
Unnamed	18.8	-35.9	158.2	low
Unnamed	14.8	-11.7	158.3	low
Unnamed	10.1	-17.7	158.4	low
Unnamed	10.7	0.7	158.5	low
Unnamed	10.4	-5.1	158.8	low
Unnamed	10.2	28.7	158.9	low
Unnamed	12.1	-25.1	158.9	low
Unnamed	18.2	6.5	159.3	low
Unnamed	24.5	15.1	159.3	low
Unnamed	33.9	38.5	159.4	low
Unnamed	10.6	5.2	160	low
Unnamed	13.3	32.7	160.5	low
Unnamed	17	3.7	160.5	low
Unnamed	16	-29.2	160.7	low
Unnamed	12.6	16.7	160.9	low
Unnamed	14.8	27.2	161.1	low
Unnamed	12.5	17.3	161.4	low
Unnamed	10	-29.5	161.6	low
Unnamed	11.1	-2.3	161.8	low
Unnamed	16.5	34.9	162	low
Unnamed	18.2	8.2	162	low
Unnamed	14.6	27	162.1	low
Unnamed	13.5	-4.1	162.2	low
Unnamed	18	-20.27	162.55	low
Unnamed	11.2	-22	162.7	low
Unnamed	13.5	4.1	162.7	low
Unnamed	13.7	27.5	162.8	low
Unnamed	24.7	-24.5	163	low
Apollodorus	39.7	30.5	163.4	low
Unnamed	23.9	-4.8	163.6	low

Unnamed	40.2	-2.3	163.6	low
Unnamed	16.2	21.2	163.9	low
Unnamed	11	-31.1	164.3	low
Unnamed	11.1	26.3	164.5	low
Unnamed	15	-37.1	164.6	low
Unnamed	14.5	33.3	164.7	low
Unnamed	13.6	37.8	164.8	low
Unnamed	16.8	20.1	164.9	low
Unnamed	26.5	-25.8	165.6	low
Unnamed	11.1	-14.8	166.3	low
Unnamed	12.4	-32.5	166.4	low
Unnamed	14.2	19.1	166.5	low
Unnamed	11	-11.6	167.5	low
Unnamed	13.2	-30.7	168	low
Unnamed	15.6	-6	168.3	low
Unnamed	22.8	2	168.3	high
Unnamed	11.5	28.3	168.4	low
Unnamed	12	-26.9	168.7	low
Unnamed	16	23.5	168.7	low
Unnamed	22.5	-18.1	168.9	low
Unnamed	11.9	-15	169.5	low
Unnamed	42.8	-34.3	169.7	low
Unnamed	10	-23.8	169.9	low
Unnamed	13.2	23.1	170	low
Unnamed	11.7	-11.1	170.1	low
Unnamed	17.1	-37.2	170.4	low
Unnamed	10.4	-39.7	170.8	low
Unnamed	45.3	-19.6	170.8	low
Unnamed	36.5	0.4	170.9	low
Unnamed	12.8	-24.6	171.2	low
Unnamed	43.2	-14.2	171.2	low
Unnamed	10.6	22.1	171.5	low
Unnamed	17.2	36.1	171.6	low
Unnamed	20.9	25.5	171.8	low
Unnamed	39.9	13.4	172.5	low
Unnamed	12.5	9	172.9	low
Unnamed	24.5	-4.1	173	low
Unnamed	11.3	0.5	173.1	low
Unnamed	11.5	28.8	173.1	low
Unnamed	21.8	38	173.4	low
Unnamed	10	-1.5	173.5	low
Unnamed	10	34	173.5	low
Unnamed	10	-6	173.7	low
Unnamed	28.9	24.1	174.1	high
Unnamed	12.3	30.7	174.5	low
Unnamed	20	-5.2	174.6	low
Unnamed	10	20.5	175	low

Unnamed	13.2	36.7	175	low
Unnamed	33.8	26.4	175.5	low
Unnamed	10	27.4	175.6	low
Unnamed	11.9	-15.8	175.6	low
Unnamed	14.2	30.7	175.6	low
Unnamed	22	-2.5	175.8	low
Unnamed	11.8	-11.1	176	low
Unnamed	13	25.2	176	low
Unnamed	34.4	-30.9	176.1	low
Unnamed	12	13.1	176.2	low
Unnamed	10	-11.35	176.5	low
Unnamed	27	5.8	176.5	low
Unnamed	10	-9.1	177.2	low
Unnamed	16	31.7	177.3	low
Unnamed	13.5	19.4	177.5	low
Unnamed	14	19.46	177.5	low
Unnamed	11.8	35.2	177.6	low
Unnamed	10.9	17.1	178.1	low
Unnamed	10.5	-9.5	178.2	low
Unnamed	15.5	-1.7	178.3	low
Unnamed	17.8	39.3	178.5	low
Unnamed	20.3	-36.7	178.5	low
Unnamed	15	-3.1	178.7	low
Unnamed	13	-29.3	178.9	low
Unnamed	17.5	0.9	179	low
Unnamed	15.5	26.6	179.2	low
Unnamed	20	9.7	179.3	low
Unnamed	56	25.5	179.4	low
Unnamed	14.5	1.8	179.7	low

Table A.3: Lunar craters with high-reflectance ejecta (Copernican group)

Name	D [km]	Lat	Lon	Ejecta	Uncertainty
Dante G	27.68	24.75	181.408	halo	low
De Vries R	13.5	-20.545	181.539	halo	low
Moore F	24.2	37.314	185.062	distinct	low
Unnamed	12	-19.065	186.051	halo	low
Unnamed	11	27.157	186.084	halo	low
Unnamed	11.5	22.441	188.037	halo	low
Zhukovskiy Z	35	9.745	192.819	halo	low
Crookes	49.65	-10.372	194.922	distinct	low
Jackson	70.9	22.013	196.703	distinct	low
Mohorovicic F	14	-18.715	196.736	halo	low
Unnamed	16.5	1.138	200.529	distinct	low
Unnamed	13.1	15.626	205.024	halo	low
Evdokimov	10	35.006	207.421	distinct	low

Unnamed	12	-12.482	210.488	distinct	low
Unnamed	14.5	27.619	211.385	distinct	low
Unnamed	12.3	6.216	214.775	intermediate	low
Unnamed	13	7.371	215.435	halo	low
Klute W	31.3	38.007	216.721	intermediate	low
Unnamed	10.8	8.195	219.623	halo	low
Vavilov	98	-0.874	222.23	intermediate	low
Unnamed	10.5	-18.69	221.42	halo	high
Kekule M	20	12.053	221.997	halo	low
Das	38	-26.597	222.993	intermediate	low
Unnamed	19	-34.648	223.013	distinct	low
Unnamed	16.5	-1.908	224.949	halo	low
Unnamed	12	-28.74	227.34	distinct	low
Unnamed	10.8	31.444	227.439	halo	low
Unnamed	11.2	-11.949	228.494	halo	high
Unnamed	16.5	25.535	229.497	halo	low
Unnamed	11	-32.731	229.747	halo	low
Unnamed	15	38.205	233.77	halo	low
Unnamed	10.2	13.504	234.331	distinct	low
Unnamed	10.2	29.532	234.595	halo	low
Unnamed	13.5	4.605	239.797	halo	low
Unnamed	10	34.281	240.003	distinct	low
Unnamed	10.3	-32.404	241.835	halo	low
Unnamed	17	-22.079	244.554	distinct	low
Ohm	63.9	18.286	246.335	distinct	low
Unnamed	12.3	15.321	250.8	halo	low
Unnamed	14	29.126	251.944	halo	low
Unnamed	18	25.594	252.154	halo	low
Golitsyn	36	-25.277	254.883	halo	high
Unnamed	10	3.314	259.79	distinct	low
Unnamed	10.8	18.464	261.716	halo	low
Lents Lenz J	15.82	-3.71	262.666	halo	low
Unnamed	11.6	10.372	265.535	halo	low
Unnamed	15	21.889	266.371	halo	low
Sundman V	18.4	11.961	266.458	halo	low
Laue G	29.24	27.883	266.689	distinct	low
Aston L	10.08	35.46	273.53	halo	low
Glushko	43	8.08	282.37	distinct	low
Riccioli H	17.5	1.106	284.961	halo	low
Darwin C	15.3	-20.53	288.89	intermediate	low
Byrgius A	18	-24.585	296.198	distinct	low
Sirsalis F	12.63	-13.603	299.865	distinct	low
de Gasparis B	11.87	-27.06	307.37	halo	low
Fourier C	13.81	-28.58	307.96	halo	low
Mersenius C	13.6	-19.77	314	halo	low
Argelander D	10.69	-17.65	4.39	halo	low
Hipparchus C	16.51	-7.404	8.235	halo	low

Godin	33.55	1.8	10.14	intermediate	low
Alfraganus C	10.3	-6.15	18.06	halo	low
Cyrillus A	15	-13.801	23.108	distinct	low
Beaumont D	12	-17.066	26.208	halo	low
Polybius A	16	-23.038	27.981	halo	low
Gutenberg A	14.8	-9.05	39.92	halo	low
Rheita P	10.32	-37.97	44.42	halo	low
Proclus	26.91	16.044	46.918	distinct	low
Tralles A	17.2	27.401	47.056	halo	low
Stevinus	74	-32.533	54.199	distinct	low
Cleomedes A	13	28.872	55.096	halo	low
Fraunhofer G	14	-38.535	58.394	halo	low
Geminus C	14	33.819	58.75	halo	low
Furnerius A	13	-33.555	59.054	distinct	low
Condorcet T	14.67	11.76	65.81	distinct	low
Palitzsch B	39	-26.4	68.4	halo	low
Behaim N	10	-16.109	73.567	halo	low
Marinus E	17.52	-36.358	76.888	intermediate	low
Gauss E	10.45	35.33	77.68	halo	low
Hecataeus L	23.95	-19.08	78.97	halo	low
Banachiewicz B	23.02	5.32	78.99	halo	low
Ansgarius N	10.23	-11.92	81.16	halo	high
Unnamed	13	25.673	82.402	halo	low
Unnamed	11	26.959	84.743	halo	low
Unnamed	10	-29.437	85.51	distinct	low
Unnamed	10	-29.993	85.601	distinct	low
Gibbs D	14.21	-13.14	85.9	halo	low
Unnamed	10	-23.699	87.992	intermediate	low
Goddard A	11.06	17.06	89.74	intermediate	low
Unnamed	10	-16.969	93.933	distinct	low
Purkyne D	12.05	1.072	96.081	halo	low
Giordano Bruno	21.4	35.995	102.914	distinct	low
Al-Khwarizmi K	22.3	4.501	108.158	halo	low
Unnamed	11.4	21.38	108.61	halo	low
Unnamed	10.5	-16.209	109.114	halo	low
Milne N	37	-35.896	111.317	distinct	low
Unnamed	20	-19.803	117.359	distinct	low
King	77	4.93	120.584	distinct	low
Necho	31.2	-5.26	123.328	distinct	low
Unnamed	10.5	23.016	126.928	halo	low
Unnamed	10	-37.376	131.852	halo	low
Unnamed	18	23.596	137.673	halo	low
Unnamed	10.1	17.211	138.299	halo	low
Unnamed	10.6	32.862	138.53	halo	low
Glazenap E	13	-1.731	139.256	halo	low
Unnamed	20	25.739	140.905	halo	low
Benedict	14.6	4.337	141.564	halo	low

Unnamed	13.5	-30.62	145.654	distinct	low
Gagarin G	15	-20.529	150.567	halo	low
Unnamed	11.2	-17.969	150.659	halo	low
Unnamed	13	-26.443	150.895	halo	low
Unnamed	18.5	15.384	151.656	distinct	low
Unnamed	10	24.194	155.069	distinct	low
Unnamed	10	-7.529	156.807	halo	low
O Day M	12	-31.596	157.117	halo	low
Steno Q	29.1	29.037	157.723	halo	low
Ventris M	18	-5.689	157.921	distinct	low
Unnamed	10.7	10.883	162.085	halo	low
Papaleksi Q	12.2	9.547	162.505	halo	low
Mandel shtam F	13	5.095	166.133	distinct	low
Unnamed	12.5	35.6	166.232	halo	low
Spencer Jones H	15.1	11.928	168.138	halo	low
Dufay B	21	8.366	171.191	halo	low
Unnamed	10	17.502	171.66	halo	low
Unnamed	11	28.18	173.454	halo	low
Aitken A	14	-13.867	173.487	distinct	low
Larmor Q	21.9	28.674	176.323	distinct	low
Virtanen	44	15.648	176.778	intermediate	low
Unnamed	10.7	0.181	176.983	halo	low
Unnamed	11.8	15.76	177.325	distinct	low
Daedalus M	12	-8.033	179.505	halo	low

Table A.4: Lunar craters with sharp rims and no high-reflectance ejecta (Eratosthenian group)

Name	D [km]	Lat	Lon	Uncertainty
Unnamed	11.9	13.6	180.45	low
Unnamed	19	36.06	180.56	low
Unnamed	10.5	2.72	181.54	high
Unnamed	16.3	8.79	181.82	low
Unnamed	16	-33.81	182.89	low
Dante E	43	26.7	183	low
Unnamed	14	30.37	183.38	low
Hayford	24.4	12.84	183.97	low
Unnamed	10	1.99	184.65	high
Unnamed	10.5	28.86	184.71	low
Unnamed	12	-28.87	185.5	low
Unnamed	11.5	6.67	185.87	low
Unnamed	12.1	-19.05	186.06	low
Amici P	24.9	-12.26	186.22	high
Oppenheimer V	29.3	-32.1	186.95	low
Ehrlich N	20.2	38.9	186.97	high
Krasovskiy F	14.7	3.74	187.57	low
Unnamed	14	-15.92	187.58	low

Unnamed	11	-36.32	187.74	low
Parsons M	24	33.81	188.32	high
Unnamed	11.6	-39.34	188.33	high
De Vries R	13.2	-20.26	188.47	low
Bok	43	-20.2	188.74	low
Unnamed	17	36.57	189.63	low
Unnamed	14	35.37	190.21	low
Unnamed	17	-6.07	191.81	high
Unnamed	13.8	11.58	192.05	low
Unnamed	13.8	6.24	192.07	low
Parsons E	24.6	37.45	192.3	low
Zhukovskiy Z	34	10	193.2	low
Unnamed	11.3	-22.16	193.4	low
Unnamed	16.3	14.05	193.63	low
Unnamed	10	-28.76	194.51	high
Unnamed	11	35.04	194.91	high
Unnamed	10	-0.66	195.03	low
Unnamed	11.8	34.32	195.12	low
Congreve G	18.3	-0.86	196.28	low
Unnamed	12	0.63	196.75	low
Unnamed	18.7	-31.72	196.84	low
Unnamed	10	14.05	197.37	low
Doppler W	15.4	-10.96	197.85	low
Korolev V	17.6	-1.26	198.18	low
Unnamed	10	-14.29	198.62	low
Unnamed	11.8	16.54	198.98	low
Van den Bergh P	15.2	29.19	199.83	high
Unnamed	15	37.09	200.64	low
Unnamed	14.1	-9.57	200.66	low
Unnamed	10.5	-25.15	201.16	low
Korolev Y	18.9	-0.56	201.61	low
Walker G	20.5	-26.63	201.71	low
Unnamed	11.3	28.36	202.05	low
Chaffee S	19.3	-39.77	202.51	low
Unnamed	13	-21.11	202.7	low
Unnamed	10	-11.02	203.35	low
Dryden	53.4	-33.19	203.77	low
Unnamed	10	4.46	203.82	low
Unnamed	12	32.36	204.18	low
Unnamed	14.3	29.47	204.56	low
Ingalls Y	21.1	29.5	205.7	low
Unnamed	13	-30.78	205.94	low
Korolev G	12.3	-5.63	206.63	low
Wilsing C	33	-19	207	low
Dirichlet	47.2	10.54	207.87	high
Korolev D	24.4	-0.36	208.22	low
Unnamed	15.8	32.21	208.55	low

Unnamed	12.3	-33.96	208.87	low
Unnamed	12.3	-1.31	209.71	low
Unnamed	10	26.76	209.8	low
Unnamed	13.3	34.37	210.69	low
Unnamed	15.2	-38.37	211.08	low
Dirichlet E	26.3	11.53	211.48	low
Unnamed	15	-14.33	211.75	low
Joule T	38	27.5	211.92	low
Blazhko	51.1	31.37	212.14	low
Unnamed	10	24.09	212.22	low
Unnamed	13.1	-30.07	212.76	high
Unnamed	10	14.57	212.79	low
Unnamed	11.5	-8.84	213.43	low
Galois F	13.8	-13.48	213.65	low
Unnamed	12	-16.62	214.36	low
Unnamed	15.3	34.27	214.44	low
Unnamed	26.4	-18.59	214.52	low
Unnamed	13.6	-35.57	215.04	low
Foster P	36	20.2	216.5	low
Unnamed	12	-15.94	216.58	low
Unnamed	13.8	8.25	217.19	high
Paschen S	44.2	-14.63	217.36	low
Joule K	16	25.67	218.17	low
Unnamed	11.7	31.95	218.46	low
Unnamed	15.2	18.31	218.56	low
Unnamed	13	-31.24	218.74	low
Unnamed	12.3	-26.91	218.8	low
Unnamed	10	-29.18	219.15	low
Unnamed	13.6	-15.86	220.23	low
Unnamed	12	36.05	220.5	low
Unnamed	12	35.11	220.51	low
Unnamed	14	24.44	220.7	high
Lovell F	27	-36.52	221.29	low
Unnamed	12.7	35.33	221.42	low
Sanford C	18.5	33.89	222.66	low
Chebyshev U	36	-33.3	223	low
Unnamed	11.2	-19.05	223.1	low
Unnamed	17	-36.92	223.52	low
Poynting X	22.3	23.17	223.54	low
Unnamed	12	25	224.03	low
Unnamed	14.6	16.96	224.09	low
Unnamed	13.5	10.56	224.21	low
Unnamed	12	-10.56	224.55	low
Stromgren X	39.6	-17.43	225.25	low
Chebyshev V	24.4	-33.55	226.02	low
Unnamed	13.4	-14.4	226.49	low
Unnamed	18.9	5.81	226.53	low

Unnamed	10	6.91	226.56	low
Hertzsprung R	30.4	-0.29	227.17	high
Unnamed	13.4	7.08	227.31	low
Unnamed	20.2	-35.39	227.41	low
Unnnamed	19	11.29	227.76	low
Unnamed	10	17.86	228.35	low
Unnamed	13	1.83	228.62	low
Unnamed	11.7	21.44	229.05	low
Unnamed	11.5	19.86	229.32	low
Unnamed	12.2	-27.84	229.58	low
Unnamed	11	10.49	231.78	low
Unnamed	20	14.93	231.85	low
Von der Pahlen H	35	-27.1	232.5	low
Unnamed	10.2	-30.51	233.45	low
Unnamed	19	8.62	233.71	high
Unnamed	17.9	11.83	234.69	low
Unnamed	13	22.41	234.71	high
Unnamed	12	-6.68	234.81	low
Hertzsprung H	19.7	-1.28	234.84	low
Houzeau P	15.8	-19.09	234.87	low
Michelson V	22.3	7.81	234.96	low
Unnamed	18.7	35.61	235.06	low
Hatanaka Q	19.6	25.99	235.36	low
Unnamed	13	23.8	235.58	high
Unnamed	15.7	-1.4	235.67	low
Lucretius U	23.3	-7.89	235.75	low
Unnamed	18	31.54	236.24	low
Unnamed	10	-25.34	236.67	low
Gerasimovich D	24.5	-22.49	237.99	low
Comstock A	20.3	24.69	238.35	low
Lucretius	63.2	-8.3	238.72	low
Unnamed	15.4	23.52	239.03	low
Ellerman	46.2	-25.56	239.5	low
Unnamed	10	25.67	239.63	low
Unnamed	11	-24.63	239.67	low
Unnamed	16.5	11.83	239.72	low
Unnamed	14	25.05	239.83	low
Unnamed	13.7	20.63	240.74	low
Unnamed	16.2	19.27	240.76	high
Unnamed	13	17.52	240.89	low
Unnamed	16.3	-20.97	241.38	low
Unnamed	11.8	26.16	241.46	low
Stetson E	35.8	-39.65	242.59	low
Unnamed	12.8	44.69	242.74	low
Unnamed	11	-34.92	242.87	low
Unnamed	14	37.78	243.1	low
Kearons U	13.2	-10.68	243.72	low

Unnamed	16	7.46	243.72	low
Unnamed	10.5	40.78	244.02	low
Unnamed	14.8	39.9	244.53	low
Unnamed	11.7	39.1	244.75	low
Unnamed	12	42.96	245.08	low
Unnamed	12.4	-14.15	245.34	low
Unnamed	13.1	32.88	245.76	low
Unnamed	13.5	-33.19	245.8	low
Unnamed	10	-39.41	247.58	low
Unnamed	14.7	13.38	248.09	low
Unnamed	12	28.28	248.14	low
Unnamed	15.2	32.9	249.27	high
Unnamed	10	39.61	249.3	low
Unnamed	13.7	-27.09	249.67	low
Leuschner Z	16.8	5.22	250.43	low
Leuschner L	18.5	-1.2	250.79	low
Leuschner	50.1	1.6	250.88	low
Butlerov	38.8	12.04	251.16	low
Grachev	36.5	-3.89	251.53	low
Unnamed	13.7	29.15	251.94	low
Unnamed	16.8	25.56	252.18	low
Lowell W	18.5	-10.28	252.67	low
Unnamed	12.5	34.89	253.13	low
Unnamed	16.2	-24.6	254.6	low
Robertson	89.9	21.82	254.63	low
Steklov	37	-36.73	254.99	low
Unnamed	11	2.67	255.1	low
Unnamed	12.8	6.64	255.49	low
Unnamed	10	15.98	256.02	low
Golitsyn J	19.3	-27.67	256.82	low
Lents Lenz C	23.3	3.28	258.28	low
Fryxell	17.6	-21.27	258.39	low
Unnamed	16.8	18.46	258.52	low
Unnamed	13	31.85	258.69	low
Lorentz U	23.4	35.46	260.13	high
Unnamed	11	18.46	261.71	low
Unnamed	10	25.82	261.74	high
Elvey G	13.5	7.77	262	low
Unnamed	14.2	34.35	262.42	low
Nernst T	26.7	35.86	263.01	low
Unnamed	12.4	37.58	263.42	low
Unnamed	14	24.83	263.53	high
Unnamed	11.4	32.82	263.93	low
Unnamed	10	31.9	263.99	low
Unnamed	10	8.55	264.2	low
Heyrovsky	17	-39.59	264.6	low
Unnamed	11.3	30.62	264.76	low

Bell K	19	18.34	264.86	high
Unnamed	11.2	4.07	265.05	high
Unnamed	11	10.36	265.54	low
Focas	22	-33.75	266.1	low
Unnamed	13	33.45	266.33	low
Sundman V	17.9	11.98	266.46	low
Unnamed	13	12.77	266.88	low
Unnamed	11	-35.02	267.05	low
Unnamed	13	18.49	267.26	low
Shuleykin	14.3	-27.14	267.34	low
Couder	18.6	-4.89	267.45	low
Unnamed	11	-2.31	267.7	low
Unnamed	11	38.62	267.91	low
Drude	23	-38.61	268.12	low
Unnamed	15.7	37.08	268.42	low
Unnamed	13	10.17	268.7	low
Maunder A	15	-3.26	269.41	low
Sundman J	10	8.84	269.8	low
Kopff E	11.2	-15.97	270.12	low
Aston K	14.5	35.01	272.14	low
Pettit	36.7	-27.57	273.27	high
Wright	38.7	-31.6	273.3	low
Schluter P	20.8	0.08	274.81	low
Nicholson	38.1	-26.26	274.85	low
Lallemand	16.7	-14.4	275.81	low
Eichstadt K	13.8	-18.29	276.63	low
Balboa A	47	17.4	278.1	high
Unnamed	10	10.39	278.63	low
Eichstadt G	11.2	-22.43	279.16	low
Bouvard S	11.7	-35.62	279.37	low
Unnamed	10	11.44	279.72	low
Krasnov D	12.2	-33.99	279.78	low
Eichstadt H	10.8	-19.1	280.03	low
Lavoisier B	25.6	39.74	280.28	low
Hedin Z	10.2	1.89	281.02	low
Hartwig B	10.2	-8.45	282.48	low
Bouvard C	14.6	-37.09	282.52	low
Cardanus C	13.7	11.16	283.74	low
Riccioli H	17.5	1.13	284.99	low
Hedin F	19.2	3.94	285.52	high
Rocca J	12.8	-15	286	low
Riccioli CA	14.1	0.63	286.87	low
Hedin L	10.5	5.11	288.56	low
Riccioli G	15	-1.27	288.89	low
Hevelius A	14	2.85	291.78	low
Byrgius D	27.1	-24.09	292.75	high
Lagrange H	10.4	-29.49	293.71	low

Lagrange C	22.4	-29.92	294.95	low
Grimaldi S	11	-6.35	295.14	low
Piazzi C	28	-37.17	297.27	low
De Vico F	12.5	-19.09	297.28	low
De Vico E	12.2	-21.18	298.51	low
Piazzi F	11	-35.72	298.85	low
Sirsalis	40.2	-12.51	299.49	low
De Vico	22.1	-19.74	299.69	low
Lehmann C	15.1	-35.57	309.83	low
Palmieri E	14.2	-29.25	311.37	low
Billy D	10.9	-14.87	311.61	low
Mersenius S	15.7	-19.24	312.94	low
Ramsden G	11	-35.36	328.25	low
Haidinger J	14.5	-37.99	335.49	low
Cichus B	13.8	-33.21	340.55	low
Gauricus D	12.3	-35.15	348.45	low
Lalande C	10.5	-5.6	353.04	low
Bancroft	12.5	28.07	353.57	low
Thebit A	19.9	-21.59	355.04	low
Herschel C	10	-5.02	356.83	low
Herschel	39.1	-5.7	357.87	low
Lexell A	34	-36.9	358.6	high
Bode A	12.2	8.98	358.8	high
Conon	21	21.66	1.95	low
Hipparchus K	10.9	-6.98	2.12	low
Hipparchus J	13.8	-7.6	3.16	low
Werner	70.6	-28.06	3.22	high
Argelander D	10.7	-17.65	4.39	low
Aratus	10.2	23.56	4.5	low
Nonius A	10.2	-35.41	5.47	low
Pickering	15.4	-2.88	6.95	low
Hipparchus G	13.7	-5.03	7.36	low
Airy A	12.2	-17.05	7.62	low
Apianus B	10.2	-27.44	8.93	low
Hipparchus L	12.7	-6.88	8.96	low
Lade M	11.2	-1.12	9.36	low
Kaiser C	12.1	-36.6	9.6	high
Abenezra B	13.8	-20.84	10.01	low
Abenezra A	22.2	-22.83	10.39	low
Agrippa	43.8	4.08	10.47	low
Abulfeda A	13.3	-16.45	10.71	low
Gemma Frisius K	10	-37.52	10.88	low
Silberschlag	13	6.19	12.51	low
Abulfeda F	17.5	-16.2	13.04	low
Gemma Frisius W	14	-36.96	13.25	low
Whewell	13.1	4.14	13.72	low
Cayley	14.2	3.93	15.07	low

Descartes A	14.3	-12.09	15.18	low
Theon Senior	18	-0.83	15.4	low
Theon Junior	17.4	-2.41	15.77	low
Sacrobosco C	12.6	-23.02	15.78	low
Zagut P	13.7	-32.48	17.38	low
Busching E	14.7	-36.72	18.36	low
Alfraganus	20.5	-5.44	18.95	high
Zollner J	10.4	-6.21	20.67	high
Pons B	13.4	-28.78	20.7	low
Zagut A	11.4	-32.07	21.63	low
Rabbi Levi L	11.9	-34.75	22.96	low
Cyrillus E	10.5	-15.92	25.28	low
Polybius B	12	-25.59	25.49	low
Theophilus	98.6	-11.48	26.25	low
Beaumont B	15.1	-18.74	26.77	low
Rothmann	43.2	-30.84	27.72	high
Rabbi Levi R	11.9	-34.2	27.9	low
Polybius A	16.3	-23.06	27.97	low
Piccolomini D	16.5	-26.97	32.23	high
Isidorus A	10	-8.08	33.19	low
Piccolomini L	12.1	-26.15	33.73	low
Isidorus D	15	-4.29	34.05	low
Fracastorius B	26.7	-22.59	37.24	low
Leakey	12.5	-3.22	37.44	low
Neander A	11.2	-30.98	39.58	low
Maury	17.2	37.09	39.65	low
Proclus D	12.3	17.41	41.01	low
Santbech B	15.7	-24.75	41.56	low
Maury A	21.1	35.96	41.87	low
Bohnenberger E	11.9	-17.42	42.08	low
Proclus A	13.6	13.32	42.22	low
Reichenbach K	10.7	-28.91	42.37	low
Newcomb	41	29.9	43.8	low
Berzelius F	11.6	32.81	45.99	high
Fredholm	13.4	18.34	46.53	high
Geminus Z	30.9	30.71	46.66	low
Tralles A	17	27.4	47	low
Geminus G	14	30.79	48.56	low
Biot A	14.9	-22.21	48.83	low
Reichenbach A	33.5	-28.29	48.86	low
Unnamed	14.2	-31.76	49.36	low
Glaisher	15.9	13.15	49.36	low
Reichenbach H	10.7	-28.88	49.59	low
Tralles B	11.5	27.23	50.64	low
Cleomedes B	10.7	27.13	55.88	low
Geminus	82.6	34.31	56.63	low
Furnerius C	20.6	-33.75	57.69	low

Geminus C	15.5	33.87	58.69	low
Messala B	17	37.34	59.77	low
Petavius C	11.2	-27.71	59.92	low
Delmotte	30.6	27.12	60.16	low
Firmicus F	10	6.51	61.74	low
Hase A	14.6	-29.07	62.93	low
Langrenus P	42.3	-12.1	63.01	low
Auzout	32.9	10.17	63.95	low
Adams B	31.3	-31.54	65.67	low
Lame Z	17.5	-15.86	65.74	low
Langrenus M	18.2	-9.82	66.39	low
Bernoulli D	11.9	35.77	66.48	low
Bernoulli C	18	35.37	67.16	low
Hahn A	18.3	29.64	69.69	low
Maclaurin D	11.2	-7.07	69.86	low
Unnamed	11	8.13	70.39	low
Plutarch C	13.2	23.15	70.93	low
Rankine	10.5	-3.88	71.49	low
Gauss C	30	39.71	72.06	low
Plutarch H	12	24.36	72.75	low
Hahn F	25.6	32.15	72.88	low
Condorcet M	12.2	9.06	73.09	low
Marinus A	26.9	-39.94	73.23	low
Phillips A	14.8	-27.14	73.57	low
Liouville	15.9	2.74	73.57	low
Gauss D	25.1	39.35	73.85	low
Alhazen A	16.7	16.18	74.32	low
Hansen A	13.5	13.36	74.64	low
Wildt	12.3	9.01	75.8	low
Unnamed	11	2.9	75.89	low
Unnamed	12.6	23.78	77.67	low
Marinus N	14.3	-37.54	77.83	low
Unnamed	11	8.28	78.65	low
Unnamed	10	-1.21	78.7	low
Schubert J	21.5	-0.01	78.94	low
Sabatier	10.1	13.17	78.98	low
Plutarch	69.6	24.12	79	low
Unnamed	14	22.83	79.73	low
Unnamed	10	30.36	79.76	high
Unnamed	15.6	19.55	79.82	low
Knox Shaw	13.4	5.34	80.16	low
Gauss W	18.2	34.62	80.24	low
Back	34.6	1.31	80.63	high
Humboldt N	14.5	-26.04	80.68	low
Hecataeus J	11.7	-22.51	80.88	low
Seneca F	16.4	29.61	81.89	low
Unnamed	12.2	25.69	82.4	low

Kastner S	30.5	-7.93	83.06	low
Humboldt B	20.9	-30.77	83.64	low
Unnamed	11	11.35	84.19	high
Gum S	34.1	-39.66	84.93	low
Unnamed	11	25.69	85.24	low
Goddard B	12.2	16.11	86.9	low
Schorr C	12.2	-13.47	88.17	low
Rayleigh B	15.5	29.03	88.54	low
Unnamed	10	36.64	89.14	low
Rayleigh D	22.3	29.01	89.73	low
Brunner N	16.8	-11.42	90.69	low
Unnamed	10	-10.03	93.14	low
Zasyadko	11.9	3.94	94.2	low
Vestine A	20.5	35.98	94.58	low
Unnamed	14	22.06	94.72	low
Lauritsen Y	13.8	-27.53	96.41	low
Sklodowska J	14.7	-19.44	97.92	low
Popov W	25	19.05	97.97	low
Fox A	12.5	1.51	98.29	low
Unnamed	12	-26.37	99.86	low
Unnamed	12.4	12.05	100.23	low
Koval skiy P	18.3	-22.43	100.55	low
Saenger R	11	3.37	100.64	low
Unnamed	10	-9	100.67	low
Saenger Q	12.4	3.43	101.97	low
Unnamed	11	-31.31	102.12	high
Saenger X	18.3	6.39	102.12	low
Unnamed	11	17.35	103.02	high
Moiseev	61.2	9.52	103.31	low
Pasteur Z	13.7	-7.02	104.48	low
Unnamed	37	28.62	104.56	low
Unnamed	11	38.26	105.12	low
Hilbert S	10.6	-18.33	106.08	low
Scaliger U	10	-26.77	106.67	low
Unnamed	15	11.78	106.83	low
Malyy G	28.2	21.7	107	low
Unnamed	15	19.72	107.23	high
Unnamed	10	34.08	107.77	low
Saha E	29.9	-0.24	108.01	low
Unnamed	10	22.1	108.8	low
Unnamed	10	22.22	109.36	high
Unnamed	12	-39.76	109.59	low
Hilbert H	15.9	-18.45	109.85	high
Sumner G	17.5	37.4	110.35	low
Einthoven L	15	-8.36	111.15	high
Unnamed	10	11.99	111.2	low
Milne N	38.7	-35.86	111.24	low

Unnamed	13	12.84	111.5	high
Unnamed	11.9	15.15	111.96	low
Unnamed	15	19.08	112.2	high
Unnamed	12	11.65	112.39	low
Alden E	25.9	-23.42	112.76	low
Alden B	15.1	-20.62	113.11	low
Milne L	26.9	-33.99	113.16	low
Unnamed	17	29.75	114.29	low
Vesalius M	30.4	-5.92	114.82	low
Izsak T	13.7	-23.34	115.22	high
Guyot W	21.5	13.87	115.48	low
Meitner J	13.9	-12.29	115.58	high
Unnamed	14	27.74	115.75	low
Viviani N	16.4	3.48	116.48	low
Unnamed	12	26.98	116.91	low
Unnamed	10.7	13.07	117.47	high
Olcott	79.9	20.39	117.54	low
Izsak	31.3	-23.33	117.55	low
Sherrington	18.4	-11.14	118	low
Pizzetti W	13.8	-33.96	118.32	low
Innes	42.8	27.84	119.13	low
Unnamed	17	25.83	119.41	high
Unnamed	11	12.47	121.31	low
Unnamed	10	-4.86	121.42	low
Neujmin Q	17.3	-30.05	121.76	low
Innes G	21.1	26.86	122.43	low
Unnamed	14	37.09	123.16	low
Unnamed	10	-39.66	123.373	low
Unnamed	10	-39.67	123.38	low
Unnamed	14	-23.32	123.41	low
Unnamed	10	-39.1	123.72	low
Unnamed	13	16.87	124.08	high
Becvar X	29	-1.01	124.45	low
Danjon K	15.7	-13.8	125.07	low
Tsiolkovskiy X	12.1	-14.74	126.42	low
Unnamed	12	18.62	127.06	low
Unnamed	12	15.27	127.65	low
Unnamed	12	39.19	128.35	low
Shirakatsi	49.7	-12.25	128.51	low
Unnamed	11	22.84	129.09	low
Unnamed	17	16.97	129.27	low
Lampland Q	12.7	-32.63	130.06	low
Unnamed	13	24.91	130.07	high
Morozov E	13.5	5.56	130.47	high
Unnamed	13	32.38	130.63	low
Eotvos T	13.3	-35.66	131.33	low
Green P	18.8	0.49	131.97	high

Unnamed	10	12.71	132.55	low
Unnamed	13	28.14	133.09	high
Green M	35.3	0.35	133.09	low
Chauvenet U	10	-11.1	135.45	low
Unnamed	11	36.77	135.45	low
Hartmann K	10.6	1.42	136.1	low
Glazenap	39	-1.87	137.77	low
Pannekoek T	23.3	-4.27	138.45	high
Unnamed	11	23.06	139.89	high
Pannekoek S	16	-4.37	140.21	low
Unnamed	16.2	35.36	140.6	high
Unnamed	13	38.98	141.04	low
Unnamed	13	1.02	143.14	low
Unnamed	10	-30	143.3	low
Harden	15.7	5.47	143.54	low
Vil ev B	12	-4.6	144.8	low
Unnamed	10	-11.51	145.41	low
Unnamed	11	-0.98	147.63	low
Unnamed	11	21.94	147.7	low
Schuster K	17.8	1.24	147.72	high
Chaplygin Q	12.1	-7.63	147.89	low
Unnamed	13	17.76	148.28	low
Unnamed	10.8	-22.42	149.78	low
Unnamed	11	-34.57	149.89	low
Unnamed	13.3	-26.46	150.9	low
Unnamed	12.6	-26.44	150.91	high
Chaplygin K	19.6	-7.67	151.37	low
Unnamed	10	-35.49	152.17	low
Schliemann W	19.3	0.25	152.4	low
Kohlschutter Q	20	12.83	152.68	high
Schliemann T	19.2	-1.94	152.68	high
Unnamed	10	24.23	155.07	low
Unnamed	13.4	-6.03	155.1	low
Nikolaev J	19.5	31.58	155.37	low
Unnamed	14	-34.97	155.5	low
Schliemann G	15.3	-2.23	156.71	high
O Day M	13.3	-31.58	157.13	low
Unnamed	10	8.3	157.14	low
Lundmark F	25.6	-39.11	157.36	low
Ventris B	16.4	-2.21	158.14	low
Ventris A	25.7	-4.2	158.32	high
Tikhomirov T	25.5	25.39	158.71	low
Van Gent X	38.3	16.29	159.58	low
Unnamed	11	-15.9	159.64	low
Obruchev X	22.1	-34.72	159.83	low
Barbier G	16.6	-24.16	159.85	low
Ventris D	22.1	-3.57	160.2	high

Cyrano E	20.9	-20.08	161.41	low
Unnamed	10	13.14	162.05	high
Unnamed	12.7	33.54	162.15	high
Thomson V	13.2	-30.72	162.43	low
Stearns	37.7	34.63	162.5	low
Unnamed	13	8.79	162.81	low
Unnamed	11	17.28	162.89	low
Plante	37.8	-10.35	163.43	low
Thomson W	18.4	-30.25	163.84	low
Stratton Q	11.9	-6.19	164.89	low
Unnamed	12	-15.04	164.9	low
Unnamed	15	2.33	165.37	high
Unnamed	12	-5.01	166.01	high
Unnamed	10	-19.99	166.01	low
Paracelsus H	10.7	-25.81	166.33	low
Zernike T	17	18.46	167.23	low
Dewar F	12.3	-2.75	167.62	low
Spencer Jones H	13.4	11.94	168.12	low
Spencer Jones J	13.2	9.65	168.27	low
Dufay Y	16.3	8.26	168.62	low
Unnamed	11	-2.29	168.69	high
Coriolis S	17.5	-0.01	169.7	low
Unnamed	10	-1.68	170.17	low
Unnamed	14	37.59	170.92	low
Anderson L	14.2	14.64	171.17	low
Dufay B	24.2	8.36	171.26	low
Unnamed	14.6	-27.61	171.35	low
Unnamed	10	-27.28	171.6	low
Unnamed	11	17.52	171.65	low
Van de Graaf C	21.7	-26.46	172.83	low
Daedalus S	22.4	-6.73	172.88	high
Unnamed	10	37.52	172.98	high
Sharonov	78.2	12.35	173.17	low
Birkeland	84.3	-30.13	173.96	low
Coriolis H	10.2	-0.74	174.23	high
Van de Graaf F	18.7	-26.79	174.69	low
Coriolis G	18.5	-0.02	174.71	low
Unnamed	20.5	38.61	177.07	low
Dante S	18.1	25.16	177.63	high
Unnamed	15.2	7.17	177.83	low
Unnamed	15.8	9.52	178.55	low
Daedalus M	12.3	-8.05	179.69	low

APPENDIX B

TERRESTRIAL SILICIC DOMES

Table B.1: List of Terrestrial Silicic Domes

Volcano	Description	D [m]	H [m]	Source
Chato W	dome	3000	300	Folguera et al., 2009, JVGR
Chao (Negro WW)	coulee	2350	260	Folguera et al., 2009, JVGR
La Leña W2	torta/coulee	2550	60	Folguera et al., 2009, JVGR
La Leña W3	torta/coulee	1630	120	Folguera et al., 2009, JVGR
Chao	dacite coulee	14000	400	de Silva et al., 1994
Lassen Peak	dacite dome	4500	725	USGS
North Deadman Creek	rhyolite dome	650	125	Miller, 1985
Wilson Butte	rhyolite dome	640	80	Miller, 1985
Medicine Lake Flow	dacite torta	1800	28	Donnelly-Nolan, 1990
Glass Creek Dome	rhyolite dome	1200	100	Miller, 1985
Obsidian Dome	rhyolite dome	1500	75	Miller, 1985; Vogel et al., 1989
South Deadman Creek	rhyolite dome	1430	132	Miller, 1985
Cerros La Torta	rhyolitic dome	3700	325	de Silva et al., 1994
Cerro Chillahuita	torta	4080	200	de Silva et al., 1994
Cerro Chascon, Bolivia	rhyolite torta	5200	425	de Silva et al., 1994
Santorini	Liatsikas	40	11	Georgalas, 1962*
Abu	"10"	480	30	Koyaguchi 1986; Moriya, 1978*
Ukinrek	E. Maar	120	40	Kienle et al., 1980*
Barcena	1952	60	8	Richards, 1959*
Novarupta	1912	380	65	Hildreth, 1983*
Galunggung	1918	500	85	Allard, 1983*
Mt. St. Helens	1980-06-01	366	45	Moore et al., 1981*
Soufriere	final shape	868	133	Huppert et al., 1982*
Primavera	field-smallest	276	68	Clough et al., 1982*
Primavera	field-largest	2186	1093	Clough et al., 1982*

Volcano	Description	D [m]	H [m]	Source
Maroa	field-smallest	134	25	Lloyd (unpub. maps)*
Maroa	field-largest	778	80	Lloyd (unpub. maps)*
Coso	field-smallest	426	85	Duffield and Bacon (1981)*
Coso	field-largest	1000	183	Duffield and Bacon (1981)*

* indicates domes mentioned in Blake (1990).

APPENDIX C

IRREGULAR MARE PATCHES (IMPS)

Table C.1: List of 75 Irregular Mare Patches (IMPs)

Informal Name	L [m]	Lat [°]	Lon [°]	Host Mare
1. Sosigenes	5000	8.335	19.071	Tranquillitatis
2. Ina	3000	18.650	5.300	Lacus Felicitatis
3. Cauchy-5	3000	7.169	37.592	Tranquillitatis
4. Hyginus	150	7.726	6.350	Vaporum
5. Manilus-1	270	14.889	6.467	Vaporum
6. Manilus-2	200	14.628	6.821	Vaporum
7. Tranq. Whale*	430	8.891	21.487	Tranquillitatis
8. Maskelyne	3000	4.330	33.750	Tranquillitatis
9. Arago-5	730	9.230	20.824	Tranquillitatis
10. Carrel-1	ellipsoid	9.817	25.519	Tranquillitatis
11. Aristarchus North	800	25.044	313.233	Oceanus Procellarum
12. Jansen-1	600	11.669	32.659	Tranquillitatis
13. Jansen-2	300	11.235	32.806	Tranquillitatis
14. Unnamed	150	7.083	38.574	Tranquillitatis
15. Unnamed	200	9.244	23.924	Tranquillitatis
16. Unnamed	ellipsoid	4.550	22.882	Tranquillitatis
17. Unnamed*	350	8.670	17.510	Tranquillitatis
18. Unnamed‡	315	7.887	21.937	Tranquillitatis
19. Unnamed	400	9.112	21.758	Tranquillitatis
20. Unnamed*	560	8.298	21.600	Tranquillitatis
21. Unnamed†	170	4.096	21.218	Tranquillitatis
22. Unnamed*	400	10.310	21.360	Tranquillitatis
23. Unnamed*	340	9.540	20.220	Tranquillitatis
24. Unnamed	300	10.163	19.228	Tranquillitatis
25. Unnamed	255	9.102	20.265	Tranquillitatis
26. Unnamed	800	9.102	20.298	Tranquillitatis
27. Unnamed	1200	10.460	23.547	Tranquillitatis
28. Unnamed	160	8.844	21.762	Tranquillitatis
29. Unnamed	500	7.348	20.897	Tranquillitatis
30. Unnamed	670	7.559	20.984	Tranquillitatis
31. Unnamed	60	7.586	21.019	Tranquillitatis
32. Unnamed**	150	8.714	19.383	Tranquillitatis
33. Unnamed	550	9.580	25.514	Tranquillitatis
34. Unnamed	350	9.564	25.392	Tranquillitatis
35. Unnamed	250	9.894	24.851	Tranquillitatis
36. Unnamed	150	10.101	25.278	Tranquillitatis
37. Unnamed	280	10.045	25.247	Tranquillitatis
38. Unnamed	350	9.432	26.287	Tranquillitatis
39. Unnamed	100	9.012	22.248	Tranquillitatis
40. Unnamed	100	9.738	22.320	Tranquillitatis
41. Unnamed	270	10.770	20.520	Tranquillitatis
42. Unnamed	350	21.653	359.135	Imbrium
43. Unnamed	250	37.121	319.374	Imbrium

44. Unnamed	230	8.279	9.319	Vaporum
45. Unnamed	160	13.131	355.639	Sinus Aestuum
46. Unnamed	150	12.931	356.194	Sinus Aestuum
47. Unnamed	125	-2.008	43.333	Fecunditatis
48. Unnamed	100	-2.113	43.512	Fecunditatis
49. Unnamed**	100	26.786	317.041	Oceanus Procellarum
50. Unnamed	300	14.44	326.344	Insularum
51. Unnamed	150	14.597	326.021	Insularum
52. Unnamed	100	14.468	326.271	Insularum
53. GEM35	100	36.937	315.879	Unnamed
54. GEM32	140	37.826	314.871	Unnamed
55. GEM30	330	37.919	314.779	Unnamed
56. GEM29	100	37.904	314.920	Unnamed
57. GEM28	175	37.304	316.372	Unnamed
58. GEM26	100	37.417	316.423	Unnamed
59. GEM24	200	37.428	316.457	Unnamed
60. GEM22	400	37.924	315.726	Unnamed
61. GEM21	150	37.882	315.712	Unnamed
62. GEM20	275	37.849	315.667	Unnamed
63. GEM19	130	37.925	315.683	Unnamed
64. GEM17	100	37.974	315.715	Unnamed
65. GEM12	100	37.995	315.841	Unnamed
66. GEM11	130	37.941	315.782	Unnamed
67. GEM9	125	38.086	315.894	Unnamed
68. GEM8	110	38.128	315.923	Unnamed
69. GEM7	140	38.058	315.927	Unnamed
70. GEM6	100	37.864	315.522	Unnamed
71. GEM5	360	37.907	315.496	Unnamed
72. GEM4	190	38.090	315.416	Unnamed
73. GEM3	170	38.115	315.323	Unnamed
74. GEM2	190	38.156	315.404	Unnamed
75. GEM1	300	38.152	315.400	Unnamed

*First mentioned in Stooke et al., 2012. **Stooke 2013 personal communication. †Schultz, 1976. ‡Schultz 2006. The informal name prefix GEM indicates that the IMP occurs in the region near the impact craters Gruithuisen E and M.